Perceived quality characterization of micro-textured injection moulded components for automotive interior applications

Dissertation submitted by:

Dipl.- Ing. Pablo Gamonal Repiso

in conformity with the requirements for the degree of
Doctor in Materials Science and Engineering

Directors (UPC)

Dra. Maria Lluïsa Maspoch Rulduà

Dr. Miguel Sánchez Soto

Responsibles (SEAT)

Dr. Jose Maria del Mazo Viñas

Dipl.-Ing. Soledad Santos Pinto

“Creativity is intelligence having fun.”

- **Albert Einstein**

Acknowledgements

The success of this research is thanks to the collaboration of institutions such as the *UniversitatPolitècnica de Catalunya Barcelona-Tech*, the *Centre Català del Plástic* and the automotive company *SEAT S.A.* They have all been essential in the development of this project. My deepest thanks to you all.

To my thesis directors, Prof. Dr. Maria Lluïsa Maspoch and Prof. Dr. Miguel Sánchez, thank you. Thank you for your contributions and fruitful discussions. Thank you for supporting and encouraging me every step of the way. Thanks for your advice and for your time. I have learnt so much with you. I would like to continue with my thesis tutors in SEAT, Dr. Jose Maria del Mazo and Ing. Soledad Santos. Thank you for your contributions, time and discussions, especially the industrial point of view that you provided to me. This has been a key point for understanding the application of this research project to the automotive industry. These few words are in no way enough at all for their efforts made during this period.

The following words of gratitude are addressed to the entire staff of the *Centre Català del Plàstic,* where I have lived incredibly good moments. Dr. Antonio Martinez, Dr. David Arencón, Dr. Jonathan Cailloux, Dr. Marcelo Antunes, Dr. Orlando Santana, Dra. Vera Realinho, Dr. TobiasAbt, Dr. Noel León, Dr. José Ignacio Velasco, Anna Carreras, Susana Ortiz, Violeta del Valle, David Loaeza, Magali Klotz, Paul Jokinen and Xavier Cruz.

I would like to express my appreciation to my colleagues in the Quality Department of SEAT (GQ-31, Materials Technology). All of them have supported this research project: Silvia, Dr. Javier, Rafael, Maria José, Cristina, Fernando, Elisabet, Xavi, Juan José, Ramón, Arantxa, Antonio, Miguel Angel, Gerardo, Adrián, Francisco, Blanca and Mercedes. Likewise, I would like to highlight the participation and collaboration of Noemi Rodriguez, Andrea Naudín and David Patiño who performed the SEM analysis. Finally, I would like to thank my PhD colleagues of SEAT. Dr. Mireia, Dr. Marcelus, Dr. Hector, Dr. Rocio,

Dr. Paola, Román, Marc, Pedro, María, Ana Cristina and Aitor. Thanks for the moments lived with you all and the shared experiences.

My gratitude is also extended to the companies that have collaborated in this project. *Basell* for providing the raw material, *Standex* for engraving the mould, *FRT* for the technical support and *BYK-Gardner* for believing in this research and lending me their new instrument. I would like to mention that all these contributions were offered free of charge.

To my family, parents and brother, thanks. Thanks for your support. You have always trusted in me. Finally, I would like to end by thanking Ana. She has been the one who most believed in me, who most encouraged me and who has given me the most important thing of all during this period, our kids Noa and Pau (and our dog Dana). This has been without any doubt the highest success I have ever achieved. From the bottom of my heart, thanks.

Thank you very much!

¡Muchas gracias a todas y todos!

Abstract

The present PhD thesis is framed within a collaborative project in which institutions such as the Universitat Politècnica de Catalunya Barcelona-Tech, the Centre Català del Plàstic and SEAT S.A have participated. The main objective of this research is to improve the surface quality of the textured injection moulded components of the car interior. To this end, a methodology that allows assessing the appearance objectively using three-dimensional characterization techniques is proposed.

The texture replication ratio of a mould cavity was first investigated. Squared samples of Polypropylene (PP) were injection moulded. It was found that the holding pressure was the most significant parameter for improving the texture replication ratio. In addition, using three-dimensional characterization techniques, it was demonstrated that the multi-scale methodology was a suitable technique to quantify the replication ratio and effectively separate the main surface components namely, roughness, waviness and form either at the macro- or the micro-scale.

Four texture types were utilized to measure the surface appearance. The first one was a leather texture, the second and the third types were obtained by applying a mould treatment on the previous original leather texture. The fourth one was obtained through a painting process. The appearance was measured using a new Total Appearance Measurement (TAM) apparatus. A relationship between topographic features such as roughness, functional height distribution (FHD), texture slope (TS) and texture aperture angle (TAA) and surface appearance properties such as gloss and reflectivity contrast was established.

Finally, the surface performance was studied by means of both scratch and mar resistance tests. The texture influence on the scratch hardness and the scratch visibility resistance was evaluated and quantified using three dimensional techniques. Topographic characteristics such as peak-to-valley symmetry and the number of micro-asperities were analysed. The results showed that surfaces with higher symmetry in their functional height

distributions yield lower lightness variations (ΔL*) between the scratch pattern and its residual background height (RBH). On the other hand, topographies with a smaller number of micro-asperities on top of the texture provided an enhanced mar resistance. In these cases, deformation mechanisms such as ironing are minimized, resulting in a lower gloss variation and lower contrast between the damaged area and its surroundings.

Resumen

La presente tesis doctoral se enmarca en un proyecto colaborativo donde instituciones como la Universitat Politècnica de Catalunya Barcelona-Tech, el Centre Català del Plàstic y la compañía SEAT S.A han participado en el desarrollo de este proyecto de investigación. El principal objetivo de esta investigación es la mejora de la calidad superficial de componentes inyectados y texturizados del interior del vehículo. Para ello se propone una metodología que permita evaluar la apariencia de una forma objetiva basándose en técnicas tridimensionales.

El ratio de replicación de la textura del molde fue primero investigado mediante el uso de técnicas basadas en las tres dimensiones. Probetas cuadradas de polipropileno (PP) fueron inyectadas. Se encontró que la presión de mantenimiento era el parámetro qué más influencia tenía para mejorar el ratio de replicación de la textura. Además, fue demostrado que la metodología de análisis superficial multi-escala era adecuada para cuantificar el ratio de replicación y separar de una forma efectiva los componentes de la superficie (rugosidad, ondulación y forma) ya sea a macro o micro-escala.

Cuatro tipos de textura imitación piel fueron utilizados para medir la apariencia. El primero era la textura piel original, el segundo y el tercer tipo fue el resultado de aplicar tratamientos de molde sobre la textura piel original. El cuarto tipo de textura piel fue obtenido mediante un proceso de pintura. La apariencia superficial fue evaluada por un equipo nuevo, llamado *Total Appearance Measurement (TAM)*. Se relacionaron características topográficas como la rugosidad, la distribución de alturas funcionales, el ángulo de la textura y el ángulo de apertura de la textura con propiedades de apariencia tales como el brillo superficial y el contraste de reflectividad.

Finalmente, la funcionalidad de las superficies texturizadas fue estudiada a través de pruebas como la resistencia al rayado y al efecto escritura. La influencia de la textura sobre la dureza de rayado y la visibilidad del rayado fue evaluada y cuantificada mediante el uso de técnicas en tres dimensiones. Características topográficas como la simetría pico-valle y la

cantidad de micro-asperezas fueron analizadas. Los resultados mostraron que superficies con una distribución de sus Alturas funcionales simétrica tienden a una menor variación en la luminosidad (ΔL^*) entre el patrón rayado y su altura residual. Por otro lado, las superficies con menor cantidad de micro-asperezas tienen una mayor resistencia al efecto escritura. En estos casos, el mecanismo de deformación conocido como "planchado" se minimiza, resultando en una menor variación de brillo y contraste entre la zona dañada y los alrededores.

Table of contents

List of figures

List of tables

Abbreviations and symbols

ΔL^*	Lightness variation
$\Delta x, \Delta y$	Sampling intervals in X and Y
μ	Coefficient of friction
a^*	Red/green axis of the CIELAB coordinate system
b^*	Blue/yellow axis of the CIELAB coordinate system
C^*	Chroma
h^*	Hue
L^*	Lightness
2D	Two-dimensional
3D	Three-dimensional
A	Sampling area
Aa	Aparent contact area
ACF	Autocorrelation function
AFH	Absolute functional height
C	Contrast
CS	Contrast sensitivity
CSF	Contrast sensitivity function
F_F	Force of friction
F_N	Normal force
f_h	High frequency limit
FHD	Functional height distribution
f_L	Long frequency limit
G	Gloss measurements at 60º
GA	Grain area

$\overline{GA}$	Average grain area
GV	Grain volume
$\overline{GV}$	Average Grain volume
Hs	Scratch hardness
h_{tot}	Total height
HST	Hill size threshold
HVS	Human vision system
l_x, l_y	Sampling lengths in X and Y
NG	Number of grains
Nx, Ny	Data points in X and Y
Ph	Holding pressure
PS	Photometric stereo
PSD	Power spectral density function
Ra	Arithmetical mean height of a profile
RBH	Residual background height
RCA	Real contact area
RCT	Reflectivity contrast threshold
R_{max}	Maximum radii
R_{min}	Minimum radii
S	Share strength of materials
Sa	Arithmetical mean height
Sal	Autocorrelation length
Sk	Core height
Sku	Kurtosis of the scale-limited surface
Smr(c)	Areal material ratio
Sp	Maximum peak height
Spk	Reduced peak height

Sq	Root mean square height
Ssk	Skewness of the scale-limited surface
Str	Texture aspect ratio
Sv	Maximum dale height
Svk	Reduced dale height
Sz	Maximum height
TAA	Texture aperture angle
TAM	Total appearance measurement
Tm	Melt temperature
Tmd	Mould temperature
TS	Texture slope
Ucal	Uncertainty of the calibrated surface
Ucwl	Uncertainty of the measurand
Up	Uncertainty of the measurement
Ures,cwl	Uncertainty of the CWL sensor
$U_{res,TAM}$	Uncertainty of the camera resolution
Usa	Extended uncertainty
Usa,Inj	Uncertainty of the injection process
U_{TAM}	Uncertainty of the measurand
Vfr	Injection volumetric flow rate

Chapter 1:   Introduction

An object's appearance is an attribute that we, as humans, learn to define over time. As adults, we certainly know whether an object is shiny, transparent or blue based on our past experiences. Therefore, it is an unconscious process that leads us to distinguish the appearance of objects [1].

Objects are usually perceived by our eyes, which receive the reflected light coming from an object's surface. This light is then converted into a signal that is processed by the brain, resulting in the identification of appearance attributes. Usually, observers are not aware that the response created by their brains is the result of a physical interaction between light and object's surface. For instance, someone who buys a new car may just enjoy its shininess without wondering whether the surface is smooth enough to achieve the desired gloss [1].

Some industries treat the object's appearance as an important characteristic, since customers' judgements can be altered as a function of their products appearance, making objects seem more or less appealing [2]. For example, in electronics the appearance of a mobile phone can alter the customer's decision regarding its purchase. Usually, smooth and shiny surfaces are preferred in this sector. In addition, a good touch feeling is an added value in the perceived quality. In regard to appearance and quality in the automotive industry there are two different scenarios, the exterior and the interior of the car. In the former case, normally shiny and smooth surface finishes are desirable, whereas in the interior, textured and matted surfaces are better suited for providing a high quality feeling [3].

Figure 1.1 Interior design of the SEAT 600 model (left) and SEAT Leon model (right)

In the particular case of the car interior design, this has evolved a great deal over the years. For example, Figure 1.1 shows the interior of the SEAT 600 model (launched in 1957) and the SEAT Leon model (launched in 2020). In the first case, the usage of plastics in the interior is almost residual, with metal being the predominant material. On the contrary, in the case of the SEAT Leon, plastics has a predominant role in the interior design. This is aligned with the trend shown in Figure 1.2, where the increase in the use of plastics in the automotive sector is depicted [4]. In addition, Figure 1.3a illustrates the polymer types used in vehicles. It is noted that polypropylene (PP) is by far the most used. PP's relative good specific mechanical properties and low cost make it a good alternative for many applications as shown in Figure 1.3b [5]. Aside from its mechanical properties and low cost, PP has characteristics such as good processing, good aesthetic finish and low emission levels that make it a suitable material for interior applications.
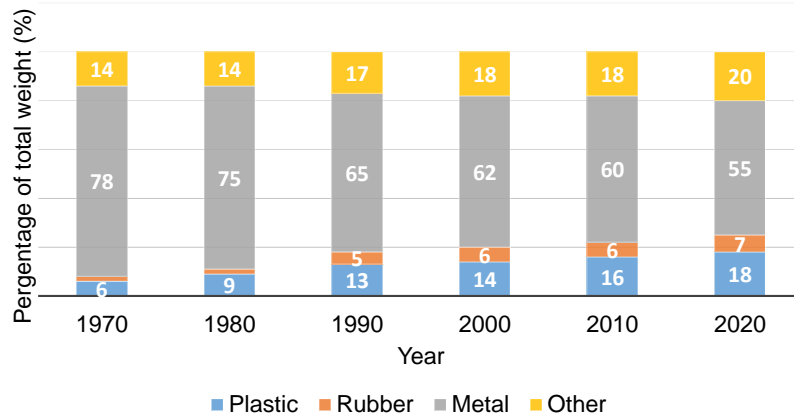
Figure 1.2 Percentages by weight of materials used in automotive over time. Modified from [4]
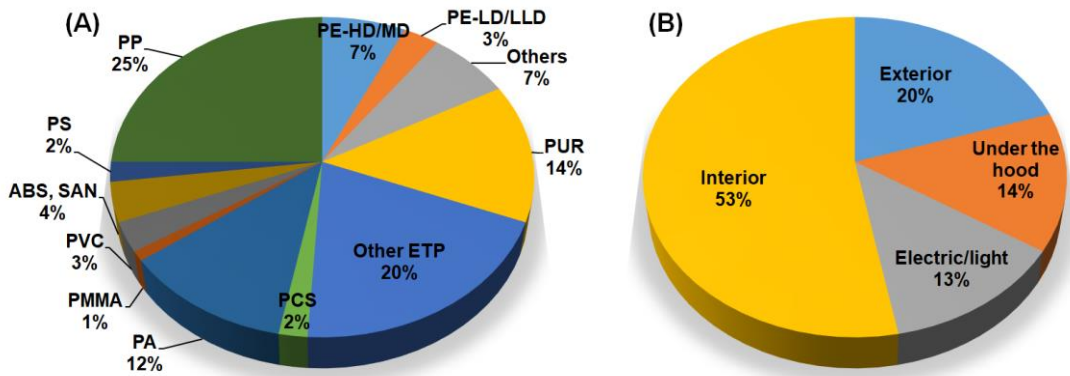
Figure 1.3 Polymeric material types used in automotive (a). Applications of polypropylene material in automotive (b). Modified from [5]

Nowadays, the car interior, rather than simply being a place to sit and drive is considered a "living space" where driver and passengers have to feel comfortable. Aesthetics is an important factor to achieve this [6]. Uniformity and harmony between components inside the car are fundamental for providing a great perceived quality.
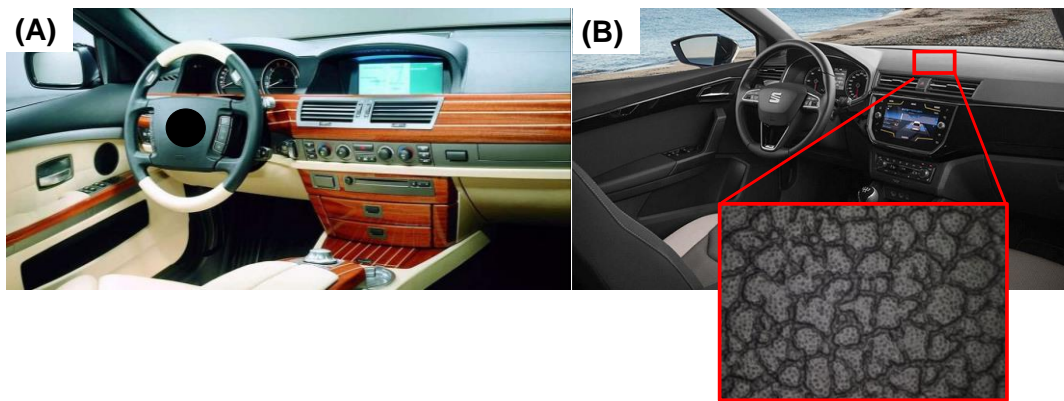
Figure 1.4 High-end interior car with materials and technologies that combines wood, leather or textile (a). Interior car with textured components that mimic leather finish by engraving the mould cavity (b).

Figure 1.4 depicts different methods that exist to enhance the aesthetics of the car interior. For example, high end cars (Figure 1.4a) combine different techniques such as leather, textile lined and painting parts for their interiors, or the use of natural materials such as wood, although this implies a high production-cost and less environmental-friendly processes. Alternative techniques such as mould engraving is nowadays usually utilized to produce textured injection moulding PP components (Figure 1.4b), having a great visual appearance and keeping production-cost low [7]–[9]. Figure 1.5 shows t injection moulded components with different texture types. Mould engraving allows designing a wide range of textures, from those that mimic leather or geometric patterns to those that are simply random textures.
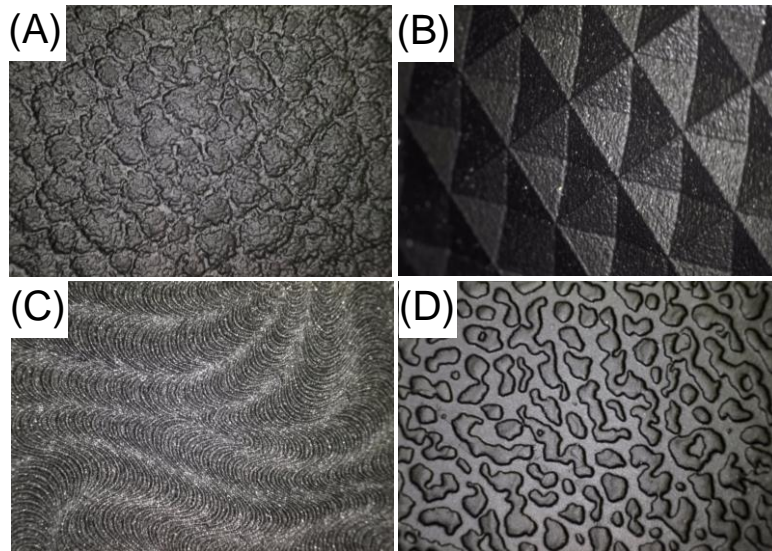
Figure 1.5 Leather texture type (a); geometric finish texture (b); random textures (c) and (d).

Currently, the appearance of interior components is evaluated taking into account attributes such as colour, gloss and texture. In addition, the matching between neighbouring parts is visually evaluated by a group of experts. Therefore, besides objective measurements of colour, gloss and texture provided by instruments, there is also an important subjective component. Despite the experience of experts, this subjective evaluation can vary from observer to observer. In this context, the present PhD thesis deals with the appearance characterization of textured interior components in an objective way. This will be done by means of three-dimension (3D) techniques that use measuring conditions simulating the human eye capabilities.

The measurement of appearance attributes requires the use of instruments such as a colorimeter, glossmeter or profilometer as shown in Figure 1.6. Each instrument can measure a single appearance attribute; hence, the measurement of the overall object appearance requires using at least three different instruments. On the contrary, it is well known that the human eye detects all appearance attributes at the same time to create perception [1]. Accordingly, a device that allows simultaneously measuring simultaneously colour, gloss and surface

reflectivity contrast as a function of its topography is tested. This instrument measures surface characteristics having resolutions that simulate those of the human eye. It certainly could be the best approach for objectively measuring object appearance.

The concept of contrast is defined as the difference in luminance between a visual target and its background [10] and it is related to the quality of an image [11]. Thus, a methodology that allows correlating surface features with perceived quality parameters such as contrast is proposed. This will allow predicting the appearance of a textured component by measuring its topography by means of 3D techniques.

Figure 1.6 Spectrophotometer (left); glossmeter (centre) and profilometer (right)

Beyond aesthetic attributes, textures are designed to accomplish a function, resulting in the so-called functional surfaces [12]. In the particular case of the automotive industry, scratches on textured surfaces can dramatically reduce the aesthetic appeal. This is caused by the different way in which incident light interacts with the original texture and the scratch. As a result, a high contrast between the original texture and the scratch path appears, making it perceivable to the human eye [13]–[15]. Textures should be therefore designed to hide the scratch damage and make it invisible. The 3D surface metrology can be used for developing a methodology to characterize both the original texture and the scratch damage. This will allow analysing the surface features of the original texture and the scratched path to optimize surface features and make a texture with greater scratch visibility resistance

1.1. Objectives

The present thesis has been developed under the framework of the Industrial Doctorate Plan founded by the company SEAT S.A. The aim is to promote company strategic research projects in cooperation with University and technological research centres, resulting in doctoral theses. This research has been conducted as a collaboration between the Universitat Politècnica de Catalunya – BarcelonaTech, the Centre Català del Plàstic, and the Materials Technology Department of SEAT S.A.

SEAT's technological objectives refer to the improvement of the perceived quality of the car interior. Thus, this thesis focusses on textured injection moulded parts as they are prevalent in the car interior.

An innovative methodology that allows objectively assessing the appearance and scratch visibility resistance is proposed. In addition, it is of great interest to assess the viability of using a novel Total Appearance Measuring (TAM) device developed by the company BYK-Gardner GmbH.

From the scientific point of view, the goals of the Universitat Politècnica de Catalunya and the Centre Català del Plàstic are mainly related to gaining deeper knowledge regarding surface characterization by means of three dimension (3D) techniques leading to a better understanding of how surface features-either at the macro- or micro-scale -can affect the appearance of textured components.

Along with these technological and scientific purposes, other objectives were defined for the present project:

- Measuring and quantifying the replication ratio of the mould cavity texture.
- Measuring the surface appearance objectively with three-dimensional (3D) techniques.
- Studying the effect of the texture on the scratch visibility resistance by means of three-dimensional (3D) techniques.

1.2. Overview of the thesis

In Chapter 1 the motivation and status of appearance measurement in the automotive industry and the objectives of this thesis have been introduced.

Chapter 2 deals with theoretical fundamentals of surface metrology, appearance attributes and surface performance.

Chapter 3 describes the materials and experimental procedures carried out in this research.

Chapter 4 shows the results of the injection parameters influence on the texture replication ratio and how it can be quantified by means of three-dimensional techniques.

Chapter 5 describes the results of surface appearance measurement using a new total appearance measurement (TAM) apparatus.

Chapter 6 presents the results of the scratch and mar performance by textured surfaces.

Finally, Chapter 7 presents the main conclusions reached in this research and suggests proposals for future research works.

1.3. References

[1]   R. S Hunter and R. W. Harold, "The Measurement of Appearance", Wiley, USA (1987).

[2]   Chowdhury, Asim, "Principles of Colour and Appearance Measurement", Elsevier, UK (2014).

[3]   S. Ignell, U. Kleist, and M. Rigdahl, "Visual perception and measurements of texture and gloss of injection-molded plastics", *Polym. Eng. Sci.*, vol. 49, no. 2, pp. 344–353, 2009, doi: 10.1002/pen.21279.

[4]   G. Klink, O. Wadivkar, G. Rouilloux and B. Znojek. Plastics. "The future for automakers and chemical companies" . A.T. Kearny Inc, 2012., p. 2012, 2012.

[5]   Plastics Europe. Automotive. "The world moves with plastics". Plastics Europe Publications, 2013

[6]   I. Ariño, U. Kleist, and M. Rigdahl, "Effect of gloss and texture on the color of injection-molded pigmented plastics", *Polym. Eng. Sci.*, vol. 45, no. 5, pp. 733–744, 2005, doi: 10.1002/pen.20330.

[7]   H. S. Wang, Z. H. Che, and Y. N. Wang, "Cost Estimation of Plastic Injection Products through Back-Propagation Network 2 Literature Review", no. 2005, pp. 54–60, 2007.

[8]   S. Ignell, U. Kleist, and M. Rigdahl, "On the relations between color, gloss, and surface texture in injection-molded plastics", *Color Res. Appl.*, vol. 34, no. 4, pp. 291–298, 2009, doi: 10.1002/col.20510.

[9]   I. Ariño, U. Kleist, G. G. Barros, P. Å. Johansson, and M. Rigdahl, "Surface texture characterization of injection-molded pigmented plastics", *Polym. Eng. Sci.*, vol. 44, no. 9, pp. 1615–1626, 2004, doi: 10.1002/pen.20159.

[10]   D. G. Pelli and P. Bex, "Measuring contrast sensitivity", *Vision Res.*, vol. 90, pp. 10–14, 2013, doi: 10.1016/j.visres.2013.04.015.

[11]   P. Barten, "Contrast sensitivity of the human eye and its effects on image quality", 1999. https://doi.org/10.1117/3.353254.

[12]   X. J. Jiang and D. J. Whitehouse, "Technological shifts in surface metrology", *CIRP Ann. - Manuf. Technol.*, vol. 61, no. 2, pp. 815–836, 2012, doi: 10.1016/j.cirp.2012.05.009.

[13]   C. J. Barr, L. Wang, J. K. Coffey, and F. Daver, "Influence of surface texturing on scratch/mar visibility for polymeric materials: a review", *J. Mater. Sci.*, vol. 52, no. 3, pp. 1221–1234, 2017, doi: 10.1007/s10853-016-0423-5.

[14]   H. Jiang, R. L. Browning, M. M. Hossain, H. J. Sue, and M. Fujiwara, "Quantitative evaluation of scratch visibility resistance of polymers", *Appl. Surf. Sci.*, vol. 256, no. 21, pp. 6324–6329, 2010, doi: 10.1016/j.apsusc.2010.04.011.

[15]   R. Browning, M. M. Hossain, J. Li, S. Jones, and H. J. Sue, "Contrast-based evaluation of mar resistance of thermoplastic olefins", *Tribol. Int.*, vol. 44, no. 9, pp. 1024–1031, 2011, doi: 10.1016/j.triboint.2011.04.009.

Chapter 2:   State of the art

Object appearance is defined by observers using terms such as shine, matte, rough, smooth, blue or yellow, to name a few. Observers make all these definitions without using a conscious analysis. In other words, the perceived appearance is not related with the object attributes that provides this sensation. For example, a person that examines the cleanness of a t-shirt is not looking for yellow or grey patterns, but these attributes lead to judge the lack of cleanness. For this reason, it is said that the perception of object appearance is based on previous experiences.

There are three main attributes that define the appearance of an object, the colour, the gloss and the texture. Colour is related to the physical phenomenon of light absorption and reflection. An object that is illuminated absorbs all the wavelengths of the visible spectrum except one that is reflected and defines colour when it is perceived by the human eye. Gloss is the portion of light reflected by the object. It can be either in the specular or diffuse mode. In the former case, a highlight is perceived (high gloss) whereas the latter case yields a matte impression. Texture is the attribute that defines the surface finish, being either rough or smooth. The interaction between all attributes conjointly defines the object appearance. On the other hand, the appearance perception by observers depends on factors such as illumination and viewing conditions, leading observers to modify their judgements about objects [1].

The appearance measurement and its correlation with the human visual system (HVS) is an interesting topic for fields of study such as psychophysics and optics. Psychophysics is defined as the science that measures the relation between a physical stimuli and its perception whereas the main topic of interest in optics is the relation between optical surface properties and its modification as a function of the surface topography. Several instruments are available for measuring surface attributes (colour, gloss and texture). It must be pointed out that although instruments are designed to measure as the human eye would do, they are only able to measure

a specific surface attribute. On the contrary, the human eye detects all surface attributes simultaneously. The human eye judgements, however, are subjective and vary from one observer to another [1]. Therefore, correlating both optical surface properties and its perception as a function of the surface topography is an appealing challenge.

The object's appearance is of great importance for some industries, being directly related with the customers' perceived quality. Perceived quality can be defined as the perception of the overall quality of a product or service with respect to its intended purpose. For instance, in cosmetics, smooth and glossy surfaces are preferred to provide high quality. The same occurs in electronics where flat, smooth and glossy surfaces are desired. On the contrary, the automotive industry selects matte surfaces as high quality finish in their car interiors [2]. Usually, materials such as leather, wood or fabric are suitable to achieve a high quality sensation inside the car. However, due to their high cost, only luxury cars can afford their usage. Alternatives such as mould engraving techniques allow obtaining injection moulding parts that mimic the desired texture reducing cost production. On the other hand, beyond appearance, textures are also used for reducing damage visibility [3]. This is because the aesthetic appeal can quickly be lost should it become scratched or marred. This normally occurs when a harder material slides across the surface under a given load. Therefore, measuring the appearance and evaluating the surface performance of textured components is necessary with the aim of enhancing the customer's perceived quality while keeping costs as low as possible.

The main theoretical fundamentals of surface metrology, surface appearance measurement and scratch visibility resistance are introduced in this Chapter.

2.1. Surface metrology

2.1.1. Historical background

Surface metrology can be defined as the science of measuring small-scale geometrical features on surfaces: the topography of the surface [4]. This was not relevant until the second decade of the 20th century, where surface analysis and measurement were conducted visually

or by touch. Figure 2.1 illustrates how the use of surface metrology has developed in accordance with manufacturing practices. Initially, during the 1920's, the design requirements of a workpiece were limited to measuring size and shape, leaving texture as incidental. During the period of 1930-90's, texture became an attribute to take into account in the part functionality, although size and shape still had the main role. It was not until the last decade of the 20th century where texture was considered as an independent factor in the design of parts. This, in fact, provided texture with a main role from the point of view of "added value" in the workpiece performance.
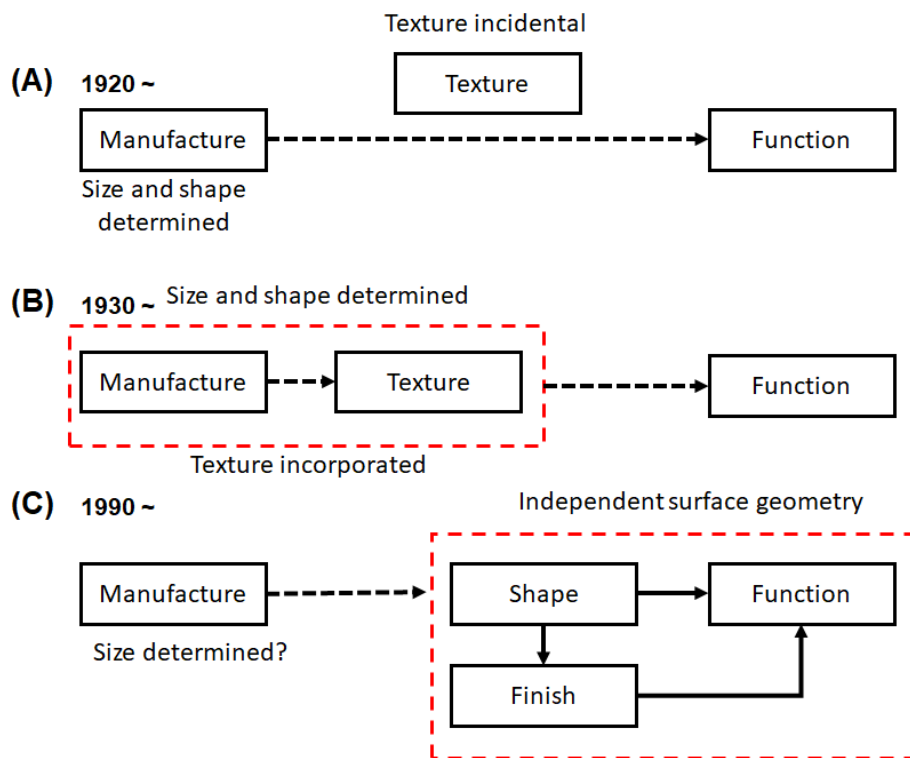
Figure 2.1 Development of the role of surface geometry. Modified from [4]

Quality control is another important application of surface metrology to guarantee the proper functionality and performance of the final workpiece. For example, in the late 1920s, Bentley Car Company was the first to use a surface quality control on the cylinder bores for their racing car engines, manufacturing surfaces as smooth as possible. It was the first time that a relation between surfaces and functionality was established. Other sectors such as

medicine or optics also use surface metrology as quality control for their products. For instance, in the former case, controlling the surface topography of orthopaedic implants allows optimizing their performance. In the latter case, the surface topography of lenses is measured to obtain the best optical performance, reducing the amount of light that is scattered [5], [6].

The need of a more efficient, economic and environmental-friendly manufacturing were the reasons behind the increase in the use of surface metrology. It also led to the development of new techniques and instrumentation that provided "added value" to the workpieces, optimizing their performance. [6]. Since then, manufacturers have been aware of the importance of the surface finish stimulating the development of instruments. In 1929 Gustav Schmalz was the pioneer in producing an instrument (light-section microscope) for quantitatively measuring surface topography. It was based on both optical and tactile methods. An image of an illuminated slit was projected on the workpiece at an angle to the vertical. The distortions in its reflection magnified the surface irregularities that were recorded on photosensitive paper [7]. However, manufacturers considered this procedure too sensitive to be used near tooling manufacturing. It was not until the 1930s when simple tactile methods (stylus) began to be used. Profilometry provided a simple approach for controlling the manufacturing by monitoring changes in surface texture. This indicated alterations in the manufacturing tooling such as vibrations or wear. The characterization of the fundamental and functional topographical features of a surface was conducted using areal surface texture methods. This technique emerged in parallel with the development of computers which made data managing easier. In 1968 Williamson and Peklenik proposed the first three dimensional (3D) stylus. This method was based on making parallel traces using conventional stylus system. In the decade of the 1990s, the first commercial areal surface instruments were available. Companies such as Somicronic in France or Taylor Hobson in the UK developed contacting systems, while Wyko in the USA developed a system based on optical interferometry. Nowadays, instruments for measuring surface topography follow a wide range

of principles, including contacting stylus, interferometry, confocal microscope, focus variation or atomic force microscopy among others [4].

The field of surface metrology was first concerned with friction and optics, giving much relevance to friction (wear) because it was fundamental for moving systems. Over the years the application fields became wider, including engineering, biology, materials science, chemistry or archaeology to name a few [7], [8]. However, during the past 20 years, with the irruption of advanced manufacturing techniques such as micromanufacturing and nanotechnology, the highest technological shift has occurred [9]–[13]. These technologies require submillimetres sizes and have texture feature sizes of a few hundred micrometer or even nanometer roughness. In the areal surface characterization, the standardization changed to include a new concept called "scale-limited surface". This is a more flexible method that allows characterizing surfaces at various scales [6]. Accordingly, surface parameters depend on the defined limited scale type as shown in ISO 25178-2 [14].

2.1.2. Instruments

There is a wide range of instrumentation for measuring surface topography. The most common classification is to divide instruments into contacting stylus type and scanning optical probe type [7]. The contacting instruments include the stylus and the atomic force microscope (AFM). Confocal microscope, chromatic confocal microscope, focus variation microscope and interferometer are based on optical principles. Another important group of instruments based on non-optical principles, such as the scanning electron microscope (SEM), provide a very high resolution image of the surface topography. It must be pointed out that although this instrument type gives a qualitative measurement it is very useful for analysing micro-features of the surface.

2.1.2.1.   *The stylus*

The stylus instrument is typically used to measure two dimension (2D) profiles across an engineering surface. This instrument is one of the most common in the industry.

The main components of this measuring instrument are (Figure 2.2) [15]:

a) the stylus

b) the probe or pick-up

c) the transducer

d) the amplifier

e) recorder
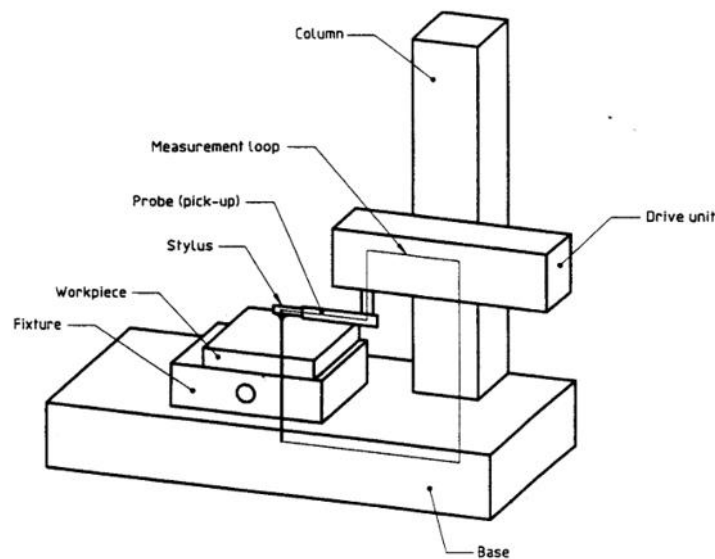
Figure 2.2 Elements of a standard stylus instrument [15].

The stylus instrument principle consists in a stylus, which is the part that physically makes contact with the sample's surface and is moved across the surface at a constant speed. The movement in the z axis of the stylus is converted into electrical signals by a transducer. Other components such as the pick-up or probe, which is also move at a constant speed by a motor and gearbox, draws the stylus over the surface. The amplifier boosts the signal from the stylus transducer to a useful level and finally a device, also driven at a constant speed, or a computer are used for recording the amplified signal [16].

The vertical range of a stylus instrument depends on the dynamic range of the transducer. The vertical resolution is limited by background mechanical vibrations and thermal noise in the electronics. The horizontal range of the stylus instrument is set by the length of pick-up traverse and its resolution depends on stylus dimensions and shape (cone or pyramid) [17]. As shown in Figure 2.3, the stylus slope has to be taken into account. The tip should be as sharp as possible but it still may not completely penetrate into slim grooves or valleys, providing distorted or filtered measurements of the surface texture. Another important factor is the force applied on the surface by the stylus. The application of a very high force can produce damage, while forces which are too low do not guarantee a proper contact with the surface, yielding poor reliable results [16], [17].
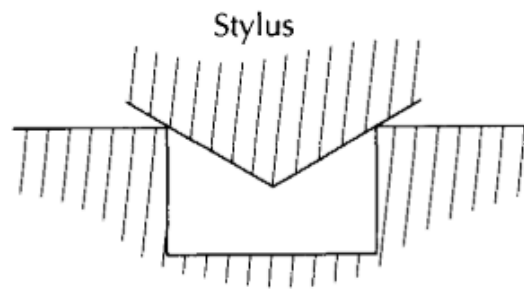
Figure 2.3 Stylus slope effect [15].

The stylus instrument needs a reference to enable a reliable measurement. Nowadays, an intrinsic reference called skid is used instead of a flat smooth mechanical reference that needs to be aligned and levelled. This tedious procedure has led to the use of a skid as more convenient method. The skid is attached to the pick-up and rests on the sample surface either beside or in line with the stylus (Figure 2.4). The main difference between both tips is that the skid-s is blunter than that of the stylus, filling the gap between surface peaks. In other words, it draws a straight line that is used as reference. The skid principle is also used in optical instrumentation [15]–[17].
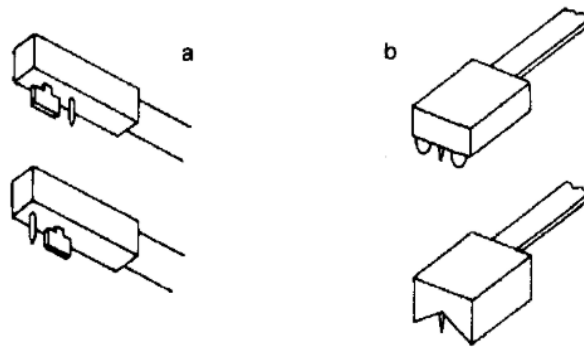
Figure 2.4 Aligned (a) and straddling skids (b) [15].

2.1.2.2. *Atomic force microscope (AFM)*

The atomic force microscope (AFM) is a technique that enables ultra-high scale 3D surface topography characterization. This technique has been essential in the development of nanotechnology, measuring samples at the nano-scale level. Among others, fields such as biology, chemistry, engineering, medicine and electronics, use this technology in their research, development and quality assurance [18].

It must be pointed out that the AFM technique enables lateral measuring range of the order of 100 µm and several microns in the vertical direction. This technology is able to measure both conductive and non-conductive samples. In the latter condition, electrostatic forces between tip and surface can occur, leading to errors in measurement. In addition, it can operate with or without vacuum, yielding more complicated measurement.

Figure 2.5 depicts the main elements that compose an AFM:

- a tip

- a cantilever

- a laser beam

- a detector
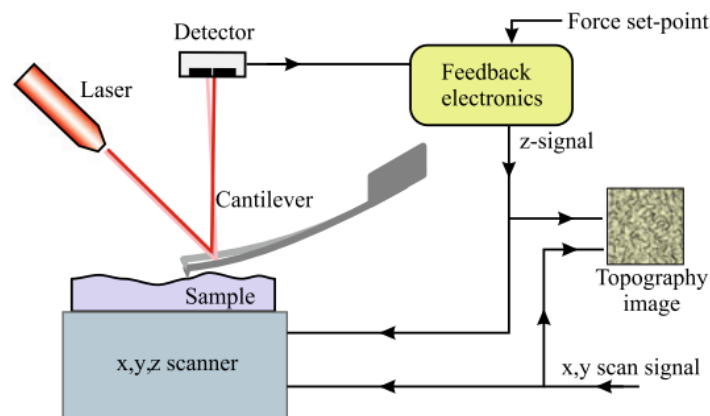
Figure 2.5 Schematics of atomic force microscope [17].

The AFM scans the surface using a fine tip located at the end of a micro-scaled cantilever. Due to the atomic interaction between the surface and the tip, the cantilever deflects. This deflection results in a displacement of the laser beam on a position-sensitive photodetector. The displacement of the beam is proportional to the force on the tip, for example, a force of 10^{-10} N causes a deflection of 0.1 nm in the cantilever. Due to this deflection method, the AFM is able to measure the 3D topography with near atomic resolution in contact and non-contact mode [19].

The AFM has three different operation modes: static, repulsive and dynamic mode. In the static mode, which is the most popular one, the tip and the sample surface is first brought into contact but is then lifted again off of the surface to avoid damaging the surface with the

tip. The surface topography is mapped while scanning by changing the z-position of the tip, keeping the tip-sample distance constant.

In the repulsive mode, both last atoms of the tip and atoms of the surface sample are very close to each other, about 1 nm. The repulsive steric force between tip and surface results in a deflection of the cantilever. This mode is the most similar to measuring the surface using a stylus tip, however the force between the tip and the sample surface is smaller and the stylus tip geometry is different. This operation mode is useful for measuring hard surfaces since it can result in surface damage or contamination due to material removal during the scanning.

Finally, the dynamic mode, also called non-contact mode, operates with an oscillator cantilever. This is important for measuring soft samples such as polymers. In this case, the cantilever is excited to vibrate close to its free resonance frequency which is in the order of 20-300 kHz. The distance between tip and sample leads to changes in the resonance frequency of the cantilever. The tip-sample force can be measured thanks to a second spring which changes the cantilever frequency into amplitude signal. This change in amplitude can be used as a detection signal for measuring the tip-sample distance. This distance regulation will be of such a constant amplitude that a constant force is provided [19], [20].

2.1.2.3.   *Confocal scanning laser microscope (CSLM)*

The technology of the confocal microscope enables us to obtain a focused surface reconstruction in all planes. This technique solves the limitations of conventional microscopes such as the depth of field (DoF). For example, classical microscopes provide a clear image for the plane within the DoF, while planes outside the microscope's DoF are blurred making measuring heights impossible. Therefore, by modifying the optical path in the microscope as shown in Figure 2.6 it is possible to obtain a focused image in all planes [19].
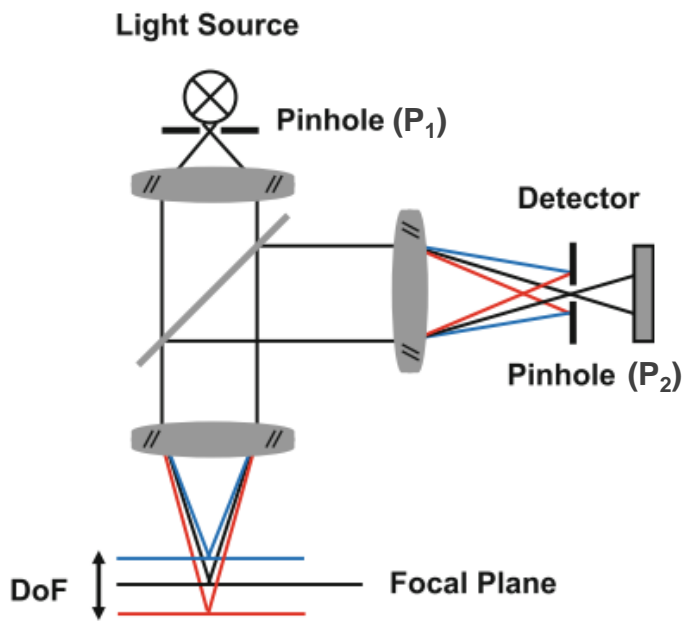
Figure 2.6 Optical path in a confocal point sensor [19].

The light coming from a given source is first collimated and then focused on the focal plane though the objective. The reflected light coming from the sample is collected by the objective and deflected by the beam splitter. It must be pointed out that the light that comes from the focal plane (within the DoF) and the portion of light that comes from a plane above and below arrive at the pinhole P_2. At this point, only the focal light passes through the pinhole and its intensity is detected. This is due to the insertion of two pinholes, P_1 and P_2. The image of these pinholes is in focus with the specimen, when it is located in the focal plane and the reflected light reaches pinhole P_2 a strong signal is detected by the detector. On the contrary, the defocused light is discriminated by pinhole P_2 due to the scattered light [19], [21]. Figure 2.7 shows the monitored signal of the photo-detector when the reflected light is at the focus point, resulting in a maximum point [22].
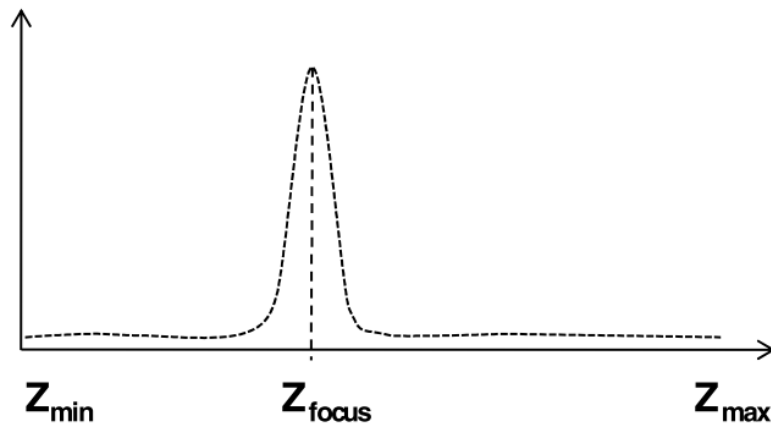
Figure 2.7 Intensity curve registered by the photo-detector [22].

The most common confocal microscope types are: the single-photon point-scanning confocal system, the multiphoton point-scanning confocal system and the spinning disk confocal microscope [23]. Table 2.1 summarizes the main characteristics of the different confocal microscope types.

Table 2.1 Main characteristics of the most common confocal microscopes. Modified from [24]

Characteristic	Single-photon CSLM	Multiphoton CSLM	Spinning disk
Light source	High intensity short-wavelength lasers	Adjustable lasers capable of long wavelength (IR)	Lasers, mercury, xenon, or metal-halide lamps
Acquisition speed	+	+	++
X-Y resolution	4096 x 4096 pixels	4096 x 4096 pixels	Depends on CCD
Z-resolution	Aprox. 0.6 µm	-	Typically fixed (micro-lenses)
Detectors	Photomultiplier tubes (PMT)	Photomultiplier tubes (PMT)	Charge-coupled device (CCD)
Multi-channel imaging	Simultaneous or sequential	Simultaneous or sequential	Sequential
Photobleaching and phototoxity	May be problematic	Typically not a problem	Reduced based on fast imaging parameters
Region-specific bleaching	Available	Available	Requires additional hardware
Depth of imaging	++	+++	+

2.1.2.4.   Chromatic confocal microscope

The chromatic confocal microscope uses chromatic aberration as a principle of measurement using a chromatic white light sensor (CWLS). This results in a simple but effective measuring technique in the field of optical profilometry to assess surface topography and roughness. One of the most important advantages of this technology is that the measurement is performed without moving the sensor head in *z*-axis, making it a vibration free system. In addition, this technique is insensitive to ambient light and stray reflections from the surface [22].

The measuring principle of this technique is based on chromatism which is a physical property of almost all optical components. I It is usually something to avoid in the design of optical instruments. Nevertheless, it has been established as a method for measuring distances. The CWLS uses the chromatic aberration of a lens system to determine the distance between the sensor head and the sample surface. The focused white light beam passes through the lenses yielding different focal lengths within the optical axis. These focal lengths are associated with colours wavelengths such as blue and red with 400 nm and 800 nm, respectively. As blue light has a higher refractive index in comparison to red light, its focal point is located closer to the lens, while the focal length of red colour is located further away. Therefore, colour wavelengths are used as references to calculate surface heights (see Figure 2.8). Subsequently, the reflected light coming from the specimen in the focal point is measured by a spectrometer, which obtains the reflectance spectrum. When the light is in the focal plane it generates a peak at the corresponding wavelength [19], [22].
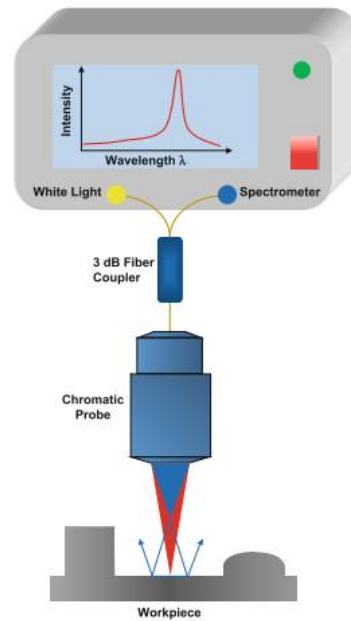
Figure 2.8 Principle of a chromatic white
light sensor (CWL) [19].

The light source is usually a while light LED type. The vertical range or measuring

range of the CWLS is defined by the distance between focal points of the extreme wavelengths

(blue and red) (Equation 2.1). Typical values for the measuring range of CWLS are between

100 and 3000 µm although the acquisition frequency can vary the measuring range, decreasing

with frequency since less light is detected by the photometer at high frequencies [22]. The

aperture angle can vary from $\alpha = 30º$ to $\alpha = 45º$ for this kind of instruments [19].

$$vertical\ range = max.\,focal\ distance - min.\,focal\ distance \qquad (2.1)$$

2.1.2.5. *Focus variation microscope*

Although its principle was published in 1924 by Helmholtz, focus variation technique

is one of the newest technologies in the field of surface metrology. This instrument allows the

areal surface topography measurement using optics with different DoF and vertical scanning.

This is combined with a mathematical algorithm that enables surface reconstruction.

The basic components of the focus variation instrument are:

a) an optical system with limited DoF.

b) a light source

c) a camera

d) a driving unit

The principle of measurement is defined in Figure 2.9. The beam of white light normally comes from a LED light source, passes through a semi-transparent mirror and the objective lens to illuminate the workpiece. The reflected light, which is used to obtain a surface image, comes from the sample surface and passes through the objective lens. Then through the semi-transparent mirror and the tube lens it is projected onto the charge-couple device sensor (CCD). As the distance between the objective and the surface is continuously varying (vertical scanning) continuous digital images are taken. It must be pointed out that for each vertical position only a thin sheet of the measuring volume is exactly in focus due to the DoF. Therefore, from the collected data, an extraction of the best focus of each obtained image can be obtained. The degree of focus varies from low to high and low again. This is because the change in focus is related to the change of contrast on the CCD sensor. Therefore, by analysing the contrast on the CCD sensor the position where the sample was in focus can be measured. Once the described procedure is done, the reconstruction of the sample topography can be obtained.
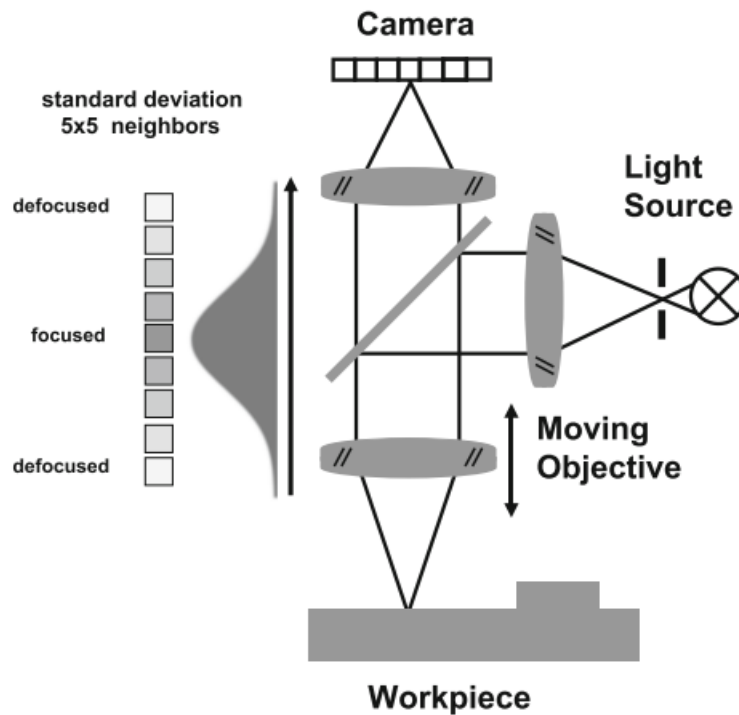
Figure 2.9 Measuring principle of focus variation [19].

The focus variation technique depends on the sample roughness level. It works well in surfaces with a roughness value of the arithmetic mean height (Ra) larger than 15 nm. The Sa is defined as the arithmetic mean of the absolute heights above and below the mean plane for a given sampling area. Therefore, the focus variation microscope will not detect topography features in those surfaces with a Sa value smaller than 15 nm. Commercial focus variation instruments have their lower limit of roughness detection in 50 nm in the Sa and 80 nm in the Ra (arithmetic mean height in two dimension profilometry). Other limitations are transparent and high reflective samples. The focus must significantly change during the measurement and for these types of samples this condition is not fulfilled. On the contrary, evaluating sampling areas from 0.1 x 0.1 mm^2 to 100 x 100 mm^2 with a vertical resolution up to 10 nm is achievable. Lateral resolution is limited by the microscope resolution whereas the vertical resolution depends on the measuring distance which normally ranges between 3 and 22 mm.

2.1.2.6.   Interferometer instrument

Interferometry is a technology that plays an important role in the surface metrology measurement. Several methods have arisen from this technique, for example interferometric inspection, white light interferometry, wavelength scanning interferometry or the digital holographic microscope to name a few [19], [24], [25].Figure 2.10 shows the main components of a classical interferometer.
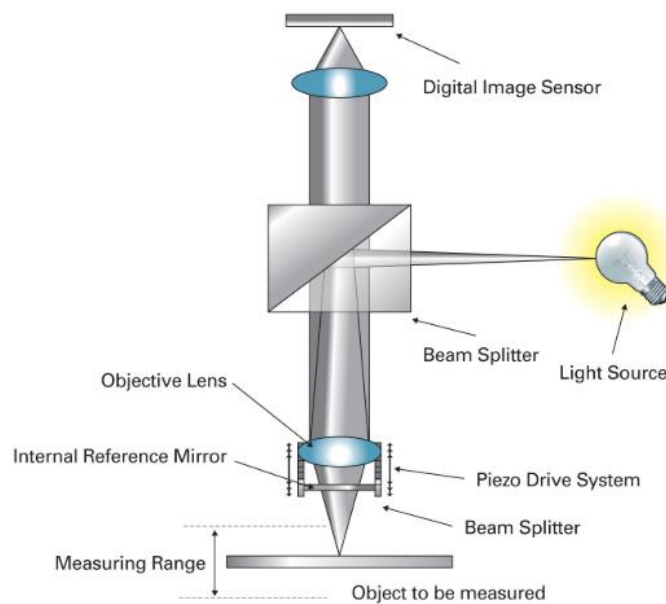
Figure 2.10 A typical interferometer design [25].

The interferometry principle is based on the concept of the amplitude of two waves with the same frequency (in phase) being added to each other (Figure 2.11a). On the contrary, waves with different frequencies (out of phase by 180º) will be cancelled, resulting in a signal with zero amplitude (Figure 2.11b). This procedure of adding and cancelling wave properties is named superposition and it results in dark and light bands, known as interference fringes [25].
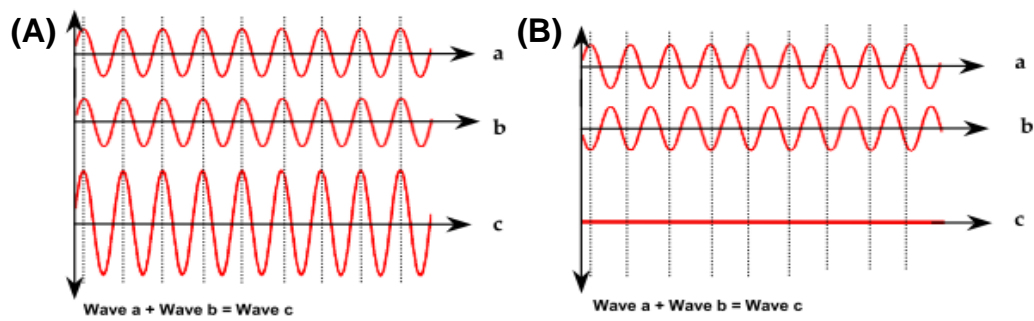
Figure 2.11 Schematic graph of amplitude against time showing constrictive interference (a) and destructive interference (b) [25].

As shown in Figure 2.12, the light normally coming from a monochromatic source with a wavelength λ splits in two when it passes through a beam splitter. Each light beam has its own path, one goes to the sample surface and the other one goes to the internal surface reference, usually a mirror [15]. The reflected light coming from the sample surface is interfered with the one coming from the reference mirror surface. If they are in phase an amplitude increment is observed, yielding a constructive interference. On the contrary, if both wavelengths are out of phase a destructive interference is produced, resulting in a decrement of the amplitude of the output. The continuous linear movement of the objective of the imaging optics results in a sinusoidal intensity variation on the detector, which finds the interference maximum. Each pixel of the sensor measures the intensity of the light and the fringe envelope obtained can be used to calculate the position of the surface. Therefore, the surface topography in 3D can be calculated correlating the sinusoidal intensity variation and the position of the objective (Figure 2.13)[19], [25]

The accuracy of the interferometer instrument depends on different factors such as the control and linearity of the vertical actuator, the performance of the camera, the design of the metrology frame, the environment, etc. In addition, this instrument is better suited for measuring very fine textures, since it provides a high-resolution image. Hence, rough surfaces cannot be properly measured using this technique [19].
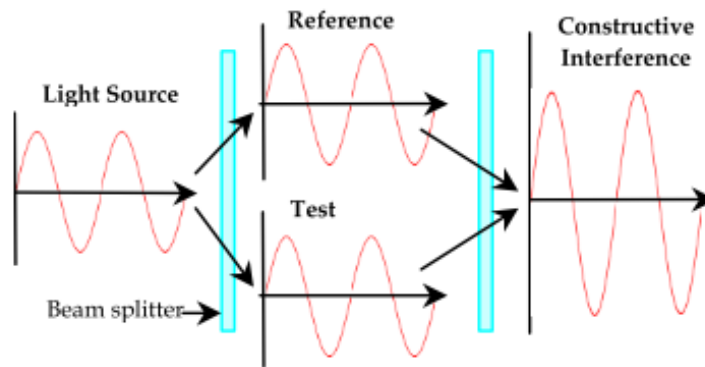
Figure 2.12 Constructive interference from one light source [25].
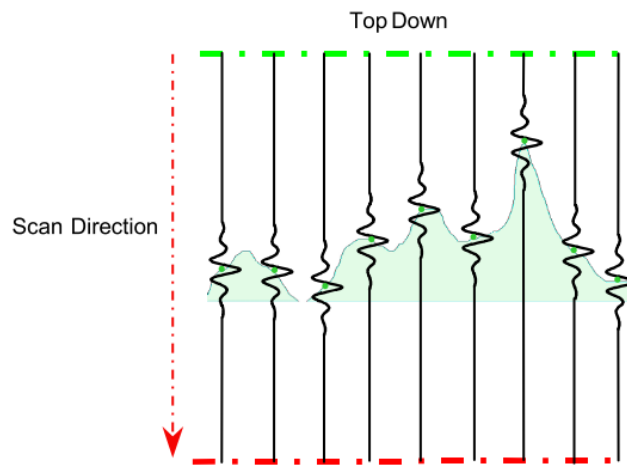
Figure 2.13 Schematic of how to build up an interferogram. The vertical lines are intensity profiles at the image sensor [25].

2.1.2.7. *Scanning electron microscope (SEM)*

The scanning electron microscope (SEM) enables visualizing surfaces in detail, having a resolution beyond that optical methods can provide using the wavelength of light. As David Whitehouse (2002) mentioned in his book entitled "Surfaces and their measurement" [15], one rule of metrology is that the unit of measurement should be close to the size of the feature of interest. Therefore, in order to have a high resolution image of the surface features, optics are

still far from systems that use electrons instead of light [15]. The elementary components and

the setup of the SEM are shown in Figure 2.14.
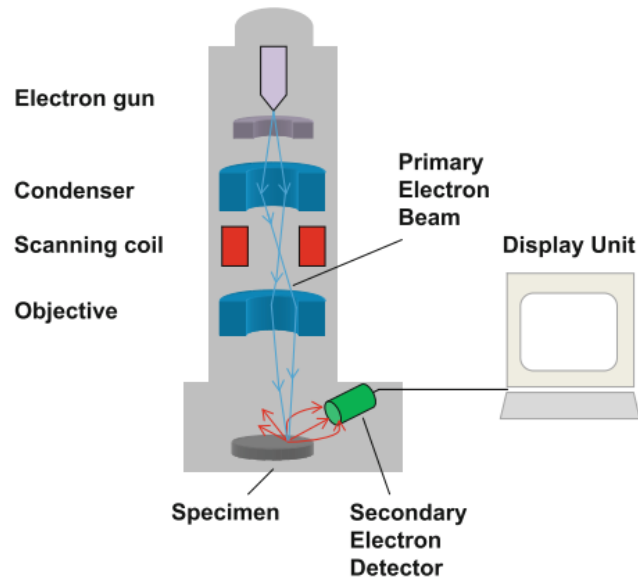
Figure 2.14 Measuring principle of a Scanning Electron Microscope (SEM) [19].

The measuring principle of the SEM is based on the idea of a primary electron beam

striking the sample surface exciting its electron emission, detecting what is known as

secondary electrons. Once the secondary electrons are collected by the detector, they are

translated into a signal. The SEM image is created after the electron beam sweeps the entire

specimen area of interest, obtaining many such signals. These signals are amplified and

translated into topography images of the sample surface after being analysed. Finally, a display

shows the images [19].

It must be taken into account that the number of secondary electrons emitted by the

specimen depends on several factors such as the angle of incidence of the primary electron

beam, the location on which the primary electron beam strikes, the nature of the specimen, its

crystalline structure and the electrical properties. These instruments need conductive samples,

however, and they can be coated with a conducting material such as gold platinum to prevent

electrostatic charging [19]. This instrument can work under conditions with and without vacuum. In addition, this technique usually provides 2D images, although with the stereoscopy and the angle-resolved scanning techniques 3D information can also be obtained. It must be pointed out that these two alternatives to the conventional SEM are listed as available techniques in the ISO 25178 standard [22].

Despite the described drawbacks, the SEM technique provides great potential for surface analysis. It has a much smaller measuring spatial wavelength scale compared to a stylus tip and optical sensors, resulting in lateral resolutions better than 5 nm. Due to its large DoF it yields a resolution of Angstroms in the vertical direction (z-axis) with a measuring range in the order of mm [17].

2.1.3. Areal parameters

One of the challenges of surface metrology is choosing parameters that adequately characterize surface properties in order to be correlated with surface topography and its functional behaviour. The adopted criteria for characterizing and representing surface topography has been aided by commonly used visualisation techniques. It means that the surface assessment has been conducted in accordance with the parameter values and visual images of the surface [26]. It should be pointed out that 3D-surface parameters cannot perfectly reproduce the topography of a surface. Some problems in parameter definition can be associated with the sampling conditions or analysis of surface topography. For example, the parameters obtained using conventional characterization techniques are scale-dependant, meaning that parameter values depend on the measurement scale. Another consideration to bear in mind is that parameter variations can be attributed to either internal or external conditions. Internal conditions such as the inherent topography of the sample or external conditions such as the selected sampling (sampling interval or sampling area) or filtering conditions can modify the parameter values [8], [26].

Four families of areal parameters have been defined and included in the ISO 25178 standard to characterize surface topography [14]. These parameter families are:

    a) Height parameters or amplitude parameters

    b) Functional parameters

    c) Spatial parameters

    d) Hybrid parameters

The definition and application of each parameter is provided below in this section.

2.1.3.1.   Amplitude parameters

<u>*Arithmetic mean height, Sa*</u>

This is defined as the arithmetic mean of the absolute value of the height above and below the mean plane within the sampling area (A) [8]. Figure 2.15 illustrates the arithmetic mean height (Ra) in a 2D profile for better understanding.
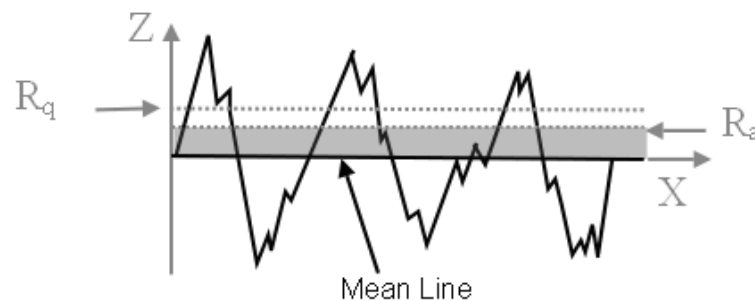
Figure 2.15 Representation of the arithmetical mean height (Ra) and the root mean square height (Rq) in a two-dimensional (2D) profile [8].

$$Sa = \frac{1}{A} \iint_A |z(x,y)| dx dy \qquad (2.2)$$

33

Root mean square height, Sq

This is defined as the root mean square value of the surface departures, z(x,y), within the sampling area (A) [8]. Figure 2.15 illustrates the root mean square height (Rq) in a 2D profile for better understanding.

$$Sq = \sqrt{\frac{1}{A} \iint_A |z^2(x,y)| dx dy} \qquad (2.3)$$

These parameters, Sa and Sq are strongly correlated to each other [7]. The Sq parameter has statistical significance, since it is the standard deviation, and it is used to specify optical surfaces. The Sa parameter is typically used for machined surfaces. It must be pointed out that both Sa and Sq are insensitive in differentiating peaks, valleys or spacing between surface features. However, once a surface is established both Sa and Sq can be used to identify surface deviations [27].

Skewness, Ssk

This parameter represents the degree of symmetry of the surface height above the mean plane. The sign of the Ssk indicates the predominance of peaks or valleys comprising the surface. If the Ssk value is zero, this means that the topography has a Gaussian height distribution with symmetrical topography. Figure 2.16a shows peak and valley distributions of a 2D profile. The Ssk< 0 means that the bulk of material is above the mean plane, with valleys prevailing over peaks. The Ssk> 0 means the opposite. In addition, this parameter is influenced by isolated peaks or isolated valleys [8], [27].

$$Ssk = \frac{1}{S_q^4} \left[\frac{1}{A} \iint_A z^4(x,y) dx dy \right] \qquad (2.4)$$
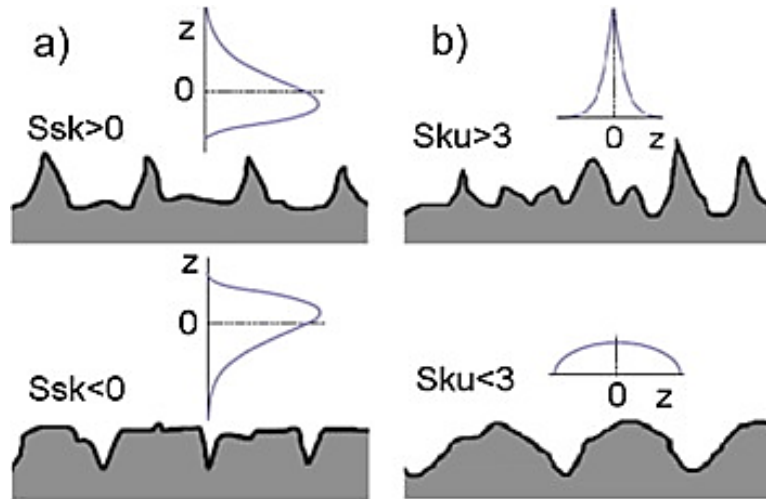
Figure 2.16 Illustration of the skewness (a) and kurtosis (b) areal parameters. Modified from [15]

Kurtosis, Sku

This parameter is a measure of the sharpness of the surface height distribution, indicating the presence of inordinately high peaks or deep valleys or the lack thereof making up the texture. Figure 2.16b depicts a surface profile with the presence of high peaks or deep valleys, resulting in a Sku> 3. On the contrary, the lack of these yields a Sku< 3. A Gaussian distribution has a Sku value of three (Sku = 3).

$$Sku = \frac{1}{S_q^4} \left[\frac{1}{A} \iint_A z^4(x,y) dx dy \right] \tag{2.5}$$

The Ssk and Sku parameters are useful for wear applications and detecting peak or valley defects that can occur on a surface[8], [27] .

Max. peak height, Sp; Max. valley depth, Sv and Max. height of the surface, Sz

Figure 2.17[28] describes the maximum peak height (Sp) and the maximum valley depth (Sv) parameters in a 2D profile. Sp is defined as the height of the highest point. Sv corresponds to the depth of the lowest point (expressed as a negative number). Therefore, the maximum surface height (Sz) is the difference between Sp and Sv (Sz = Sp – Sv).
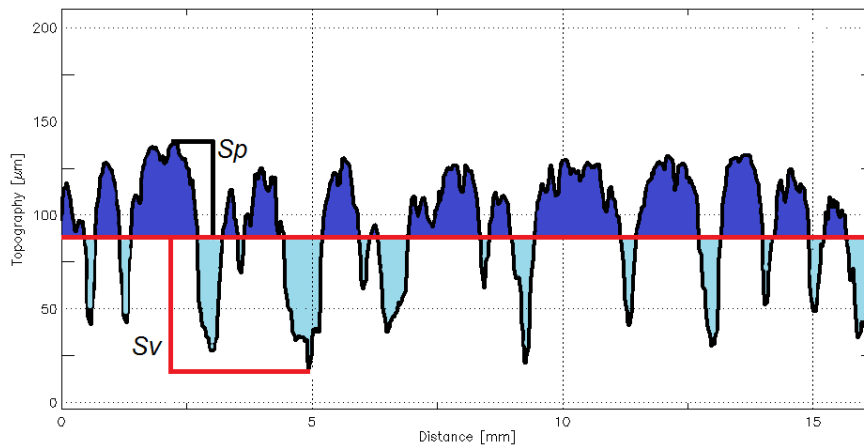
Figure 2.17 Illustration of the máximum peak height (Sp) and the maximum valley depth (Sv) [28].

As these three parameters come from the measurement of single points, they tend to be unrepeatable. Therefore, spatial filtering bandwidths must be properly set in order to avoid erroneous peaks or valleys. In addition, making multiple measurements at random locations of the sample to obtain significant statistically results is recommended.

Typical applications of these parameters can be included in sealing surfaces and coatings, sliding contact surfaces or fluid retention systems [8], [27].

2.1.3.2. *Functional parameters*

Material ratio curve

The material ratio curve also known as the Abbot Firestone Curve (Figure 2.18) is established by evaluating the material ratio (mr) at various levels from the highest peak (where the curve equals 0%) to the lowest valley (where the curve equals 100%). The mr is the ratio of the intersecting area of a plane passing through the surface at a given height to the cross-sectional area of the evaluation region.
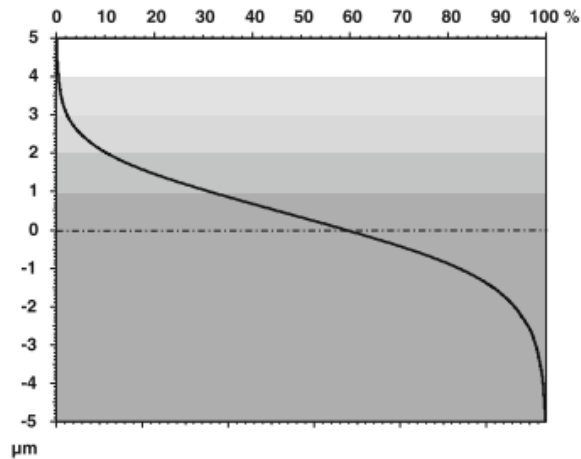
Figure 2.18 Material ratio curve [8].

<u>*Areal material ratio, Smr(c)*</u>

The areal material ratio indicates the material ratio (mr) of the cross-sectional evaluation area at a given height (c) (Figure 2.19). It is expressed as a percentage and the heights are taken from the reference plane [8], [27].

This parameter can be used as requirement of the surface wear behaviour. For example, engine cylinders have a specification of a Smr(c) prior to running-in. This is because piston friction leads to surface wear before it stabilizes [27].
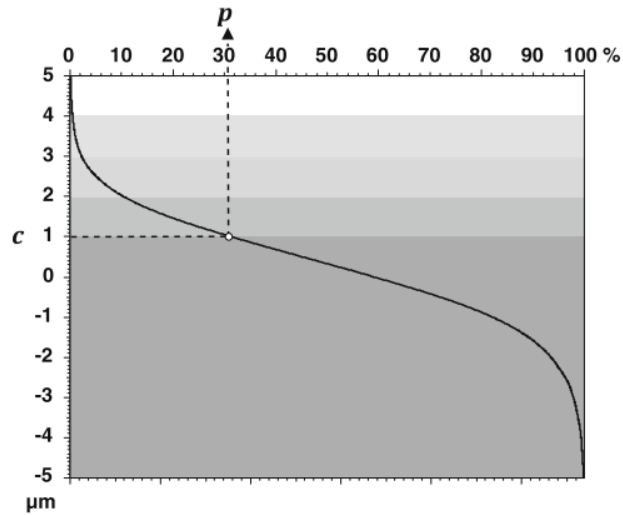
Figure 2.19 Representation of the Smr(c) parameter.
p is the material ratio corresponding to a given section
height c [8].

Inverse areal material ratio, Smc (mr)

The inverse material ratio parameter indicates the height c at which a given material ratio (mr) is satisfied [14].

The application of this parameter could be used to assure that an optimum crevice volume is reached. This allows lubricant entrapment in a sealing surface but prevents leakage [27].

Reduced peak height, Spk

Figure 2.20 depicts the reduced peak height, which is a measure of the peak height above the core roughness [29].
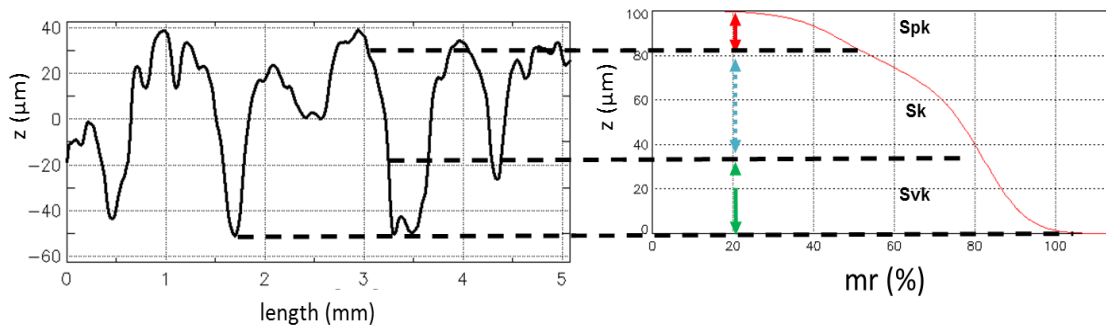
Figure 2.20 Representation of functional parameters: the reduced peak height (Spk), the core roughness (Sk) and the reduced valley depth (Svk) [29].

Core roughness depth, Sk

The core roughness depth is a measure of the peak-to-valley height removing predominant peaks and valleys. (Figure 2.20)

Reduced valley depth, Svk

The reduced valley depth is a measure of the valley depth below the core roughness. (Figure 2.20).

Peak material portion, Smr1

The peak material portion indicates the percentage of material corresponding to peak structures of Spk.

Valley material portion, Smr2

The valley material portion is related to the percentage of material corresponding to valley structures of Svk.

The parameters Spk, Sk, Svk, Smr1 and Smr2 are obtained from the areal material ratio curve based on the ISO 13565-2:1996 (Figure 2.21). Filtering of surface prior to the calculation of these functional parameters is recommended [8], [27].

39

In the case of the Spk parameter, the application could be related to contact operations. Thus, it would represent the height that is removed during a running-in operation. Consequently, Smr1 is the percentage of material that may be removed during running-in. Sk represents the surface height over which a load is distributed after a running-in operation. Finally, the Svk can be used for lubricant retention applications [27].

Void volume, Vvv(mr)

The void volume parameter indicates the void volume calculated for a material ratio (mr). This parameter is calculated by intersecting the volume enclosed above the surface and below a horizontal cutting plane set at a given height [8], [27].
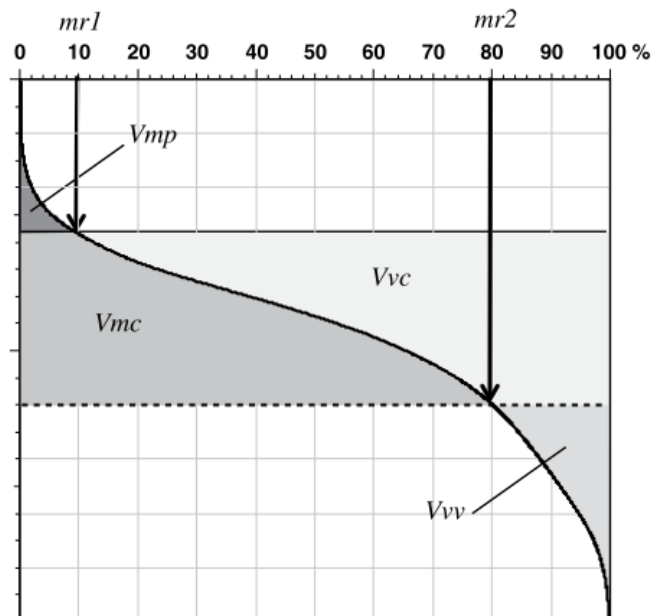
Figure 2.21 Definition of volume parameters on the bearing areal ratio curve [8].

Dale void volume, Vvv(p)

The dale void volume indicates the volume of space bounded by the surface texture from a plane at a given height corresponding to a material ratio (mr) level, "p" to the lowest valley [8], [27].

Core void volume, Vvc(p,q)

The core void volume is the volume of space bounded by the texture at a given height corresponding to the material ratio (mr) values of "p" and "q"[8].

The three void volume parameters, Vv(mr), Vvv(p) and Vvc(p,q) can be useful in the application of fluid flow surfaces, since these parameters indicates how much fluid would fill the surface [8], [27].

Material volume, Vm(mr)

The material volume parameter is the material volume for a given material ratio (mr) to the highest peak of the surface [27].

Peak material volume, Vmp(p)

The peak material volume is calculated by comprising the surface from the height corresponding to a material ratio (mr) level "p" to the highest peak [27].

Core material volume, Vmc(p,q)

The core material volume corresponds to the volume comprising the texture between the heights corresponding to the material ratio (mr) values of "p" and "q" [27].

2.1.3.3.   Spatial parameters

Autocorrelation function, ACF

The autocorrelation function (ACF) described in Equation 2.6 is a measure of the similarity of the texture at a given distance from the original location. It is found by taking a duplicate of the original texture z(x,y) with a relative displacement z(x-τ_x, y-τ_y). These two surfaces are multiplied, integrated and normalized to Sq, yielding a measure of the degree of overlap between the two functions. The ACF results in values compressed between -1 to +1 for each point of the surface. An ACF value of -1 means that the resultant surface is such that all peaks align with valleys of the original surface. A value of +1 means a perfect correlation between surfaces. On the contrary, a value of zero means no correlation [8], [27].

$$ACF\left(\tau_x, \tau_y\right) = \frac{\iint_A Z(x,y)Z\left(x-\tau_x, y-\tau_y\right)dxdy}{\iint_A Z^2(x,y)dxdy} \tag{2.6}$$

Autocorrelation length, Sal

The autocorrelation length is defined as the horizontal distance measured on the shifted surface at which the minimal correlation with the original surface is found. As shown in Figure 2.22, it is calculated from the minimum radius (Rmin) of the central lobe of the ACF surface in any direction after applying a threshold. Therefore, Sal = Rmin [8], [27], [30].
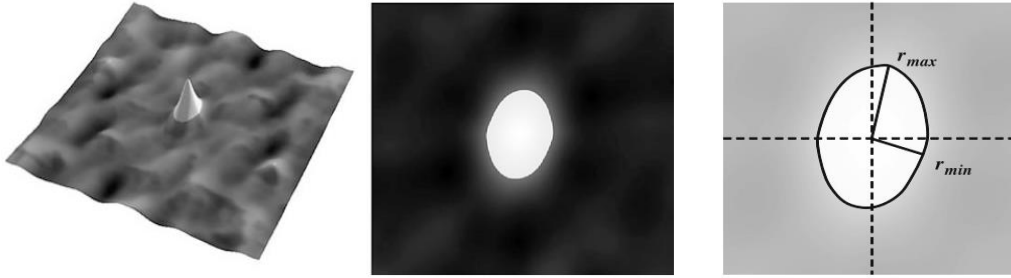
Figure 2.22 Autocorrelation peak (left) and central lobe after applying a threshold (centre). Minimum and maximum radius measured on the central lobe of the autocorrelation plot (right). Modified from [8]

Texture aspect ratio, Str

The texture aspect ratio provides the degree of isotropy of a given texture. The Str is the result of the ratio between the minimal correlation distance of the shifted surface (Rmin = Sal) and the maximum distance at which the correlation decays (Rmax). Both, Rmin and Rmax are determined following the same procedure described in Figure 2.22, and it is expressed in Equation 2.7. In textures with a dominant lay, the Str will tend to 0, while in spatially isotropic textures Str will tend to 1 [27], [30], [31].

$$Str = \frac{Rmin}{Rmax} \tag{2.7}$$

Power spectral density function, PSDF

The power spectral density function is a measure of the amplitude of all sine waves that compose the surface texture. It is made for a particular spatial frequency along a given direction. The PSDF is found by integrating the amplitude of each component of the sine wave as a function of angle [27].

$$PSDF\ (s) = \int_{R2}^{R1} r|F[rsin(s - \theta), rcos(s - \theta)]^2\ |dr \tag{2.8}$$

Where *s* is the specified direction, R1 and R2 are the range of integration in the radial direction (r), F is the Fourier analysis of the sine waves that compose the surface texture for a given direction and θ is the specified direction in the plane of the definition area [14].

Texture direction, Std

The texture direction is determined from the PSDF and is a measure of the angular direction of the dominant lay comprising a texture. The amplitudes are integrated between two spatial frequencies f_{min} and f_{max} at a given direction θ, resulting in A(θ) which is the spatial frequency content in that direction. The direction that corresponds with the maximum value of spatial frequency is the Std expressed in degrees between 0º to 180º. Figure 2.23 shows how the Str is determine with a polar spectrum [8], [27].
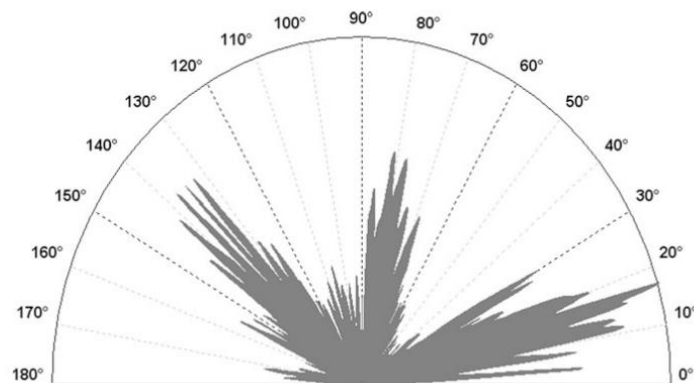
Figure 2.23 Polar spectrum graph representing the direction of the texture [8]

2.1.3.4.   Hybrid parameters

Root mean square gradient, Sdq

The root mean square gradient is a general measurement of the slopes that comprise the surface. The Sdq is then calculated on the whole surface using Equation 2.9. Where A is the projected area, (dz/dx) and (dz/dy) are the gradients of a surface point [8].

$$Sdq = \sqrt{\frac{1}{A} \iint_A \left[\frac{dz(x,y)^2}{dx}\right] + \left[\frac{dz(x,y)^2}{dy}\right] dxdy} \qquad (2.9)$$

It should be pointed out that this parameter is affected by both texture amplitude and spacing. Therefore, for a given Sa, wider spaced texture features may indicate a lower Sdq than for textures with the same Sa but finer spacing between surface features [8], [27].

Developed interfacial area ratio, Sdr

The developed interfacial area ratio is defined as the additional surface area that corresponds to the texture in comparison to an ideal plane. In this particular case, it can be said that this parameter expresses the excess value above 100% [8], [27].

$$Sdr = \frac{\sum\sum A_{ij} - A}{A} \qquad (2.10)$$

Where A_{ij} is the mean area calculated at a point and A is the projected area calculated by the product of the length in *x* and *y*.

2.1.4. Areal filtering techniques

Filtering techniques are used to separate surface components. This is because roughness, waviness and form are of different origin and affect part functionality in different ways [15], [32]. Therefore, the application of restrictions on signal frequencies (transmitted bandwidth)

is an important aspect in surface metrology in order to separately analyse surface features of interest [24], [32].

2.1.4.1.   Filtering: Historical background

Historically, the elimination of wavelengths such as waviness and form deviation has been conducted without a clear functional criteria in 2D profiles, analyzing only the roughness component [26]. Weingraber (1956) and Reason (1961) were the first in making a proposal of filtering systems [5]. In the first case, Weingraber proposed the so-called envelope system (E-system). This filtering procedure was based on a mechanical approach, simulating the contact of a converse surface using a ball. Therefore, on a measured profile the deviations from the envelope would be fine texture or roughness [32]. In the second case, Reason proposed a filtering system based on graphical methods. The raw profile was divided into segments of equal length and the mean line was drawn. The roughness was obtained taking into account deviations of the points from the mean line. This procedure was called the mean line system (M-system) and it was cumbersome and time-consuming [32]. The result was that neither of the proposed methodologies were completely satisfactory. In the E-system case, no practical instrument using mechanical filters could be made. On the other hand, the M-system was not accurate enough [5]. Nevertheless, the M-system was preferred over the E-system by almost all instrument manufacturers [5], [8], [15], [26].

Figure 2.24 depicts the 2CR electrical filtering system on which most stylus instruments were based on to obtain the mean line (M-system). The electric mean line is formed when the original signal passes through a single-stage CR filter, which is then stored on a magnetic tape. This tape is reversed and the signal is passed through the filter again. For this reason, the 2CR is known as a two-stage capacitor-resistance. The 2CR filter works well for sinusoidal measured signals, while it suffers phase distortions for complex signals.
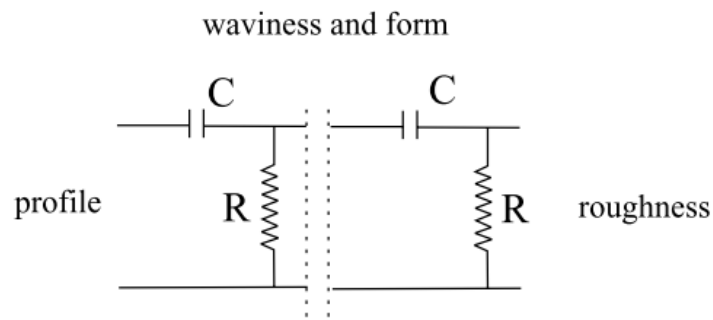
Figure 2.24 Two-stage high-pass filter [15].

In order to understand and rectify the 2CR phase distortions, Reason and Whitehouse (1965) simulated the 2CR filter digitally. They used a function that depended on a cutoff. This cutoff was used to divide the signal in segments of the same size as in the graphical analysis. The aim was to be able to separate the short-wavelength components from the long-wavelength components. It was demonstrated that the obtained mean line using the 2CR digital filter was identical to the one obtained using the electrical 2CR filter. Therefore, the implementation of the digital 2CR filter was a significant step forward in surface metrology. As a consequence of the advent of practical computer systems, the electrical filter became obsolete, in such a way that filtering began to be accomplished using computers. However, the phase distortions were not possible to fix.

Around 1986, the three main instrument manufacturers reached a consensus. The Gaussian filter was selected as the new filter for separating the surface wavelengths. This recommendation was adopted by the International Organization for Standardization (ISO) and the Gaussian filter was included [5], [26]. This was another significant milestone in surface metrology since it has been considered as one of the major developments in surface texture filtering. The Gaussian filter corrected the phase distortions, and it was digitally implemented.

2.1.4.2. Scale-limited surface

Unlike the profile characterization, the 3D measurement does not require three different groups of surface texture parameters. For example, in areal parameters the root mean square is only defined by Sq whereas in the profile case, the Pq, Wq and Rq exist for the definition of primary surface, waviness and roughness, respectively [5], [8], [15], [24].

Three different filters are defined in the ISO 25178. The S-filter, the L-filter and the F-operator. In the first case, the S-filter removes unwanted small-scale lateral components or short-wavelengths. In the second case, the L-filter is utilized for removing the large-scale lateral components or long wavelengths. Finally, the F-operator is used for removing the nominal form of the surface using a least squares method [24].

The scale at which the filters operate is defined by the nesting index. The nesting index is the new notation of the original cut-off used in 2D profiles and it is useful for all filter types. The described filters are combined to obtain the SF and SL surfaces as shown in Figure 2.25 [33].
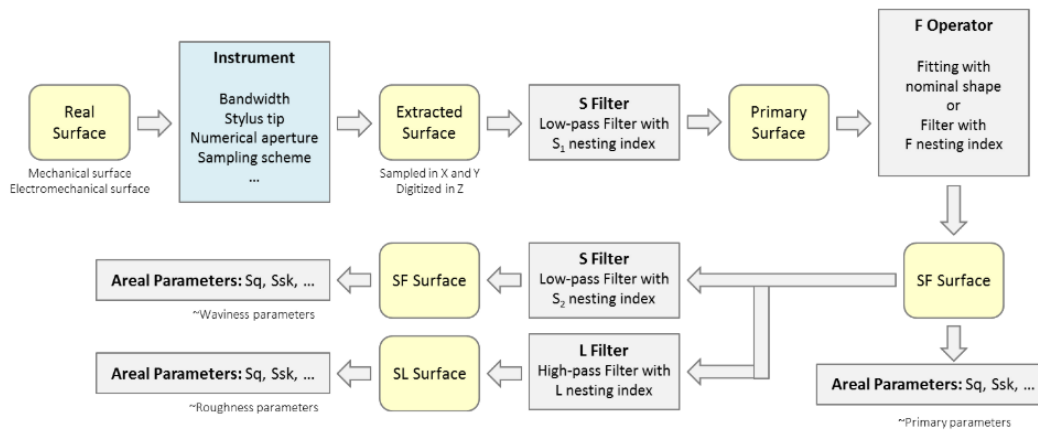
Figure 2.25 Combination of S-filter, L-filter and F-operator for achieving an SF or SL scale limited surface [33].

An SF surface is obtained after using the S-filter in combination with the F-operator, resulting in the equivalent to a primary surface. The SL surface is the result of applying the L-filter on a SF-surface. Both SF and SL surfaces are called scale-limited surfaces.

It is important to keep in mind that the visualization of the surface features depends on the measurement method and sampling conditions. This limits the finite transmitted bandwidth and thus the obtained results can be different. For example, the short-wavelength components (high frequency) are limited by the instrument resolution or sampling interval. On theother hand , the long-wavelength components (low frequency) depends on the sample size or the area of interest [26].

2.1.4.3.   New filtration techniques

The Gaussian filter type is a good general filter to separate roughness, waviness and form. However, it is not applicable to all functional aspects of the surface, for example in contact applications where the upper envelope of the surface is more important. The Gaussian filter has three main drawbacks:

(i)   It suffers distortions near the edges, mainly in the waviness profile.

(ii)   The waviness profile does not follow the texture in the presence of large form.

(iii)   It is not robust against outliers. A large peak or valley can distort the waviness profile.

For these reasons, a standardised framework has been established to provide a mathematical foundation for filtration. This information is still being developed and is not yet fully published in the ISO 16610 series [5], [8], [24], [26]. The main objective of this standardization is to allow metrologists to characterize the utility of the recommended filters according to the corresponding application. The described filters are:

a) Linear filters

b) Morphological filters

c) Robust filters

d) Multi-scale analysis

2.1.4.4. Linear filters

The Gaussian filter and the Spline filter belong to this class of filters. They are defined in this section.

Gaussian filter

The Gaussian filter used in profilometry was easily extrapolated to the 3D surface topography by instrument manufacturers [30]. The implementation of this filter into the areal measurement was carried out by using 2D convolution in the spatial domain or using the Fourier transform in the frequency domain [32]. The main characteristic of this filter type is its zero/linear phase property and 50% transmission at the nesting index wavelength as it is shown in Figure 2.26 [6], [33].

The weighting function (Figure 2.27) of the 3D Gaussian filter is the product of two Gaussian filters (Equation 2.11) [32]:

$$S(x,y) = \frac{1}{\alpha^2.\lambda xc.\lambda yc} exp\left[-\left[\pi(\frac{x}{\alpha.\lambda xc})^2 + \pi(\frac{y}{\alpha.\lambda yc})^2\right]\right] \qquad (2.11)$$

Where λxc and λyc are the cutoff or nesting index in the x and y directions. $\alpha = \sqrt{\frac{ln2}{\pi}} = 0.4697$. This definition is simply an extension of the 2D Gaussian filter.
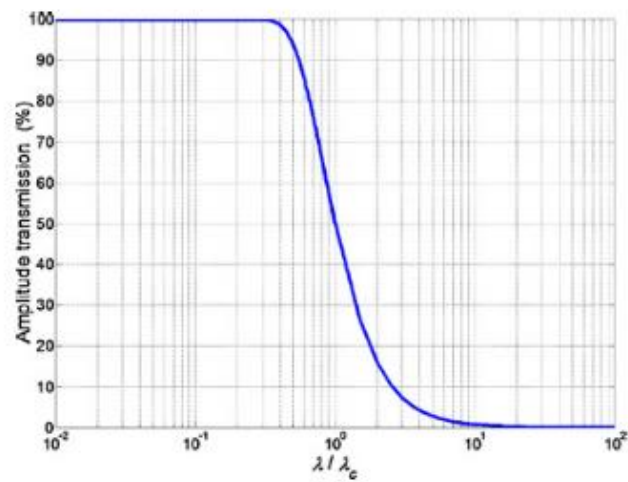
Figure 2.26 Amplitude transmission characteristic of linear Gaussian filter [6].
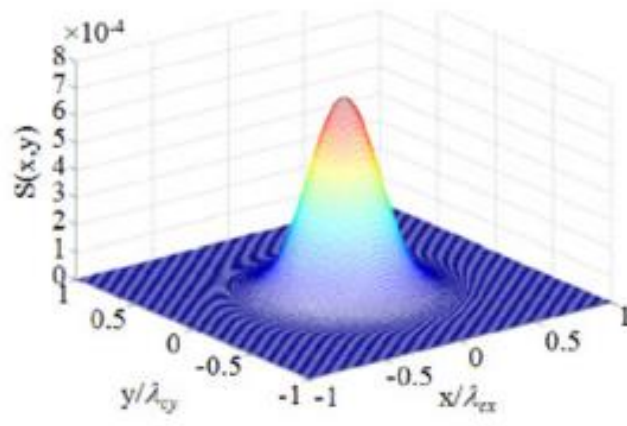
Figure 2.27 Areal Gaussian filter [6].

Some considerations must be taken into account in order to apply the areal Gaussian filter [6]:

a) The measured area has to be truncated at the boundaries of both sides remove distortions due to edges effect.

b) The form must be removed before filtering.

c) The surface texture is assumed to be nearly symmetric.

Spline filter

The spline filter was proposed by Krystek [34] to overcome the above defined drawbacks of the Gaussian filter. There are two types of Spline filters: the non-periodic and periodic. The first type is used to filter open profiles (flat surfaces) while the periodic filter type is utilized for filtering closed profiles (roundness). These filter types are defined in ISO 16610-22.

By definition, the spline filter is a series of geometrical curves that smoothly link a series of points (Figure 2.28). After its application the spline curve does not pass through data points but through suspended points. Data points and the suspended ones are connected to each other using a spring constant (β), called tension parameter. Setting this tension parameter (from 0 to 1) makes it possible to control the filter behaviour. The default value of the tension parameter is β=0.6252, yielding a similar behaviour of a Gaussian filter except for the fact that the spline filter allows the entire measurement without subtracting edges.

Equation 2.12 defines the spline filter:

$$[I + \beta \alpha^2 P + (1 - \beta \alpha^4 Q]W = Z \tag{2.12}$$

Where I is a *n x n* identity matrix. P is a *n x n* tridiagonal symmetric matrix, Z is the vector of the measurement data, W is the vector the filtered data, Q is a *n x n* five-diagonal symmetric matrix, $\alpha = (1/2)\sin(\pi\Delta x/\lambda c)$ and β is the tension parameter [6].
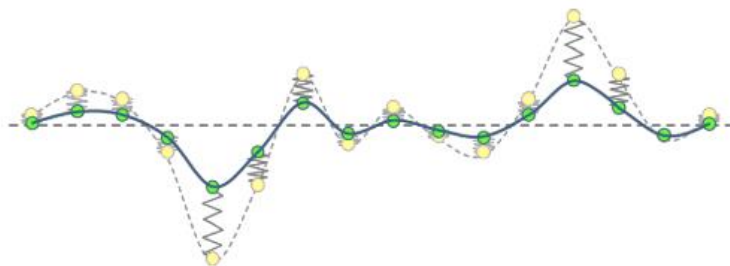
Figure 2.28 Representation of a spline filter. The suspended points (green) are connected to the original data point by a virtual elastic spring. The spline curve (blue) now represents the filtered profile [33].

2.1.4.5.   Morphological filters

The morphological filter is based on the envelope system (E-system). Two different operations namely dilation and erosion compose this filter (Figure 2.29). A structuring element of a given size is used to make a path over the surface of interest.

In the dilation procedure, a disk of a certain radius rolls over the surface and the path of its centre is recorded. This approach tends to enlarge peaks and fills holes in. When dilation is followed by erosion it is called a morphological closing. This filter type creates the upper envelope. In this particular case, the disk is rolled below the dilation line. The envelope closes holes and pores while following the upper shapes of peaks and hills.
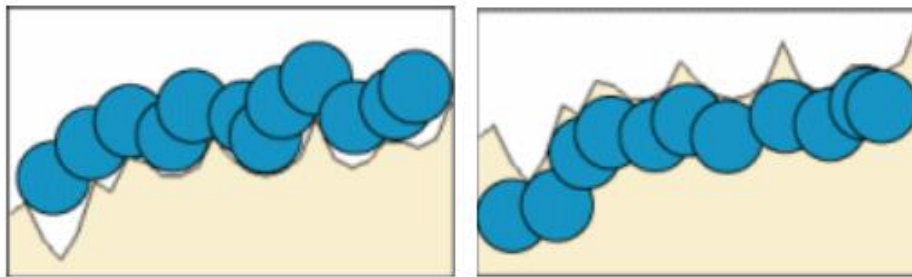
Figure 2.29 Dilation (left) and erosion (right) [30].

When the filtering procedure is reversed, erosion followed by dilation, it is called morphological opening. This creates the lower envelope. It must be pointed out that both morphological closing and morphological opening are filters while dilation and erosion are only operations [30].

2.1.4.6.   Robust filters

The robust filter was designed to be insensitive to deviations due to peaks or valleys (Figure 2.30). The robust Gaussian filter (ISO 16610-71) and the robust spline filter (ISO 16610-62) are included in this class [30].

The robust Gaussian filter is based on an iterative algorithm which calculates local heights based on the distance between the primary surface and the waviness component. This

filter is better suited for structured surfaces, stratified surfaces and in presence of pores, form or grooves. In the case of the robust spline filter the output is quite similar to that obtained with the robust Gaussian filter but its implementation is much more complex. Therefore, it is not common to find this kind of filter in analysis software [30], [33].
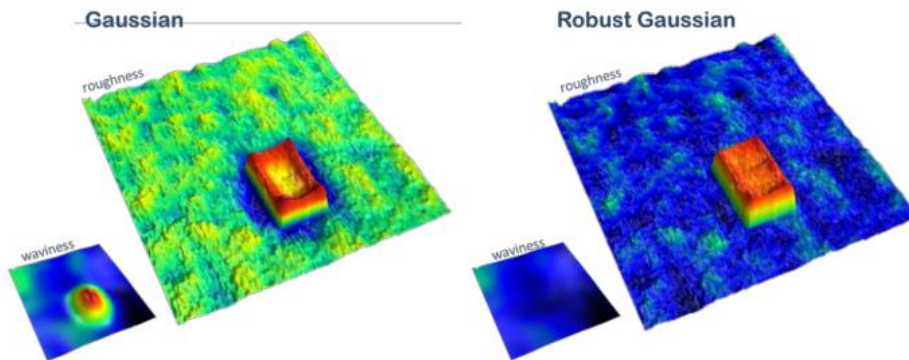
Figure 2.30 The Gaussian filter (left) is disturbed by local discontinuities. On the contrary, the Robust Gaussian filter is not [30].

2.1.4.7.   *Multi-scale analysis*

It is recognised that surfaces have multi-scale topographies within the topography of the surface. This means that a surface can contain fine-scale texture superimposed on other scales of texture [6].

The multi-scale analysis or wavelet filter is used to decompose the surface scales and generate a new surface with the elements that belong to the specified scale level (Figure 2.31). This allows identifying the scale at which a phenomenon occurs. The filter is based on localized harmonic analysis using short-term signals called mother wavelets. This filter type is defined in the ISO 16610-69 for 3D surfaces.
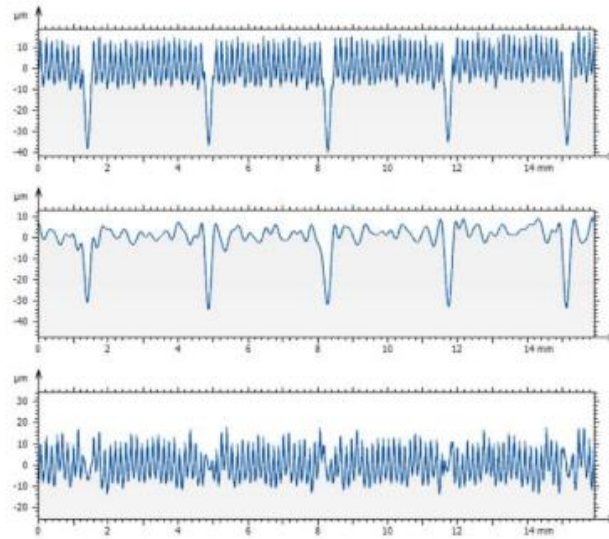
Figure 2.31 The upper signal is filtered by a discrete wavelet filter, being separated in two signals for further analysis [6].

2.1.5. Surface classification

Surface classification has been a topic of interest for engineers, designers and manufacturers over the years. However, it was not until the decade of 1980-1990s when the first proposal to classify surfaces was made. Suh and Sake (1987) [35] and Stout (1998) [36]proposed dividing surfaces into two different classes: engineered and structured surfaces. In the first case, the engineered surface was that in which the surface and the underlying surface were modified in order to achieve a specific functional performance. In the second case, the structured surface was that on which a pattern (geometric features) was designed on the surface to reach a given function. Some years later, Stout and Blunt (2001) modified the division and proposed differentiated surfaces in engineered and non-engineered surfaces. In the former case, the definition remained as described above. However, the non-engineered surface was defined as a surface created as a direct consequence of the manufacturing process. Therefore, no attempt is made to modify the surface performance. In addition each surface category was sub-divided as shown in Figure 2.32 [6].

54
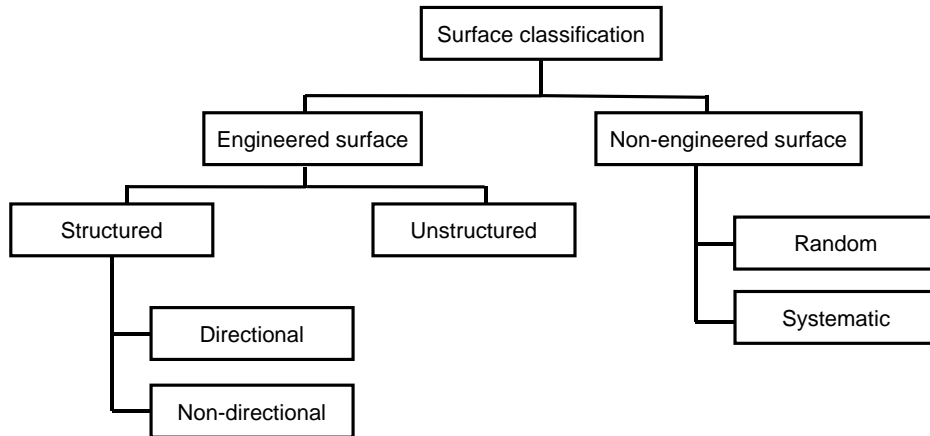
Figure 2.32 Surface classification. Modified from [6]

Nowadays, with the evolution in fields such as surface texture, instrumentation and surface manufacturing processes several authors have reviewed the surface classification and proposed building a new one based on the relationship between surface features and its functionality. The hierarchical structure of surface classification is shown in Figure 2.33
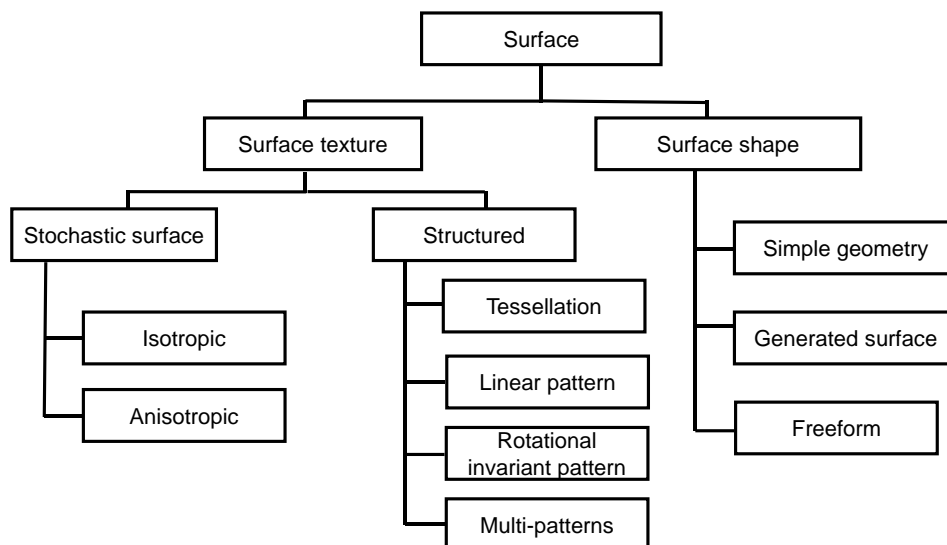
Figure 2.33 New structure of surface classification. Modified from [6]

2.1.5.1.   *Stochastic surface*

Stochastic surfaces are those in which surface features have no specific location, therefore, they do not follow any pattern. For example, in manufacturing processes such as polishing, honing or lapping to name a few, the organization of the surface features is stochastic by nature.

Figure 2.34 depicts the most significant stochastic surface types: the isotropic and anisotropic surfaces. In the case of isotropic surfaces, there is no predominant direction in the surface features. On the other hand, anisotropy can be found in a stochastic surface. For example, in turned or milled surfaces where fundamental periodic components form the surface finish, there can still be a significant stochastic structure. This is because the contact between the tool and the workpiece, yielding material fracture mechanisms or ploughing on the surface workpiece [4], [6].
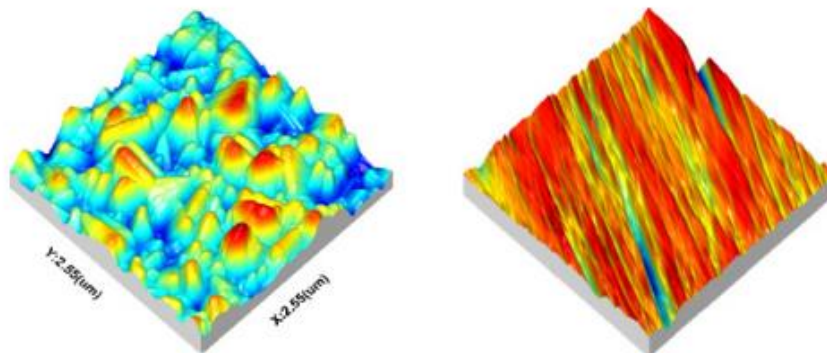
Figure 2.34 Isotropic (left) and anisotropic (right) stochastic surfaces [6].

2.1.5.2.   *Structured surface*

The structured surface type is characterized by having a deterministic structure with high aspect ratio geometric features. In this surface category are included:

a) Tessellations

b) Linear patters

c) Rotationally invariant patterns

d) Multi-patterns

Tessellations

The tessellated surfaces have a repeated structured formed by a collection of tiles that fills the entire surface without overlaps or gaps. One example of this surface type is a golf ball, hexagonal prisms, etc. Figure 2.35 shows an example of this surface category [6].
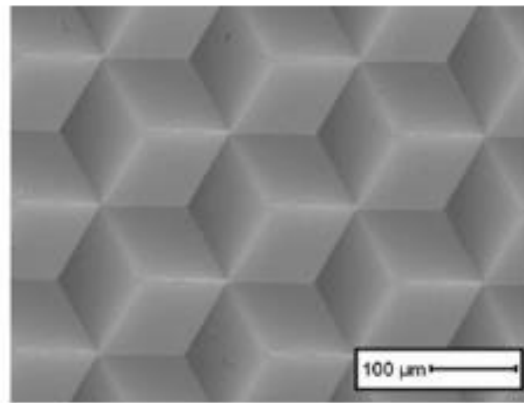
Figure 2.35 Tessellation surface [6].

Linear patterned surface

Linear patterned surfaces are a variant of tessellated surfaces. In this case, linear patterned surfaces have only a single linear cell (Figure 2.36). These surface types are employed in friction and lubrication applications [6].
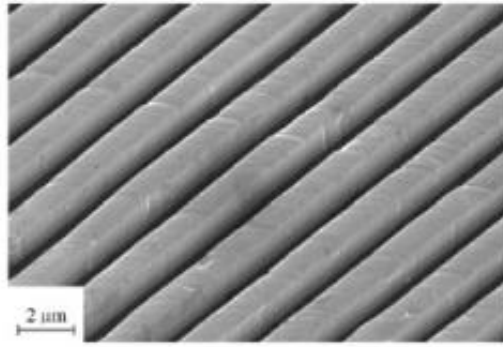
Figure 2.36 Surface with a linear pattern [6].

Rotational invariant patterned surfaces

Unlike the tessellated and linear patterned surfaces, which have their periodic structures in a Cartesian coordinate system, rotational invariant patterned surfaces have their periodicity in a polar coordinate system. Figure 2.37 depicts a Fresnel lens which is one of the most common examples of this surface type [4], [6].
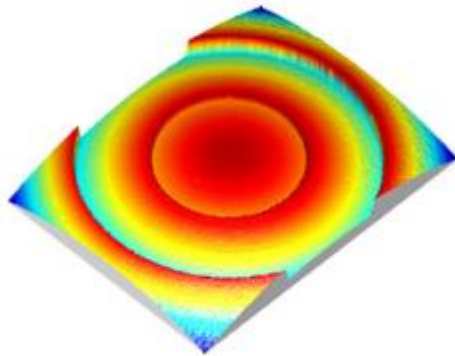
Figure 2.37 Rotational invariant patterned surface [6].

Multi-patterned surfaces

Multi-patterned surfaces include all structured surfaces with the exception of the three surface types described above. Surfaces with no periodic structures but having steps, faces or

edges are considered multi-patterned surfaces. For example, in electronics (MEMS/NEMS), microfluidics or IC industries it is possible to find these type of surfaces (Figure 2.38) [4], [6].
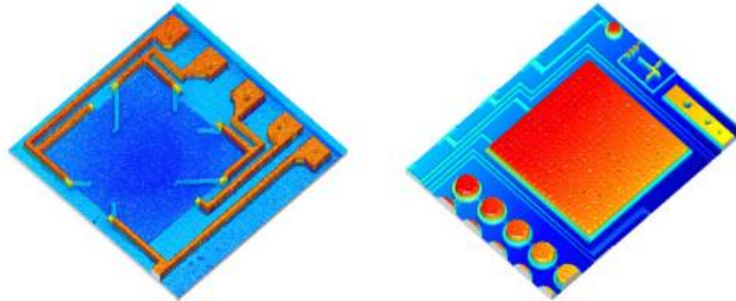
Figure 2.38 Non-repeating structured surfaces (MEMS) [6].

Simple geometries, generated geometries and freeform surfaces

Simple and generated geometries have the same design foundation in industry. In the case of simple geometries, planes, cylinders and spheres are included in this category. On the other hand, generated surfaces include surfaces of revolution, prisms and helicoids. However, with the advent of surface manufacturing and design, freeform surfaces without axes of rotation or translation symmetries have been recognised as important design forms. The F-theta lens and high beam reflector are two typical examples of freeform designs (Figure 2.39) [4], [6].

Figure 2.39 Open ring reflector (left) and F-theta lens (right) [6].

2.2. Appearance measurement

Human judgements about an object's appearance are based on experiences. This means that decisions about whether an object is useful, fresh or new are normally unconscious. For instance, a mobile phone owner simply enjoys the glossiness of his new phone without associating it with any phenomenon involving the interaction between light and object. In this section, appearance attributes, interaction modes between light and object, appearance measuring techniques and perception of the human visual system (HVS) are defined in order to objectively understand the factors affecting object appearance.

2.2.1. Modes of appearance

The perception of objects can vary in accordance to the illumination and visual conditions. Modes are the manner in which light can be perceived as a function of the spatial and temporal variations. There are three different modes [1], [37]:

1. Illuminant mode: this mode occurs when light comes directly from a source of light, namely sun, lamp, etc.

2. Object mode: this mode take place when light comes from an object. This mode can be classified into two sub-modes, surface and volume mode. In the first case, the light comes from the object's surface, while in the second case the light passes through the object.

3. Aperture mode: this mode of appearance occurs when the perception depends neither on the light source nor on the light coming from objects. This mode happens when light is perceived through an opening or a field aperture of photometers or visual colorimeter. It could be associated to an illuminated room through an open window/door.

The appearance of an object can vary completely as a function of the mode. For example, when a room is illuminated with orange light and the observer sees it through a window (aperture mode) at a given distance, the observer perceives that the room is orange.

However, if the observer comes closer to the room, it is possible to distinguish the white colour of the walls (object mode) although the light source is orange (illuminant mode) [1], [37].

2.2.2.Appearance attributes

The appearance of objects depends on the interaction of different factors such as the light source, the object shape, the human eye and the human nervous system. All of these variables can affect the final judgement of an object. Thus, it is important to understand how objects are seen. The evaluation of the surface appearance can be conducted considering the two main surface attributes or specific visual qualities, namely colour and geometric attributes. The colour is determined by the part of the incident light that is reflected or transmitted. The geometrical attributes are defined by the directional distribution of reflected or transmitted light. These can be described as being glossy, transparent, matte, clear, turbid, among others.

Although colour is the most important appearance attribute it cannot be exclusively used to define the appearance of an object. Geometric attributes provide additional information regarding the appearance on an object. The quality and quantity of reflected light coming from an object with uniform colour can be perceived differently due to geometric attributes such as texture or gloss. For example, the colour of a rough surface is perceived less saturated in comparison to the one coming from a smooth surface. This is because geometric attributes affect the spatial distribution of light [1], [37].

2.2.2.1.   *Colour attributes*

The colour is present in many aspects of our daily life, for example in clothes, cosmetics, plastics, leather, etc. In almost all cases the colour is introduced using pigments. This attribute is normally used to describe three different aspect of the reality. The first one is the property of an object i.e. "a blue object". The second one describes a characteristic of light. In the case of blue objects, all the wavelengths of visible light are absorbed with the exception of the blue component. The third aspect describes the sensation interpreted by the brain, yielding a perception [37].

Figure 2.40 depicts the three-dimensional characteristics that are used to define colour. The first one refers to the attribute of lightness, the second and third ones are related to chromatic attributes, namely hue and saturation, respectively [1].
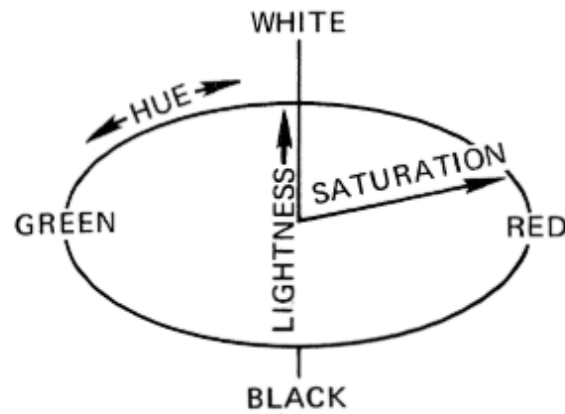
Figure 2.40 Chromatic coordinates to define colour [1].

Lightness is defined by the International Commission of Illumination (CIE) as follows: 'Attribute of a visual perception according to which an area appears to emit, or reflect, more or less light' (CIE 1987). This property is related to brightness. In this case, lightness is the brightness of a given area judged relative to the brightness of a similarly illuminated area that appears to be white or highly transmitting. Therefore, it can be said that lightness is the perceived brightness of a non-white object compared to that of a perfect white object [37], [38]. The hue is the attribute of a visual perception according to which an area appears to be similar to another one of the perceived colours of red, yellow, green and blue (CIE 1987). In other words, it can be said that the hue is the perceived colour of an object. The saturation is the attribute of a visual perception according to which an area appears to exhibit more or less of its hue (CIE 1987) [38]. In this case, saturation (or chroma) can also be related to lightness since the colourfulness is proportional to the level of illumination. For example, in bright daylight the scene may look very colourful, while on a cloudy day the colourfulness decreases. This means that colour remains independent of the lighting conditions, however the vividness

of colours is dependent on illumination. This slight difference in how the human visual system (HVS) perceives colours is the saturation.

2.2.2.2. *Geometric attributes*

The geometric attributes of an object can be classified according to the way in which it interacts with the incident light as follows:

a) Specular reflection – associated to smooth surfaces

b) Diffuse reflection – associated to rough surfaces

c) Specular transmission – associated to transparent objects

d) Diffuse transmission – associated to translucent objects

Specular reflection

Figure 2.41 depicts the specular reflection, which takes place on perfectly flat surfaces and follows the well-known law of reflection. This law says that the angle of incidence is equal to the angle of reflection (Equation 2.13).

$$Angle\ of\ reflection\ \theta = Angle\ of\ incidence\ \theta \qquad\qquad (2.13)$$

Reflection occurs when the waves encounter a surface that does not absorb the energy of the radiation completely, bouncing waves away from the surface. In the case of specular reflection, when a light beam strikes on a very smooth surface at a given angle, the reflected light is distributed in a narrow set of directions. This results in a judgement of a glossy surface as a polished metallic surface or a mirror.
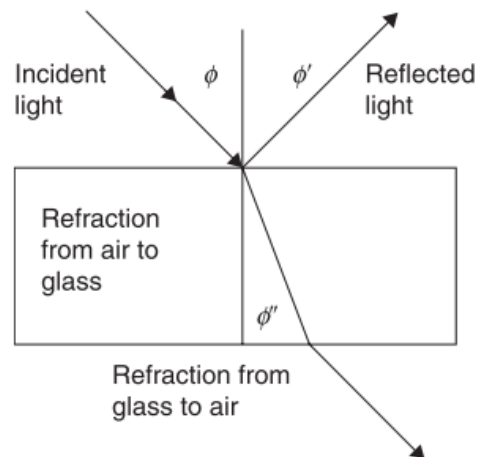
Figure 2.41 Reflection and refraction of light in the specular mode [37].

Diffuse reflection

Unlike specular reflection, in the case of diffuse reflection the incidence light beam is reflected at many angles. An ideal case of diffuse reflection is the Lambertian reflectance (Equation 2.14), in which an illuminated surface will have equal luminance from all directions. This reflection type is common in rough surfaces, where each individual light ray strikes with a portion of the surface having different orientations. Therefore, the normal line at the point of incidence is different per each ray, yielding scattering in different directions as shown in Figure 2.42. This light reflection type is usually associated with matte surface finishes.

$$E_\theta = Ecos\theta \tag{2.14}$$

Where E_θ is the light intensity, E is the maximum light intensity at 0º regarding the surface normal and θ is the angle of incidence between the light source and the normal to the surface.
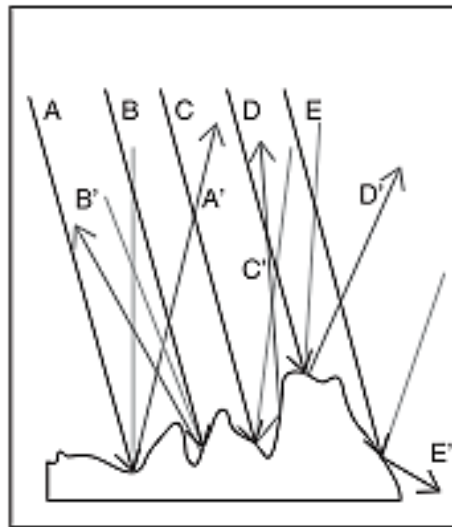
Figure 2.42 Reflection of light in the diffuse mode. Modified from [37]

Specular transmission

Specular transmission or transparency is the physical property that allows light to pass through a material. This behaviour follows Snell's law (Equation 2.15). An incident light beam travels through a medium (normally air) with a given refractive index η at a given angle θ. The light meets and enters into a medium with a refractive index η', leaving it with an angle θ'' (Figure 2.41). This phenomenon usually occurs in materials such as glass or liquids

$$\frac{\eta'}{\eta} = \frac{\sin\theta}{\sin\theta''} \tag{2.15}$$

Diffuse transmission

Diffuse transmission has a similar behaviour to the above described diffuse reflectance. In this case, light goes through a textured transparent or semi-transparent object. Light is thus transmitted in a diffuse mode, yielding less contrast and intensity. This will generate clearer shades, having smoother transition between highlight and shadows than direct light. This phenomenon is normally called translucency.

2.2.3.Human visual system (HVS)

The eye together with the brain forms the so-called human visual system (HVS) which is essential for getting an idea about the surrounding world. Eyes act as detectors of light coming from object reflections or transmissions. The perception of objects is created by the eyes and the brain. This perception depends on the physical qualities of light, and physiological and psychological processes occurring in the eye and brain [38].

2.2.3.1.   Construction of the eye

The main representative parts of the human eye are illustrated in Figure 2.43. It is well known that the cornea has most of the optical power, providing 40 diopters to the total 60 diopters of the eye. The additional optical power is provided by lens which focus the image for either distant or near objects. This is possible thanks to the modification of its thickness, which becomes thinner or thicker for viewing distant or near objects, respectively. An inverted image is created between cornea and lens, which is projected onto the retina, the light-sensitive layer of the eye. The iris is the coloured part of the eye and the central aperture diameter can be modified from 2 to 8 mm for bright light and dim light conditions, respectively. The central aperture is called the pupil and it is the area where light passes through [38].
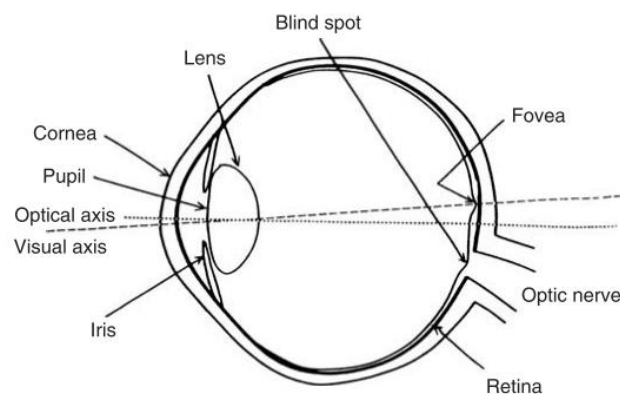
Figure 2.43 Diagram of the human eye [37].

One of the most important part in the eye structure is the fovea. Taking into account that the field of vision of the eye is of 40º from the visual axis, the fovea corresponds to the central

5.2º of this field of vision with an axis offset of 4º from the optical axis. In addition, an area within this field of vision corresponds to the sharpest vision, having 1.5º of field of vision known as the foveola [38].

Figure 2.44 represents the light rays' path through the optical system. The light coming from a given object, in this case the object AB, reaches the eye. To be noted is that only a small portion of reflected light coming from the object is detected by the eye. The light of the central part of both points A and B hit the cornea normal to the surface and then strikes the retina at points A' and B', resulting in an inverted image. The point within the eye where these beams cross is known as the nodal point of the eye.
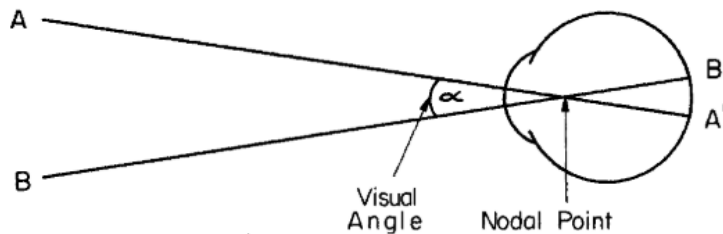
Figure 2.44 Representation of rays' path through the optical system [1].

2.2.3.2. *Optics of the eye*

The human eye receives light coming from objects and surroundings. The light is characterized for having its own intensity (number of photons per unit of time), wavelength or energy per photon and a polarization state. It must be pointed out that all these properties can vary when, being detected by the human eye. This detection occurs separately, meaning that eyes detect variations in intensity or wavelength. Polarization is not detected.

Human eye detection capabilities are normally determined using a sine wave grating that varies in orientation with light and dark bands. The width of the bands is related to the so-called spatial frequencies. In this case, wide bands are related with low spatial frequencies whereas thin bands define high spatial frequencies shown in Figure 2.45 [39]. Usually, the

frequency of the sine wave is defined as the number of oscillations per unit distance or time. In spatial vision it refers to the dimensions of the visual stimuli. However, it is more convenient to express spatial frequency in terms of the angle subtended at the eye (visual angle) using cycles per degree visual angle (c/deg). A cycle is one dark and one light band of the sine waveform. The amplitude of a sine wave is half the peak to valley distance. Finally, the contrast of a visual pattern is the difference in luminance between peaks and valleys of a given waveform. The contrast is often measured using the Michelson contrast equation (Equation 2.16) [40].

$$C = \frac{L_{max} - L_{min}}{L_{max} + L_{min}} \quad\quad\quad (2.16)$$

Where C is the contrast, L_{max} and L_{min} are the luminance of the peak and valley of the waveform, respectively.
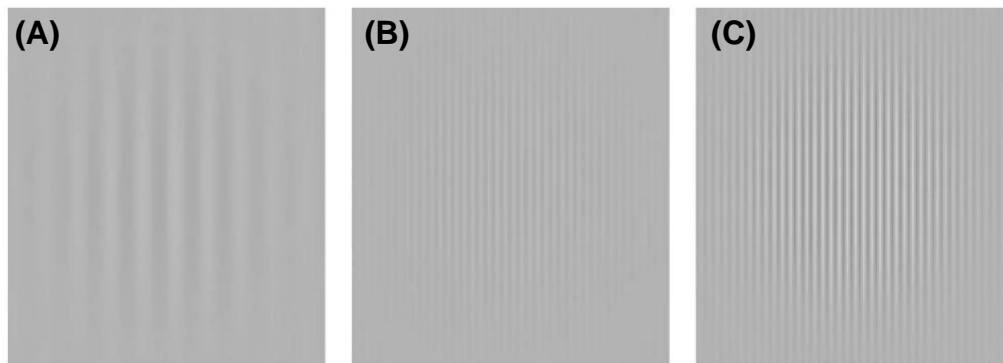
Figure 2.45 Sinusoidal grating of low frequencies (a); sinusoidal grating of same contrast than (a) but at higher frequency (b); sinusoidal grating of same frequency than (b) but with higher contrast (c). Modified from [39]

Contrast sensitivity function (CSF) and visual acuity

One of the most important methods to quantify visual capabilities is by determining the contrast sensitivity or contrast threshold across a variety of spatial frequencies and contrast conditions. In this case, the contrast sensitivity for a given spatial frequency is defined as the minimum contrast required to distinguish between a sine wave grating having a uniform background of the same average luminance. These results can be plotted, obtaining the contrast sensitivity function (CSF) (Figure 2.46)[41]–[46].
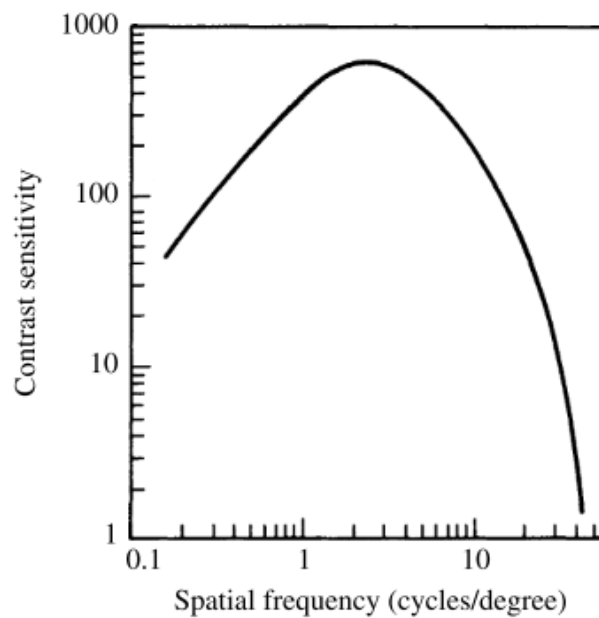
Figure 2.46 Representation of the contrast sensitivity function (CSF) [42].

It should be pointed out that the CSF is dependent on distance, hence, visibility and detectability of details at a given frequency is a function of the viewing distance. For instance, if an observer moves away from an image, fixed size features, it increases fewer degrees of visual angle. This action moves to the right on the CSF curve and likely requiring higher contrast to perceive finer details. On the contrary, moving closer to the grating, previous invisible features become visible because it rises above the visibility threshold [40]–[42].

Therefore, the visual acuity, which depends on the distance, affects the visual angle formed between the observer and the object. The visual angle is dependent on two factors:

1. It is proportional to the object size
2. It is inversely proportional to the object-eye distance.

It can be said that the larger the object size the larger the visual angle. On the contrary, the larger the distance the smaller the visual angle will be. Figure 2.47 and Equation 2.17 depicts how the visual angle can be calculated [47].
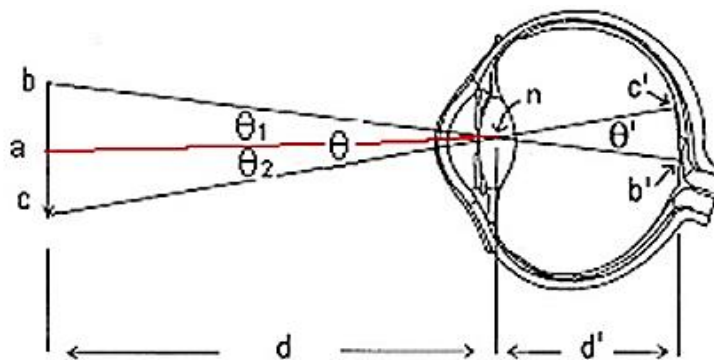
Figure 2.47 Visual angle subtended by an object on a human eye [47].

$$\frac{\theta}{2} = \arctan\left(\frac{ab}{d}\right) \qquad\qquad (2.17)$$

Campbell and Gubish (1966) [48] demonstrated that the eye's optics under optimal illumination conditions do not pass beyond about 60 c/deg. Therefore, taking into account this statement and Equation 2.17 the visual acuity can be calculated as a function of distance or the object size. For example, for a viewing distance of 200 mm the maximum feature size that the human eye can resolve is of approximately 60 µm.

In the field of optics, the sampling theorem provides valuable information to study the visual system. It is used to define how many points are needed to determine a complex waveform. The answer to this is that for a given number of points, all frequencies below N/2 can be specified. For instance, 40 regularly spaced samples across 1° visual angle will specify the frequency of all frequencies below 20 c/deg that compose the complex waveform [26], [40].In this particular case, the sampling theorem is useful in considering the spacing of the visual receptors. As discussed above, the optical system is not able to resolve anything less than 60 c/deg, therefore there is no reason to have more than 120 receptors per degree of visual angle. In addition, it should be remarked that no additional information is obtained when sampling a given waveform with a frequency higher than two times its highest frequency.

Equations 2.18 and 2.19 define frequency bandwidths according to the sampling conditions.

$$f_h = \left(\frac{1}{2\Delta x}\right) = \left(\frac{1}{2\Delta y}\right) \; (\text{mm}^{-1}) \tag{2.18}$$

$$f_L = \left(\frac{1}{Nx\Delta x}\right) = \left(\frac{1}{Ny\Delta y}\right) \; (\text{mm}^{-1}) \tag{2.19}$$

Where f_h is the high frequency limit and f_L is the long frequency limit. Δx and Δy are the sampling intervals in the x and y-axis, respectively. The sampling interval can be approached to the width of the sine bands of the grating, limiting the visual resolution. Nx and Ny are the number of data points in the x and y-axis used to define a complex waveform, respectively

Visual sensitivity

It is well known that psychology provides a fundamental role in the description of the human visual system. It was started by E. H. Weber (1795-1878) who demonstrated that the sensory response to a given stimuli is not lineal with the number of stimuli. According to Weber's Law, the differentiation between stimuli is dependent on the percentage of variation. For example, in the visual detection field, the difference between three ceramic tiles reflecting 80%, 40% and 20% of the incidence light, respectively, is equal. This is because the change in lightness from 80% to 40% and from 40% to 20% is the same, a 50% variation. This concept is also related to the theory of G. T. Fechner (1801-1887) who introduced the word psychophysics in his book entitled *Elemente der Psychophysik (1860)*. This science enables quantifying the relation between a physical stimulus and its perception. It can be said that after G. T. Fechner's book, where many procedures for measuring threshold and still in use today were described, the modern era in the field of perception-detection began, [1], [43], [49].

The eyes and brain are the main parts constituting the HVS. The eyes are responsible of detecting light and converting it into signals that are transmitted to the brain. These signals are processed by the brain making decisions regarding an object's perception. In the field of human vision, several studies have been performed to determine the visual sensitivity in regard to a given stimuli. In other words, the aim was determining the minimum detectable stimuli by the human eye at different viewing conditions. In this case, the contrast threshold is defined as the minimum contrast needed to detect a change in lightness intensity by an observer [1], [50].

Fechner established the contrast threshold to be 1% regardless of the illumination conditions. This statement still remains valid. For example, it is used in the identification of the Sloan letters, which is a set of optotypes used to determine visual acuity [43]. Many authors have been working on determining the contrast threshold. Studies have been conducted modifying illumination and viewing conditions, using different methodologies [44], [46], [50]–[56] and studying the effect of the interrelation of attributes (gloss, lightness or texture)

on appearance perception [2], [57]–[71]. For instance, it has been demonstrated that textured surfaces having different gloss levels are perceived to be dissimilar. The texture of surfaces with higher gloss level is perceived as more vivid. On the other hand , the same texture with lower gloss level is perceived as less intense [58]. The reason is that appearance attributes such as gloss and texture interact, modifying the observer's visual perception and judgement. Another example of interaction between appearance attributes was reported by Schmid and Anderson [67]. They demonstrated that the perception of lightness constancy is dependent on the reflectance properties of the object's surface. This means that for surfaces where specular reflection prevails (smooth surfaces or high-gloss finish) lightness constancy was better. On the contrary, in surfaces with a predominant diffuse reflection t (rough surfaces or matte finish) the lightness constancy was perceived worse.

2.2.4. Factors affecting optical properties

The overall object appearance can be defined through the main four attributes, colour, gloss, translucency and texture.

The interaction between incident light and an object leads to obtaining a given appearance. For instance, if a given object tends to reflect light in the specular mode this leads to perceiving the surface as shiny or high gloss finish. On the contrary, if the reflection is produced in the diffuse mode, the surface is perceived as matte or low gloss. These two phenomena are directly related with the texture. In the former case, the object's surface was likely smooth yielding a reflection with the same angle as the incident one. However, in the latter case, the diffuse reflection is produced when light encounters a rough interface. Therefore, the appearance of an object must be evaluated taking into account the interaction between attributes.

Figure 2.48 shows the attributes that affect optical properties of objects and its interactions.
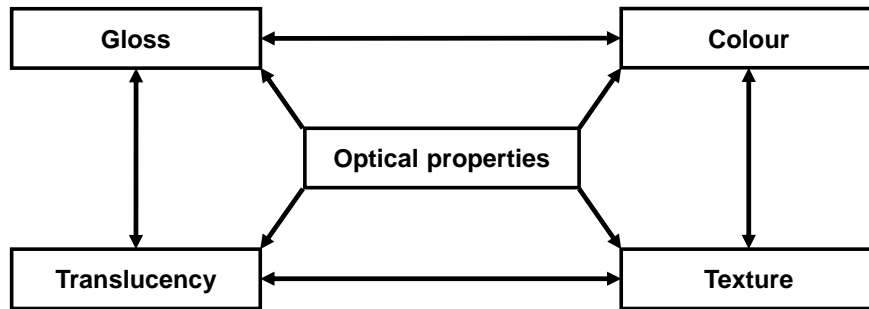
Figure 2.48 Appearance attributes that affect object's appearance. Modified from [37]

2.2.4.1.　　Colour

There are three phenomenon that can occur and affect colour appearance namely successive contrast, simultaneous contrast and assimilation.

Successive contrast occurs when the eye is stimulated with a given stimuli, i.e. the colour yellow for a few seconds or minutes, and the retina adjusts its sensitivity to compensate the general intensity and colour of the stimulation. When the stimulation is over, surrounding objects have an appearance that tends towards the prior stimuli. For example, when an observer is watching a television screen with a white colour point and then looks at objects in a room lit with light of significantly lower correlated colour temperature, they appear to be yellower than usual. Figure 2.49 shows an example of successive contrast.
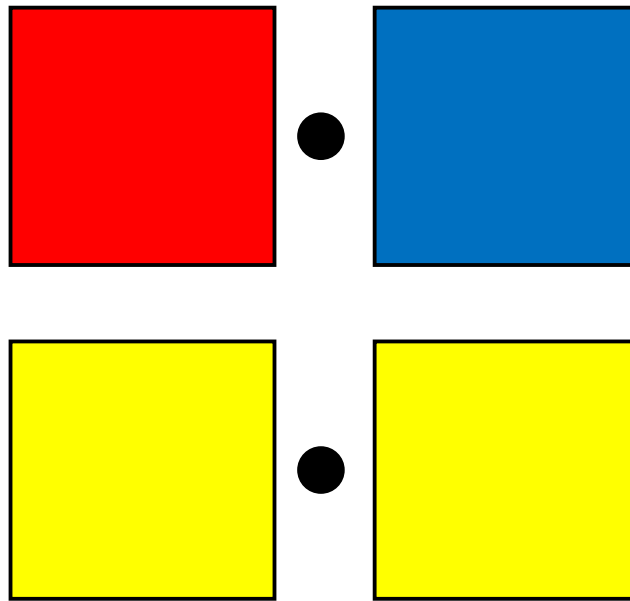
Figure 2.49 A demonstration of successive contrast.

Modified from [37]

The simultaneous contrast takes place when the object's colour is affected by its surroundings. In other words, the presence of other colours around an object can alter the appearance of the object's own colour. For example, it is demonstrated that a light or dark environment can modify colour lightness. A light ambient makes a colour become darker, while a dark surrounding has the opposite effect. Figure 2.50 shows the effect of simultaneous contrast. Two scale-grey bars are shown having the same colour degradation. The unique difference is the background. It is noted that the bar with a lighter background is perceived to be darker than the one with a dark background.
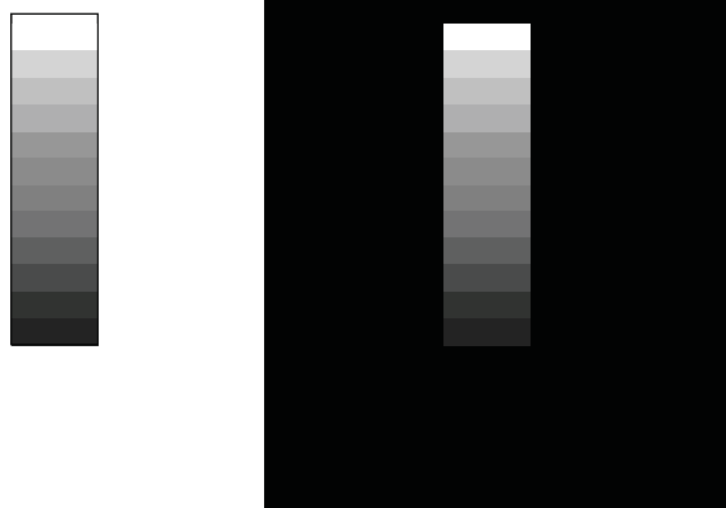
Figure 2.50 A Demonstration of simultaneous contrast [37].

Finally, assimilation is the third factor that can alter colour perception. It is defined as the opposite of simultaneous contrast. This phenomenon take place when a colour becomes "more" than its surrounding instead of "less". In other words, a colour becomes darker with a dark surrounding and lighter in a light surrounding. This is the opposite of simultaneous contrast. Figure 2.51 shows an example of assimilation. The upper rectangles have the same colour as the lower ones. It should be pointed out that the white pattern makes the background (the rectangle colour) lighter than the black pattern, which results in a darker background. This is the effect of assimilation on the colour perception. This likely occurs due to the light scattering in the eyes and because the HVS has lower resolution for chromatic signals than for achromatic as demonstrated by Hunt [72]. In addition, it is noted that this effect can be enhanced by viewing patterns at a certain distance.
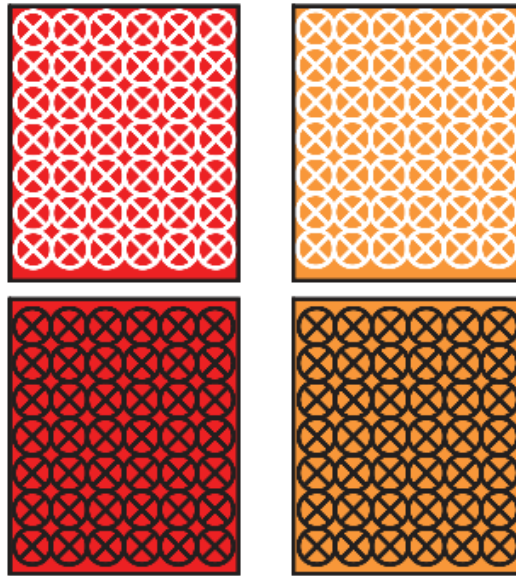
Figure 2.51 A demonstration of assimilation effect [37].

2.2.4.2.   *Gloss*

Gloss is the most important geometric attribute for the visual appearance of objects. This is because gloss can modify the observer's visual perception, affecting the perceived quality [49], [73].

This geometric attribute is related to the specular reflection of the object surface. Therefore, it is a measurement of how shiny an object is. An ideal reflecting surface will follow the law of reflection where the angle of incidence is the same as the angle of reflection (Equation 2.13). However, not all surfaces are perfect in reflection as a mirror. There are many surfaces with imperfections that yield diffuse reflection e.g. rough surfaces. The degree of specular reflection of surfaces can be measured in three different ways:
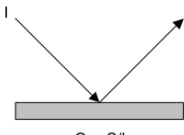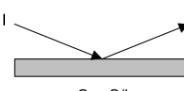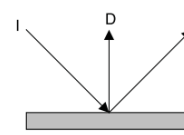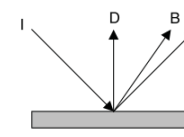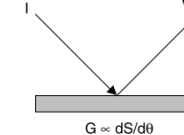
1. Portion of light reflected following the laws of reflection.

2. Angular spread of reflecting light.

3. Dependence of regular reflection on the angle of incidence.

It must be pointed out that the above instrumental measures are not able to assess all visual phenomena involving gloss. This is because the human eye has a higher resolution than most of the reflectance measuring instruments. The human eye is capable of distinguishing two reflected light beams with a separation of 0.01°, whereas photometric measurements are limited to the receptor's field angle, being 100 times larger [38]. Recently, the number of studies on gloss perception have grown exponentially. It has been studied in either fixed [74] and variable [56] illumination conditions. In the former case a new light reflection model was introduced. It was based on experimental studies of gloss perception. This model allows relating physical parameters used to describe the reflection properties of glossy surfaces with the perceptual dimension of glossy appearance. In the latter case, Obeinet al. [58] demonstrated that gloss appearance was independent of the direction of illumination, introducing the concept of gloss constancy. In addition, as reported by Hunter [75] , there are six different gloss types that can be perceived: Table 2.2 summarizes these gloss types.

- The specular gloss as proportional to S/I

- The sheen as proportional to S/I at grazing angles of incident light

- The contrast gloss or lustre as proportional to D/S

- The absence of bloom gloss as proportional to (B-D)/I

- The distinctness of image gloss as the sharpness of the specular reflected light.

Where *I* is the amount of incident light, *S* is the amount of specularly reflected light, *D* is the diffuse reflectance normal to the surface and *B i*s the off-specular light.

Table 2.2 Gloss types. Modified from [37]

Types of gloss	Visual evaluation	Reflectance function	Types of surfaces
Specular gloss	Shininess and highlights	$G \propto S/I$	Medium-gloss surfaces
Sheen	Shininess at grazing angles	$G \propto S/I$	Low-gloss surfaces
Contrast gloss or lustre	Contrast between specularly reflecting areas and other areas	$G \propto D/S$	Low-gloss surfaces
Absence of bloom gloss	Absence of haze adjacent to reflected highlights	$G \propto (B-D)/I$	High and semi-gloss surfaces
Distinctness of image gloss	Distinctness and sharpness of mirror images	$G \propto dS/d\theta$	High-gloss surfaces
Surface uniformity gloss	Surface without texture	Not a function of reflectance	Medium to high gloss surfaces

2.2.4.3.   *Translucency*

As reported by Hutchings and Luo [76] translucency plays an important role in the total appearance of an object. The appearance of the object can be modified or perceived in a different way depending on the relationship between the light scattered, reflected or transmitted.

The phenomenon of translucency occurs between the extremes of transparency and opacity. When an object or scene can be clearly seen through a material, it is said that this

material is transparent. On the contrary, if light does not pass through the material and it is not possible to distinguish anything through it, the material is opaque. However, if it is possible to see a blurred scene or object through the material, it is translucent. This blurred image is associated to a loss of information in comparison to optimal viewing conditions like viewing an object through an ideal transparent material. Translucency is a consequence of diffuse light transmission.

2.2.4.4.   Surface texture

The perception of surface texture is the most complex factor. This is because its perception can be considered as a function of the other three appearance attributes (colour, gloss and translucency). However, surface texture can also alter the colour tone and lightness intensity of objects, modifying its appearance [37].

Usually, surface texture is defined as fine, coarse or smooth. Alternative definitions such as roughness, smoothness, orange peel etc. are also valid to describe surface texture perception. All these definitions have the objective of describing a variation. The perception of a surface texture can vary with the viewing direction and the angle of illumination. This means that a texture appears differently under the following two conditions [77]–[79]:

1. Different viewing directions but keeping the illumination angle constant.

2. Different angles of illumination but keeping the viewing direction constant.

Ho et. al. [78] demonstrated that the texture of a given object is perceived differently as a function of the illumination angle and roughness level. In this particular case, three different angles were defined: 50º, 60º and 70º degrees (Figure 2.52).
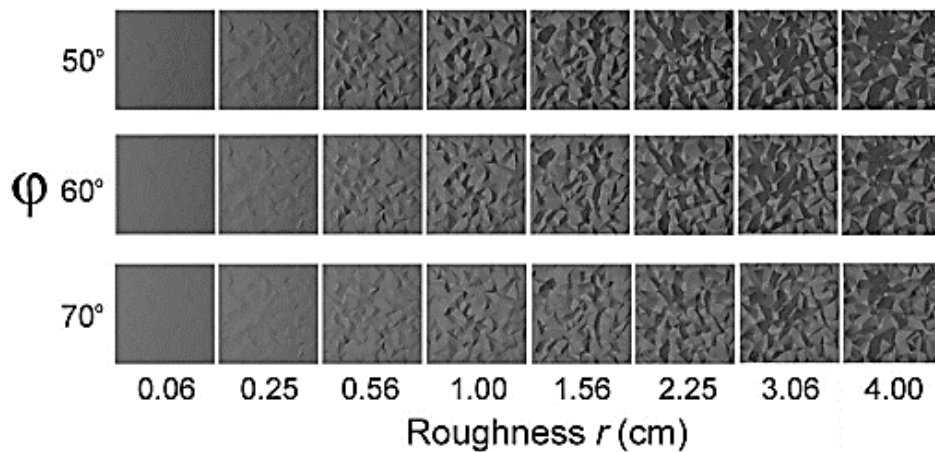
Figure 2.52 Effect of illumination direction on the texture perception [78].

In a later work, Ho et. al. [79] demonstrated that texture perception is also affected by the observer's viewpoint. Figure 2.53 depicts the effect of the observer's position, keeping the location of the light source constant, on surface texture perception. It was concluded, in both studies, that the surface texture was perceived to be rougher when the contrast between light and dark areas was greater.
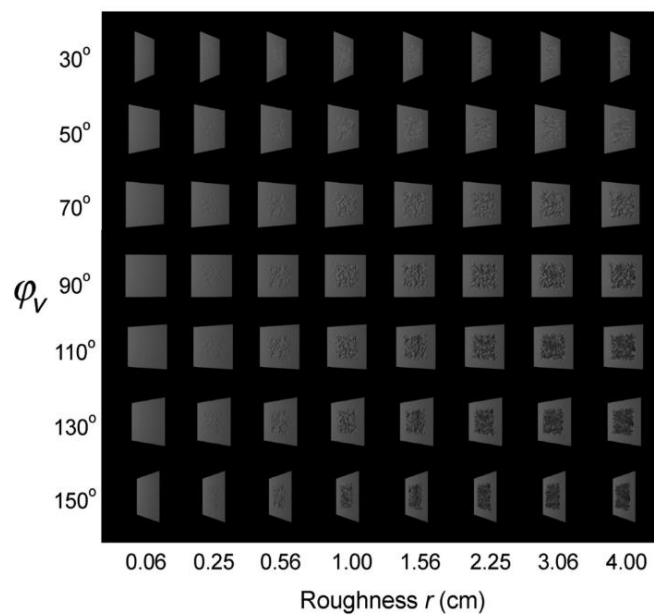
Figure 2.53 Effect of the observer's view of point on the texture perception [79].

The interaction between attributes can also modify the perception of the surface texture. As defined by Koenderink and Van Doorn[54] surface texture can be classified in three different scale ranges according to the visual perception field: the megascale, the mesoscale and microscale. The megascale refers to the object's shape, i.e., the spherical shape of a golf ball. The mesoscale is related to surface irregularities, in the case of the golf ball it would be the bumpiness (mesotexture) of the ball's surface which in comparison to a smooth rubber ball is dramatically different. Finally, the microscale is associated with those features that are invisible to the human eye, although they are crucial for the object's glossy appearance. For example, in the case of gloss and shape (megascale), it was demonstrated that gloss can modify shape perception. Objects with highlighted gloss areas appear more curved than those with lower gloss levels [80], [81]. Similarly, it was shown that the shape of an object can alter the surface reflectance judgements made by observers [62]. Therefore, the object's perception does not only depend on a single attribute. The conjoint evaluation of surface attributes leads to a more accurate judgement of object appearance.

In the case of surface texture, glossiness plays an important role in its perception. Ho et al.[58] and Qi et al. [70] show how gloss and surface texture interact with each other. The results demonstrate that observers' judgements were conditioned by gloss and bumpiness levels. Surfaces with high gloss were perceived as bumpier and bumpier surfaces were perceived as glossier. Therefore, both gloss and surface texture perception were linked to each other.

2.2.5. Instrumentation for measuring appearance attributes

Appearance attributes have been grouped into two different categories: chromatic and geometric. The former refers to the colour. Attributes such as gloss, translucency and texture are included in the geometric attribute group.

It should be pointed out that the human visual system (HVS) detects the interaction between all appearance attributes simultaneously to make decisions regarding object appearance. Instruments, on the contrary, are not yet able to measure all appearance attributes

jointly. Nevertheless, instrumentation is needed to provide a quantitative, reproducible and objective assessment of appearance.

In this section, the main types of instrument used for measuring the appearance attributes of an object are described.

2.2.5.1. *General considerations*

Instrument types

As discussed in the prior section, a specific instrument is necessary to measure each appearance attribute. Thus, four considerations should be borne in mind to select the proper instrument.

The first consideration is related to how the HVS detects objects. The appearance is analysed considering the two main groups of attributes namely chromatic and geometric ones. Instruments can also be grouped into these two categories.

The second consideration is associated with the instrument analysis type. There are physical and psychophysical analysis instruments [1].

1. Physical analysis instruments such as photometers and gonio-photometers detect and measure the physical properties of the light dispersed by objects. These instruments provide information about how objects reflect and transmit light, but they do not give information regarding how objects are seen by observers.

2. Psychophysical analysis instruments such as tristimulus colorimeters, reflectometers, and glossmeters among others, provide information about how objects are perceived by the HVS. These instruments seek to correlate the human impression regarding an object's appearance judgement.

The third consideration involves the instrument measuring geometry. Three different optical modes to assess objects appearance have been defined.

1. Illuminant mode

2. Object mode

3. Aperture mode

The measuring object mode is preferred to build an instrument. It can be divided in the following subcategories:

a) Colour measurement through diffuse reflection and gloss, if any, is seen by specular reflection.

b) Colour measurement through specular reflection

c) Translucency measurement through diffuse transmission

d) Transparency measurement through specular transmission

The fourth distinction is differentiating between laboratory and on-line or continuous-process instruments. In the first case, laboratory instruments are more accurate and trustworthy under favourable operation conditions when used by skilled operators. In the second case, the on-line or continuous-process instruments are better suitable for hostile environments and are maintained-dependants by users with production skills. Instead of accuracy these instrument are characterized by a higher precision and stability since they are designed to detect production deviations [1]. Figure 2.54 shows a scheme of the instrument classification.

```
                    ┌─────────────────┐
                    │   Instruments   │
                    └─────────────────┘
              ┌──────────┴──────────────┐
    ┌──────────────────┐      ┌────────────────────────┐
    │ Colour attributes │      │  Geometric attributes  │
    └──────────────────┘      │ Gloss, haze, texture, etc. │
                              └────────────────────────┘
       ┌──────────┴──────────┐
  ┌──────────────────┐  ┌──────────────────┐
  │ Physical analysis │  │  Psychophysical  │
  └──────────────────┘  │     analysis     │
                        └──────────────────┘
    ┌──────┴──────┐        ┌──────┴──────┐
┌──────────────────┐ ┌──────────────────┐ ┌──────────────┐
│ Spectroradiometer │ │ Spectrophotometer │ │  Colorimeter │
│ (illuminant mode) │ └──────────────────┘ └──────────────┘
└──────────────────┘        └──────┬──────┘
                          ┌──────────────┐
                          │  Object mode │
                          └──────────────┘
                      ┌──────────┴──────────┐
                ┌──────────────┐    ┌──────────────┐
                │  Reflectance │    │ Transmittance │
                └──────────────┘    └──────────────┘
```
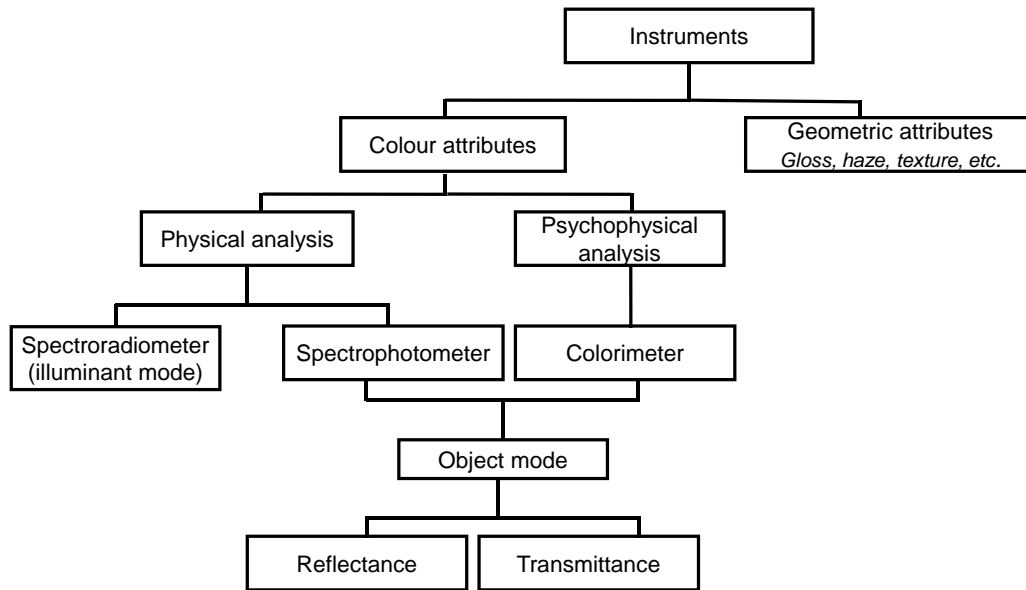
Figure 2.54 Classification of measuring instruments. Modified from [37]

Measuring geometry

Instruments seek to measure an object's colour similar to the way it is perceived by the HVS. As previously stated, the appearance of an object depends on the illumination and viewing conditions. Therefore, the geometry of a colour measurement instrument is an important factor to take into account in its design. There are two types of geometry of illuminating and measuring lights in such instruments:

a) Bidirectional geometry - encoded as 45º/0º

b) Diffuse geometry using integrated sphere - encoded as d/8º

According to the CIE the first encoded number refers to the illumination geometry, whereas the second refers to the observation geometry.

Figure 2.55 shows the geometry illumination and viewing condition types for a colour measuring instrument.
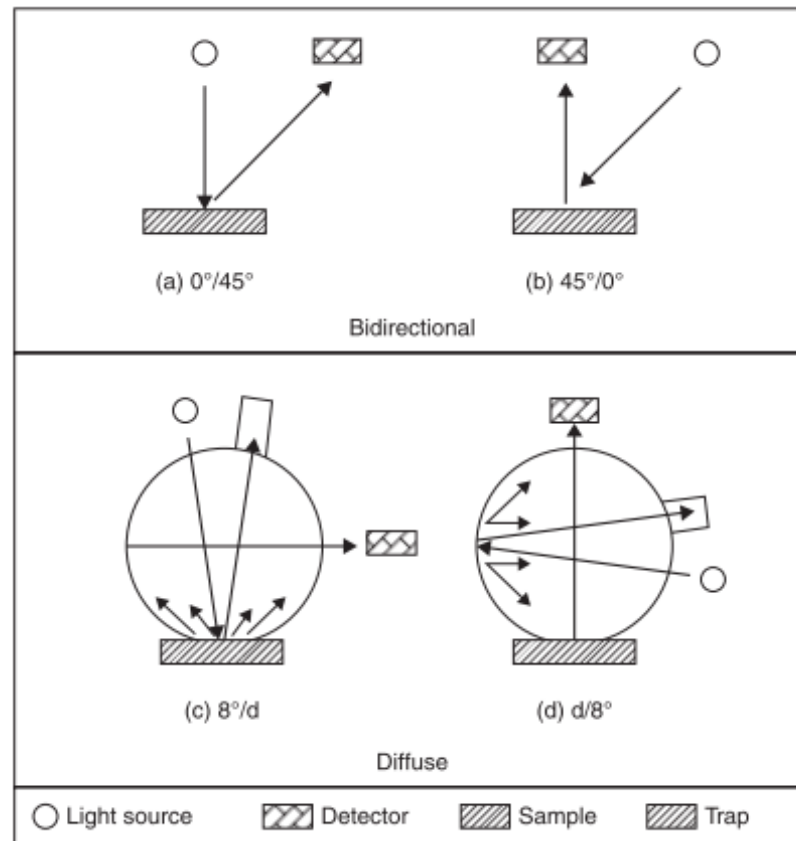
Figure 2.55 Geometry of illumination and viewing [37].

As shown in the above figure there are four combinations of geometry illumination and measurement:

a) 0° illumination and 45° viewing

b) 45° illumination and 0° viewing

c) 8° illumination and diffuse viewing

d) Diffuse illumination and 8° viewing

The bidirectional geometry normally uses two directions: 0° and 45° for the reflectance measurement and 0° and 180° for the transmission measurement. In the case of diffuse geometry, both the illumination and measuring conditions are not directional. This is due to the use of a device called integrating sphere. This device directs the source of light onto an object, collecting all the reflected light using a spherical cavity that is totally diffuse and white.

In addition, the integrating sphere is useful to control the distance of the light source and the receiver from the sample.

2.2.5.2. Colorimeter

Colour measurement is in accordance with the Comission Internationale de l'Eclairage system (CIELAB or CIE L*, a*, b*). It is considered as a three-dimensional color-space. Figure 2.56 shows the coordinate system to define a colour. The L* axis is the grey scale, comprising values from 0 (white) to 100 (white). The a* is the red/green axis. The negative value indicates green whereas positive ones indicate red. Finally, b* is the yellow/blue axis. In this case, the positive values indicate yellow while negative indicates blue. In addition, from the CIELAB system the chroma (C*) and hue (h*) can be extracted. Equations2.20 and 2.21 define C* and h* [82].

$$C^* = ((a^*)^2 + (b^*)^2)^{1/2} \qquad\qquad (2.20)$$

$$h^* = arctan\frac{b^*}{a^*} \qquad\qquad (2.21)$$
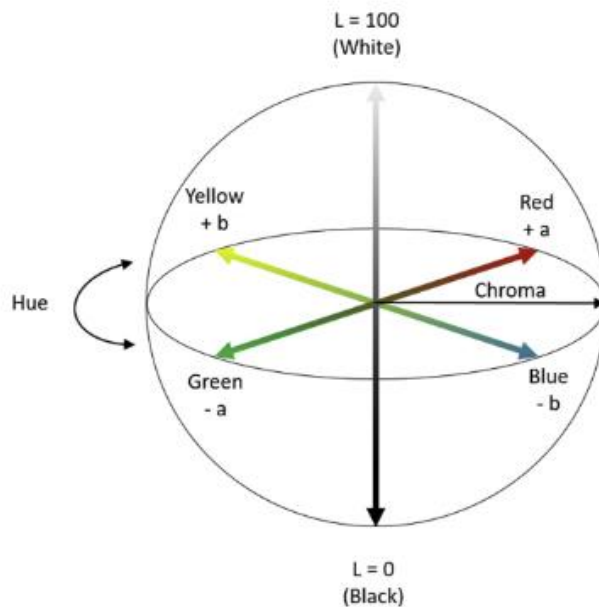
Figure 2.56 Coordinate's system to define colour [82].

The measuring principle of a colorimeter is based on the absorbance of light wavelengths. In colour measurement, the change in intensity of the electromagnetic radiation is measured in the visible wavelength region of the spectrum after being transmitted or reflected by an object. This instrument measures colour by comparison. It compares the amount of light passing through a solution with the amount of light that can cross a sample of a pure solvent. The amount of light that passes through the solvent is detected by a photocell, which produces a current signal. The intensity of this current depends on the quantity of light hitting the photocell after passing through the coloured solution. Therefore, the higher the light absorption the higher is the colorant concentration. The colour estimation of a coloured sample is reached using three filters that simulate the HVS. These filters provide the reading of three wideband along the visible spectrum: L, a, b.

There are two types of colourimeters, visual and photoelectric. The visual colourimeter in turn, can be divided into two types:

- Visual absorption meters comparators
- Tri-stimulus colorimeters

In the first colorimeter type (visual absorption meter comparator) the device compares the colour of a sample with a standard. Then a match between the two measurements is found. Usually, this instrument is used for chemical analysis and concentration determination.

The tri-stimulus colorimeter is based on the theory developed by Grassmam and Maxwell [83]. This theory says that colour could be mathematically specified in three independent components, which matches well with the theory that the human eye has three receptors. In addition, it was demonstrated that any additive colour mixture could be reproduced with the proper amount of the three primary colours, resulting in the so called tri-stimulus response. Accordingly, the CIE used this fact for establishing a standard for the numerical specification of colour in terms of three coordinates or tri-stimulus values (X, Y, Z) [83].

The measuring principle of the tri-stimulus colorimeter is based on the psychophysical estimation or visual equivalence. This instrument employs a light source that strikes on the sample. The reflected light passes through one of the three tri-stimulus filters and falls onto the photodetector. The photo-detector transfers the data to a microprocessor for the computation of the absolute CIE tri-stimulus values as shown in Figure 2.57 [38].
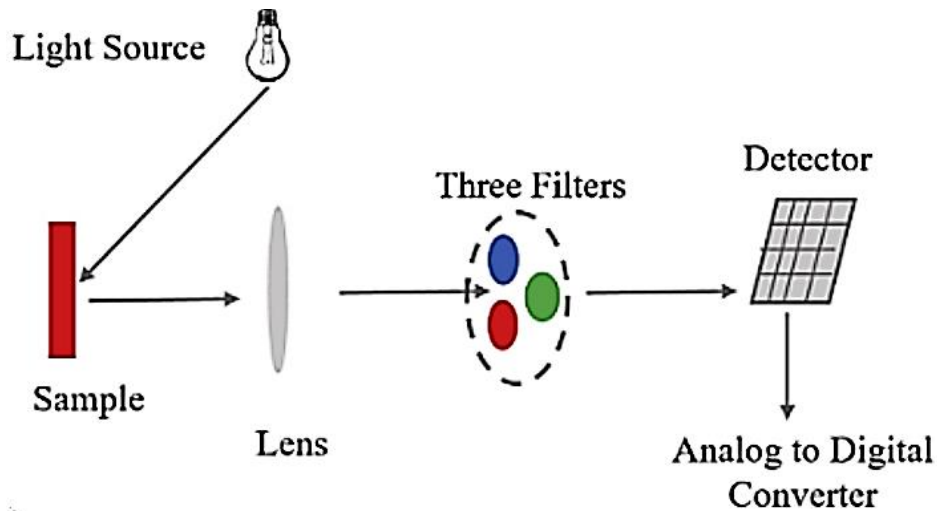
Figure 2.57 Operating principle of colorimeter. Modified from [82]

2.2.5.3.   *Spectrophotometer*

The spectrophotometer measures the wavelength distributions of light responsible for colour appearance. This device, in fact, is composed of two instruments, namely a spectrometer and a photometer. The spectrometer produces light of any specified wavelength (colour) using a light source and a monochromator while the photometer measures light intensity.

The measuring principle is based on the quantification of the reflected or transmitted light coming from or passing through a sample at a discrete wavelength. Usually, a spectrophotometer hits the sample surface with a monochromatic light, which has been created by a diffraction grating using a light source. Then, through a galvanometer, it is possible to measure the amount of light reflected or transmitted by means of the delivered voltage signal.

The signal changes as a function of the amount of light absorbed by the object. Usually, the perceived colour of an object is determined by the relative amount of light transmitted or reflected throughout the visible spectrum (380-760 nm of wavelength). If objects are opaque, then reflectance property gains more importance in colour measurement. Equation 2.22 defines the spectral reflectance, which is the ratio of the reflected radiant flux to incident radiant energy under specified conditions of irradiation.

$$\rho(\lambda) = \frac{P_\lambda}{P_{0\lambda}} \tag{2.22}$$

Where P_λ is the spectral concentration of the radiant power reflected by the medium and $P_{0\lambda}$ is the spectral concentration of radiant power incident on the medium.

The output of the spectrophotometers are spectral curves, which indicates the percentage of light reflected or transmitted throughout the visible spectrum. Figure 2.58 depicts an example of a spectral curve. These curves are the physical analysis from which colour can be computed through the tri-stimulus colour values. This is possible thanks to the knowledge of the specific spectral light-absorbing properties of materials [1], [38], [84].
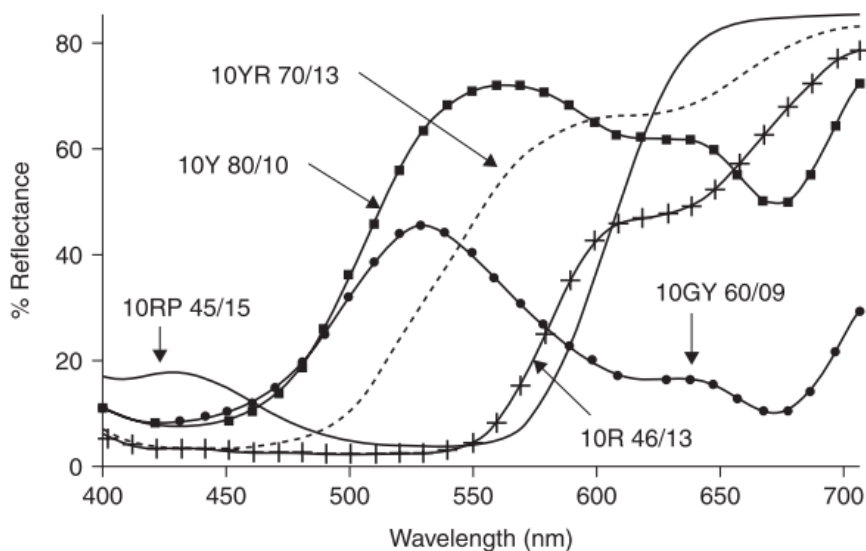
Figure 2.58 An example of a spectral curve for measuring colour [37].

2.2.5.4. Goniophotometer

Geometric attributes are those associated with the capacities of surfaces to emit light in different directions. Illumination and viewing conditions alter the object's perception. However, it has been demonstrated that geometric attributes such as gloss or translucency can modify the appearance of an object. In addition, the interaction between them also affects the perception of the appearance.

The goniophotometer measures the amount of light reflected or transmitted as a function of the change in the incident and/or view directions. In other words, it measures the amount of light reflected or transmitted at different angles. It can be said that for geometric appearance, the goniophotometer is analogous to spectrophotometers.

Figure 2.59 depicts the goniophotometer's design. A beam light is projected on the sample surface from the light source. A detector receives light from the specimen in a specific direction. Both the light source and the detector modify its position, thus directions from which light is incident and received are variable. The detected light is then converted into an electrical signal by the detector. It can be plotted as a continuing curve on which the amount of light reflected or transmitted changes as a function of the incident and viewing direction [1].

The uses of a goniophotometer are the measurement of both luminous flux of a light source and luminous intensity. This information can be useful to select the best fixed-angle conditions for measuring gloss, transparency or other geometric appearance attributes.
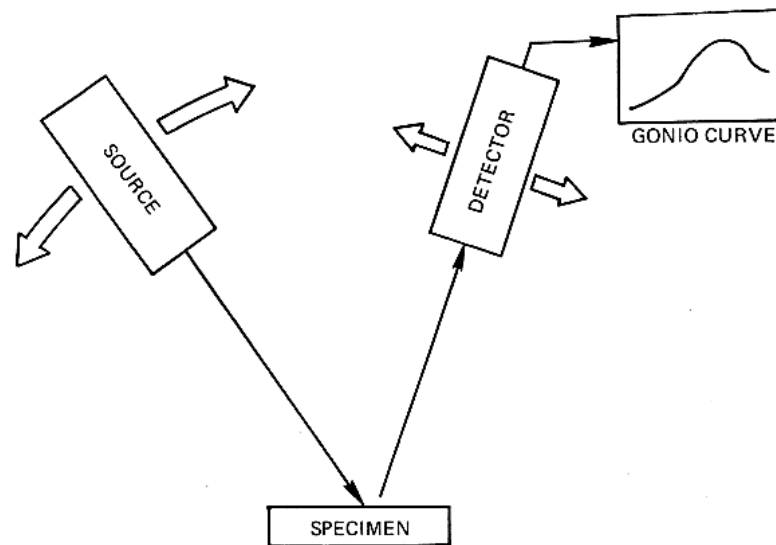
Figure 2.59 Diagram of a goniophotometer [1].

2.2.5.5.   Glossmeter

The gloss measurement is related to the amount of light reflected coming from the object surface at the specular angle. This amount of light is quantified and indicates how shiny an object is. The instrument to measure the gloss level of an object is a glossmeter [85]. The configuration of the glossmeter allows changing the incident light coming from a source to be perpendicular to the surface or at a given angle relative to normal. A detector which is placed at the opposite side but having the same angle than the incident light measures the reflected light at the specular angle.

The intensity of the reflected light depends on both the material and the angle of incidence. In the case of non-metal materials, the amount of reflected light increases with the increase of the illumination angle. On the other hand, metallic materials are less angle dependent. Three different incident angles of light are defined to cover the whole gloss range, matte, semi-gloss and high gloss.

In the case of low gloss surfaces the recommended incidence angle is 85° to the normal. This angle is preferred for surfaces having less than 10 Gloss Units (GU) at 60°. Semi-gloss

surfaces are measured using the standard angle of 60º. This is a universal angle that is used as reference for all products. However, best results are obtained in products with gloss levels between 10 and 70 GU. Finally, high gloss surfaces are measured using an incident angle of 20º, which yields improved resolution. Figure 2.60 shows positions of both the light source and the detector for gloss measurement of low, semi-gloss and high gloss surfaces [38] and Figure 2.61 depicts the measurement of a series of samples at three angles as a function of visual assessment of their gloss [37].
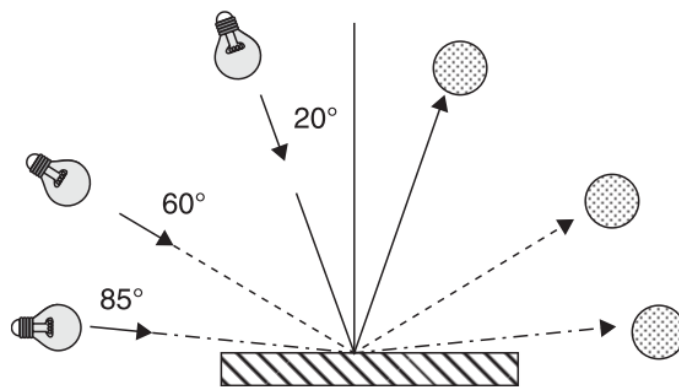
Figure 2.60 Position of light source (left side) and detector (right side) for measuring gloss at different angles. Modified from [37]
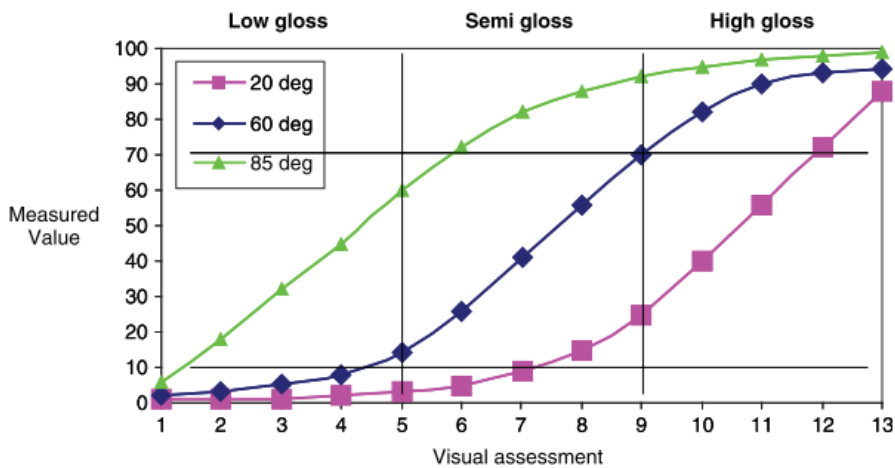
Figure 2.61 Measurements of samples gloss at three angles as a function of visual assessment of their gloss. Modified from [38]

2.3. **Surface performance.**

Surfaces have become a fundamental attribute of the final product. Nowadays textures play a main role in both design and manufacturing necessities [6]. For example, in biologics, texturing surfaces at the scale range is a suitable method for obtaining self-cleaning surfaces [86]. In the automotive industry, the surface texturing is a common technique to enhance the appearance of interior parts. In addition, textures are useful for improving scratch resistance. In this way, textures reduce the real contact area between interfaces, decreasing damage visibility [3].

2.3.1. Principles of friction

Tribology is defined as the science and technology of interacting surfaces in relative motion. This embraces concepts such as friction, wear and lubrication. All of them are related with aspects of the transmission and dissipation of energy [87].

Friction is defined as the resistance of two bodies that are in contact under a normal load (F_N) to the relative motion under the action of an external force. The minimum force required to initiate sliding is the force of friction (F_F). From this situation, three empirical rules arouse [88], [89]:

1. F_F is independent of the apparent area of contact.
2. F_F is almost independent of the sliding velocity once sliding is established.
3. F_F is proportional to the normal force (F_N). From this relationship, the friction coefficient (μ) is defined (Equation 2.23).

$$\mu = \frac{F_F}{F_N} \tag{2.23}$$

The friction coefficient is a dimensionless scalar value which is defined as the ratio of F_F to F_N. The friction coefficient is dependent on the normal load (F_F), apparent contact area (A_a) and sliding velocity. It should be pointed out that the friction coefficient is an empirical parameter and it cannot be found by calculations [89].

In the case of polymers, the tribology consists of three main elements involved in friction:

a) Real contact area (RCA)

b) Adhesive component

c) Deformation or ploughing component

2.3.2. Friction mechanisms

2.3.2.1.   *Real contact area (RCA)*

As is well known there are no perfect surface. All surfaces contain defects or asperities at a certain scale. On top of these asperities is where the first contact between two interfaces occurs. Therefore, loading is supported by the deformed contacting asperities, in such way the RCA is reduced to a small fraction of the apparent contact area (A_a) as depicted in Figure 2.62. Usually, the RCA is exceedingly small in comparison to the A_a. The RCA is not dependant on size, shape or roughness of the surface, it depends only on loading. Nevertheless, during sliding the RCA changes rapidly with the surface movement as new asperities come into contact while other contacts break.
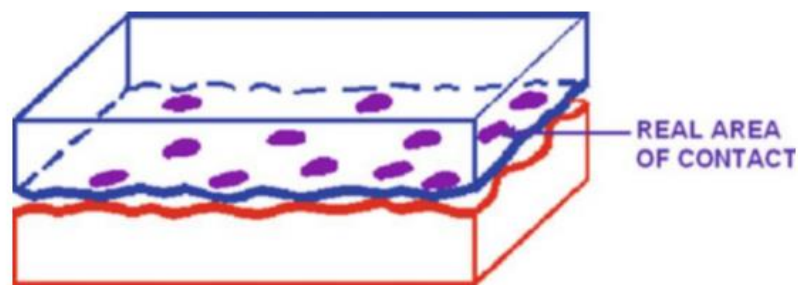
Figure 2.62 Representation of the real contact area (RCA) between two bodies. Purple dots represent the RCA [89].

2.3.2.2. Adhesion component of friction

When two bodies come into contact the load is supported by the highest asperities. This contact area corresponds to the RCA. Initially, the RCA is small, hence loading leads to a plastic deformation which yields an increment of the RCA until reaching a size suficient to support loading. In this way, the normal load (F_N) is defined as a function of the RCA as follows:

$$F_N = AH \tag{2.24}$$

Where *A* is the real contact area and *H* is the hardness of the softer material.

The adhesive bonding can occur at the RCA of asperities depending on both the degree of interpenetration of asperities and the surface energy. Under a lateral motion between two bodies, a tangential force is required to shear the adhesive bonds formed at the interface in the region of the RCA. Therefore the friction force (Equation 2.25) will depend on the surface shear strength of materials (*S)* [87], [89]–[92].

$$\mu = \frac{F_F}{F_N} = \frac{S}{H} \tag{2.25}$$

2.3.2.3. Deformation or ploughing component of friction

The deformation component of friction results from the resistance of the softer material to be "ploughed" by the asperities of the harder counterface. In this case, during sliding contact, plastic deformation is the result of energy dissipation. This phenomenon takes place with major probability in those materials with a low adhesive component of friction and during abrasion processes [87], [89]. In this particular case, ploughing is the consequence of two different mechanisms namely by asperities or by penetrated wear particles.

In the case of ploughing by asperities, the simplest model approach which describes the case of a sliding conical asperity, the friction coefficient is related to the tangent of the asperity

conical slope (Figure 2.63). This model (Equation 2.26) neglects the fact that during the sliding

a pile-up of material ahead of the grooving path occurs [87].

$$F_F = \frac{2}{\pi} tan\theta \qquad (2.26)$$
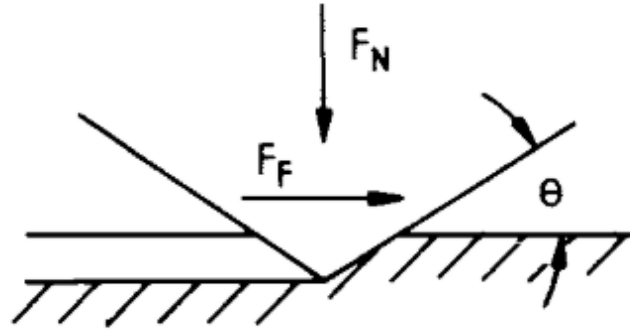
Figure 2.63 Representation of the ploughing by asperities model [87].

The ploughing by wear particles mechanism is very sensitive to the ratio of the radius

of curvature of the particle to the depth of penetration as shown in Figure 2.64. Beyond the

material properties that are in contact, the geometry of particles plays a significant role in the

behaviour of sliding surfaces. Therefore, the F_F can be described as follows [87]:

$$F_F = \frac{2}{\pi} \left\{ \left(\frac{2r}{F_N}\right)^2 \cdot sin^{-1} \cdot \frac{F_N}{2r} - \left[\left(\frac{2r}{F_N}\right)^2 - 1\right]^{\frac{1}{2}} \right\} \qquad (2.27)$$
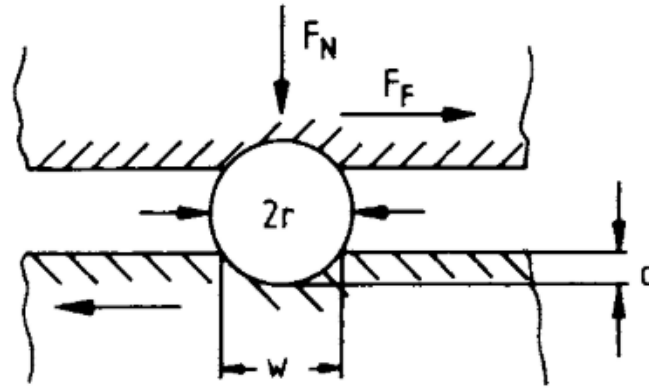
Figure 2.64 Representation of the ploughing by wear particles [87].

2.3.3. Scratch resistance

The scratch principle is based on the friction ploughing component. In this particular case, a stainless steel indenter is slipped across the polymer surface at a given load and velocity, leaving a mark on the polymer surface. From this methodology, properties such as the friction coefficient, the scratch hardness (Hs), the fracture toughness, the abrasion resistance and the identification of surface deformation modes can be determined. This is a useful technique when polymers are utilized to improve contact mechanical or tribological performance or when polymers are designed for optical applications in consumer products. For this reason, the scratching methodology has gained increasing interest in recent years [93], [94].

Figure 2.65 shows a commercial scratching apparatus. It is formed by an adjustable lever arm, at which the indenter is attached through a thin rigid holder. The movement of the sample under the indenter is provided through a micro-step motor stage, which is controlled by a computer.

Figure 2.65 Commercial scratching machine.

2.3.3.1.   *Factors affecting scratch resistance*

Factors such as scratch test conditions [93]–[95] and material type [96]–[100] can alter scratch resistance. In the former case, the applied load (W), the scratch velocity (v) or the bulk material temperature (T), among other test conditions, can modify the scratch hardness (Hs) of a given material. In the latter case, as shown in Figure 2.66 the material type can induce different deformation maps. Figure 2.66a and 2.66b depict the deformation mechanisms of UHMWPE and PC material, respectively.

(A)

(B)
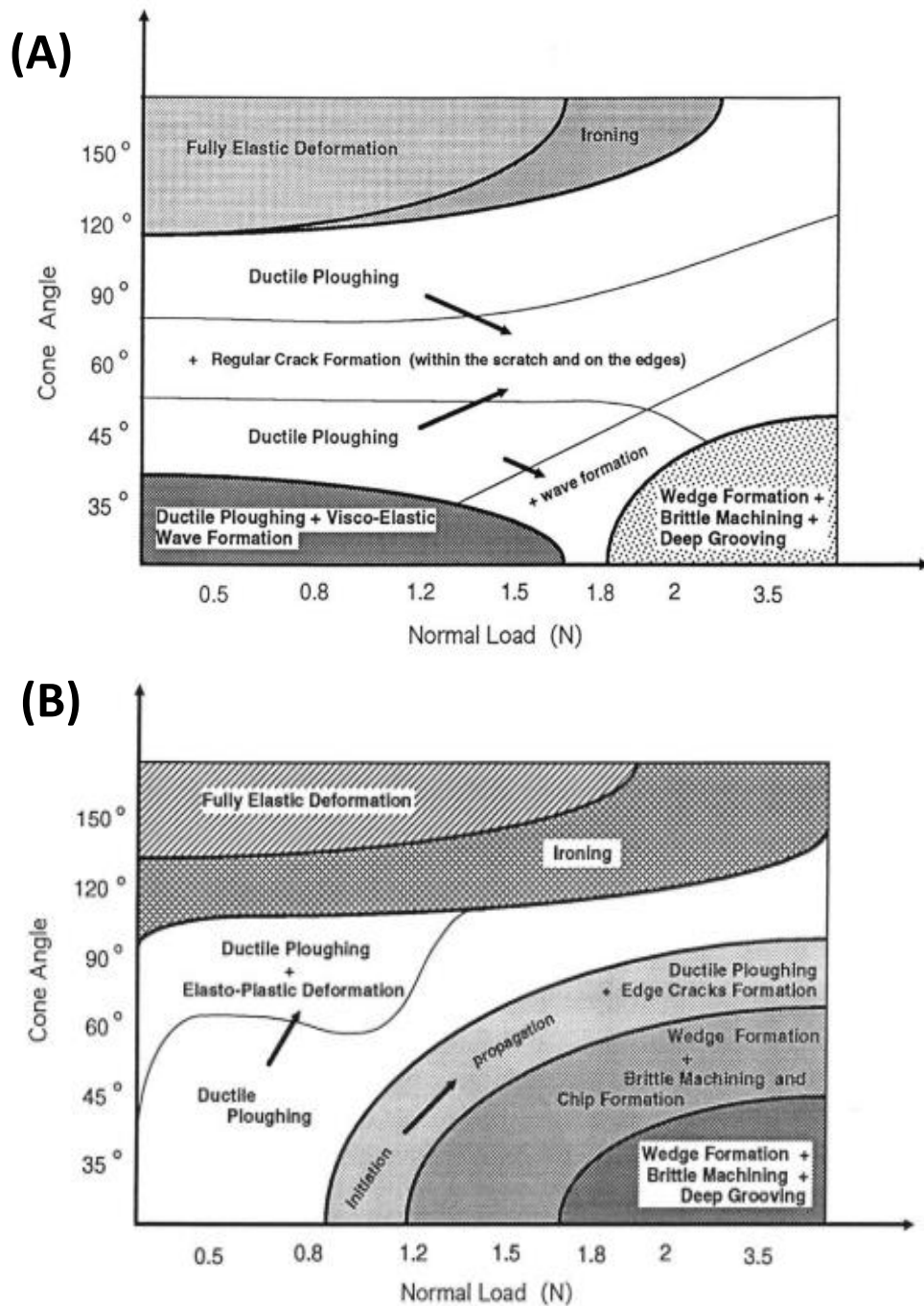
Figure 2.66 Scratch deformation map for PE (a); Scratch deformation map for PC (b). Modified from [93]

Scratch test conditions

Mechanical properties such as scratch hardness (Hs) or friction coefficient (μ) can be obtained by modifying the scratching test conditions [93], [94]. This is possible through the

identification and analysis of the surface deformation patterns. Equation 2.28 describes the scratch hardness as a ratio of the applied normal load (W) and the projected load supporting area (A). The parameter q is a constant that varies as a function of the material response type. Whether the material has plastic deformation $q = 2$, whereas for a viscoelastic-plastic response $1 < q < 2$. The parameter d corresponds to the width of the groove left by the indenter. Figure 2.67 shows the groove left by the conical indenter during the sliding motion in a scratch test.

$$Hs = \frac{W}{A} = \frac{q4W}{\pi d^2} \qquad (2.28)$$
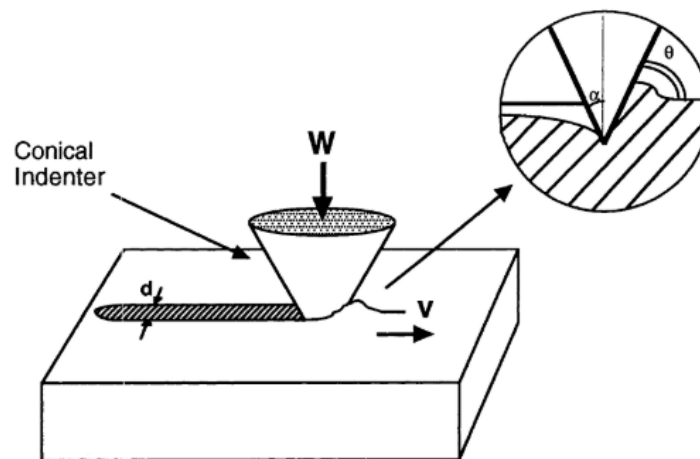
Figure 2.67 Groove created after performing the scratch test [93].

The main variables of the scratch test are:

- The applied normal load (W)

- The indenter geometry

- Scratch velocity

- Bulk material temperature

The scratch hardness (Hs) and deformation mechanisms of two different commercial materials namely ultrahigh molecular weight polyethylene (UHMWPE) and polycarbonate (PC) were studied by Briscoe et. al [93]. This was conducted varying scratching conditions. It

was found that the applied load, scratch velocity, the indenter geometry and the bulk material temperature influence the scratch hardness trends. In addition, different deformation mechanisms were observed as a function of the defined scratching conditions.

Figure 2.68 shows the influence of the cone angle on the Hs for both PC and UHMWPE materials. In the particular case of PC material, it was observed that for lower cone angle ranges (from 35º to 60º) the Hs tended to increase. On the contrary, a decrement of the Hs was obtained for higher cone angles (from 90º to 120º). This was due to the effective strain as described by Johnson et al. [101]. Accordingly, the strain is proportional to the tangent of the slope of the indenter (Equation 2.29). On the other hand, the UHMWPE exhibited an Hs decrement trend with the increment of the cone angle (θ) (see Figure 2.67).

$$\epsilon_s = 0.2 \cdot tan\theta \qquad (2.29)$$

The UHMWPE presented smaller values of Hs for the lower cone angle ranges (35 to 60º) in comparison to the PC material. This could be because the material removal process requires less energy for UHMWPE than for PC material [93].
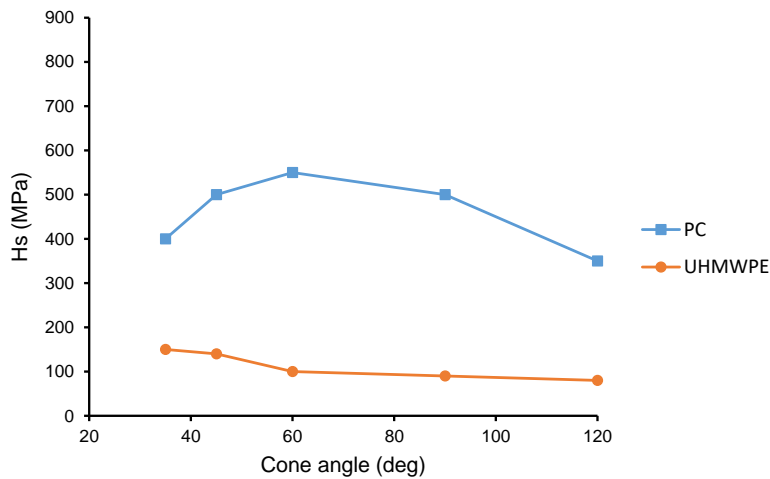
Figure 2.68 Influence of the cone angle on the scratch hardness (Hs). Modified from [93]

Figure 2.69 shows that in the case of PC Hs increases as the scratch velocity is increased. This indicates that the strain rate of the material is governed by the scratch velocity. The strain rate is defined as the ratio of the scratch velocity (v) to the scratch width (d) (Equation 2.30).

In this case, the material provides high resistance to plastic deformation, which yields the so-called hardening effect [93]. This effect is a response of the bulk material, since during the scratching a considerable plastic deformation takes place. In the particular case of high scratching velocities, a local heating is produced between surface contact regions, known as interfacial heating. Heat dissipation is more difficult at high applied velocities, yielding ductile material deformation in the contact zone. In addition, the interfacial heating can also lead to a decrement of friction because the softened interfacial layer acts as a lubrication. [93].

$$\epsilon_S = \frac{v}{d} \tag{2.30}$$
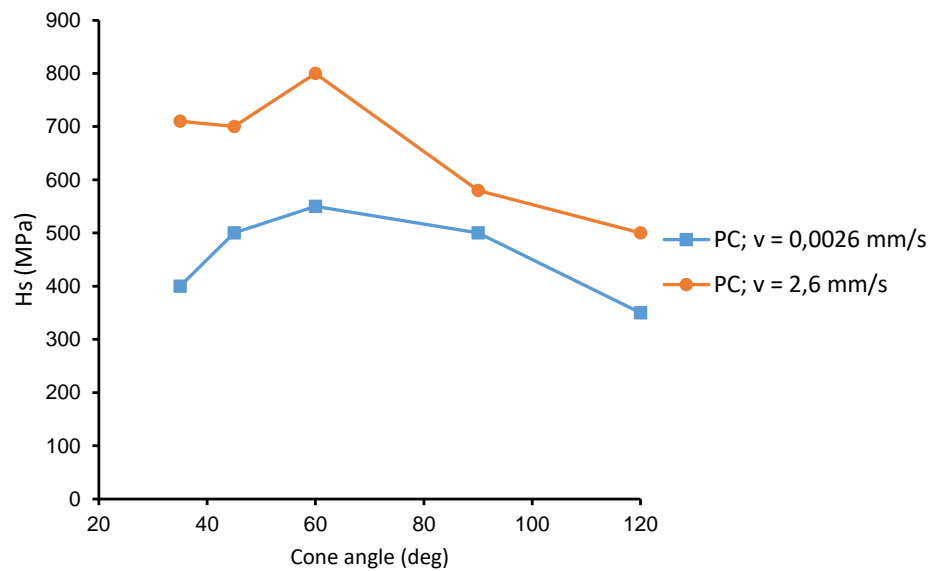
Figure 2.69 Influence of the scratch velocity on the scratch hardness (Hs). Modified from [93]

The influence of the bulk material temperature on the Hs is shown in Figure 2.70. To be noted is that an increment in the temperature showed a decrement of the Hs. This was caused by the bulk material softening [93].
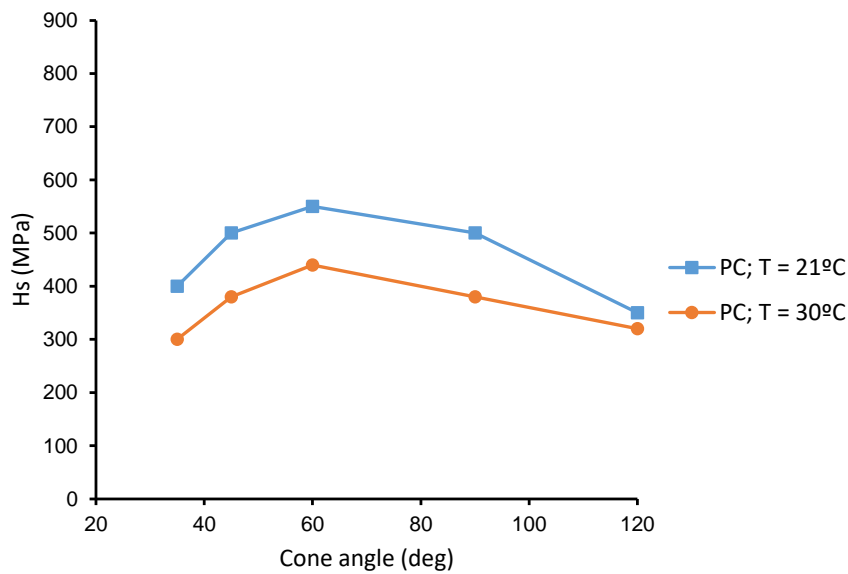
Figure 2.70 Influence of bulk material temperature on the scratch hardness (Hs). Modified from [93]

Material type

Unlike metals and ceramics, the scratch-induced deformation mechanism is a complex process in polymers. This is because of the non-linear material behaviour. For this reason, four material categories were established by Jiang et al. [99].

1. Ductile and strong, i.e. Polycarbonate material (PC)

2. Ductile and weak, i.e. Thermoplastic olefins (TPO)

3. Brittle and weak, i.e. Polystyrene (PS)

4. Brittle and strong, i.e. Epoxy

The deformation mechanisms were studied per each material group. The scratch damage features were defined as a function of the applied normal load as mar damage, fish scale and material removal, among others. Figure 2.71 summarises the most common features of the scratch damage as loading increases. It is possible to distinguish different deformation zones,

namely, the initial damage, the fish-scale, the parabolic crack and the material removal zone [99].

The initial deformation zone (mar) is common for all material types, being defined as a small amount of non-recoverable deformation resulting from the compression during indentation. This deformation mechanism usually occurs under low loading yielding no material removal. It can be noticed due to a gloss variation which results from the ironing of surface asperities [102].
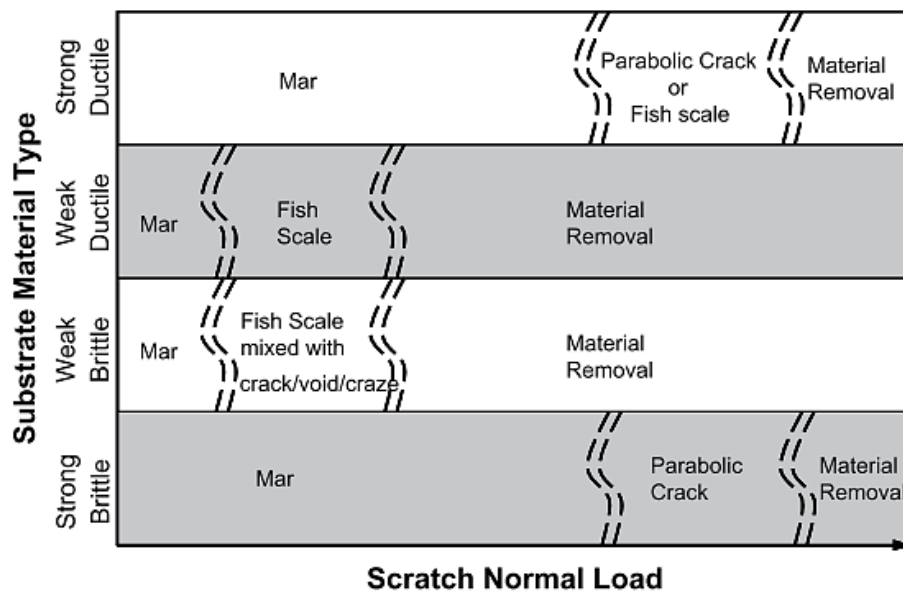
Figure 2.71 Evolution map of polymer scratch damage [99].

The fish scale zone is a plastic deformation mechanism that results from the stick-slip phenomenon. During the scratch motion, frictional forces do not remain constant, but significantly oscillates. This occurs when the static friction coefficient is greater than the kinetic one. In the stick phase, a critical value of the frictional force is built. Once this force is overcome slip occurs at the interface, releasing energy which leads to a decrement of the frictional force. As shown in Figure 2.72 the result is a well-shaped and spaced pattern of parabolic features (fish-scale)
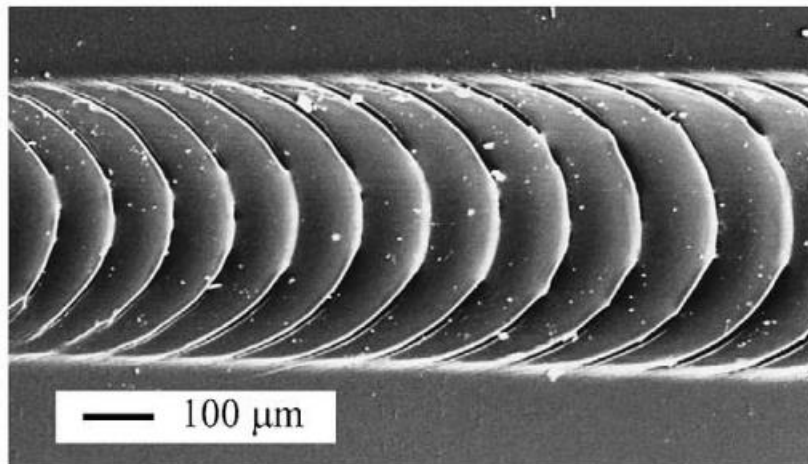
Figure 2.72 Fish scale damage [99].

The parabolic cracking zone becomes the dominant damage mode at high normal loads. This is a periodic convex damage feature pointing opposite the scratch direction as shown in Figure 2.73.
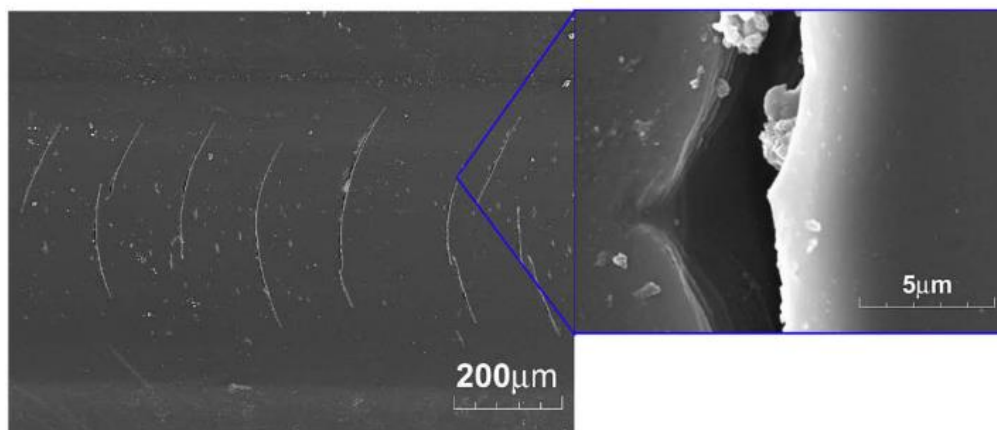
Figure 2.73 Parabolic crack pattern [99].

Finally, the material removal zone takes place when scratch loading continues increasing. In this zone, the indenter tip penetrates significantly, removing material from the substrate to the surface. Figure 2.74 illustrates this phenomenon, showing the transition from

the fish-scale zone to the material removal zone.
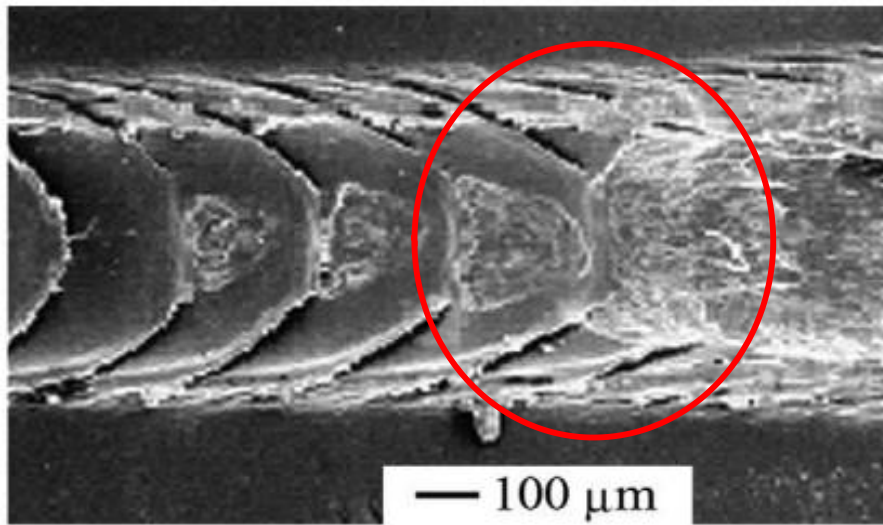
Figure 2.74 Transition from the fish scale zone to the material removal zone. Modified from [99]

2.3.4. Role of texture on scratch damage

The introduction of textures on top of the surface of polymeric materials can modify the interaction between the indenter tip and the surface, altering the scratching behaviour [99], [103]. The main scratching factors that are affected by texture are:

1. The real contact area (RCA).

2. The scratch damage type.

2.3.4.1. Influence of texture on real contact area (RCA)

Unlike a smooth surface, the real contact area in a textured surface is limited to the top asperities area, reducing friction forces during scratching. Hamdi & Sue [104] and Browning et. al [102] studied the effect of surface texturing on scratch performance. They used two variants of TPO material, with and without slip agent. Two surface finishes were employed-one smooth and one textured. Both studies concluded that the addition of textures mimicking leather had a similar effect on scratch performance as the addition of slip agents on a smooth

surface. Jieang et. al [105] studied the influence of surface roughness and contact load on friction coefficient and scratch behaviour in a thermoplastic olefin (TPO) material. It was found that high roughness levels implied lower friction coefficients, hence scratch behaviour was enhanced. This was because the RCA was reduced to the highest surface asperities as shown in Figure 2.75, minimizing the adhesive component between both indenter tip and surface. Nevertheless, as the contact load increased the frictional force proportionally increased, tending to level off the friction coefficient at high loadings. At high loading, regardless of the roughness, the indenter penetrates the sub-texture and the material displacement begins, obtaining less dependence between roughness and coefficient of friction.
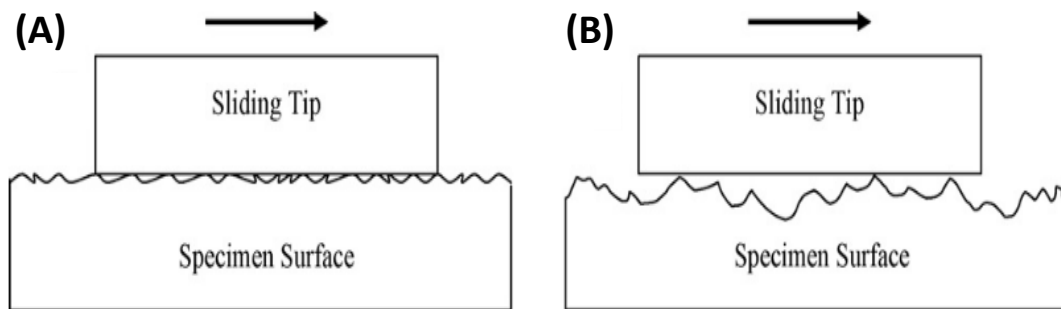
Figure 2.75 Effect of roughness on the real contact area with a smooth sliding. Low surface roughness (a) and high surface roughness (b). Modified from [105]

2.3.4.2.   *Influence of texture on scratch damage*

As described, surface textures are employed to mitigate scratch damages. This is possible by reducing the RCA between the indenter tip and the surface, which is limited to the highest surface asperity. With this in mind, textured surfaces concentrate the applied load over a small area. Therefore, the stress rate in this area is higher in comparison to a smooth surface where the stress is evenly distributed along the entire surface. This situation leads to a premature damage of texture asperities, yielding deformation mechanisms such as cracking, stress whitening or in more severe cases, the complete removal of the surface features [3], [106].

Texture design plays and important role in scratch resistance. The relation to the size and distribution of the surface features with the indenter has to be taken into account [107], [108]. Figure 2.76 illustrates the effect of the ratio *b/R* on the scratch damage, where *b* is the spacing between surface features and *R* is the radius of the indenter tip. If the ratio is lower (less spacing between surface features), the indenter tip has less space to penetrate between feature gaps. Therefore, the tip is forced out of the gap and the vertical oscillations of the tip are limited. This leads to a reduction of the tangential forces with the lateral sides of adjacent features, yielding lower frictional forces. On the contrary, with a high space between surface features, the indenter tip penetrates the gaps increasing frictional forces. Therefore it is expected that high *b/R* ratios lead to higher scratch damage due to the additional tangential force required to overcome surface features [106].
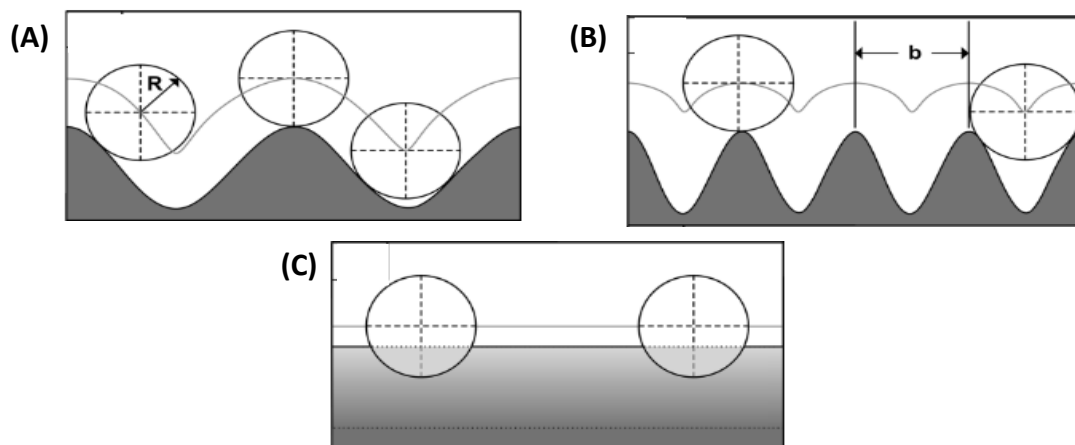
Figure 2.76 Effect of the b/R ratio on the path of the indenter. When the b/R is reduced from (a) to (b) limits tip and the path becomes smoother. In (c) no effect is detected when scratching is performed. Modified from [3]

Texture effectiveness upon scratch resistance depends on the orientation relative to the scratch motion [109]. In textures that mimic grooves, two different behaviours were observed depending on the parallel or perpendicular slide of the indenter in regards to the texture orientation [108]. In the case of parallel sliding, no variations in friction were detected, in fact the friction coefficient decreased as *d/R* ratio increased. In that particular case, the contact area

shifted to the edge of the groove ridges. On the other hand, in the case of perpendicular motion, larger tangential forces were observed when the *d/R* ratio increased [110]. As shown in Figure 2.77, the scratch damage is less visible when the sliding is parallel to the texture orientation (Figure 2.77a), whereas for the perpendicular sliding the scratch damage is more perceptible due to the high tangential force inducing more plastic deformation (Figure 2.77b).
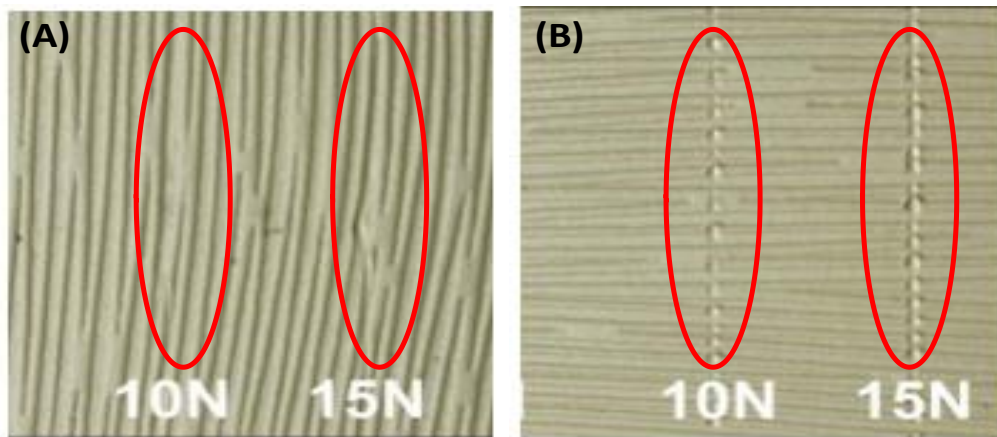
Figure 2.77 Effect of the texture orientation on the scratch visibility resistance. Parallel (a) and perpendicular (b) orientations. Modified from [110]

2.3.5. Effect of surface texturing on scratch visibility

Unlike smooth surfaces, where scratch damage is easy to detect because it is the unique feature on the surface, finding the scratch damage superimposed on a textured surface is sometimes very difficult. In this case, scratch detection onset depends on factors such as the human vision system (HVS) capabilities (see section 2.2.3), lighting and viewing conditions and appearance attributes such as the colour, gloss and texture [3], [105], [106], [108], [112].

2.3.5.1.   *Influence of lighting and viewing conditions on scratch visibility*

As described by Ho et. al [78], [79] texture perception depends on both illumination and viewing conditions. In addition, as described in prior sections (see section 2.2.4) in a smooth surface the prevalent reflection mode is specular, whereas in a rough surface the diffuse mode is the most significant. Therefore, the light reflectance mode, either specular or diffuse,

depends on the micro-texture scale. The texture perception will depend on the ability of the texture in controlling the levels of specular and diffuse reflection. Figure 2.78 depicts the effect of the texture on light reflection for a given illumination angle. The incident light interacts with texture features, resulting in primary reflection, secondary reflection and shadowing areas. The asperities block the reflected light coming from the neighbouring asperities. This effect has two main results: (i) light redirection onto their neighbours which creates self-reflections and (ii) shadowing affect. In this case, the micro-texture which controls the reflection mode and the macro-texture which governs the local incidence angle leads to obtaining both highlighted and shadowing regions. This phenomenon provides the distinctive look to the textured surface [3], [111].
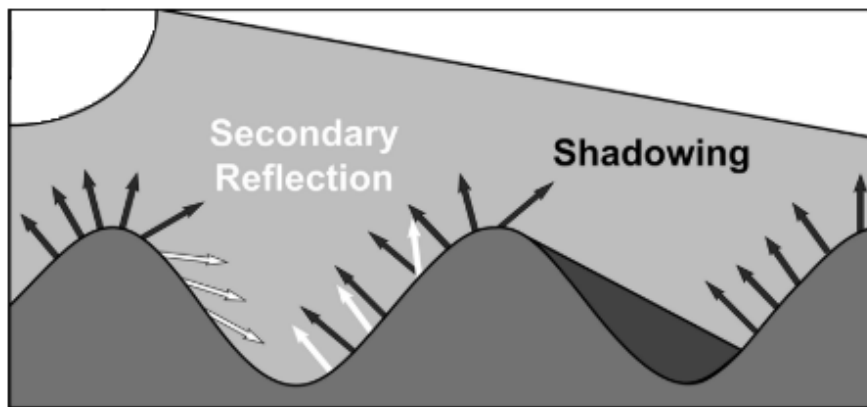
Figure 2.78 Effect of surface roughness and light orientation on reflection [3].

Figure 2.79 depicts the effect of the illumination direction on the scratch damage detectability onset. Figure 2.79a shows the sample illuminated at 20º from the normal, whereas Figure 2.79b depicts the same sample illuminated at 60º from the normal. The viewing angle was fixed at 20º for both illumination conditions. It is noted that for the illumination angle of 20º, scratch marks are detectable at low applied loads (2-7 N), the consistency of this line makes the scratch visible. At higher loading (10-15 N) the scratch mark is more visible. This is because of the combination of both the shadowing effect and the specular highlights at the scratch edges. On the contrary, by increasing the illumination angle (Figure 2.79b), shadowing

111

becomes the principle highlighting mechanism. For this reason only scratch marks above 3 N loading are perceptible, hiding scratch marks at low loading [3].
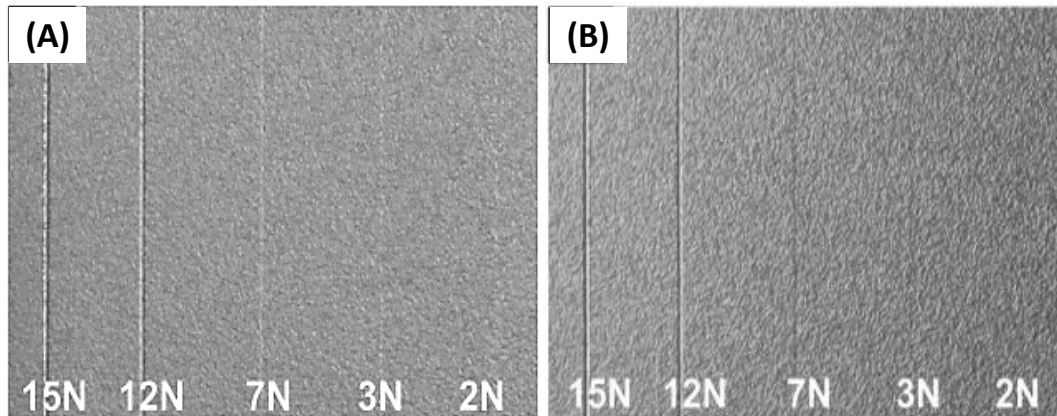
Figure 2.80 Effect of the illumination direction on the scratch visibility resistance of textured surfaces. 20⁰ from the normal (a) and 60⁰ from the normal (b). Modified from [3]

2.3.5.2.   Influence of appearance attributes on scratch visibility

The ability of a surface texture in obscuring and hiding scratch damage depends on the cognitive abilities of the brain to perceive and discern between different visual patterns [3], [112]. Scratch damage induces a new macro-scale pattern (grooves) on the textured surface. This new pattern has very different light interaction in comparison to the virgin texture or original background. Therefore, the texture effectiveness in obscuring the scratch damage mainly depends on three factors:

1. The scratch damage type on the textured surface

2. The similarity between the scratch damage and the textured surface or background

3. Controlling the spatial distribution of the scratch damage

Figure 2.80 depicts a textured surface mimicking leather. At low applied loading (2 – 7 N), texture features are not equally flattened, resulting in inconsistencies in scratch appearance. The bright appearance of the ironed features is visually similar to the specular highlights of the surroundings or texture background. This provides a greater scratch visibility

resistance at low normal loads, as the visual appearance and spatial distribution of the scratch path is similar to its surroundings. On the contrary, when high loading is applied (12 – 15 N), the similitudes between both the scratch path and the original texture become lost. This eliminates the ability of hiding and obscuring the scratch damage by surface texturing. The scratch path is deeper and other deformation mechanisms such as ploughing or fish-scale appear modifying the interaction with the light [113].
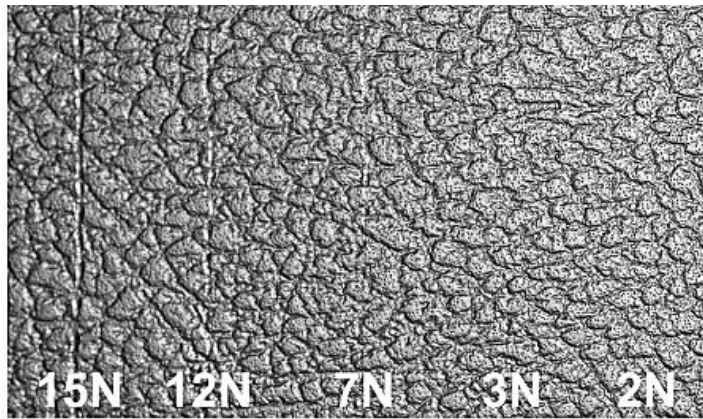
Figure 2.81 Effect of texture on scratch damage under constant loading [3].

In addition, the scratch features size is significant in scratch visibility [113], [114]. For example, Jiang et. al [114] defined a feature sizing criteria of 90 μm. Scratch features below 90 μm were not detected by the human eye. This is based on the human visual system (HVS) capabilities, where the sharpest eye has a visual acuity of 60 cycles/deg. Therefore, for a typical distance of inspection of 30 cm from the eyes to the sample, the smallest feature size that is possible to distinguish is about 90 μm.

Rangaranjan et. al [113] reported that the scratch path had a significant role in damage visibility, being the size and shape the most important factors. Figure 2.81 shows a section of a typical groove. In this case W is the groove width and h_{total} is the total height of the groove. The light interaction with the groove is very different in comparison to the groove's surroundings because they are in a different plane, i.e. the groove's shoulders. The scratch path

irregularities such as fish-scale, voiding, or cracking alter the light interaction which results in off-specular scattering. This leads to a contrast of lightness between the scratch and its surrounding, yielding less scratch visibility resistance.
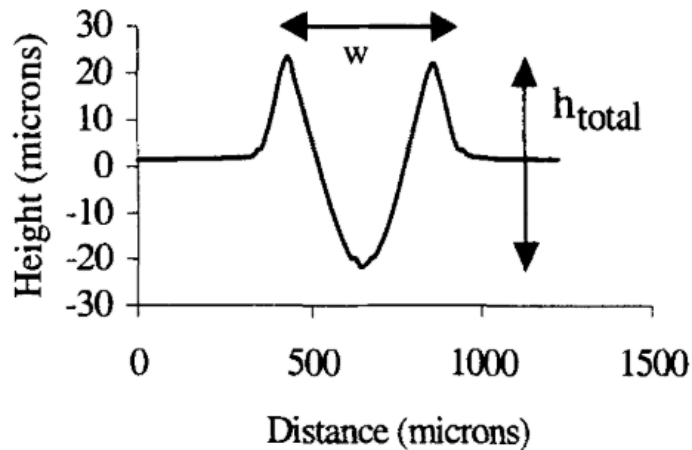
Figure 2.82 Cross-section of a typical groove. W is the groove width and h$_{total}$ is the groove height [113].

Beyond texture, other appearance attributes such as colour and gloss also have an influence on scratch visibility resistance [104], [112], [113]. Jiang et. al [112] reported that colour can affect scratch visibility onset. In this case, using the same material, green, red and blue samples were tested. The results showed that green samples were the ones with the earliest onset of scratch visibility. This was because of the three retina colour receptors, green is the most sensitive. A similar conclusion was reached by Hamdi et al. [104]. In that particular case, smooth, glossy and green samples tended to have less mar visibility resistance. Therefore, as in the case of texture, colour and gloss can also alter scratch visibility onset.

Methodologies based on the observer's criteria have been carried out to determine scratch visibility onset [104]. It has been demonstrated that subjective judgements either by individual observers or by a set of trained observers have critical drawbacks. For this reason, objective methods such as the Delta-L or the contrast (C) are preferred. In the case of the Delta-L method, it was used to determine scratch visibility resistance by measuring the change of

114

the surface lightness (L*) before and after scratching, obtaining a Delta-L (ΔL*). The higher the difference in ΔL* the lower the scratch visibility resistance. The scratch damage results visible because of loss of colour constancy[115]. On the other hand, the contrast method is based on the principle of the human eyes detecting both light intensity reflected on objects and its contrast against the background [112], [113]. The contrast, C, is commonly defined using the Michelson contrast equation (see Equation 2.16).

2.4. References

[1]   R. S Hunter and R. W. Harold, "The Measurement of Appearance", Wiley, USA (1987).

[2]   S. Ignell, U. Kleist, and M. Rigdahl, "Visual perception and measurements of texture and gloss of injection-molded plastics," *Polym. Eng. Sci.*, vol. 49, no. 2, pp. 344–353, 2009, doi: 10.1002/pen.21279.

[3]   C. J. Barr, L. Wang, J. K. Coffey, and F. Daver, "Influence of surface texturing on scratch/mar visibility for polymeric materials: a review," *J. Mater. Sci.*, vol. 52, no. 3, pp. 1221–1234, 2017, doi: 10.1007/s10853-016-0423-5.

[4]   Jiang X, Scott PJ, Whitehouse DJ, Blunt L. "Paradigm shifts in surface metrology. Part I". Historical philosophy. Proceedings of the Royal Society Series A 2007;463:2049–70. doi:10.1098/rspa.2007.1874.

[5]   Jiang X, Scott PJ, Whitehouse DJ, Blunt L. "Paradigm shifts in surface metrology. Part II". The current shift. Proceedings of the Royal Society Series A 2007;463:2071–99. doi:10.1098/rspa.2007.1873.

[6]   X. J. Jiang and D. J. Whitehouse, "Technological shifts in surface metrology," *CIRP Ann. - Manuf. Technol.*, vol. 61, no. 2, pp. 815–836, 2012, doi: 10.1016/j.cirp.2012.05.009.

[7]   L. Blunt and X. Jiang, "Advanced Techniques for Assessment Surface Topography: Development of a Basis for 3D Surface Texture Standards" "Surfstand." 2003.

[8]   Leach R. "Characterisation of Areal Surface Texture"; 2013. p. 1-353. ISBN 9783642364587.

[9]   Alting, Leo & Kimura, Fumihiko & Hansen, H. & Bissacco, Giuliano. (2003). "Micro Engineering". CIRP Annals - Manufacturing Technology. 52. 635-657. 10.1016/S0007-8506(07)60208-X.

[10] E. Brinksmeier and W. Preuss, "Micro-machining," *Philos. Trans. R. Soc. A Math. Phys. Eng. Sci.*, vol. 370, no. 1973, pp. 3973–3992, 2012, doi: 10.1098/rsta.2011.0056.

[11] H. N. Hansen, K. Carneiro, H. Haitjema, and L. De Chiffre, "Dimensional micro and nano metrology," *CIRP Ann. - Manuf. Technol.*, vol. 55, no. 2, pp. 721–743, 2006, doi: 10.1016/j.cirp.2006.10.005.

[12] H. H. Gatzen and M. Beck, "Wear of single crystal silicon as a function of surface roughness," *Wear*, vol. 254, no. 9, pp. 907–910, 2003, doi: 10.1016/S0043-1648(03)00245-X.

[13] T. Masuzawa, "State of the art of micromachining," *CIRP Ann. - Manuf. Technol.*, vol. 49, no. 2, pp. 473–488, 2000, doi: 10.1016/S0007-8506(07)63451-9.

[14] ISO 25178-2, Geometrical Product Specifications (GPS) - Surface texture: Areal - Part 2: Terms, definitions and surface texture parameters, First ed., 2012.

[15] D. Whitehouse, "Surface and their Measurement", First ed., Hermes Penton Science, London, 2002.

[16] R. K. Leach, "The measurement of surface texture using stylus instruments.," Meas. Good Pract. Guid. No. 37, no. 2, p. 100, 2001,

[17] T.R. Thomas, "Rough surfaces", Second ed., Imperial College Press, London, 1999.

[18] Santos, Nuno & Carvalho, Filomena. (2019). "Atomic Force Microscopy Methods and Protocols: Methods and Protocols". 10.1007/978-1-4939-8894-5.

[19] Quinten, Michael. (2019). "A Practical Guide to Surface Metrology". 10.1007/978-3-030-29454-0.

[20] Voigtländer, Bert. (2019). "Atomic Force Microscopy Designs". 10.1007/978-3-030-13654-3_4.

[21]   G. Abramovich, C. Nafis, Y. Williams, K. Harding, and E. Tkaczyk, "Three-dimensional embedded defect detection and localization in a semi-transparent medium," *Opt. Insp. Metrol. Non-Optics Ind.*, vol. 7432, p. 74321C, 2009, doi: 10.1117/12.830444.

[22]   Brown, Alistair. (1995). "Rapid optical measurement of surfaces". International Journal of Machine Tools & Manufacture - INT J MACH TOOL MANUF. 35. 135-139. 10.1016/0890-6955(94)P2363-K.

[23]   Price, Robert & Jerome, W.. (2003). "More Basic Confocal Microscopy: A Tutorial. Microscopy and Microanalysis". 9. 1568-1569. 10.1017/S1431927603447843.

[24]   Leach, R.. (2014). "Fundamental principles of engineering nanometrology". 10.1016/B978-1-4557-7753-2.00011-6.

[25]   R. Leach, X. J. Leigh Brown, R. Blunt, and D. M. Mike Conroy, "Guide for the Measurement of Smooth Surface Topography using Coherence Scanning Interferometry," *Manual*, no. 108, p. 56, 2008.

[26]   Stout K, Sullivan P, Dong W, Mainsah E, Luo N, Mathia T, et al. "The development of methods for the characterisation of roughness in three dimensions". EUR(Luxembourg) 1993:358.

[27]   Michigan Metrology. "Surface Texture Parameters Glossary", 2014.

[28]   P. Gamonal-Repiso, M. Sánchez-Soto, S. Santos-Pinto, and M. L. Maspoch, "Improvement of the replication quality of randomly micro-textured injection-moulding components using a multi-scale surface analysis," *J. Manuf. Process.*, vol. 42, no. April, pp. 67–81, 2019, doi: 10.1016/j.jmapro.2019.04.010.

[29]   P. Gamonal-Repiso, T. Abt, M. Sánchez-Soto, S. Santos-Pinto, and M. L. Maspoch, "Influence of topographical features on the surface appearance measurement of injection moulded components," *Polym. Test.*, vol. 93, 2021, doi: 10.1016/j.polymertesting.2020.106968.

[30]   Blateyron F. "New 3D parameters and filtration techniques for surface metrology". Quality Magazine 2006:1–7.

[31]   E. Richard, S. T. Aruna, and B. J. Basu, "Applied Surface Science Superhydrophobic surfaces fabricated by surface modification of alumina particles," *Appl. Surf. Sci.*, vol. 258, no. 24, pp. 10199–10204, 2012, doi: 10.1016/j.apsusc.2012.07.009.

[32]   Leach, R.. (2014). "Fundamental principles of engineering nanometrology". 10.1016/B978-1-4557-7753-2.00011-6.

[33]   Blateyron, François. (2014). "Good practices for the use of areal filters". 10.13140/2.1.1007.9361.

[34]   M. Krystek, "Form filtering by splines," Meas. J. Int. Meas. Confed., vol. 18, no. 1, pp. 9–15, 1996, doi: 10.1016/0263-2241(96)00039-5.

[35]   Suh NP, Saka N (1987) Surface Engineering. CIRP Annals – Manufacturing Technology 36(1):403–408

[36]   Stout KJ (1998) Engineering Surfaces – "a Philosophy of Manufacture (a Proposal for Good Manufacturing Practice). Proceedings of the Institution of Mechanical Engineers Part B", Journal of Engineering Manufacture 212(3):169–174

[37]   Chowdhury, Asim, "Principles of Colour and Appearance Measurement", Elsevier, UK (2014).

[38]   Hunt, Robert. (1991). "Measuring Colour". 10.1002/9781119975595.ch9.

[39]   H. R. Wu, A. R. Reibman, W. Lin, F. Pereira, and S. S. Hemami, "Perceptual visual signal compression and transmission," *Proc. IEEE*, vol. 101, no. 9, pp. 2025–2043, 2013, doi: 10.1109/JPROC.2013.2262911.

[40]   De Valois, R.L, De Valois, K.K., "Spatial vision", Fourth ed., Oxford University Press, New York, 1988.

[41]   Seshadrinathan, Kalpana & Pappas, Thrasyvoulos & Safranek, Robert & Chen, Junqing & Wang, Zhou & Sheikh, Hamid & Bovik, Alan. (2009). "Image Quality Assessment. The Essential Guide to Image Processing". 10.1016/B978-0-12-374457-9.00021-4.

[42]   Barten P. "Contrast sensitivity of the human eye and its effects on image quality". 1999. doi:10.1117/3.353254.

[43]   D. G. Pelli and P. Bex, "Measuring contrast sensitivity," *Vision Res.*, vol. 90, pp. 10–14, 2013, doi: 10.1016/j.visres.2013.04.015.

[44]   F. Hou *et al.*, "Evaluating the performance of the quick CSF method in detecting contrast sensitivity function changes," *J. Vis.*, vol. 16, no. 6, p. 18, 2016, doi: 10.1167/16.6.18.

[45]   L. A. Lesmes, Z.-L. Lu, J. Baek, and T. D. Albright, "Bayesian adaptive estimation of the contrast sensitivity function: The quick CSF method," *J. Vis.*, vol. 10, no. 3, pp. 1–21, 2010, doi: 10.1167/10.3.17.

[46]   a B. Watson, "Visual detection of spatial contrast patterns: evaluation of five simple models.," *Opt. Express*, vol. 6, no. 1, pp. 12–33, 2000, doi: 10.1364/OE.6.000012.

[47]   A. P. Sawant and C. G. Healey, "A Survey of Display Device Properties and Visual Acuity for Visualization," *NCSU Tech. Rep.*, 2005,

[48]   F.W. Campbell, R.W. Gubisch, "Optical quality of the human eye", The journal of physiology. 186 (1966) 558–578 .

[49]   P. Gamonal-Repiso, T. Abt, M. Sánchez-Soto, S. Santos-Pinto, and M. L. Maspoch, "Influence of topographical features on the surface appearance measurement of injection moulded components," *Polym. Test.*, vol. 93, 2021, doi: 10.1016/j.polymertesting.2020.106968.

[50]   Sukumar, Vinesh. (2010). "Study on Threshold Patterns with Varying Illumination Using 1.3m Imaging System". Intelligent Information Management. 02. 21-25. 10.4236/iim.2010.21003.

[51]   B. Pelli, D.G., and Farell, "Why use noise?," J. Opt. Soc. Am. A, Opt. Image Sci. Vis., vol. 16, no. 3, p. 647, 1999, doi: 10.1364/JOSAA.16.000647.

[52]   Bex, Peter & Makous, Walter. (2002). "Spatial frequency, phase, and the contrast of natural images". Journal of the Optical Society of America. A, Optics, image science, and vision. 19. 1096-106. 10.1364/JOSAA.19.001096.

[53]   C. Marois, D. Lafreniere, B. Macintosh, and R. Doyon, "Confidence Level and Sensitivity Limits in High-Contrast Imaging," *Astrophys. J.*, vol. 673, no. 1, pp. 647–656, 2008, doi: 10.1086/523839.

[54]   J. J. Koenderink and A. J. Van Doorn, "Illuminance texture due to surface mesostructure," vol. 13, no. 3, pp. 452–463, 1996.

[55]   T. J. Rink and R. Y. Tsien, "Application fo fourier analysis to the visibility of gratings," vol. 50, no. August 1968, pp. 531–548, 1981.

[56]   G. Obein, F. Viénot, U. Claude, and B. Lyon, "Difference scaling of gloss : Nonlinearity , binocularity , and constancy Kenneth Knoblauch," pp. 711–720, 2004, doi: 10.1167/4.9.4.

[57]   M. Olkkonen, "Joint effects of illumination geometry and object shape in the perception of surface reflectance," vol. 2, pp. 1014–1034, 2011.

[58]   Ho, Xian & Landy, Michael & Maloney, Laurence. (2008). "Conjoint measurement of gloss and surface texture": Research article. Psychological science. 19. 196-204. 10.1111/j.1467-9280.2008.02067.x.

[59]   S. Ignell, U. Kleist, and M. Rigdahl, "On the relations between color, gloss, and surface texture in injection-molded plastics," *Color Res. Appl.*, vol. 34, no. 4, pp. 291–298, 2009, doi: 10.1002/col.20510.

[60]   I. Ariño, U. Kleist, and M. Rigdahl, "Effect of gloss and texture on the color of injection-molded pigmented plastics," *Polym. Eng. Sci.*, vol. 45, no. 5, pp. 733–744, 2005, doi: 10.1002/pen.20330.

[61]   L. Sharan, Y. Li, I. Motoyoshi, S. Nishida, and E. H. Adelson, "Image statistics for surface reflectance perception," *J. Opt. Soc. Am. A*, vol. 25, no. 4, p. 846, 2008, doi: 10.1364/josaa.25.000846.

[62]   S. Nishida and M. Shinya, "Use of image-based information in judgments of surface-reflectance properties," *J. Opt. Soc. Am. A*, vol. 15, no. 12, p. 2951, 1998, doi: 10.1364/josaa.15.002951.

[63]   T. T. Negri and A. Gonzaga, "Color Texture Classification under Varying Illumination," no. October, pp. 61–66, 2014, doi: 10.13140/2.1.1690.3684.

[64]   R. W. Fleming, R. O. Dror, and E. H. Adelson, "Real-world illumination and the perception of surface reflectance properties (a) (c) (b) (d)," pp. 347–368, 2003.

[65]   G. Wendt and R. Mausfeld, "Disparity , motion , and color information improve gloss constancy performance," vol. 10, pp. 1–17, 2010, doi: 10.1167/10.9.7.Introduction.

[66]   M. A. R. Ogers and K. E. K. Noblauch, "Maximum likelihood conjoint measurement of lightness and chroma," vol. 33, no. 3, pp. 184–193, 2016.

[67]   A. C. Schmid and B. L. Anderson, "Do surface reflectance properties and 3-D mesostructure influence the perception of lightness ?," vol. 14, pp. 1–24, 2014, doi: 10.1167/14.8.24.doi.

[68]   K. Doerschner and L. T. Maloney, "Perceived glossiness in high dynamic range scenes," vol. 10, pp. 1–11, 2010, doi: 10.1167/10.9.11.Introduction.

[69]   S. Hansmann-Roth and P. Mamassian, "A glossy simultaneous contrast: Conjoint measurements of gloss and lightness," *Iperception.*, vol. 8, no. 1, 2017, doi: 10.1177/2041669516687770.

[70]   L. Qi, M. J. Chantler, J. P. Siebert, and J. Dong, "The joint effect of mesoscale and microscale roughness on perceived gloss," *Vision Res.*, vol. 115, pp. 209–217, 2015, doi: 10.1016/j.visres.2015.04.014.

[71]   I. Motoyoshi, S. Nishida, L. Sharan, and E. H. Adelson, "Image statistics and the perception of surface qualities," vol. 447, no. May, pp. 206–209, 2007, doi: 10.1038/nature05724.

[72]   Hunt, R. W. G., "The strange journey from retina to brain", J. Roy. Television Soc., 11, 220–229 (1967).

[73]   A. C. Chadwick and R. W. Kentridge, "The perception of gloss : A review," Vision Res., vol. 109, pp. 221–235, 2015, doi: 10.1016/j.visres.2014.10.026.

[74]   F. Pellacini, J. A. Ferwerda, and D. P. Greenberg, "Toward a psychophysically-based light reflection model for image synthesis," *Proc. ACM SIGGRAPH Conf. Comput. Graph.*, pp. 55–64, 2000, doi: 10.1145/344779.344812.

[75]   R. S. Hunter, "Methods of determining gloss," *J. Res. Natl. Bur. Stand. (1934).*, vol. 18, no. 1, p. 19, 1937, doi: 10.6028/jres.018.006.

[76]   Hutchings, J. B., and Luo, M. R., "Translucency, its perception and measurement", AIC Congress - Color '05 , 10th Congress of the International Colour Association, pp. 835–838. Granada, Spain (2005)," p. 2005, 2005.

[77]   M. J. Chantler, "Why illuminant direction is fundamental to texture analysis Why illuminant direction is fundamental to texture analysis," *Image (Rochester, N.Y.)*, vol. 142, no. 4, pp. 199–206, 2000.

[78] Ho, Xian & Landy, Michael & Maloney, Laurence. (2006). "How direction of illumination affects visually perceived surface roughness". Journal of vision. 6. 634-48. 10.1167/6.5.8.

[79] H. Yun-Xian, L. T. Malney, and M. S. Landy, "The effect of viewpoint on perceived visual roughness," *J Vis*, vol. 23, no. 1, pp. 1–7, 2014, doi: 10.1167/7.1.1.The.

[80] J. T. Todd, J. F. Norman, J. J. Koenderink, and A. M. L. Kappers, "on Stereoscopic Shape Perception," vol. 26, pp. 807–822, 1997.

[81] J. T. Todd and E. Mingolla, "Perception of surface curvature and direction of illumination from patterns of shading," J. Exp. Psychol. Hum. Percept. Perform., vol. 9, no. 4, pp. 583–595, 1983, doi: 10.1037/0096-1523.9.4.583.

[82] Ly, Bao & Dyer, Ethan & Feig, Jessica & Chien, Anna & Bino, Sandra. (2020). "Research Techniques Made Simple: Cutaneous Colorimetry: A Reliable Technique for Objective Skin Color Measurement". The Journal of investigative dermatology. 140. 3-12.e1. 10.1016/j.jid.2019.11.003.

[83] Hunt, Martin & Goddard, James & Hylton, Kathy & Karnowski, Thomas & Richards, Roger & Simpson, L. & Tobin, Kenneth & Treece, Dale. (1999). "Imaging Tristimulus Colorimeter for the Evaluation of Color in Printed Textiles". Proceedings of SPIE - The International Society for Optical Engineering. 3652. 10.1117/12.341131.

[84] Billmeyer, Fred & Saltzman, Max. (1981). "Principle of Color Technology".

[85] Pfund, A.H.. (2021). "The measurement of gloss". J Opt Soc Am. 20. 23-26. 10.1364/JOSA.20.000023.

[86] J. Hasan, S. Jain, R. Padmarajan, S. Purighalla, V. K. Sambandamurthy, and K. Chatterjee, "Multi-scale surface topography to minimize adherence and viability of nosocomial drug-resistant bacteria," *Mater. Des.*, vol. 140, pp. 332–344, 2018, doi: 10.1016/j.matdes.2017.11.074.

[87]   Yamada, Yoshinori. (1988). "Friction and wear of polymers and polymer composites". Journal of Japan Society of Lubrication Engineers. 33. 727-732.

[88]   M. Nosonovsky, "Modelling size, load and velocity effect on friction at micro/nanoscale," *Int. J. Surf. Sci. Eng.*, vol. 1, no. 1, pp. 22–37, 2007, doi: 10.1504/IJSURFSE.2007.013619.

[89]   Editors, & Menezes, Pradeep & Ingole, Sudeep & Nosonovsky, Michael & Kailas, Satish & Lovell, Michael. (2013). "Tribology for Scientists and Engineers". 10.1007/978-1-4614-1945-7.

[90]   Sinha, Sujeet. (2018). "Handbook of Polymer Tribology". 10.1142/10647.

[91]   Tabor, David. (1992). "Friction as a Dissipative Process". 10.1007/978-94-011-2811-7_1.

[92]   Berthier, Y.. (2005). "Wear-materials mechanisms and practice". Third-body Reality-Consequences and Use of the Third-body Concept to Solve Friction and Wear Problems. 291-316.

[93]   B.J. Briscoe, E. Pelillo, S.K. Sinha, "Scratch hardness and deformation maps for poIyca rbonate and PolyethyIene", Polymer Engineering and Science. 36 (1996) 2996-3005.

[94]   B.J. Briscoe, P.D. Evans, E. Pelillo, S.K. Sinha, "Scratching maps for polymers", Wear. 200 (1996) 137–147. doi:10.1016/S0043-1648(96)07314-0.

[95]   B.J. Briscoe, P.D. Evans, S.K. Biswass, S.K. Sinha, "The hardnesses of poly (methylmethacrylate)", Tribology International. 29 (1996) 93–104. doi: 0301-679X/96.

[96]   J. L. Bucaille, C. Gauthier, E. Felder, and R. Schirrer, "The influence of strain hardening of polymers on the piling-up phenomenon in scratch tests: Experiments and numerical modelling," *Wear*, vol. 260, no. 7–8, pp. 803–814, 2006, doi: 10.1016/j.wear.2005.04.007.

[97]   P. Kurkcu, L. Andena, and A. Pavan, "An experimental investigation of the scratch behaviour of polymers: 1. Influence of rate-dependent bulk mechanical properties," *Wear*, vol. 290–291, pp. 86–93, 2012, doi: 10.1016/j.wear.2012.05.005.

[98]   C. Xiang, H. J. Sue, J. Chu, and B. Coleman, "Scratch behavior and material property relationship in polymers," *J. Polym. Sci. Part B Polym. Phys.*, vol. 39, no. 1, pp. 47–59, 2001, doi: 10.1002/1099-0488(20010101)39:1<47::AID-POLB50>3.0.CO;2-2.

[99]   H. Jiang, R. Browning, and H. J. Sue, "Understanding of scratch-induced damage mechanisms in polymers," *Polymer (Guildf).*, vol. 50, no. 16, pp. 4056–4065, 2009, doi: 10.1016/j.polymer.2009.06.061.

[100]   B. J. Briscoe and S. K. Sinha, "Scratch Resistance and Localised Damage Characteristics of Polymer Surfaces– a Review," *Materwiss. Werksttech.*, vol. 34, no. 1011, pp. 989–1002, 2003, doi: 10.1002/mawe.200300687.

[101]   L. M. Spring, M. R. Marshall, and E. T. Warner, "K. L. Johnson - Contact Mechanics- Cambridge University Press (1985)," vol. 123, no. 3, pp. 401–409, 2011.

[102]   R. Browning, M. M. Hossain, J. Li, S. Jones, and H. J. Sue, "Contrast-based evaluation of mar resistance of thermoplastic olefins," *Tribol. Int.*, vol. 44, no. 9, pp. 1024–1031, 2011, doi: 10.1016/j.triboint.2011.04.009.

[103]   E. Felder and J. L. Bucaille, "Mechanical analysis of the scratching of metals and polymers with conical indenters at moderate and large strains," *Tribol. Int.*, vol. 39, no. 2, pp. 70–87, 2006, doi: 10.1016/j.triboint.2005.04.005.

[104]   M. Hamdi and H. J. Sue, "Effect of color, gloss, and surface texture perception on scratch and mar visibility in polymers," *Mater. Des.*, vol. 83, pp. 528–535, 2015, doi: 10.1016/j.matdes.2015.06.073.

[105] H. Jiang, R. Browning, J. Fincher, A. Gasbarro, S. Jones, and H. J. Sue, "Influence of surface roughness and contact load on friction coefficient and scratch behavior of thermoplastic olefins," *Appl. Surf. Sci.*, vol. 254, no. 15, pp. 4494–4499, 2008, doi: 10.1016/j.apsusc.2008.01.067.

[106] Chivatanasoontorn, Vadee & Tsukise, Shun & Kotaki, Masaya. (2012). "Surface texture effect on scratch behavior of injection molded plastics". Polymer Engineering & Science. 52. 10.1002/pen.23142.

[107] B. He, W. Chen, and Q. Jane Wang, "Surface texture effect on friction of a microtextured poly(dimethylsiloxane) (PDMS)," *Tribol. Lett.*, vol. 31, no. 3, pp. 187–197, 2008, doi: 10.1007/s11249-008-9351-0.

[108] C. Yu, H. Yu, G. Liu, W. Chen, B. He, and Q. J. Wang, "Understanding topographic dependence of friction with micro- and nano-grooved surfaces," *Tribol. Lett.*, vol. 53, no. 1, pp. 145–156, 2014, doi: 10.1007/s11249-013-0252-5.

[109] L. Xue, J. Iturri, M. Kappl, and H. Butt, "Bioinspired Orientation-Dependent Friction," 2014.

[110] D. Frommel, J. Moullec, P. Lambin, and J. M. Fine, "Selective Serum IgA Deficiency: Frequency among 15,200 French Blood Donors," *Vox Sang.*, vol. 25, no. 6, pp. 513–518, 1973, doi: 10.1016/j.wear.2017.05.007.

[111] X. D. He, K. E. Torrance, F. X. Sillion, and D. P. Greenberg, "A comprehensive physical model for light reflection," Proc. 18th Annu. Conf. Comput. Graph. Interact. Tech. SIGGRAPH 1991, vol. 25, no. 4, pp. 175–186, 1991, doi: 10.1145/122718.122738.

[112] H. Jiang, R. L. Browning, M. M. Hossain, H. J. Sue, and M. Fujiwara, "Quantitative evaluation of scratch visibility resistance of polymers," *Appl. Surf. Sci.*, vol. 256, no. 21, pp. 6324–6329, 2010, doi: 10.1016/j.apsusc.2010.04.011.

[113] P. Rangarajan, M. Sinha, V. Watkins, K. Harding, and J. Sparks, "Scratch visibility of polymers measured using optical imaging," *Polym. Eng. Sci.*, vol. 43, no. 3, pp. 749–758, 2003, doi: 10.1002/pen.10062.

[114] P. Liu, R. Lee Browning, H. J. Sue, J. Li, and S. Jones, "Quantitative scratch visibility assessment of polymers based on Erichsen and ASTM/ISO scratch testing methodologies," *Polym. Test.*, vol. 30, no. 6, pp. 633–640, 2011, doi: 10.1016/j.polymertesting.2011.04.015.

[115] K. Lehmann and P. Tomuschat, "New additive technology provides scratch resistance," *Plast. Addit. Compd.*, vol. 10, no. 2, pp. 20–23, 2008, doi: 10.1016/S1464-391X(08)70055-2.

Chapter 3:   Materials and methods

This Chapter describes the materials and methodologies employed in this thesis. A semi-crystalline polymer (PP) was selected. Squared samples having a texture engraved on top of the surface were injection moulded. A design of experiments was defined to analyse the influence and effect of the main injection conditions on the texture replication ratio. Subject to the criterion of maximum texture replication ratio, a three dimensional (3D) surface characterization either at the macro- and micro-scale was performed to determine the optimal injection conditions. Then, two different mould treatments were applied to the engraved mould cavity for measuring the surface appearance in comparison to a painted sample. A new total appearance measurement (TAM) instrument was utilized for assessing the appearance of textured surfaces under conditions that mimic the human eye capabilities. The surface performance was analysed by means of the scratch visibility resistance criterion. The effect of the texture on both the scratch hardness and the scratch visibility resistance was studied on three different texture types smooth, fine and leather.

3.1. Materials

The relative good specific mechanical properties, good processability and low cost of the PP material make it suitable for a wide range of applications such as electric, lighting, under the hood or interior.

The selected commercial grade of polypropylene (PP) was a black polypropylene copolymer filled with 5% talc, HC TKC 2007N from Basell S.L (Tarragona, Spain). It was characterized by a melt flow index of 16 g/10min (230 ºC, 2.16 kg) and ethylene content of about 8% wt.

The employed material for the mould tool was a DIN 1.2311 40CrMnMo7 steel with a hardness of 307HB obtained from Lugand Aciers (Barcelona, Spain).

A black methylmethacrylate resin composed by two components (Technovit 3040, 1:1 ratio, Kulzer GmbH,Hanau, Germany) was poured into the mould cavity and allowed to cure for five minutes. This allows creating a high-precision replica of the engraved texture. This methodology is widely used and known as replica moulding. It is suitable for indirect surface measurements of inaccessible features or geometries [1].

3.2. Sample preparation & experimental techniques

3.2.1. Texture types

As shown by Figure 3.1 different texture finishes have been studied in this research project in order to analyse both appearance and performance qualities, namely, the texture replication ratio, the surface appearance and the scratch visibility resistance.
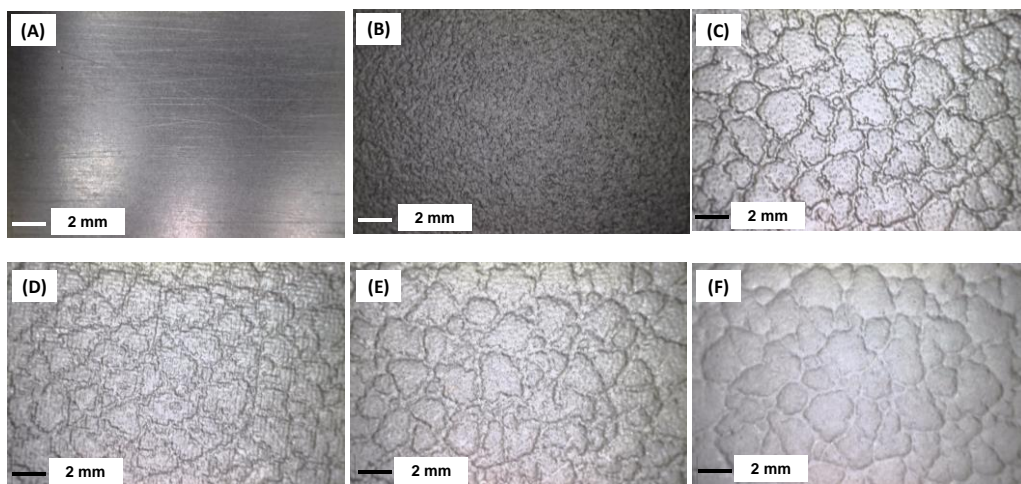
Figure 3.1 Smooth texture (a); fine texture (b); leather texture (c); leather texture + micro-features (d); leather texture + coating (e); leather texture + paint (f)

The smooth surface type (Figure 3.1a) was the result of replicating a mirror-like polished mould cavity. The fine and leather texture types, Figure 3.1b and 3.1c, respectively, were obtained through chemical engraving performed on the mould cavity as it is shown in Figure 3.2. The mould cavity must be first cleaned and protected. After that, an acid-resistant ink with the texture pattern is printed on the mould cavity surface. An acid immersion is conducted several times until achieving the desire texture depth. Finally, the mould cavity is cleaned using filtered air.
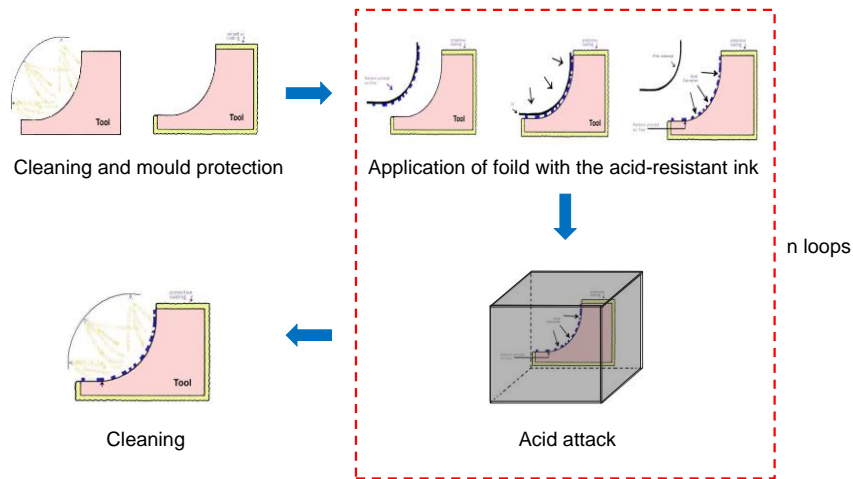
Figure 3.2 Mould engraving process by chemical attack.

Two different treatment were applied on the previously textured mould cavity with the leather texture type (Figure 3.1d and 3.1e). The first treatment consisted in the addition of micro-features on top of the cavity surface, resulting in a modified leather texture (Figure 3.1d). It was done following the same chemical engraving procedure described above. The second treatment consisted in a coating made of a mixture of polytetrafluoroethylene and graphite (Figure 3.1e). This mixture was uniformly applied on the obtained leather texture and cured in an oven at 350 ± 10ºC. It is widely used in automotive industry for reducing the friction coefficient between the mould wall and the polymer, allowing an easier cavity filling. Figure 3.3 shows the mould cavity surface with the different leather texture finishes: the chemical engraving, the addition of micro-features and the surface coating.
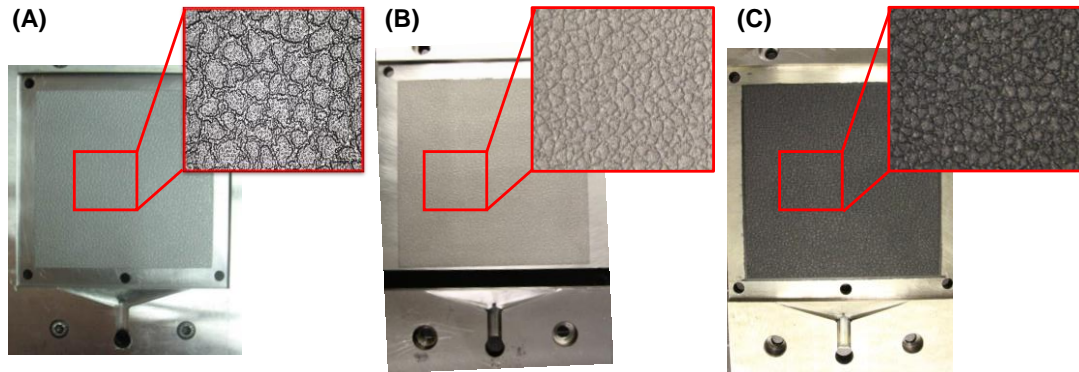
Figure 3.3 Mould cavity of the leather texture (a); mould cavity of the leather texture with micro-features added (b); mould cavity of the leather texture with the applied coating (c).

Finally, the last texture type was the result of painting Texture A injection moulded samples. This texture leather type is shown in Figure 3.1f. A black water-based paint from Mankiewicz Iberica S.L (Barcelona, Spain) was applied. This procedure was performed manually in a standardized painting room with controlled temperature of 23 ± 0.5 ºC.

The leather texture types were encoded as follows:

Table 3.1 Code of the leather texture types

Leather texture type	Code
Original leather texture	Texture A
Leather texture + micro features	Texture B
Leather texture + coating	Texture C
Leather texture + paint	Texture D

3.2.2. Injection moulding

A 110 Tn Engel Victory (Engel Austria GmbH) injection moulding machine equipped with a 40 mm screw diameter and a clamping force of 1100 kN was used to inject squared samples with dimensions 100 x 100 x 3 mm^3 (length x width x thickness) as shown in Figure 3.4A and 3.4B, respectively. A fan gate in one of the sides was used to inject the samples. Figure 3.4C shows the cavity pressure sensor used from Kistler Iberica S.L (Barcelona, Spain) with a sensitivity of 9.4 pC/bar for recording the internal mould pressure [2], [3]. This machine was available in the Centre Català del Plàstic (CCP) facilities.
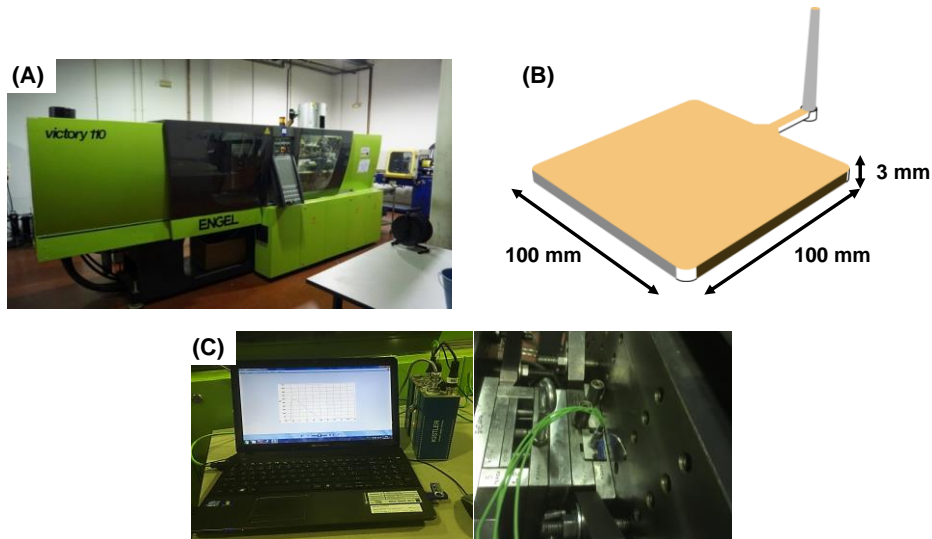
Figure 3.4 Injection moulding machine Engel Victory (a); dimensions of injected moulding samples (b); sensor for measuring and recording the mould cavity pressure (c).

The influence and effect of the main injection parameters on the textured surface replication by polymer was analysed by means of a two-level factorial design of experiments (DOE). An analysis of the variance (ANOVA) was carried out using the Minitab 17 software.

3.3. Characterization techniques

3.3.1. Surface characterization techniques

3.3.1.1. Chromatic confocal microscope

A three dimensional topographic analysis of the surface was carried out using a contactless chromatic confocal microscope, FRT Microprof 200 (Bergisch Gladbach, Germany) employing a LED as light source (Figure 3.5). The chromatic white light sensor (CWL) had a lateral and vertical resolution of 6 µm and 30 nm, respectively, a working distance of 22 mm and a numerical aperture of 0.5 that allowed measuring surface angles of 90º±30º. The data processing was performed using the software FRT Mark III V3.11.5.2.

Figure 3.5 FRT Microprof 200. Chromatic confocal microscope.

3.3.1.2. White light confocal microscope

A white light confocal microscope, S lynx from Sensofar Metrology S.L (Terrassa, Spain) (Figure 3.6), was employed for high-precision 3D areal measurements. This instrument was equipped with a 20x magnification lens having 0.69 µm and 8 nm of lateral and vertical resolution, respectively. The maximum field of view (FOV) was an area of 877 x 660 µm2, the working distance and the numerical aperture were of 4.5 mm and 0.45, respectively. The data processing was perform using the software SensoSCAN V6.4.

Figure 3.6 S lynx. White light confocal microscope.

3.3.1.3. *Scanning electron microscope (SEM)*

A scanning electron microscope (SEM), Zeiss Sigma 300 VP (Jena, Germany) (Figure 3.7), was also utilized for obtaining ultra-high resolution images of the studied textured surfaces. This instrument has a variable pressure (VP) chamber which varies from 10 to 133 Pa, allowing the investigation of electrically non-conductive samples. The resolution of this instrument ranges from 1.2 to 2.5 nm for a current of 15 or 1 KV, respectively. The working distance was of 8.5 mm and the take-off angle was of 35º. The data acquisition software was the SmartSEM.

Figure 3.7 Zeiss Sigma 300 VP. Scanning electron microscope.

3.3.2. Sampling conditions

The sampling conditions were determined for measuring the surface topography either at the macro- or the micro-scale level. This was conducted using the chromatic confocal microscope, FRT Microprof 200.

In the macro-scale analysis, the sampling conditions were selected to mimic the visual acuity of the human eye. In that particular case, the lateral resolution which provides the minimum size of the features detectable by the sensor in the x and y-axis was set to 40 µm. This resolution was selected because the human eye is limited to resolve a spatial pattern separated by a visual angle of 1/60º, which for a viewing distance of ≈200 mm represents a feature with a characteristic dimension of approximately 58÷60 µm [4], [5]. From an industrial point of view, the texture quality of a certain part is guaranteed (with a safety factor of 1.5) if the possible defects are lower than 40 µm in size. In addition, different sampling areas were analysed in order to obtain statistically representative topographical data including all surface components, namely roughness, waviness and form. The dimensions of the sampling areas were varied from 4 mm^2 to 1600 mm^2 corresponding to low frequency limits (f_L) of 0.5 mm^{-1} and 0.025 mm^{-1}, respectively. To avoid edge errors, 1/7 of the square length in the x and y-axis was removed from the sampling area.

A high-resolution analysis was conducted to properly analyse the micro-features engraved on top of the textured samples at the micro-scale range. Two different sampling conditions were selected. In the first case an evaluation area of 1.46 x 1.46 mm^2 and a lateral resolution of 8 µm was selected. In the second case, the evaluation area and the lateral resolution were set at 3.65 x 3.65 mm^2 and 10 µm, respectively.

3.3.3. Multi-scale surface analysis

The surface characterization was conducted by means of the multi-scale analysis methodology using the chromatic confocal microscope. This methodology allows making multiple observations on a single topography by filtering at different scales [6], [7]. The

measuring scale can be narrow or wide in order to assess small or large topographies features sizes, respectively. Appropriate filtering conditions yield a spatial frequency decomposition, simulating the effects of measuring at different magnifications. Figure 3.8 depicts the filters used to extract the topographic data at the desired scale. The S-filter was used to remove the short spatial wavelength or small features. The L-filter was employed to remove the large spatial wavelength (large features) and the F-Operator was applied to remove the base form of the surface. The combination of these three filters yielded SF and SL surfaces as defined by the standard ISO 25178-2 [8]. The SF-surface was derived by removing the lateral components (surface features) smaller than the selected S-filter and larger than the F-Operator value. The SL-surface was obtained after applying the L-filter on the previously defined SF-surface, establishing the scale at which the surface was assessed. Filtering by feature size yielded a better topography discernibility for a given scale, leading to an adequate separation of the three surface components [9].
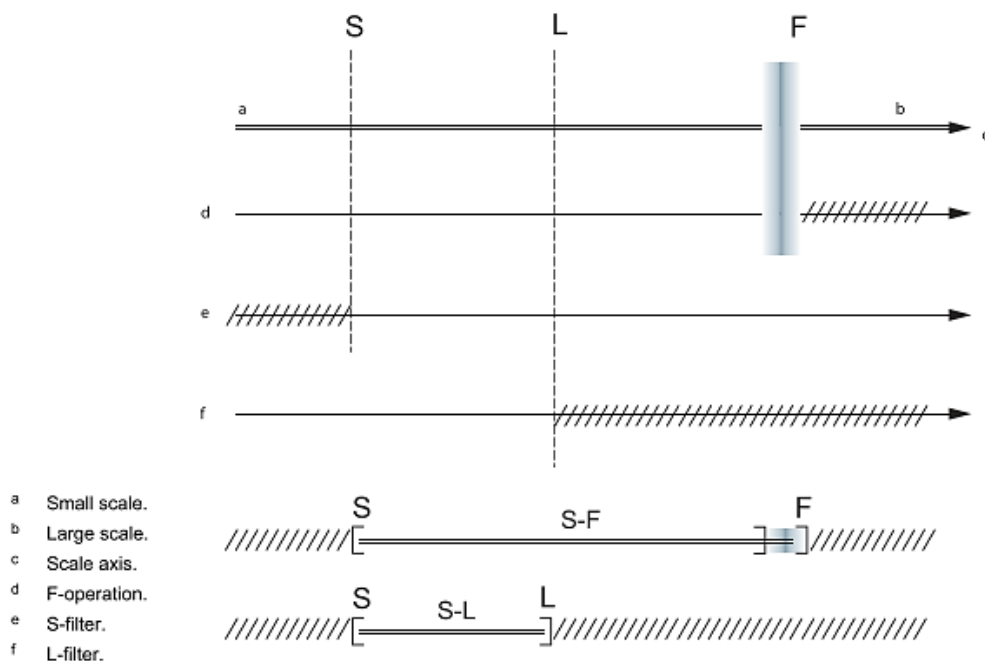
Figure 3.8 Relationship between the S-filter, L-filter and F-operator with S-F and S-L limited scales [8].

In the macro-scale analysis, the SL-surface was obtained using the following method: The S-filter was set first at 40 µm and the L-filter was varied following the series: 0.1, 0.2, 0.25, 0.5, 0.8, 1 mm, until no variations were detected in the surface information. These settings were denoted as S-L 0.04 – 5, where S-L denotes the surface type, 0.04 mm is the S-filter nesting index setting and 5 mm is the L-filter nesting index value.

Finally, the SF-surface was obtained from the previous analysis in order to calculate the form deviation. The notation used for these settings was: S-F 5– 15, where S-F denotes the surface type, 5 mm is the S-filter nesting index setting and 15 mm is the F-Operator nesting index value.

In the micro-scale analysis case, the multi-scale methodology was conducted as follows: For the first condition where the evaluation area was of 1.46 x 1.46 mm^2 and the lateral resolution was of 8 µm, the S-filter was fixed at 0.008 mm and the L-filter was varied within the range of 0.01mm to 1.46 mm following the series as previously described.

For the second condition where the evaluation area was of 3.65 x 3.65 mm2 and the lateral resolution was of 10 µm, the S-filter was fixed at 0.01 mm and the L-filter was varied within the range of 0.01mm to 3 mm following the series as previously described.

3.3.4. Appearance characterization techniques

3.3.4.1. *Total appearance measurement apparatus (TAM)*

The surface appearance was measured using a total appearance measurement instrument (TAM) from BYK-Gardner GmbH (Geretsried, Germany). This device was a prototype that enables analysing at the same time surface topography and reflectivity by means of the photometric stereo technology (PS) [10]. This technique allows making surface reconstruction in three dimensions (3D) through successive images by varying the direction of the incident illumination but keeping constant the scene and the viewing direction (Figure 3.9). For this reason, the prototype instrument incorporates four white tri-phosphor-LEDs as light source,

each one at 60° in regards to the horizontal axis. A top camera, equipped with tele-centric lenses is located at 0° with respect to the surface normal.
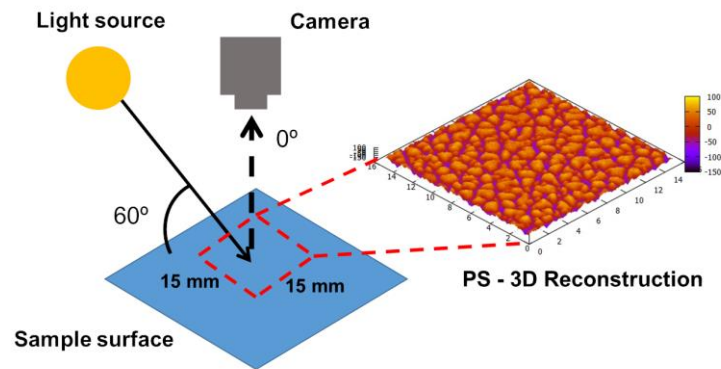
Figure 3.9 Measuring principle of the photometric stereo (PS) technology and reconstruction of the surface in three dimensions (3D).

For measuring the reflectivity the prototype assumes the surface as Lambertian or ideal diffusion type [11]. These Lambertian surfaces are characterized by having equal brightness in any viewing direction at a fixed light source. However, the intensity of the surface image changes if the illumination directions are modified. Thus, reflectivity measurements were carried out using a top light source located at 0° with respect to the surface normal. The evaluation area was approximately 15 x 15 mm^2, taking 512 x 512 pixels per image which resulted in an optical resolution of around 60 µm. This mimics a human visual angle of 0.11° at a distance of 300 mm [4].

3.3.4.2. *Spectrophotometer instrument*

The surface lightness (L*) and gloss (G*) was measured using a spectro-Guide 45/0 Gloss-spectrophotometer from BYK-Gardner GmbH (Geretsried, Germany). It was equipped with a 45/0° measuring geometry and D65/10° as illuminant. The gloss measurements were acquired at 60° and relative to a highly polished black glass standard with 100 gloss units (GU).

3.3.5. Scratch and mar resistance tests

The scratch and mar resistance tests were carried out utilizing an Erichsen 430 scratch machine from Erichsen GmbH & Co. KG (Hemer, Germany) in a temperature controlled room (23±0.5ºC).

The scratch test was performed using a stainless steel 1 mm diameter (Ø) spherical tip. A constant scratching rate of 1000 mm/min and three different loads of 7, 10 and 15 N were applied.

The mar resistance test was conducted using a 16 mm Ø metal disk as indenter, having a thickness of 1 mm and an edge with radius r= 0.5 mm as it is shown in Figure 3.10. The indenter speed was set at 1000 mm/min and three constant contact forces were applied, 1, 3 and 5 N, respectively. A 45 x 10 mm^2 (length x width) test area was created after 20 disk slides. The space between each slide line was 0.5 mm
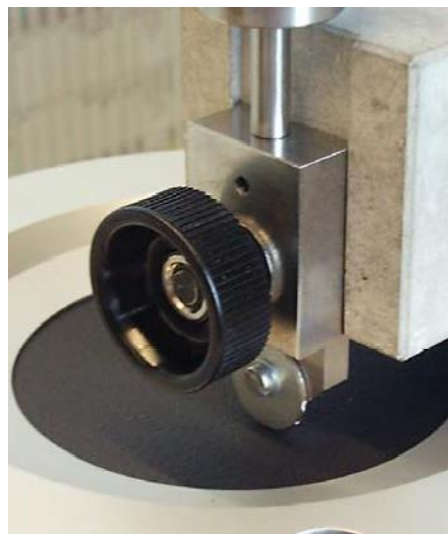
Figure 3.10 Metal disk of 16 mm diameter used for evaluating the mar resistance of textured surfaces.

3.4. Uncertainty contribution measurement

The importance of uncertainty on the measurement reliability was determined following the procedure described by Haitjema et al. [12]. This methodology allowed estimating the instrument uncertainty by repeated measurements on a calibrated item, having similar surface characteristics with the actual measurand [13]. The uncertainty contribution of both the chromatic confocal microscope and the total appearance measurement instruments has been determined following the substitution method described in Equation 3.1.

$$U = \sqrt{U_{cal}^2 + U_p^2 + U_{res}^2} \tag{3.1}$$

Where U is the uncertainty contribution of the instrument under evaluation. U_{cal} is the uncertainty of the calibrated item. U_p is the standard uncertainty related to the measurement procedure. U_{res} is the resolution uncertainty related to the declared resolution of the instrument under evaluation. The measurements were done in a temperature-controlled room at 23 ± 1 °C.

3.5. References

[1]   F. Baruffi, P. Parenti, F. Cacciatore, M. Annoni, and G. Tosello, "On the application of replica molding technology for the indirect measurement of surface and geometry of micromilled components", *Micromachines*, vol. 8, no. 6, 2017, doi: 10.3390/mi8060195.

[2]   H. Hassan, "An experimental work on the effect of injection molding parameters on the cavity pressure and product weight", *Int. J. Adv. Manuf. Technol.*, vol. 67, no. 1–4, pp. 675–686, 2013, doi: 10.1007/s00170-012-4514-4.

[3]   M. Kurt, O. Saban Kamber, Y. Kaynak, G. Atakok, and O. Girit, "Experimental investigation of plastic injection molding: Assessment of the effects of cavity pressure and mold temperature on the quality of the final products", *Mater. Des.*, vol. 30, no. 8, pp. 3217–3224, 2009, doi: 10.1016/j.matdes.2009.01.004.

[4]   F.W. Campbell, R.W. Gubisch, "Optical quality of the human eye", The journal of physiology. 186 (1966) 558–578

[5]   De Valois, R.L, De Valois, K.K., "Spatial vision", Fourth ed., Oxford University Press, New York, 1988.

[6]   C. A. Brown *et al.*, "Multiscale analyses and characterizations of surface topographies", *CIRP Ann.*, vol. 67, no. 2, pp. 839–862, 2018, doi: 10.1016/j.cirp.2018.06.001.

[7]   Biguerelle. M, Van Gorp. A, Lost. A, "Multiscale roughness analysis in injection-molding process". Polymer Engineering and Science 2008;48: 1725-36. doi: 10.1002/pen.21131.

[8]   ISO 25178-2, Geometrical Product Specifications (GPS) - Surface texture: Areal - Part 2: Terms, definitions and surface texture parameters, First ed., 2012.

[9]   Blateyron F. "New 3D parameters and filtration techniques for surface metrology". Quality Magazine 2006:1–7.

[10]   R. J. Woodham, "Photometric Method For Determining Surface Orientation From

Multiple Images", *Opt. Eng.*, vol. 19, no. 1, pp. 139–144, 1980, doi: 10.1117/12.7972479.

[11] E. F. Taylor. "Illumination fundamentals". Rensselaer, 2000.

[12] R. M. Rodríguez, L. Martínez, V. Torra, Z. S. Xu, and F. Herrera, Hesitant Fuzzy Sets: "State of the Art and Future Directions", *Int. J. Intell. Syst.*, vol. 29, no. 2, pp. 495–524, 2014, doi: 10.1002/int.

[13] JCGM 100:2008, "Evaluation of measurement data – Guide to the expression of uncertainty in measurement", *Jt. Comm. Guid. Metrol.*, no. September, 2008, doi: 10.1373/clinchem.2003.030528.

Results and discussion

Chapter 4: Improvement of the texture replication ratio
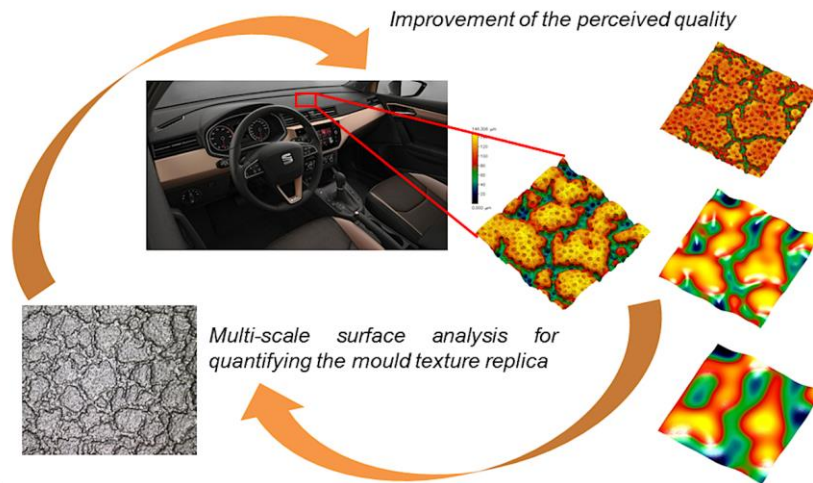
In this chapter the effect of the injection parameters on the replication ratio of the mould cavity texture has been evaluated by means of three dimensional (3D) surface techniques. It was found that under sampling conditions that mimic the human eye acuity only surface defects associated to form deviation can be detected. On the contrary, the micro-scale analysis demonstrated an improvement of the replication ratio up to 30%.

Publication derived from this work [1]

Improvement of the replication quality of randomly micro-textured injection-moulding components using a multi-scale surface analysis

Pablo Gamonal-Repiso[a,b], Miguel Sánchez-Soto[a,*], Soledad Santos-Pinto[b], Maria Lluïsa Maspoch[a]

[a] Centre Català del Plàstic, Universidad Politécnica de Cataluña Barcelona Tech (UPC-EEBE), C/Colom 114, 08222 Terrassa Spain
[b] Departamento de Tecnología de Materiales de SEAT S.A. Autovía A-2, Km 585. Apartado de correos 91. 08760 Martorell, Spain

4.1. Experimental section

4.1.1. Material

In all cases, the material used was a black polypropylene copolymer filled with 5% talc, HC TKC 2007N from Basell S.L (Tarragona, Spain).

A black, two-component methylmethacrylate resin (Technovit 3040, 1:1 ratio, Kulzer GmbH,Hanau, Germany) was poured in the mould and allowed to cure for five minutes, creating a high-precision replica of the cavity texture.

4.1.2. Samples preparation

Squared samples with dimensions 100 x 100 x 3 mm^3 (length x width x thickness) were obtained by injection moulding. A leather texture engraved on the mould cavity was replicated on top of the surface (Figure 4.1).
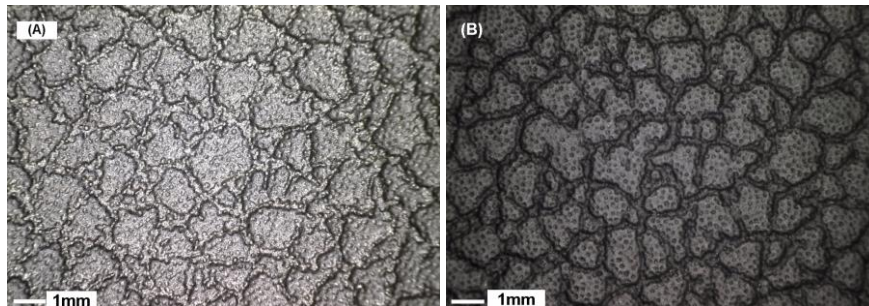
Figure 4.1 Mould cavity with the random coarse texture engraved on it. Optical micrograph of the textured mould cavity (a) and micrograph of the replica obtained using an acrylic resin (b)

The effect and influence of the injection moulding parameters on the texture replication ratio was determined by means of a two-level factorial design of experiments (DOE). An analysis of the variance (ANOVA) was carried out using the Minitab 17 software. The parameters and levels selected for analysis are shown in Table 4.1.

Table 4.1 Injection parameters under study and its levels.

Factor	Low level	Medium level	High level
A: Melt Temperature (°C) (T_m)	200	235	270
B: Mould Temperature (°C) (T_{md})	30	50	80
C: Injection volumetric flow rate (cm^3/s) (V_{fr})	100	300	500
D: Holding pressure (bar) (P_h)	400	500	600

Two extra tests using the medium level parameters were also performed to minimize curvature effects that can appear due to the interaction between factors. A total of 18 experiments were conducted to complete the full factorial design ($2^4 + 2$ medium level runs).

4.1.3. Surface characterization

The surface topography was analysed using the chromatic confocal microscope, equipped with a chromatic white light sensor (CWL) having 30 nm and 6 µm of vertical and lateral resolution, respectively.

The surface was characterize at the macro-scale and at the micro-scale range. In the former case, the sampling conditions were selected in order to mimic the visual acuity of the human eye. The lateral resolution was set to 40 µm and the sampling area was experimentally determined for obtaining statistically representative topographical data including all surface components, namely roughness, waviness and form. In the latter case, the evaluation area and the lateral resolution were 1.46 x 1.46 mm^2 and 8 µm, respectively.

4.1.4. Surface parameters

To characterize and quantify the rate of micro-cavities replication, four types of surface parameters were considered. The arithmetical mean height (Sa), the root mean square height (Sq) and the maximum height (Sz), as defined by Equations 4.1, 4.2 and 4.3 were selected from the family of amplitude parameters.

From the functional family the areal material ratio (S_{mr} (c)) was selected. It is defined as the ratio of material at a specified height (c) to the total of material in the evaluation area.

In our case, c is referred to the maximum dale height (S_v). Therefore, the $S_{mr}(c)$ expresses the amount of material contained in the peaks of the surface above c.

The power spectral density function (PSD) (Eq. 4.4) was chosen from the spatial parameter family to measure the amplitude of each sine wave within the spatial frequency for a given direction where high frequency refers to small features and low frequencies to large ones.

Finally, from the hybrid parameters, the root mean square surface slope (S_{dq}) (Eq. 4.5) was utilized for analysing the spacing between features in all directions. The higher the S_{dq}, the thinner is the space between surface features and vice versa.

Moreover, using the software FRT Mark III V3.11.5.2$^©$, other surface characteristics such as the number of micro-cavities (NG) filled above a given height (c =S_v), its averaged area ($\overline{GA}$) and volume ($\overline{GV}$) were considered for quantifying the amount of material replicated as a function of the injection parameters.

$$Sa = \frac{1}{A} \iint_A |z(x,y)| dx dy \tag{4.1}$$

$$Sq = \sqrt{\frac{1}{A} \iint_A |z^2(x,y)| dx dy} \tag{4.2}$$

Where *z* denotes the surface height measured at the coordinates (x, y) within the area *A*

$$Sz = Sp - Sv \tag{4.3}$$

Where the *Sp* is the maximum peak height and the Sv is the maximum dale height.

$$PSD\ (s) = \int_{R2}^{R1} r|F[rsin(s-\theta), rcos(s-\theta)]^2 |dr \tag{4.4}$$

Where *s* is the specified direction, R1 and R2 are the range of integration in the radial direction (r), F is the Fourier analysis of the sine waves that composed the surface texture for a given direction and θ is the specified direction in the plane of the definition area.

$$Sdq = \sqrt{\frac{1}{A} \iint_A \left[\frac{dz(x,y)^2}{dx}\right] + \left[\frac{dz(x,y)^2}{dy}\right] dxdy}$$

(4.5)

4.1.5. Uncertainty measurement contribution of the CWL sensor

In the CWL sensor particular case, both the engraved mould cavity surface and the resin replica were employed as calibrated items. The arithmetical mean height (Sa) was selected as representative parameter since it provides information regarding the areal average roughness. It was analysed through the entire spatial frequency domain without applying any cut-off filters. The uncertainty related to the surface roughness measurements using the chromatic white light (CWL) sensor (U_{CWL}) was calculated for both the mould cavity and the resin replica (Equation 4.6) [1].

$$U_{CWL} = \sqrt{U_{cal}^2 + U_p^2 + U_{res,CWL}^2}$$

(4.6)

Where U_{cal} is the standard deviation of 5 measurements performed on the engraved mould steel ($U_{cal, mould}$) and the resin replica ($U_{cal, resin}$), respectively (Figure 4.1). U_p is the standard deviation of ten repeated measurements carried out on the engraved steel and resin central location and $U_{res,CWL}$ is the resolution uncertainty related to the declared 30 nm vertical resolution of the CWL sensor.
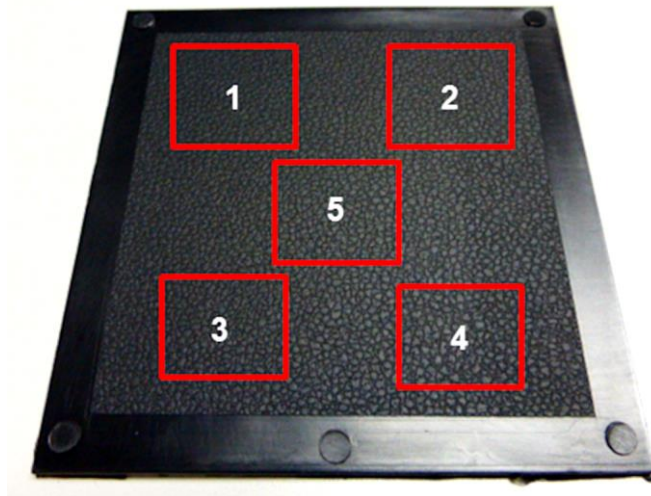
Figure 4.2 Location where the surface characterization has been performed.

The repeatability of the injection process ($U_{sa,Inj}$) was obtained once the process was stabilized, as detected by the constancy of the mould pressure curves. A total of 50 samples were injected per each condition of which 10 were randomly selected. Measurements were performed on the central area (Figure 4.2). The extended uncertainty (U_{Sa}) that combines both process and instrument deviations derived from the mould cavity and the resin replica was calculated using (Equation 4.7):

$$U_{Sa} = k \; x \; \sqrt{U_{CWL}^2 + U_{Sa,inj}^2} \tag{4.7}$$

Where *k* is the coverage factor, equal to 2 for the 95% confidence interval.

4.2. Results and discussion

4.2.1. Uncertainty contribution of the CWL sensor

The different sources of uncertainty which take either the mould cavity or resin replica as calibrated surfaces are collected in Table 4.2.

The uncertainty is a parameter associated with the result dispersion that can be ascribed to the measurand. It is of prime importance for checking the quality of the measurements. Since the accuracy of the CWL sensor (30 nm) was much higher than the order of magnitude of the measurand ($\sim$ 20-30 µm), it was expected that errors arising from the measurements were negligible.

Table 4.2 Uncertainty contribution to the roughness measurements (Sa) of the engraved mould and the resin replica.

Uncertainty contribution	Condition 1	Condition 2	Condition 3
$U_{cal, mould}$ (μm)	0.5	0.5	0.5
$U_{cal, resin}$ (μm)	0.5	0.5	0.5
U_p (μm) (x10^{-3})	2	2	2
$U_{res,CWL}$ (μm) (x10^{-2})	1	1	1
$U_{CWL, mould}$ (μm)	0.5	0.5	0.5
$U_{CWL, resin}$ (μm)	0.5	0.5	0.5
$U_{sa, Inj}$ (μm) (x10^{-2})	5	7	7
$U_{sa, mould}$ (μm)	1	1	1
$U_{sa, resin}$ (μm)	1	1	1

4.2.2. Determination of the optimal sampling conditions

The lateral resolution is related to the sampling interval or number of data points acquired per unit length [2]. The selection of large sampling intervals leads to missing high frequency or short wavelength components that are the small features. Generally, this yields a poor visualization of the original topography. Alternatively, fine sampling intervals result in redundant data points and increased computing time. The selection of a suitable sampling interval is critical for a reliable three-dimensional (3D) surface reconstruction. The sampling interval and the number of data points acquired govern the spatial frequency range, limiting both the short and the long wavelengths as defined by Equation 4.8 and Equation 4.9, respectively [3].

$$f_h \; = \; (\frac{1}{2\Delta x}) \; = \; (\frac{1}{2\Delta y}) \;\; (\text{mm}^{-1}) \tag{4.8}$$

$$f_L = \; (\frac{1}{N_x \Delta x}) = (\frac{1}{N_y \Delta y}) \quad (\text{mm}^{-1}) \tag{4.9}$$

Where f_h is the high frequency limit and f_L is the long frequency limit. Δx and Δy are the sampling intervals in the x and y-axis respectively. N_x and N_y are the number of data points in the x and y-axis, respectively [3]. In this study the selected sampling interval was 20 μm which provided a lateral resolution of 40 μm according to the Nyquist theorem [3].

Once the sampling interval was defined, the next step was to determine the sampling area. The optimal sampling area is one that represents the global surface under analysis and takes into account the three main surface components (roughness, waviness and form). The determination of the optimal sampling area was carried out using the cast resin. In this study, the sampling area (A) was defined by Equation 4.10 [3].

$$A = lx \cdot ly = (Nx - 1)\varDelta x \cdot (Ny - 1)\varDelta y \tag{4.10}$$

Where lx and ly are the sampling length in the x and y-axis, respectively, N_x and N_y are the single data points acquired in the x and y axis, respectively, and $\varDelta x$ and $\varDelta y$ are the sampling interval in the x and y axis respectively. As the analyzed region is a square, $lx = ly$ and $\Delta x = \Delta y$.
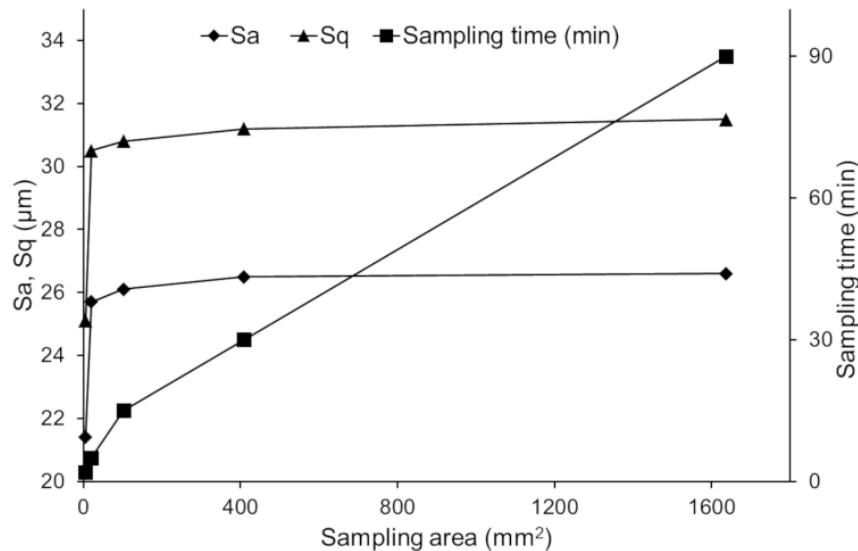
Figure 4.3 Evolution of the Sa and Sq parameters accordingly to the sampling area and sampling time.

The sampling area was initially unknown. To determine the optimum area, the cut-off length was increased incrementally from 2.54 x 2.54 mm^2 to 40.94 x 40.94 mm^2 [4]. In Figure 4.3, the evolution of Sa and Sq as a function of the sampling area and sampling time is shown. Both Sa and Sq increased with the sampling area until the area reached 104 mm^2. Areas below this level do not accurately represent the original surface because long wavelengths (large

features or form deviation) are ignored. For sampling areas between 104 and 1676 mm^2 a

plateau was reached where Sa and Sq are relatively constant within this range. This stability

means that any of these sampling areas would yield a good reconstruction of the surface

topography. However, a balance between reliable data acquisition and sampling time should

be found. The characteristics of the three chosen sampling areas within the plateau are shown

in Table 4.3. Both the data points and the sampling time increased rapidly as a function of the

sampling area increment. Collecting more data points results in a better surface reproduction.

However, the sampling area B was selected because it had a good balance between the number

of data points acquired and the sampling time needed.

Table 4.3 Specifications of the sampling areas within the plateau range.

Code	Sampling area (mm^2)	Data points (N$_x$ x N$_y$)	f$_L$ (mm^{-1})	Largest wavelength (mm)	Sampling time (min)
A	104.44	512 x 512	0.097	10.24	15
B	418.61	1024 x 1024	0.048	20.48	30
C	1676.08	2048 x 2048	0.024	40.96	90

In Figure 4.4, the surface sampled by the CWL sensor using the optimal settings is

compared to the true surface obtained via scanning electron microscopy (SEM). In the

enlarged image shown in Fig. 4b the similarities between the results of these two analysis

methods are illustrated. The 3D reconstruction was able to detect and accurately reproduce

surface features under 200 µm in the x and y-axis. For instance, the micro-pores located on

the raised portions of the surface are well reproduced on the 3D map. It should be mentioned

that the differences between the two images arise from the fact that the SEM image is planar

whereas the CWL image reproduces the volume and relief of the polymer surface.
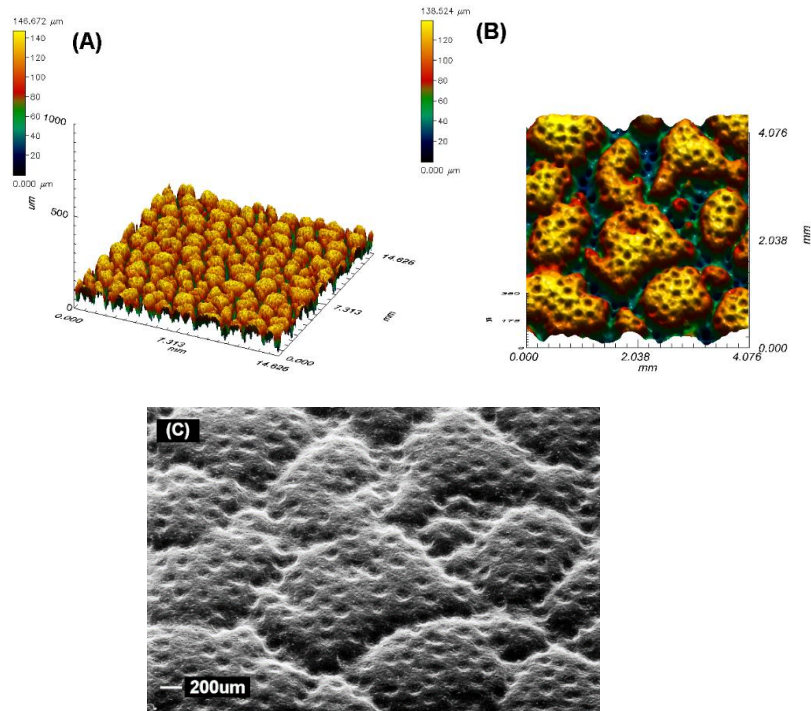
Figure 4.4 Reliability of the 3D reconstruction in regards with the true surface. (A): 3D map of the textured surface. (B): Enlargement of the region of interest from the 3D map. (C): Electronic micrograph (SEM) of the region of interest.

4.2.3. Assessment of the mould replication fidelity obtained by the casted resin

Usually, the injection moulds are large and heavy, making impossible the direct assessment of its cavity texture using common instruments such as optical devices, interferometers or confocal microscopes. A method to solve this problem is replica moulding. It consist in obtaining a replica of the measurand and performing indirect analysis on the resultant reverse surface [5]. However, in this case, the mould cavity was portable and was small enough to be directly characterized using the CWL sensor. Therefore, both the mould cavity texture and the casted resin were characterized and compared to guarantee the replication fidelity [6], [7].
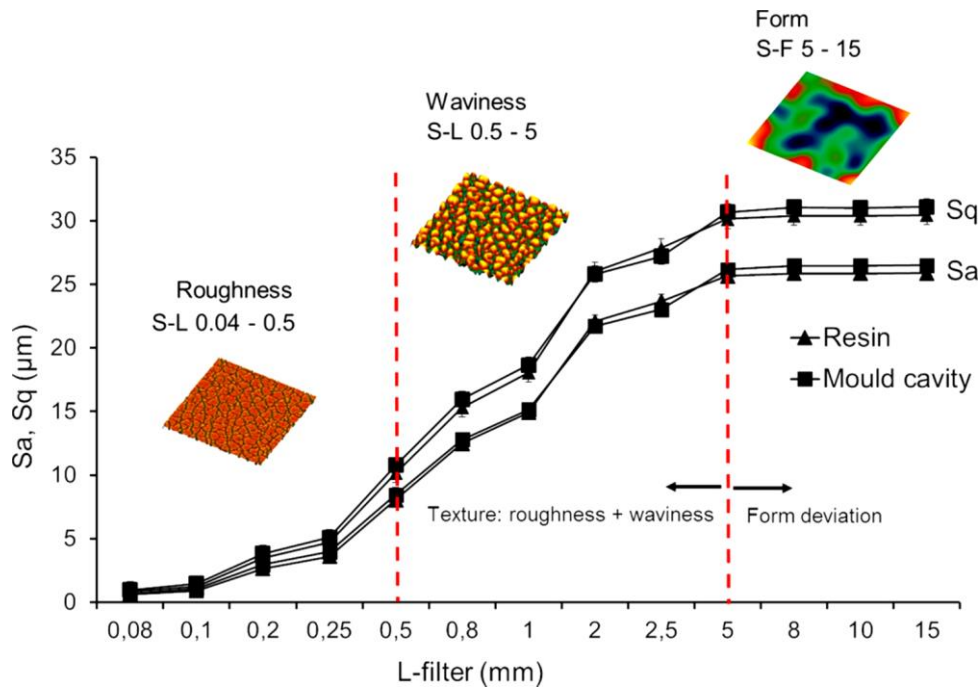
Figure 4.5 Mould cavity and resin surfaces assessment at each scale. The red lines distinguish the scales at which the surface components can be separated. The surface texture is considered as the roughness and waviness sum at the limited scale S-L 0.04-5. Form deviation is compressed at the limited scale S-F 5-15.

In Figure 4.5 the evolutions of Sa and Sq in the multi-scale analysis of the five analysed locations (Figure 4.2) are shown and both the mould cavity and the cast resin are represented. Throughout all the scales of L-filter the mould texture was well copied by the resin and there were no significant differences between Sa and Sq. It should be emphasized that larger wavelength components (roughness, waviness and form) are added to the topography calculation if the L-filter is increased. Hence it is expected that the amplitude of both Sa and Sq increase. In this case, Sa and Sq increased until 5 mm of L-filter, meaning that lateral components of the surface up to this value contributed to the roughness and waviness calculations, obtaining as a result the texture. From 5 to 15 mm a plateau was reached. Since both were flat, there was no contribution of the form deviation and therefore Sa and Sq were constant. It can be concluded that it was possible to assess the surface topography without form deviation until the scale of 5 mm, resulting in a separation of the texture (roughness plus waviness) and form at the settings S-L 0.04-5. On the contrary, form deviation can appear

between the scale range from 5 to 15 mm. The texture was assessed in a further analysis within the scale S-L 0.04-5, whereas the form deviation was analysed within the scale S-F 5-15.

Table 4.4 and Table 4.5 contain the topographic results obtained after measuring the mould cavity texture (M_{cav}) and the reverse surface of the casted resin. Both were analysed at five different locations as shown in Figure 4.2. The Smr(c), NA and its $\overline{GA}$ and $\overline{GV}$ (the functional and the complementary parameters) were quantified above Sv in the moulded part, whereas in the mould cavity the calculations were performed below Sv, since it is the reversed surface of the samples. As can be seen, the results obtained from the mould cavity and the cast resin matched well in all measurement ranges. At the texture scale, the amplitude parameters Sa, Sq and Sz were very close between topographies, meaning that the absolute heights measured were the same regardless of the analysed location. Nevertheless, as the amplitude parameters only provided absolute height values it was not possible to distinguish between mould cavity surface and its reverse (cast resin or moulded component). The use of functional and complementary parameters allows the quantitative determination of the amount of material replicated in a certain surface portion (e.g. surface peaks). Therefore, they constitute an alternative way for investigating the ratio of replication. As given in Table 4.4 the referred portion of material to the peaks (Smr(c)) as well as the NG above the Sv and its averaged $\overline{GA}$ and $\overline{GV}$ were within the standard deviation limits, hence it can be concluded that the casted resin accurately reproduced all the mould cavity features. Moreover, Table 4.5 contains the results at the form deviation scale S-F 5-15. As in the previous case, the mould and resin matched well. It is important to remark that long surface components such as form deviation are also transferred to the cast resin. The standard deviation of measurements is very low in both scales, implying that the cast resin can be considered a very good representative of the mould cavity. Therefore, the resin replica can be used as a calibrated element for verifying the surface quality of moulds and the resultant injected parts over time. As the differences between locations (Figure 4.2) were negligible, the central area (5) was selected as representative for the assessment of the whole injected sample surfaces.

Table 4.4 Results of the mould cavity and cast resin topographies at the limited-scale S-L-0.04-5, n=5.

	S_a (µm)	S_q (µm)	S_z (µm)	$S_{mr}(c)$ (c=Sv)(%)	NG (h=Sv)	$(\overline{GA})$ (mm^2)	$(\overline{GV})$ x10^7 (µm^3)
M_{cav}	26.2±0.4	30.8±0.5	144.6±2.5	58.0±0.2	174±9	0.7±0.1	1.6±10^5
Resin	25.5±0.5	29.9±0.6	144.5±7.4	58.2±0.4	176±8	0.7±0.1	1.6±10^5

Table 4.5 Results of the mould cavity and cast resin topographies at the limited-scale S-F-5-15, n=5.

	S_a (µm)	S_q (µm)	S_z (µm)
M_{cav}	1.3 ± 0.2	1.7 ± 0.2	8.7 ± 1.8
Resin	1.3 ± 0.1	1.7 ± 0.1	9.3 ± 1.4

4.2.4. Influence of the injection parameters

It is well known that the injection parameters have a great influence on the quality of the moulded components [8]–[16]. Therefore, it was necessary to analyse the effect of the injection parameters on the mould texture replication of the polymer surface. The moulding parameters under study here were the melt and mould temperature, the injection volumetric flow rate and the holding pressure. These parameters were considered to govern the injection moulding process.

In quality control, macro-surface defects such as shrinkage, warpage or sink marks are more detectable than micro-scale defects. For this reason, the form deviation was selected as DOE response. The analysis of the variance (ANOVA) is shown in Table 4.6. It indicates that the holding pressure (P_h) was by far the most significant parameter (p-value of factor $D < 0.05$) affecting the form deviation of the moulded sample. Moreover, the interaction between the melt (T_m) and mould temperature (T_{md}) also have a significant contribution (p-value of factor AB < 0.05). A prediction model (Equation 4.11) for minimizing the form deviation was obtained through the selection of the most significant factors, P_h, T_m and T_{md}. The contribution of these three parameters explains the 60.35% of the form deviation of the surface. On the

contrary, the injection volumetric flow rate was less significant than the other injection parameters (p-value of 0.25) and it marginally affected the form deviation by 3.6%.

Table 4.6 ANOVA results for the 2^4 design of experiments (DOE).

Factor	Contribution (%)	Adjusted SS	F-value	P-value
Tm (A)	1.15	5.21	0.53	0.50
Tmd (B)	4.67	21.18	2.14	0.19
Vfr (C)	3.60	16.34	1.65	0.25
Ph (D)	45.40	206.14	20.80	0.004
AB	14.95	67.86	6.85	0.04
AC	0.05	0.22	0.02	0.89
AD	0.10	0.47	0.05	0.83
BC	1.95	8.84	0.89	0.40
BD	4.75	21.55	2.17	0.19
CD	3.34	15.15	1.53	0.26
Error	13.10	59.46		

$$Sa\,(form) = -5.3 + 0.113 \cdot A + 0.599 \cdot B - 0.0358 \cdot D - 0.002 \cdot AB \qquad (4.11)$$

Equation 4.11 represents the model that allows minimizing form deviation by manipulating a combination of significant variables. Melt and mould temperature have a positive contribution to form deviation as individual terms. A constant cooling time of 40 s was selected. This time was long enough to guarantee the complete solidification of samples inside the mould. Nevertheless, due to the low thermal conductivity of the polypropylene the inner part or core of the samples has higher temperature than the external layers. The subsequent core cooling outside the mould leads to a post-contraction and decrease in sample volume, which may yield slight shape deformations of the samples.

Holding pressure and the interaction between melt and mould temperatures have a negative contribution on form deviation. By increasing these values, the surface deformation can be minimized. As long as the material remains formable, it is forced against the mould wall, limiting the free contraction of the part and leading to an accurate replication of the

mould geometry at higher pressures [17]. The negative effect of the interaction can also be explained in terms of the drop of the polymer viscosity caused by the high temperatures and a concomitant better pressure transmission inside the mould cavity.

Table 4.7 contains the form deviation of two extreme injection conditions, referenced as good and bad replica. The results correspond to the measurement of the central location (Fig. 6) of 10 randomly selected samples from a series of 50 per each injection condition. They are compared with the resin and the predicted results of the model (Equation 4.11). As can be seen, low form deviation is reached at high levels of melt, mould temperature and packing pressure, yielding 84.6% ± 7.7 of replication ratio in regards to the resin geometry. On the contrary, high form deviation occurs when high level of mould temperatures, low holding pressures and low melt temperatures are selected. Under these last injection conditions only a 7.8% ± 0.6 of replication ratio in regards to the resin geometry is obtained. As it can be seen in the contour plots depicted in Figure. 4.6a and Figure. 4.6b, the prediction model provides results that initially seemed to differ from the experimental ones, mainly for the good replica. This is because the model did not take into account the original form deviation of the reference resin geometry (mould and resin), which is about 1.3 μm in Sa. Accordingly, the prediction model is corrected by the original form deviation as shown in (Equation 4.12) and Table 4.7.

Table 4.7 Experimental results of form deviation, comparing both the good and the bad mould replicas in regards to the resin.

Factor	A	B	D	Original model form deviation: Sa (μm)	Corrected model form deviation: Sa (μm)	Experimental form deviation: Sa (μm)
Good replica	270	80	600	0-1	1.3 + (0-1)	1.5 ± 0.2
Bad replica	200	80	400	>13	1.3 + (>13)	16.8 ± 1.2

$$Sa\ (form) = -4.0 + 0.113 \cdot A + 0.599 \cdot B - 0.0358 \cdot D - 0.002 \cdot AB \qquad (4.12)$$
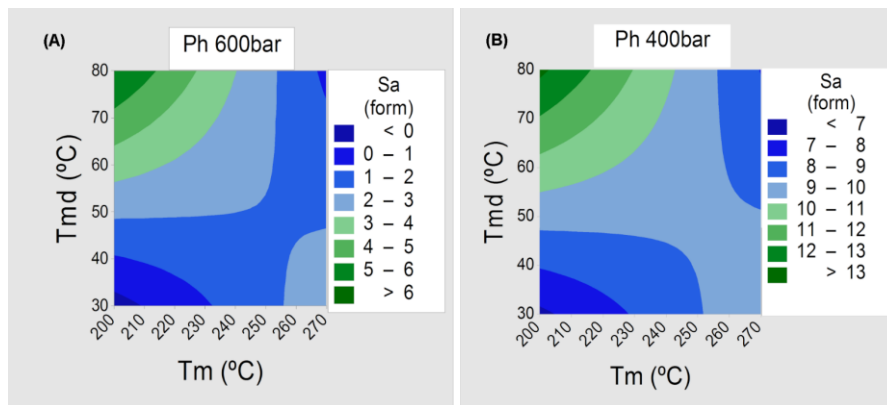
Figure 4.6 Contour plots of the good (A) and bad (B) replicas.

Figure 4.7 shows the pressure inside the mould cavity of the good and the bad replica conditions. The maximum pressure (P_{max}) was significantly higher for the good replica (P_{max}= 480 bar), rather than for the bad one (P_{max}= 208 bar), because the low melt temperature had a poor pressure transmission, yielding a non-proper mould replication. Low melt temperature can lead to incomplete micro-feature filling due to the fast melt solidification at the cavity wall. In addition, a low level of holding pressure causes shape deformations in the moulded samples. This phenomenon can also be explained considering the pressure evolution inside the mould cavity, which is also affected by the cavity surface temperature. At high mould temperatures the rapid polymer solidification is avoided, allowing a better transfer of pressure and an accurate replication of the micro-features [18].
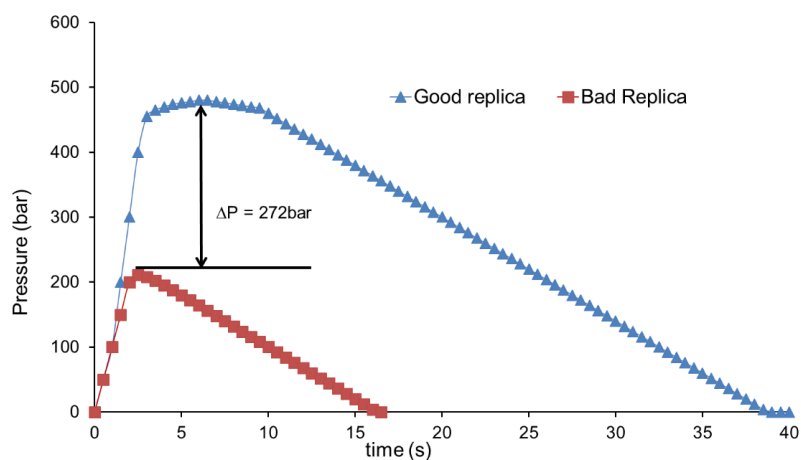
Figure 4.7 Pressure evolution inside the mould cavity.

160

Figure 4.8 shows the comparison of the form deviation of both good (B) and bad replica (C) samples with regard to the resin (A). As can be seen, the form deviation of the good replica was very similar to the one of the resin. On the contrary, the bad replica exhibited a significant amount of form deviation on the surface as compared to the resin.
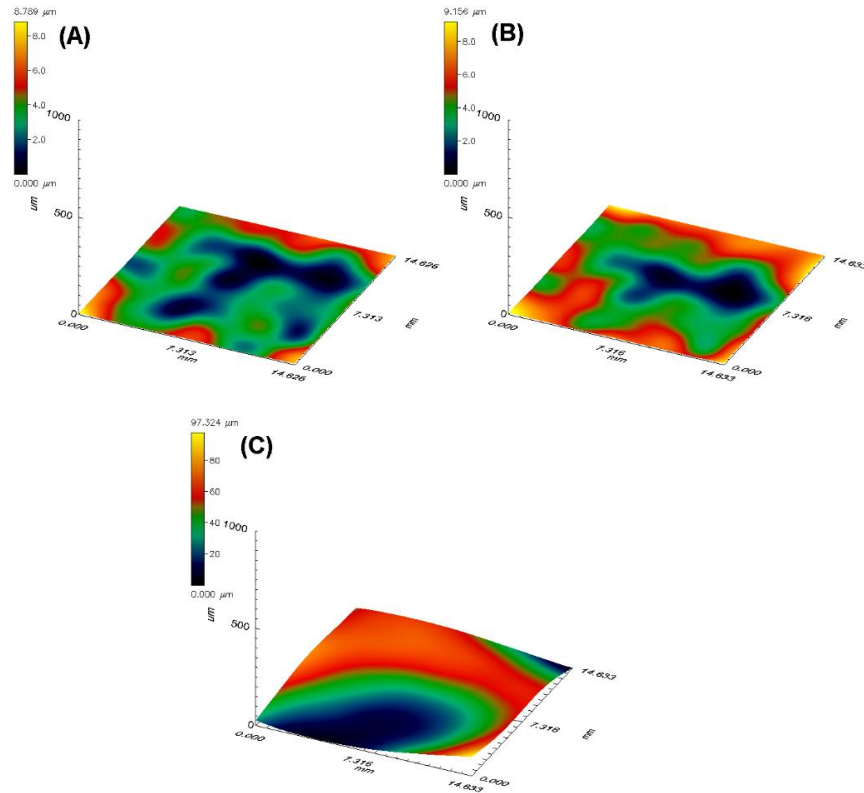
Figure 4.8 3D reconstruction of the form deviation of (A): resin replica, (B): good mould replica sample and (C): bad mould replica sample.

4.2.5. Multi-scale surface analysis at the human eye acuity

A multi-scale surface analysis was carried out comparing the two previously set extreme injection conditions with the cast resin, studying roughness, waviness and form deviation.
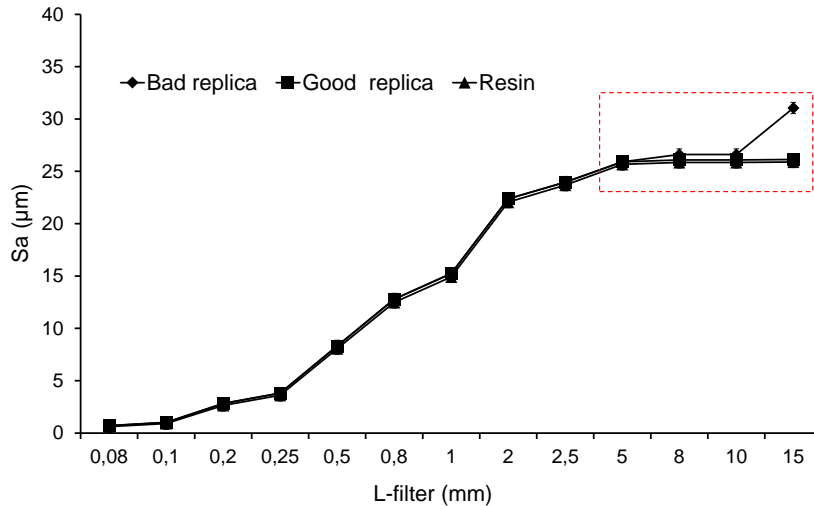
Figure 4.9 Multi-scale analysis of both the good and the bad replica samples in regards the resin. The remarked area shows that the replication difference appears at scales corresponding to the form deviation.

Figure 4.9 shows the comparison between the good and bad replicas regarding their fidelities to the resin. As it can be seen, significant differences were found in the limited-scale from 5 to 15 mm region at which the form deviation can appear. Within this scale range, the Sa of the bad replica increased rapidly, whereas the Sa of resin and good replica remained stable due to their flat geometry. The strong influence of the long wavelength component height can modify the topographic results as can be seen in Table 4.8, which contains the topographies at the limited-scale of S-L 0.04-15. The amplitude parameters are strongly affected by long wavelength components (form deviation). For instance, the bad replica amplitude parameters had an increment up to 17.1%, 22.0% and 38.5% in regards to the resin in Sa, Sq and Sz, respectively, which can lead to a result misinterpretation that the topography with the highest value in amplitude parameters has the highest replication quality. For this reason, alternative surface parameters such as NG, $\overline{GA}$ or $\overline{GV}$ must be taken into account to properly distinguish between good or bad texture replication.

Table 4.8 Topographies results at the limited-scale S-L 0.04-15.

	Sa (µm)	Sq (µm)	Sz (µm)	$S_{mr}(c)$ (c=Sv)(%)	NG (c=Sv)	$(\overline{GA})$ (mm²)	$(\overline{GV})$ x10⁷ (µm³)
Resin	25.7 ± 0.5	30.4 ± 0.4	147.8 ± 66.2	58.3 ± 0.2	172 ± 8	0.7 ± 0.1	1.6 ±10⁶
Good replica	26.1 ± 0.1	30.7 ± 0.1	144.2 ± 1.0	58.3 ± 0.1	169 ± 6	0.7 ± 0.1	1.6 ±10⁶
Bad replica	30.3 ± 0.7	37.2 ± 0.7	212.5 ± 8.8	52.9 ± 0.9	119 ± 38	1.2 ± 0.8	4.5 ±4x10⁷

For the case of good replica, it can be seen that all considered parameter values were almost coincident to the ones of the reference resin, indicating a perfect mould surface replication on the injected polymer specimen. On the contrary, the $S_{mr}(c)$, $\overline{GA}$ and $\overline{GV}$ of the bad replica increased in regards to the resin whereas NG fell drastically (Table 4.7). These differences were caused by an underlying form distortion (waving) in the injected sample, resulting in asymmetry from the mean plane. This asymmetry was the reason for the increment of the total height Sz as well as in Sa and Sq.

Regarding NG, the presence of form deviation resulted in an inadequate discrimination of the number of micro-cavities above the reference height, leading to a clustering of grains as can be seen in the blue area of Figure 4.10. Due to this effect the amount of material above the reference height was much higher in comparison to the resin, thus $S_{mr}(c)$, $\overline{GA}$ and $\overline{GV}$ increased.

On the other hand, no significant differences were found within the limited-scale S-L 0.04-5. This implies that, if the form factor was removed, the CWL sensor detected no differences on the texture topography as is shown in Table 4.9. Hence, no differences could be detected at the roughness and waviness scales using sampling conditions mimicking the human eye. All detected topography differences were only attributable to the form deviation. Table 4.10 contains the macro-morphology results of the three surfaces at the limited-scale S-F 5-15.
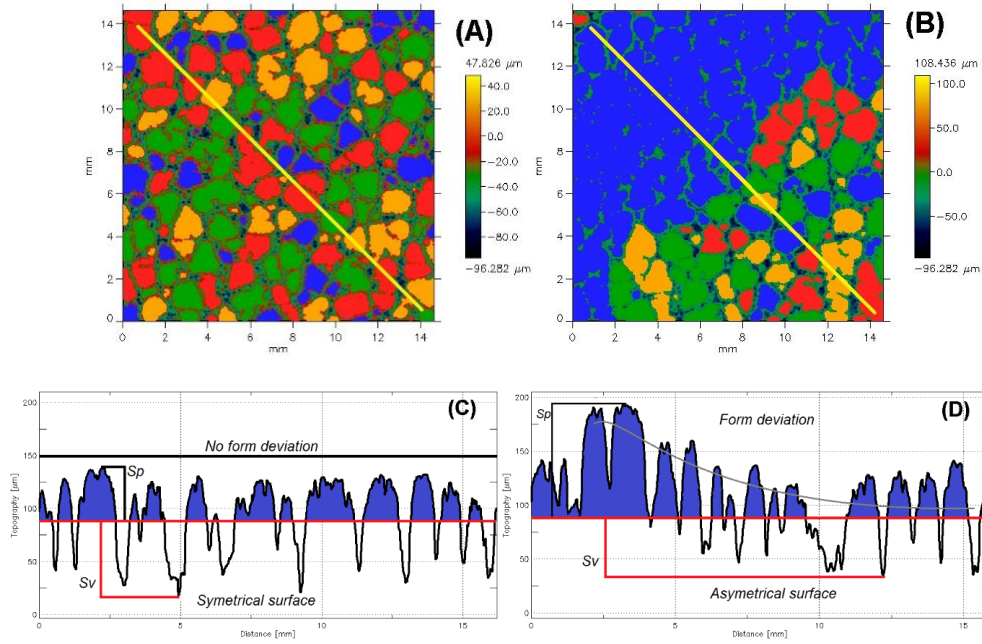
Figure 4.10 Form deviation effect on the functional and complementary parameters. (A) and (B) show the number of micro-cavities replicated on the good and bad replica samples respectively. (C) and (D) are the profiles from (A) and (B) respectively, showing the effect of the surface asymmetry on the grains clustering.

Table 4.9 Topographies results at the limited-scale S-L 0.04-5.

	Sa (µm)	Sq (µm)	Sz (µm)	$S_{mr}(c)$ (c=Sv)(%)	NG (c=Sv)	$(\overline{GA})$ (mm²)	$(\overline{GV})$ x10⁷ (µm³)
Resin	25.5 ± 0.5	30.0 ± 0.6	144.5 ± 7.4	58.2 ± 0.4	176 ± 8	0.7 ± 0.1	1.6 ± 10^5
Good replica	25.9 ± 0.1	30.4 ± 0.2	142.3± 1.0	58.3 ± 1.0	174 ± 7	0.7 ± 0.1	1.6 ± 10^6
Bad replica	25.8 ± 0.2	30.3 ± 0.2	146.9 ± 0.9	58.2 ± 1.0	179 ± 2	0.7 ± 0.1	1.5 ± 10^6

Table 4.10 Topographies results at the limited-scale S-L 5-15.

	S_a (µm)	S_q (µm)	S_z (µm)
Resin	1.3 ± 0.1	1.7 ± 0.1	9.3 ± 1.4
Good replica	1.5 ± 0.2	1.9 ± 0.2	10.5 ± 1.3
Bad replica	16.8 ± 1.2	19.2 ± 1.1	87.3 ± 11.3

As expected, both resin and good replica matched well whereas there was a lack of fit between the bad replica and the resin. It is important to point out that, like in case of the resin, not only the micro-features but also the surface macro-morphologies such as form deviation were well transferred to the injected samples. Figure 4.11 shows the surfaces obtained by the multi-scale analysis. The primary surface of the bad replica at the limited scale S-L 0.04-15 with all surface components included is shown in Figure 4.11a. This image can be considered as the sum of texture and form deviation scales, as is given by the Figure. 4.11b and Figure 4.11c respectively.
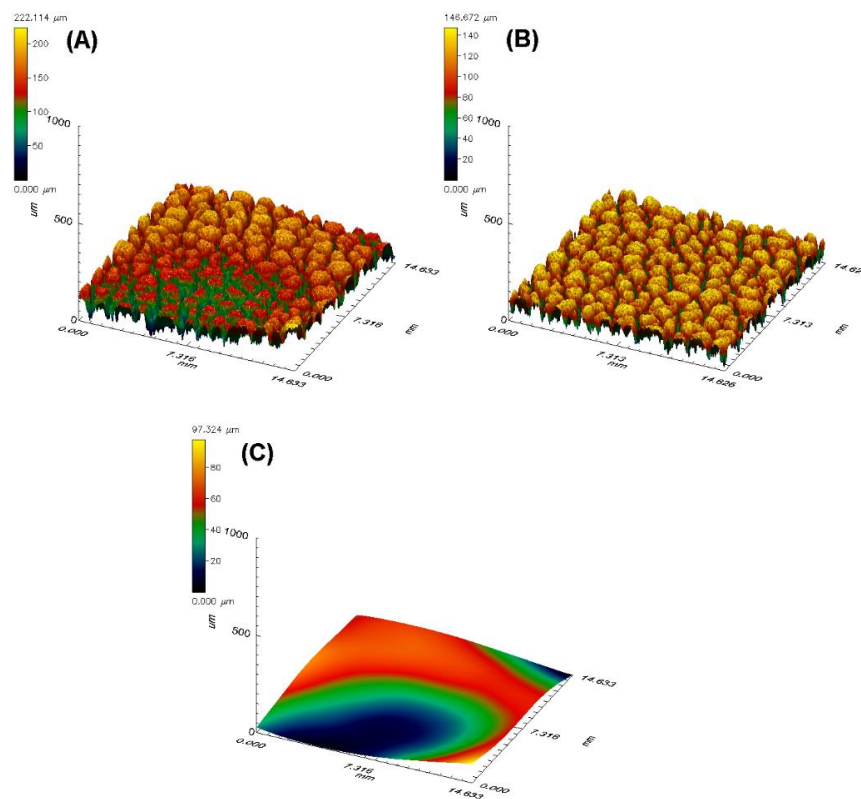
Figure 4.11 Influence of the long wavelength components (form deviation) on the surface assessment. (A): The primary surface can be successfully separate in (B) texture (roughness + waviness) and (C) form deviation.

4.2.6. Multi-scale surface analysis at the micro-scale

The micro features were analysed on the good and bad replica surfaces in regards to the resin [19]. A lateral resolution of 8 µm and the resulting evaluation area of 1.46 x 1.46 mm^2

were selected. The analysis was conducted at three different locations in regards to the injection gate as it is shown in Figure 4.12
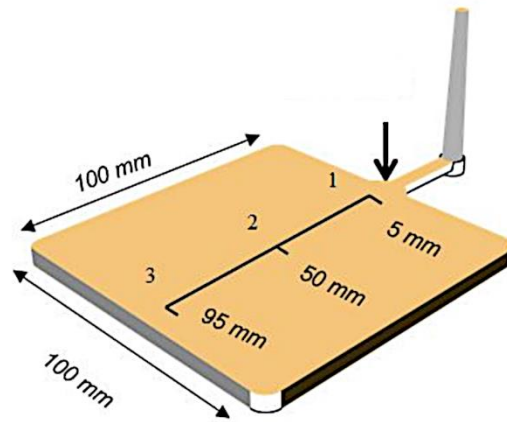
Figure 4.12 Locations where the micro-analysis was performed from the injection gate (arrow).

As shown in Figure 4.13, both the good and the bad replicas exhibited significant differences in the micro-scale level, namely the greatest ones between 25 and 50 µm. On the contrary, variation in Sa tended to decrease as the L-filter increaseed because larger feature sizes were added to the topography calculation. Thus, the larger the lateral components are the most significant weight have on the amplitude surface parameters, as is shown by Figure 4.14. The 3D surface reconstruction of the good and bad replica are depicted in Figure 14a and Figure 4.14c respectively, both at the largest limited scale considered, S-L 0.008-1.46. As can be seen, the Sa value between the two figures was very similar. On the contrary, when the analysis was focused on the short wavelength components (e.g. small feature size), relatively great topography differences up to 30% in Sa were found (Figure 4.14.b and 4.14.d).
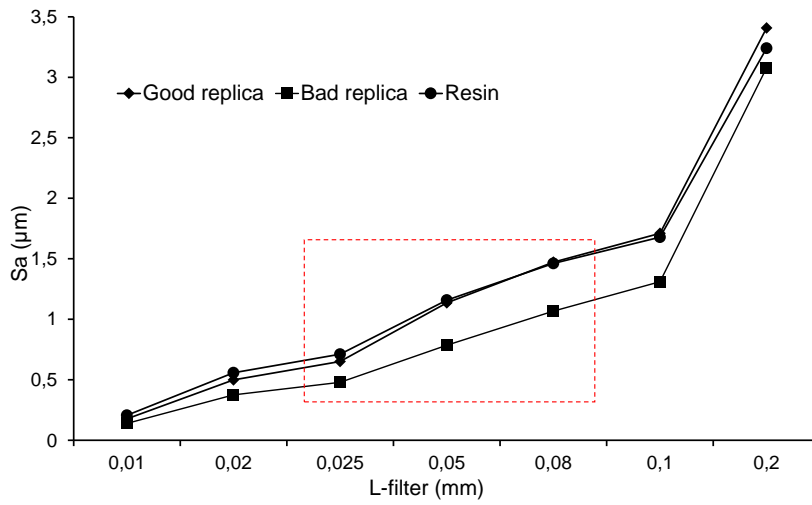
Figure 4.13 Multi-scale analysis at the micro-scale of both the good and the bad replica samples in regards the resin. The remarked area shows the scales at which the largest differences are reached between samples.
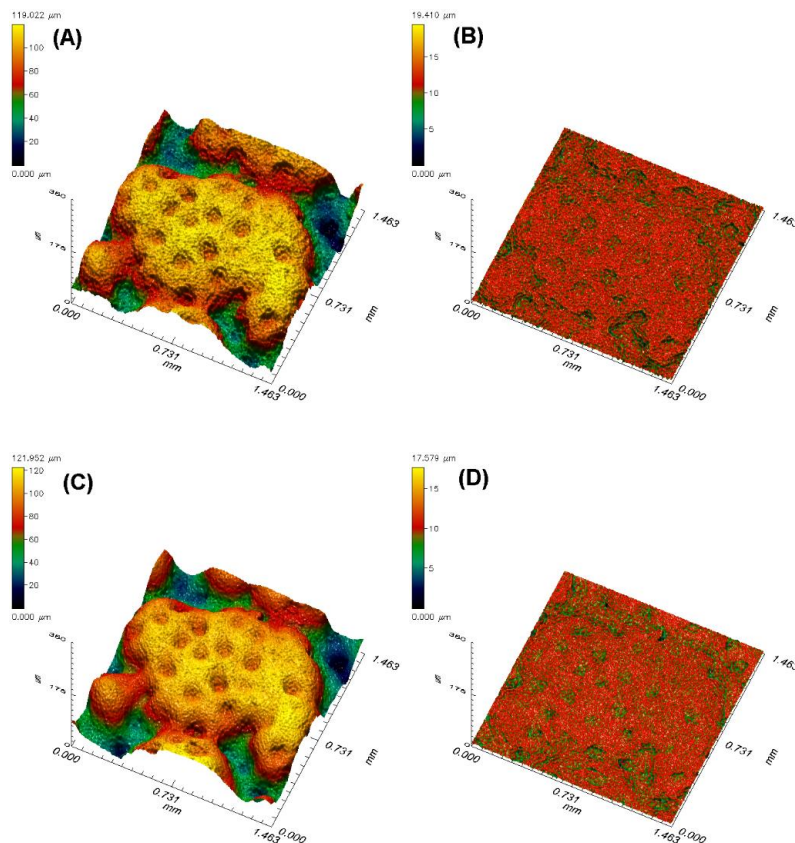
Figure 4.14 3D map reconstruction of the surface micro-analysis at the location 2. (A) and (C) are the full scale analysis of the good and the bad replicas respectively. (B) and (D) are the scale limited surface analysis, L-filter 50µm, of both the good and the bad replicas respectively, achieving a 30% of difference in Sa.

Figure 4.15 shows the power spectral density function (PSD) of the three surfaces. The largest differences in the sine wave amplitude were found in the spatial frequency within the range of 35 to 50 mm^{-1}. This spatial frequency corresponded to features of approximately 30 to 20 µm in x- and y-axis. This was close to the results of the multi-scale analysis where the greatest differences corresponded to features ranging from 25 to 50 µm.
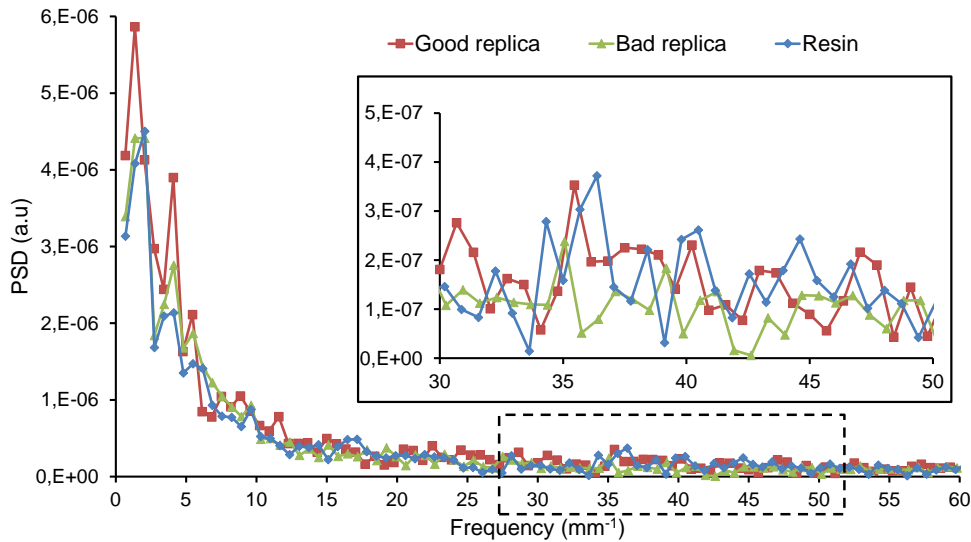
Figure 4.15 Power Spectral Density function (PSD) of the three surfaces. The enlargement corresponds to the frequencies at which the main differences were found.

Figure 4.16 shows the 2D-profiles extracted from the 3D reconstruction of the grain located at position 2 for the good and bad replicas. Although in both cases the absolute height (Sa) was around 80 µm, the amplitude of the micro-roughness located on top of the good profile replica (Figure 4.16a) was higher than the bad one (Figure 4.16b), indicating its better replication quality. Moreover, the larger the Sdq value, the shorter the micro-features spacing was, suggesting better replication ratio as can be seen in Table 4.10. Therefore, assessing the surface at the right scale is of great importance for an accurate determination of topographic differences. Hence, the multi-scale analysis is a powerful tool which allows analysing the topographies by focusing only on the desired feature size, but without losing the perspective of the total surface.
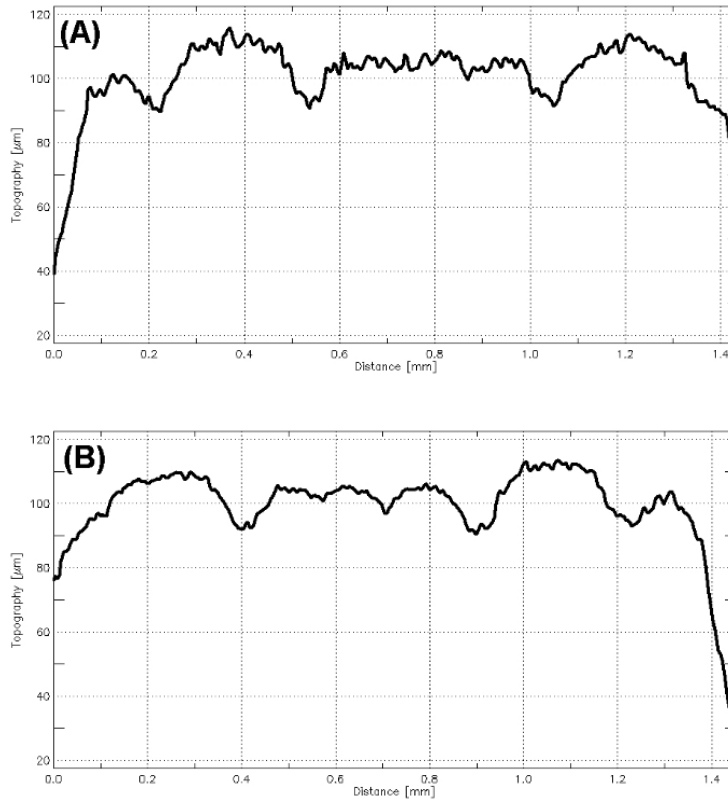
Figure 4.16 Profiles extracted from the micro-scale analysis of the good (A) and bad (B) replicas.

Table 4.11 collects the amount of material replicated at the micro-scale. The analysis of $S_{mr}(c)$, GA, GV and Sdq was carried out on exactly the same grain of the three samples (resin, good and bad replica) located at the positions shown in Figure 4.12. The good replica matched well with the resin in the three studied locations. On the contrary, a drop in $S_{mr}(c)$, GA and GV was found in the bad replica. This confirms the greater replication fidelity obtained with the good replica injection conditions. Due to the random nature of the texture, all grains were different in shape and size and therefore analysing the influence of the location on the replication fidelity was not possible. To solve this problem, the amount of material replicated per unit of grain area was normalized, taking as reference the GA of the resin ($S_{mr}(c)/GA_{resin}$). The effect of the measuring location on the results was found negligible. The quantity of material available for replicating at each micro-cavity was almost the same regardless the location ($\approx 46\%$ material/mm^2). The decrement of the replication ratio at the micro-scale for the different injection conditions was found to be 98% and 95% for the good and bad replica

respectively. Therefore, the differences between both cases can be directly attributed to the amount of micro-roughness on the topographies, where the good replica had a 30% more roughness in Sa than the bad one at the limited scale of SL-0.008-0.05.

Table 4.11 Grain area and volume in regards to the peak portion replicated.

	Location 1			Location 2			Location 3		
	Resin	Good replica	Bad replica	Resin	Good replica	Bad replica	Resin	Good replica	Bad replica
$S_{mr}(c)$ (%)	59.7±0.1	58.9±1.8	56.9±1.7	62.4±0.1	60.9±1.2	59.1±1.9	66.7 ± 10^{-2}	65.8± 1.4	65.4±1.2
GA (mm^2)	1.3±0.1	1.3±0.1	1.2±0.1	1.3±0.1	1.3±0.1	1.3±0.1	1.4±0.1	1.4±0.1	1.4±0.1
$S_{mr}(c)$/GA_{resin}	46.6±0.1	45.9±1.7	44.5±1.6	46.9±0.1	45.8±1.2	44.5±1.7	46.7±0.1	46.0±1.3	45.8±1.2
$GV\times10^7$ (μm^3)	2.9 ± 10^4	2.9 ± 10^5	2.8 ± 10^5	2.3 ± 10^4	2.2 ± 10^5	2.1 ± 10^5	2.4 ± 10^4	2.4 ± 10^5	2.0 ± 10^5
Sdq (rad)	0.6±0.1	0.6±0.1	0.6±0.1	0.5±0.1	0.5±0.1	0.4±0.1	0.5±0.1	0.5±0.1	0.5±0.1

The electronic micrographs of the good and the bad replicas are depicted in Figure 4.17a and Figure 4.17b, respectively. As can be seen, the good replica contained a much higher amount of micro-features on its surface in comparison to the bad replica. This is in accordance with the analysis done at the limited scale S-L 0.008-0.05 where the most significant differences between samples were found at the feature size of approximately 20 to 50 µm. It is also supported by the results obtained by the spatial (PSD), the hybrid (Sdq) and the alternative parameters (Smr (c), GA and GV).
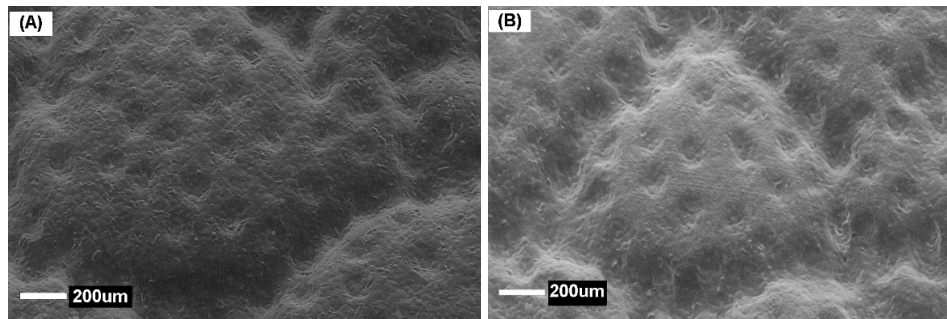
Figure 4.17 Electronic micrograph (SEM) of the good (A) and bad (B) texture replicas. The replication of the micro-, or even sub-micro features, is more accurate on the good replica than in the bad replica surface

4.3. Conclusions

The injection process parameters had a great influence on the mould texture replication, being the holding pressure the most important one either at macro- or micro-scale.

The multi-scale surface analysis methodology is a powerful tool for analysing the surface at the desired scale, avoiding result misinterpretations if the entire frequency domain is analysed. It allowed determining the primary causes of surface defects in terms of roughness, waviness and form.

The surface analysis using sampling conditions (lateral resolution of 40 µm) mimicking the human eye acuity at a distance of 200 mm allowed detecting only differences within the waviness or form deviation space range. This was in agreement with the multi-scale surface analysis at the micro-scale where the largest difference in the replication fidelity between injected samples was found at a lateral feature sizing of approximately 25 to 50 µm.

It was demonstrated that alternative parameters such as, GA, GV, NG and $S_{mr}(c)$ could be used as suitable complementary parameters for surface analysis. They provided information about the desired surface portion (e.g peaks), resulting in another way for investigating the replication ratio providing quantitative values at either the macro or micro-scale.

4.4. References

[1]   P. Gamonal-Repiso, M. Sánchez-Soto, S. Santos-Pinto, and M. L. Maspoch, "Improvement of the replication quality of randomly micro-textured injection-moulding components using a multi-scale surface analysis", *J. Manuf. Process.*, vol. 42, no. April, pp. 67–81, 2019, doi: 10.1016/j.jmapro.2019.04.010.

[2]   H. Zahouani, R. Vargiolu, P. Kapsa, J. L. Loubet, and T. G. Mathia, "Effect of lateral resolution on topographical images and three-dimensional functional parameters", *Wear*, vol. 219, no. 1, pp. 114–123, 1998, doi: 10.1016/S0043-1648(98)00235-X.

[3]   Stout K, Sullivan P, Dong W, Mainsah E, Luo N, Mathia T, et al. "The development of methods for the characterisation of roughness in three dimensions". EUR(Luxembourg) 1993:358

[4]   A. Calvimontes, K. Grundke, A. Müller, and M. Stamm, "Advances for the topographic characterisation of SMC materials", *Materials (Basel).*, vol. 2, no. 3, pp. 1084–1103, 2009, doi: 10.3390/ma2031084.

[5]   F. Baruffi, P. Parenti, F. Cacciatore, M. Annoni, and G. Tosello, "On the application of replica molding technology for the indirect measurement of surface and geometry of micromilled components", *Micromachines*, vol. 8, no. 6, 2017, doi: 10.3390/mi8060195.

[6]   J. Pina-estany, C. Colominas, J. Fraxedas, J. Llobet, F. Perez-murano, and J. M. Puigoriol-forcada, "A statistical analysis of nanocavities replication applied to injection moulding", *Int. Commun. Heat Mass Transf.*, vol. 81, pp. 131–140, 2017, doi: 10.1016/j.icheatmasstransfer.2016.11.003.

[7]   M. Sahli, C. Millot, C. Roques-Carmes, C. Khan Malek, T. Barriere, and J. C. Gelin, "Quality assessment of polymer replication by hot embossing and micro-injection moulding processes using scanning mechanical microscopy", *J. Mater. Process. Technol.*, vol. 209, no. 18–19, pp. 5851–5861, 2009, doi: 10.1016/j.jmatprotec.2009.06.011.

[8]   M. Altan, Reducing shrinkage in injection moldings via the Taguchi, "ANOVA and neural network methods", *Mater. Des.*, vol. 31, no. 1, pp. 599–604, 2010, doi: 10.1016/j.matdes.2009.06.049.

[9]   C. C. Huang, M.C. & Tai, "The effective factors in the warpage problem of an injection-mold part with a shell", *J. Mater. Process. Technol.*, vol. 110, pp. 1–9, 2001.

[10]   W.-C. Chen, M.-H. Nguyen, W.-H. Chiu, T.-N. Chen, and P.-H. Tai, "Optimization of the plastic injection molding process using the Taguchi method", RSM, and hybrid GA-PSO, *Int. J. Adv. Manuf. Technol.*, vol. 83, no. 9–12, pp. 1873–1886, 2016, doi: 10.1007/s00170-015-7683-0.

[11]   S. K. Lal and H. Vasudevan, "Optimization of Injection Moulding Process Parameters in the Moulding of Low Density Polyethylene (LDPE)", *Int. J. Eng. Res. Dev.*, vol. 7, no. 5, pp. 35–39, 2013.

[12]   C. A. Griffiths, S. S. Dimov, E. B. Brousseau, and R. T. Hoyle, "The effects of tool surface quality in micro-injection moulding", *J. Mater. Process. Technol.*, vol. 189, no. 1–3, pp. 418–427, 2007, doi: 10.1016/j.jmatprotec.2007.02.022.

[13]   D. Masato, M. Sorgato, and G. Lucchetta, "Analysis of the influence of part thickness on the replication of micro-structured surfaces by injection molding", *Mater. Des.*, vol. 95, pp. 219–224, 2016, doi: 10.1016/j.matdes.2016.01.115.

[14]   G. Lucchetta and M. Fiorotto, "Influence of rapid mould temperature variation on the appearance of injection-moulded parts", *Stroj. Vestnik/Journal Mech. Eng.*, vol. 59, pp. 683–688, 2013, doi: 10.5545/sv-jme.2013.1001.

[15]   G. Lucchetta, M. Sorgato, S. Carmignato, and E. Savio, "Investigating the technological limits of micro-injection molding in replicating high aspect ratio micro-structured surfaces", *CIRP Ann. - Manuf. Technol.*, vol. 63, no. 1, pp. 521–524, 2014, doi: 10.1016/j.cirp.2014.03.049.

[16]   R. Surace, V. Bellantone, G. Trotta, and I. Fassi, "Replicating capability investigation of micro features in injection moulding process", *J. Manuf. Process.*, vol. 28, pp. 351–361, 2017, doi: 10.1016/j.jmapro.2017.07.004.

[17]   V. Speranza, S. Liparoti, M. Calaon, G. Tosello, R. Pantani, and G. Titomanlio, "Replication of micro and nano-features on iPP by injection molding with fast cavity surface temperature evolution", *Mater. Des.*, vol. 133, pp. 559–569, 2017, doi: 10.1016/j.matdes.2017.08.016.

[18]   S. Liparoti, A. Sorrentino, and G. Titomanlio, "Fast cavity surface temperature evolution in injection molding: Control of cooling stage and final morphology analysis", *RSC Adv.*, vol. 6, no. 101, pp. 99274–99281, 2016, doi: 10.1039/c6ra22968a.

[19]   H. N. Hansen, R. J. Hocken, and G. Tosello, "Replication of micro and nano surface geometries", *CIRP Ann. - Manuf. Technol.*, vol. 60, no. 2, pp. 695–714, 2011, doi: 10.1016/j.cirp.2011.05.008.

Chapter 5:   Measurement of textured surfaces appearance

Surface appearance

3D Techniques
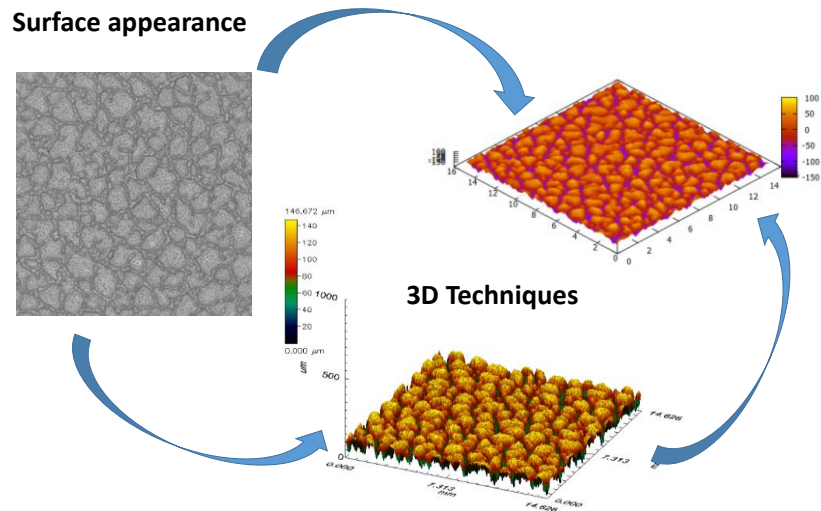
The influence of topographical features on the surface appearance of textured components has been studied in this chapter. It has been demonstrated that appearance attributes such as the reflectivity contrast between peaks and valleys can be related with topographical features such as the new introduced parameters texture slope (TS) and texture aperture angle (TAA).

Publication derived from this work [1]
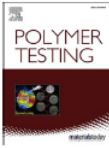
Influence of topographical features on the surface appearance measurement of injection moulded components

P. Gamonal-Repiso [a,b], T. Abt [a], M. Sánchez-Soto [a,*], S. Santos-Pinto [b], M. Ll. Maspoch [a]

[a] *Centre Català Del Plàstic, Universidad Politècnica de Catalunya Barcelona Tech (UPC-EEBE), C/Colom 114, 08222, Terrassa, Spain*
[b] *Departamento de Tecnología de Materiales de SEAT S.A, Autovía A-2, Km 585. Apartado de Correos 91, 08760, Martorell, Spain*

5.1. Experimental section

5.1.1. Material

In all cases, the material used was a black polypropylene copolymer filled with 5% talc, HC TKC 2007N from Basell S.L (Tarragona, Spain).

5.1.2. Samples preparation

Squared samples with dimensions 100 x 100 x 3 mm^3 (length x width x thickness) were obtained by injection moulding.

Four different leather texture types were studied in this chapter.

The first texture was a leather type with a random design. This was the result of the chemical engraving process.

Two different mould treatments were applied on the previously textured mould cavity. The first treatment consisted in the addition of micro-features on top of the surface. The second treatment consisted in uniformly applying a mixture of polytetrafluoroethylene and graphite on the engraved mould cavity.

Finally, for comparison, a painted surface was created as follows. A black water-based paint from Mankiewicz Iberica S.L (Barcelona, Spain) was applied on top of injection moulded samples with the leather texture on top. This procedure was performed manually in a standardized painting room with controlled temperature of 23 ± 0.5 ℃

The different leather texture types were encoded as follows:

Table 5.1 Code of the leather texture types

Leather texture type	Code
Original leather texture	Texture A
Leather texture + micro features	Texture B
Leather texture + coating	Texture C
Leather texture + paint	Texture D

5.1.3. Surface characterization

The surface topography was analysed using the chromatic confocal microscope, equipped with a chromatic white light sensor (CWL) having 30 nm and 6 µm of vertical and lateral resolution, respectively.

The surface was characterized at the macro-scale and at the micro-scale range. In the former case, the area under analysis was 14.65 x 14.65 mm2 with a lateral resolution of 40 µm. The analysis at the micro scale was conducted on a 3.65 x 3.65 mm2 area and using 10 µm of lateral resolution.

5.1.4. Surface parameters

For accurately characterizing the different topographies, parameters from the amplitude, functional and spatial families were considered. From the amplitude parameter family, the arithmetical mean height (Sa) and the root mean square height (Sq) were selected. They are defined by Equation 5.1 and 5.2, respectively. Both represent the overall surface roughness but are insensitive in differentiating peaks and valleys.

$$Sa = \frac{1}{A} \iint_A |z(x,y)| dx dy \qquad\qquad (5.1)$$

$$Sq = \sqrt{\frac{1}{A} \iint_A |z^2(x,y)| dx dy} \qquad (5.2)$$

From the functional parameter family, the core height (Sk), the reduced peak height (Spk) and the reduced dale height (Svk) were taken into account. They were obtained from the areal material ratio curve also known as the Abbot Firestone curve, which is established by evaluating the material ratio at various levels from the highest peak to the lowest valley. Sk represents the core roughness or the averaged peak to valley height. The Spk represents the height above Sk, hence it can be considered as representative of aberrant high peaks. Finally, Svk is the height under Sk, representing the aberrant deep valleys. Figure 5.1 depicts the different functional parameters employed.
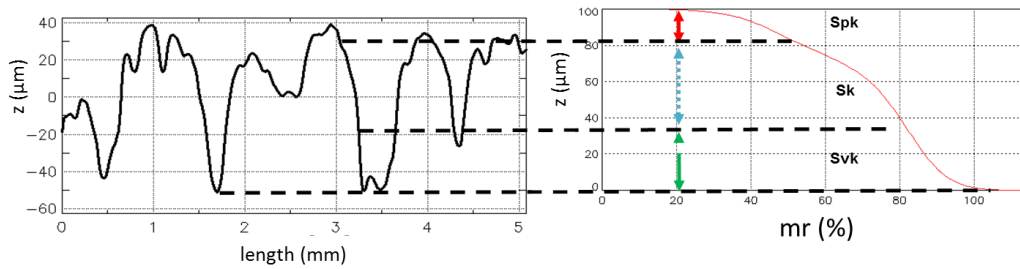
Figure 5.1 Scheme of the distribution of the different functional parameters, reduced peak height (Spk), core roughness (Sk) and reduced dale height (Svk).

The autocorrelation function (ACF), the texture aspect ratio (Str) and the autocorrelation length (Sal) were selected from the spatial parameters family. They were used to quantify the degree of isotropy of the textures. The ACF is described by the following equation (Equation 5.3) [2]

$$ACF\left(\tau_x, \tau_y\right) = \frac{\iint_A Z(x,y)Z(x-\tau_x, y-\tau_y) dx dy}{\iint_A Z^2(x,y) dx dy} \qquad (5.3)$$

Where Z(x,y) is the measured surface, $Z\left(x - \tau_x, y - \tau_y\right)$ is a duplicate surface with a lateral displacement $\left(\tau_x, \tau_y\right)$ and Z^2(x,y) is the variance which is employed as normalising

factor. Therefore, the ACF is a measure of how similar the texture is at a given distance from the original location. This function allows obtaining an image with a central peak from which the degree of isotropy of the surface can be quantified. This central peak is the result of normalizing the surface height distribution with the variance ($Z^2(x,y)$). The texture aspect ratio (Str) is used as indicator of the surface isotropy. Spatial isotropic textures will have a Str value close to 1 while anisotropic spatial textures will have a Str close to 0. Finally, the autocorrelation length (Sal) is defined as the minimum distance over the surface so that the new location will have the minimal correlation with the original one.

Figure 5.2 shows a graphical representation of the procedure to calculate Str and Sal parameters. The 3D reconstruction of texture A corresponds to the Figure 5.2a. The resultant image after applying the ACF with the peak in the centre is shown in Figure 5.2b. Finally, Figure 5.2c shows the measurement of the maximum and minimum radii of the peak base. In the latter figure, the original peak has been removed from the surface using a threshold that assures that the central lobe edges are well defined. Thus, the Str is defined as the ratio between the length of fastest decay of ACF in any direction (R_{min}) and the length of slowest decay of ACF in any direction (R_{max}) (Equation 5.4). The Sal corresponds to the minimum radii (R_{min}).

$$Str = \frac{R_{min}}{R_{max}} \tag{5.4}$$

Where R_{min} is the minimum radii and the R_{max} is the maximum radii of the resultant base lobe.

A surface with the same characteristics in every direction will present an approximately circular base lobe, resulting in almost the same minimum and maximum radii. On the contrary, in surfaces with strong privileged orientation, the central lobe will present a great difference between the maximum and minimum radii, obtaining an elliptic form of the base lobe.
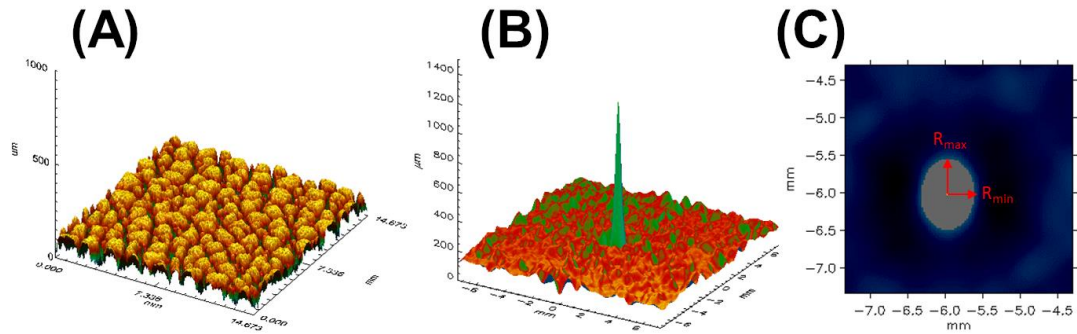
Figure 5.2 Methodology to determine the isotropy of the surface. (a) Reconstruction of the original surface in 3D; (b) resultant surface after applying the autocorrelation function (ACF); (c) maximum and minimum radii measurement of the lobe

The relationship between the surface topography and its reflectance properties was established through the introduction of four novel parameters. The absolute functional height (AFH), the functional height distribution (FHD), the texture slope (TS) and the texture aperture angle (TAA). The AFH is defined as the sum of the three above described functional parameters (Spk + Sk + Svk). This parameter allows determining the averaged texture depth within the sampling area. The FHD allows determining the relative amount of each functional parameter, providing information about which functional parameter prevail on the overall topography, having textures where peaks predominate over valleys or vice versa. Figure 5.3 depicts the influence of each functional parameter on the surface reflectivity properties. Surfaces with deep valleys (Svk) yield high reflectivity contrast with peaks (light area) due to the reflected light coming from valleys is blocked, creating a dark area. On the contrary, surfaces where the core roughness (Sk) prevails over all functional parameters, lower reflectivity contrast is expected between valleys and peaks. This is because the blocked light coming from valleys is reduced, leading to higher light area as compared to the dark one.
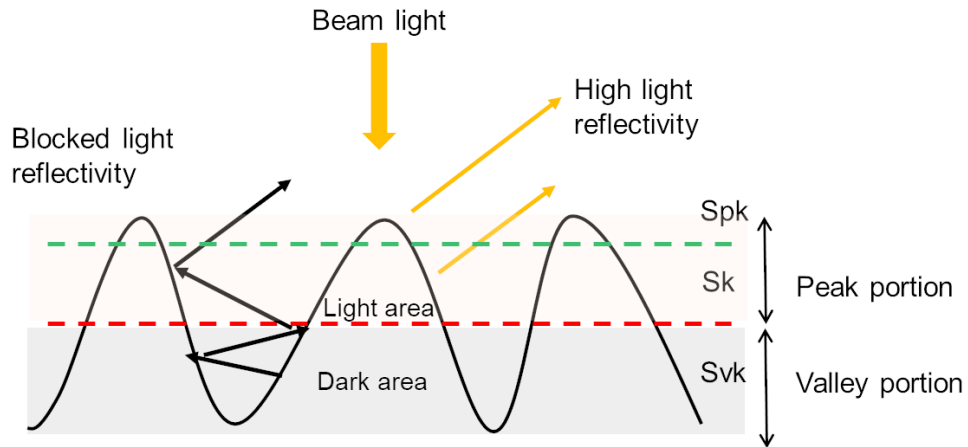
Figure 5.3 Surface reflectivity performance as a function of the functional height parameters.

The TS is described as the angle formed between the grain surface and its horizontal (underlying surface) and the TAA is the angle between two consecutive grain surfaces. Both TS and TAA were measured as shown in Figure 5.4. These two parameters helped to understand the importance of valleys on the light reflectivity performance of a given texture.

Finally, alternative surface parameters such as the number of cells (NG) within the sampling area and the average hill area ($\overline{GA}$) were considered as reference for adequately setting the TAM prototype instrument to each texture finish [3].
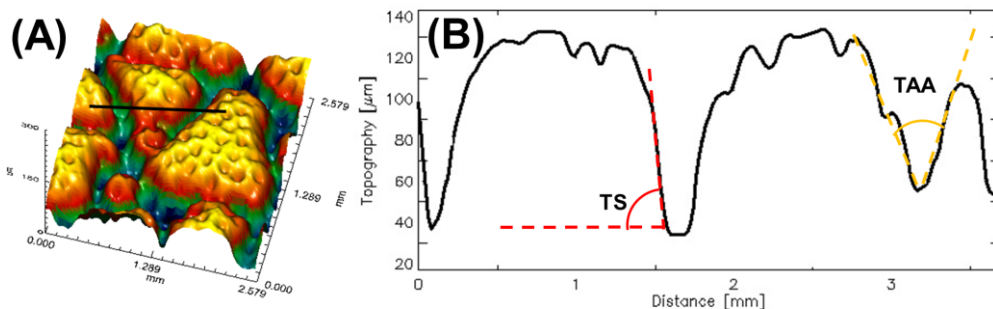
Figure 5.4 Texture slope (TS) and texture aperture angle (TAA) measurement methodology. The TS is the slope of the cell wall and the TAA is the angle created by two neighbor cells. Both are extracted from the 3D reconstruction (a).

181

5.1.5. Surface appearance measurement

The surface appearance was measured using a total appearance measurement instrument (TAM) from BYK-Gardner GmbH (Geretsried, Germany). This device was a prototype that enables analysing at the same time surface topography and reflectivity by means of the photometric stereo technology (PS) [4].

The surface gloss (G*) was measured using a spectro-Guide 45/0 Gloss-spectrophotometer from BYK-Gardner GmbH (Geretsried, Germany). It was equipped with a 45/0º measuring geometry and D65/10º as illuminant. The gloss measurements were acquired at 60º and relative to a highly polished black glass standard with 100 gloss units (GU).

5.1.6. Uncertainty contribution of the TAM instrument

In the TAM case, Texture A was employed as calibrated item. The number of cells detected within the evaluated area, the mean reflectivity, the reflectivity contrast and the mean hill size were selected as representative parameters for estimating TAM uncertainty (U_{TAM}) according to Equation 5.5.

$$U_{TAM} = \sqrt{U_{cal}^2 + U_p^2 + U_{res,TAM}^2} \qquad (5.5)$$

Where U_{cal} is the standard deviation of 10 measurements performed on different locations of the sample. U_p is the standard deviation of 10 repeated measurements performed at the same location and U_{resTAM} is the resolution uncertainty related to the declared 60 µm optical resolution of the TAM instrument, which it is equal to 0.03. All the measurements were performed in a temperature-controlled room at 23 ± 1 ºC.

5.2. Results and discussion

5.2.1. TAM uncertainty contribution

The different sources of uncertainty are collected in Table 5.2. It is noted that the highest source of uncertainty was due to the deviation of the Texture A itself (U_{cal}). This was because its random nature mimicking leather did not follow any regular pattern or sequence. In the case of the measuring deviation (U_p) the obtained values were almost zero. Therefore, it was concluded that the measurements of the TAM instrument were reliable and repeatable.

Table 5.2 Uncertainty contribution to the TAM prototype instrument.

Uncertainty contribution	Nº cells	Mean reflectivity (a. u)	Reflectivity contrast	Mean hill size (mm^2)
U_{cal}	166 ± 11	186 ± 7	0.24 ± 0.01	0.72 ± 0.04
U_p	160 ± 0.4	193 ± 0.4	0.23 ± 0.03	0.74 ± 0.01
U_{TAM}	11.0	7.0	0.04	0.05

5.2.2. TAM settings as a function of the texture type

Once the uncertainty contribution of the prototype instrument was established, the next step before characterizing any surface was to perform a comparison with a known technique. The chromatic confocal microscope was selected as a reliable and suitable method for characterizing surface topographies. The measurements obtained with the chromatic confocal microscope were used for reaching the adequate settings of the TAM prototype for each surface finish.

The surfaces under study were first measured with the CWL sensor under the previously described measuring conditions at five different locations (Figure 5.5). Table 5.3 collects the results of the number of cells (NG), the mean hill area ($\overline{GA}$), the absolute functional height (AFH) and its relative portion of deep valleys (Svk) obtained using the CWL sensor.

Table 5.3 Topographic results of each texture finish measured with the CWL sensor and took as reference for TAM setting.

	NG	$\overline{GA}$ (mm^2)	AFH (µm)	Svk (%)
Texture A	174 ± 6	0.72 ± 0.03	107 ± 2	43.4 ± 1.7
Texture B	258 ± 8	0.46 ± 0.01	90 ± 2	26.7 ± 1.2
Texture C	227 ± 5	0.51 ± 0.01	87 ± 1	26.0 ± 0.8
Texture D	145 ± 13	0.81 ± 0.08	72 ± 2	25.9 ± 2.6

Figure 5.5 Measurement locations.

The TAM prototype had different filters for adequately measuring the topography of a surface and its reflectivity properties. These filters are the offset, plateau offset, the reflectivity contrast threshold (RCT) and the hill size threshold (HST). The filter and plateau offset control the smoothing of the input data and the truncation of the crest of peaks, respectively. They directly affect the watershed algorithm, which detects the number of cells within the evaluated area as shown in Figure 5.6. Figure 5.6a corresponds to the obtained topography with a filter offset value of 5, resulting in 47 detected cells. On the contrary, Figure 5.6b shows the same evaluated area setting the filter offset to 50, which resulted in 302 cells. Therefore, the number

of cells (NG) detected by the CWL sensor was used as reference to adequately set the filter offset and avoiding over- or under-segmentation.
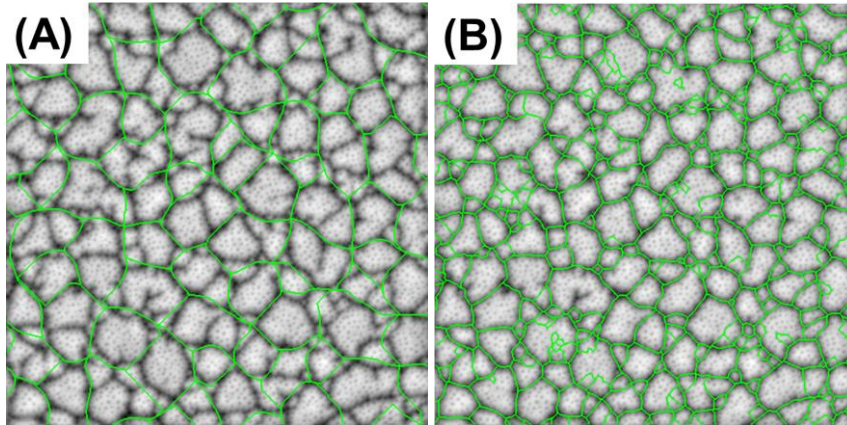
Figure 5.6 Effect of the filter offset on the cells segmentation. (a) Under segmentation, filter offset = 5, detecting 47 cells. (b) Over segmentation, filter offset = 50, detecting 302 cells.

The RCT and the HST control the segmentation of hills and valleys, measuring the reflectivity contrast and the hill size, respectively. The filter ranges from -1 to 1, where – 1 means that the lowest point of the topography is used as threshold, hence 100% of data is selected as peak. The value +1 leads to the reverse output. It should be pointed out that the RCT filter takes into account relative values to differentiate peaks from valley portions throughout the entire topography. For this reason, the relative amount of deep valleys (% Svk) was used as reference to set this filter. Finally, the $\overline{GA}$ measured was used to properly set the HST filter of the TAM prototype instrument. As said before, all these measurements were first obtained with the CWL sensor to calibrate the TAM prototype.

The obtained setting and results of TAM prototype instrument are shown in Table 5.4. It should be remarked that the texture types with higher number of cells (Texture B and Texture C) exhibited as well higher filter offset values. This means that, for the same evaluated area (15 mm^2), the higher the number of detected cells the finer is the topographic mesh obtained by the watershed algorithm. In addition, it matches well with the fact that the resultant $\overline{GA}$ of

both Texture B and Texture C were smaller having 0.46 and 0.51 mm², respectively. As shown in Table 2, texture A was the one showing a different RCT filter value (-0.1) in comparison to the rest of analysed surfaces (-0.5). This was because Texture A had the highest relative amount of deep valleys in its topography, accounting for 43% of the total, whereas for the other textures it was 26% in average. On the other hand, the HST filter was set through trial-error approach using the CWL data as reference (Table 5.3).

Table 5.4 Settings and topographical results obtained with TAM prototype.

	TAM's setting			TAM's results	
	Filter offset	RCT	HST	NG	$\overline{GA}$ (mm²)
Texture A	20	-0.1	-0.2	164±8	073±0.03
Texture B	30	-0.5	-0.1	243±9	0.44±0.02
Texture C	25	-0.5	-0.2	217±5	0.53±0.02
Texture D	20	-0.5	-0.2	149±6	0.77±0.03

As shown in Table 5.3 and Table 5.4, the obtained results of NG and $\overline{GA}$ by both CWL sensor and TAM instrument were within the deviation range. Hence, it can be assumed that the settings of TAM were adequately selected for each of the texture finish types.

The proper setting of the TAM instrument is of prime importance because this novel equipment allows to quantify the reflected light coming from both peaks and valleys, resulting in a contrast based on the Michelson equation (Equation 5.6) [7], [8].

$$C = \frac{R_{peak} - R_{valley}}{R_{peak} + R_{valley}}$$
(5.6)

Where *C* is the reflectivity contrast, R_{peak} is the reflectivity on the peaks portion and R_{valley} is the reflectivity in the valleys portion. The contrast sensitivity criteria was established

at 2% [8]. When the reflectivity contrast is larger than this value it is expected that peaks can be distinguished from the valleys background. In the present case, deep valleys (Svk) were selected as surface background, since this surface portion was less illuminated. Therefore, the appearance of the surface can be measured in terms of the reflectivity contrast between peaks and valleys. It can be related with objective data such as %Svk, NG or AFH, coming from the measurement of the surface topography.

5.2.3. Characterization of the topography

5.2.3.1. Measurement of the surface isotropy

The four engraved textured surfaces under study were analysed for determining its degree of isotropy. It was quantified at the S-L 0.04-5 scale with 40 µm of lateral resolution. Table 5.5 collects the results of the R_{min}/Sal, R_{max} and Str. As it can be seen, the degree of isotropy is higher than 0.70, resulting in surfaces without any preferential orientations. Therefore, it can be said that the textures under study are random surfaces, since they do not follow any defined pattern or sequence. In addition, the R_{min} and Sal value provide an indication of the spectral content of the surface. A high Sal value implies high amount of long wavelength components. Therefore, it can be expected a higher level of micro roughness in Textures A, B and C in comparison to Texture D.

Table 5.5 Isotropy results of the four textures under study at the macro-scale.

S-L 0.04-5	R_{min} / Sal (mm)	R_{max} (mm)	Str
Texture A	0.36	0.50	0.72
Texture B	0.36	0.44	0.82
Texture C	0.36	0.48	0.75
Texture D	0.46	0.62	0.74

5.2.3.2.   Surface analysis at the macro-scale

The three injection moulded samples (Texture A, B and C) were compared with the painted one (Texture D) in terms of topographical features and surface reflectivity contrast to determine the feasibility of obtaining unpainted engraved surfaces having similar appearance than the painted one. The relationship between surface characteristics such as roughness, functional distribution heights (FDH), texture slope (TS) and texture aperture angle (TAA) with the surface reflectance properties (reflectivity contrast) were studied for quantitatively measuring the surface appearance. The two parameters TS and TAA are of great importance in order to understand the role of valleys in the light reflectivity of the textured surface. As described in Equation 5.7, in a Lambertian surface the intensity of the light reflected depends on the angle between the incident beam light and the surface normal [9], [10].

$$E_{\theta} = Ecos\Theta \tag{5.7}$$

Where E_{Θ} is the light intensity, E is the maximum light intensity at 0° in regards to the surface normal and Θ is the angle of incidence between the light source and the surface normal.

Therefore, in the case of the TS, the closer the angle to 90° the lower the reflectivity from valleys portion is expected. In the TAA case, the lower the angle between grains walls the lower will be the reflected light coming from valleys.

Table 5.6 contains the topographic results obtained at the limited scale of S-L 0.04-5 of the textures under study. It should be pointed out that in comparison to the other textures, In comparison to the other textures, texture A exhibited in average the highest roughness values of Sa and Sq and the highest AFH with a total of 107 µm (Spk + Sk + Svk). However, it should be pointed out that the FHD was different between textures. Texture A had a FHD of Spk, Sk and Svk of 3%, 53% and 43%, respectively. This means that from the total topography, 3% pertains to aberrant peaks, 53% to peak-to-valley height and 43% to aberrant deep valleys, which were selected as surface background to adequately measure the reflectivity contrast between peaks and valleys. Texture A had the lowest Spk value, which indicated low roughness level on top of the surface, leading to specular reflections. Therefore, high reflectivity contrast can be expected because of the apparition of dark areas coming from valleys portion and specular reflections coming from the top of peaks. Textures B, C and D exhibited similar ranges of FHD in their topographies with 6.0%, 67.7% and 26.2% of Spk, Sk and Svk in average. In these cases, their FHD lead to expect less reflectivity contrast between top surface and its background. This is because when the amount of peaks (i.e. Spk) is high, the diffuse light component prevails over the specular one. In addition, due to the low amount of deep valleys (i.e. Svk) in their topographies, smaller dark areas coming from deep valleys portion are expected. Another parameter to take into account is the relative core roughness height (Sk). This surface portion represents the peak-to-valley height and it is homogeneously illuminated, as described in a previous work [11].

Table 5.6 Topographic results at the limited scale S-L 0.04 – 5.

	Sa (µm)	Sq (µm)	AFH (µm)	Spk (%)	Sk (%)	Svk (%)
Texture A	25.4 ± 0.4	30.0 ± 0.5	107 ± 2	3.3 ± 0.5	53.3 ± 1.3	43.4 ± 1.7
Texture B	21.6 ± 0.7	25.0 ± 0.9	90 ± 2	6.6 ± 1.1	66.6 ± 0.9	26.7 ± 1.2
Texture C	22.4 ± 0.4	25.4 ± 0.5	87 ± 1	4.9 ± 1.0	69.1 ± 0.7	26.0 ± 0.8
Texture D	15.9 ± 0.8	18.8 ± 1.0	72 ± 2	6.6 ± 1.0	67.5 ± 2.4	25.9 ± 2.6

5.2.3.3. *Surface analysis at the micro-scale*

The textures were also analysed at the micro scale. Figure. 5.7a and 5.7b show the values of Sa and Sq at each limited scale. As can be appreciated, at the lower limited scales (L-Filter of 0.025 and 0.05 mm), the Texture C showed relatively higher roughness values in both Sa and Sq. On the other hand, when the evaluation scale (L-filter) was increased to 0.2 mm, Texture B was the one exhibiting higher roughness values.

The secondary operations during the mould engraving such as the addition of micro roughness and the mould coating modified the underlying Texture A (Figure 5.8a). In the former case (Texture B), the micro-asperities included during the engraving process were of approximately 200 µm in the lateral dimension (x, y) as shown in Figure 5.8b. In the latest case (Texture C), the applied coating induced micro-asperities ranged from 25 to 50 µm (Figure 5.8c) while the painted surface (Texture D) had the lowest micro roughness values at all scales that ranges from 0.6 to 1.4 µm in Sa for 0.025 and 0.2 mm of L-filter, respectively. This indicates that the painting process smoothed the original texture, reducing both top micro-asperities on peaks and deep valleys by filling the gaps as illustrated in Figure 5.8d
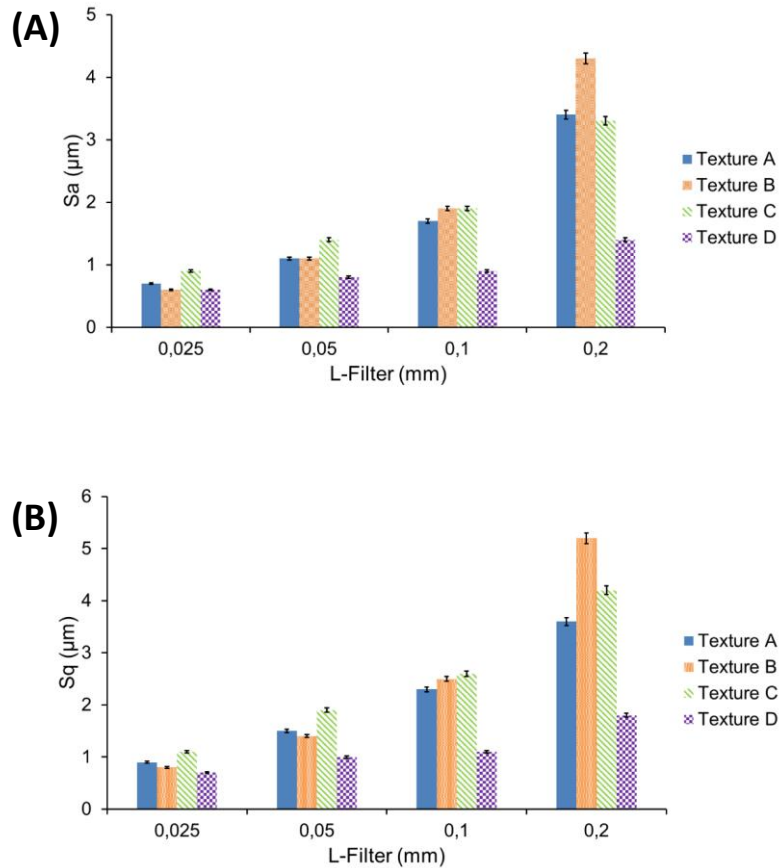
Figure 5.7 Results of roughness at different limited scales. (a) arithmetic roughness and (b) root mean square roughness.

It should be remarked that the gloss of each texture finish (Table 5.7) matched well with its obtained roughness level at the micro scale (Figure 5.7a and 5.7b). High surface micro roughness implies low gloss level. The reason behind this behaviour is that the surface gloss is mainly controlled by the diffuse component of the reflected light. In addition, the gloss measurement was done at 60º, having as main source of reflected light the one coming from peaks portion. Valleys have no contribution to the surface gloss measurement. The reflected light coming from valleys is blocked by the surface peaks and does not enter into the glossmeter's detector. However, the surface appearance does not only depend on peaks portion and its gloss. The human eyes can visualize the total surface, taking into account both the light reflected from peaks and from valleys. As well, the TAM prototype instrument allows

quantifying the light reflected from peaks and valleys, measuring the reflectivity contrast objectively.

Table 5.7 Results of gloss measurements at 60⁰.

	Texture A	Texture B	Texture C	Texture D
Gloss (GU)	1.7 ± 0.1	1.2 ± 0.1	1.3 ± 0.1	1.9 ± 0.1
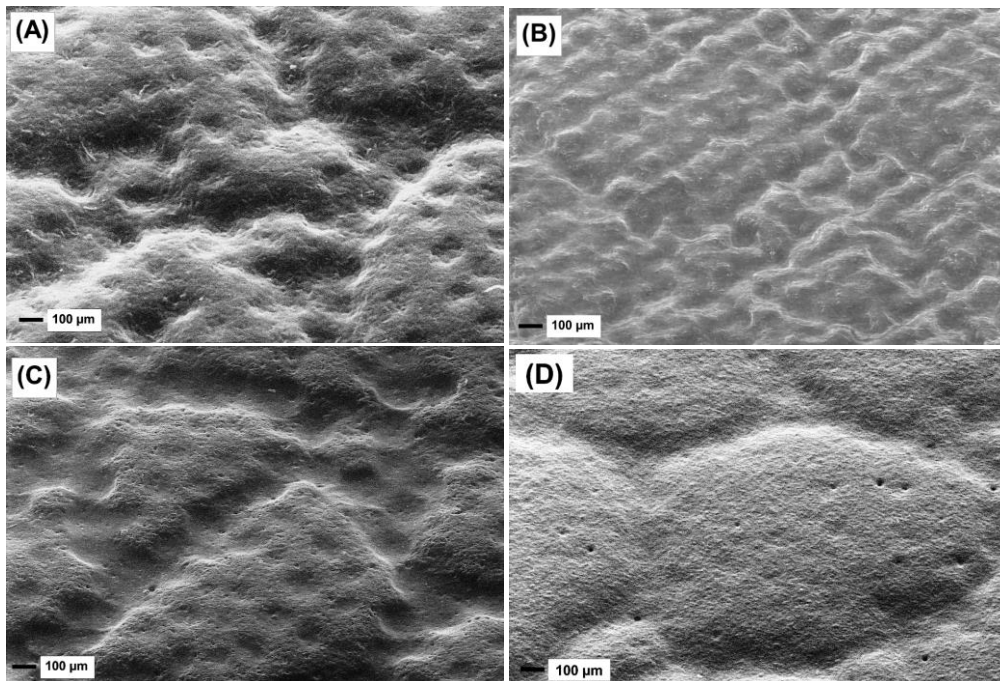
Figure 5.8 SEM images of (a) texture A, (b) texture B, (c) texture C and (d) texture D.

5.2.4. Measurement of the surface appearance

The quality of a certain surface is mainly dependent on its gloss, colour and texture [12]–[15]. For instance, in cosmetics industry smooth and glossy surfaces are preferred to provide high quality to their customers. On the contrary, in automotive, high quality surface is achieved with matte finishes. In this case, gloss level lower than 2.0 GU at 60º is preferred because it provides a better surface appearance to the customers. Texturing is a common

employed technique to reach the desired quality, although painting textured surfaces provides the best quality and appearance finish in automotive sector.

In the present case, the painted texture (Texture D) was selected as reference of high quality surface appearance. Hence, textures A, B and C, obtained directly from the mould cavity, were then compared to texture D. The aim was to determine if injection moulded components can achieve reflectivity properties that allow reaching similar quality appearance than the painted one.

Figure 5.9 shows the reflectivity values coming from peaks and valleys for all texture types. It can be appreciated that texture A had by far the higher reflectivity coming from peaks. Moreover, Texture A exhibited the highest difference between the light reflected from peaks and valleys, resulting in the highest contrast with a value of 24% $\pm$ 2. On the contrary, both texture B and texture C had a more balanced reflectivity from peaks and valleys. This leads to a low reflectivity contrast with 3% $\pm$ 1 and 0% $\pm$ 3 for texture B and C, respectively. Finally, texture D presented negative reflectivity contrast between peaks and valleys with $-$ 6% $\pm$ 1. This was attributed to the amount of reflected light coming from valleys was higher than the one coming from peaks.
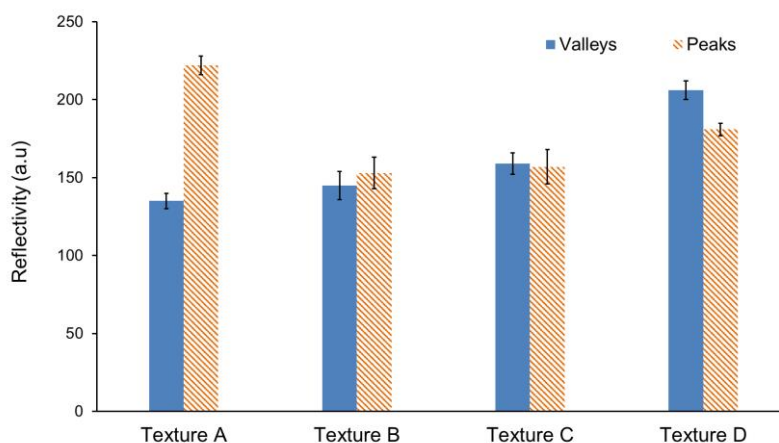
Figure 5.9 Results of reflectivity in both peaks and valleys of the four surface finishes.

The above described behaviour can be related to the topographical features of each particular texture type. As previously mentioned, the amount of deep valleys (i.e. %Svk) was selected as surface background. It is shown in Figure 5.10, where the reflectivity maps of the different texture types are shown. The black area of the figure corresponds to deep valleys portion (background) and the illuminated one to the peaks portion. Texture A had 43% of deep valleys in its total topography (Figure 5.10a), which was the one with the lowest amount of reflected light coming from this surface portion. In addition, the low level of micro roughness on top of peaks led to specular reflections, resulting in the highest reflectivity contrast. On the contrary, textures B and C (Figure 5.10b and 5.10c, respectively) with 26% of deep valleys contained in their topographies exhibited a higher amount of light reflected from valleys. In both cases the amount of light reflected from peaks was the lowest one. This last factor correlated well with their high amount of micro roughness on top of the peaks. Finally, texture D (Figure 5.10d) had a similar amount of deep valleys (26%) as compared to textures B and C. However, it exhibited the highest amount of reflected light coming from valleys, resulting in a negative reflectivity contrast. This can be explained through the two proposed novel parameters, TS and TAA.
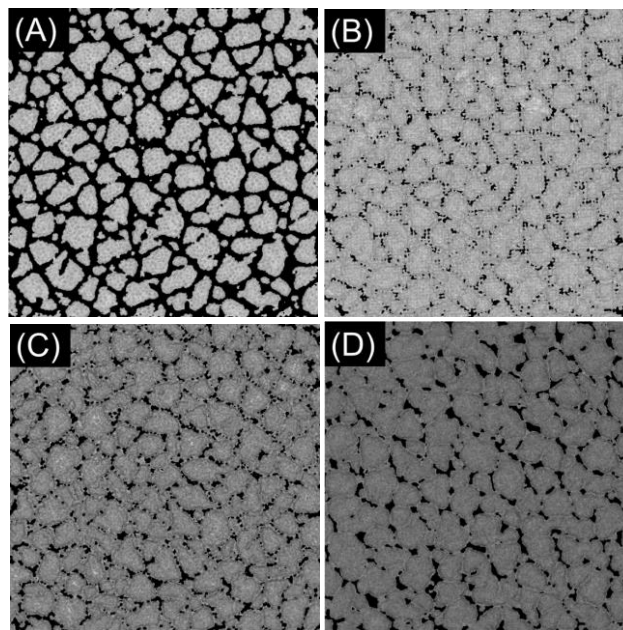
Figure 5.10 Reflectivity map of (a) texture A, (b) texture B, (c) texture C and (d) texture D.

194

Unlike glossmeter instruments, the human eyes capture light coming from the entire surface, taking into account both peaks and valleys. For this reason, the TAM prototype instrument, which considers the reflected light coming from peaks and valleys, provides a measurement of appearance closer to the one of human eyes. From the topographical point of view, measuring TS and TAA provides a forecaster about the amount of reflected light coming from valleys of each texture type. As described by Equation 5.7, the light intensity in a particular direction is proportional to the cosine of the reflected angle. In the present case, the light source was located at 0º in regards to the surface normal, hence the light reflected in the same direction yielded 100% of intensity. On the contrary, by increasing the reflected angle the intensity of the reflected light decreased. The valleys contribution to the reflectance properties of a textured surface such as the reflectivity contrast depends on the TS and TAA. Combining it with the micro roughness level of peaks, the reflectivity contrast between peaks and valleys can be estimated. Table 5.8 collects the TS and the TAA averaged results after 20 measurements done at different locations of each texture type.

Table 5.8 Results of the texture slope (TS) and texture aperture angle (TAA) of the four texture finishes.

	Texture A	Texture B	Texture C	Texture D
TS (degree)	19.4 ± 6.8	15.2 ± 7.3	13.8 ± 4.9	8.2 ± 1.7
TAA (degree)	140.7 ± 11.4	149.6 ± 13.1	152.4 ± 5.3	164.9 ± 2.9

Texture A had the highest TS and therefore yielded the lowest TAA. Hence, the low reflectivity in valleys matched well with the described Lambertian surface. The higher the surface TS the closer to 90º degrees is the angle between the reflected light and the light source, resulting in low light reflectivity. In addition, topographical features such as the relative amount of deep valleys (%Svk) yielded low level of reflected light coming from this surface portion. This texture design blocked light coming from valleys and it did not allow illuminating the surface uniformly. As a consequence, a high reflectivity contrast between

peaks and valleys was obtained (24%). On the other hand, textures B and C had less acute TS, resulting in a higher TAA. This led to a more uniform illumination of the total surface. Unlike texture A, the design of textures B and C allowed the reflected light that came from valleys to be quantified by the TAM prototype instrument, reducing light blocking by peaks. Combining it with their micro roughness level on peaks a less reflectivity contrast can be obtained, having 3% and 0% in texture B and C, respectively. For the case of texture D, the lowest TS and the highest TAA values were found, resulting in even higher reflectivity in valleys than in peaks as it is shown in Figure 5.9. It can be concluded that by modifying the underlying design textures that do not block light from peaks portion and yield similar surface appearance to the painted surface can be obtained directly by injection moulding. Therefore, applying surface treatments to the mould cavity is an appealing method for enhancing the surface appearance of injection moulded components, avoiding the high cost and environmental impact of painted surfaces.

5.3. Conclusions

The contribution of valleys in the surface reflectance properties and thus in its appearance was considered for better understanding of surface perception in terms of reflectivity contrast. It was demonstrated that the functional height distribution (FHD) plays an important role in the reflectivity contrast of the surfaces. The larger the amount of deep valleys (Svk) the larger was the reflectivity contrast reached. The angle of incidence between the light beam and the surface normal was the main responsible of the reflectivity values in valleys portion. The TS and TAA measurements showed that the texture A, with the sharpest TS and thus the closer TAA, was the one with lower reflectivity in valleys, resulting in higher contrast values between peaks and valleys. On the contrary, textures B and C had values of TS and TAA closer to the ones measured on texture D (painted), resulted in turn in similar values of contrast. Therefore, a relationship between topographic features such as roughness, functional height distribution (FHD), texture slope (TS) and texture aperture angle (TAA) with surface appearance properties such as gloss and reflectivity contrast have been established.

It can be concluded that it is possible to achieve similar surface reflectance properties to the ones obtained by painting. Mould treatments can be an appealing methodology for obtaining surfaces with a high quality aspect ratio at lower cost-production and using an environmental friendly process.

5.4. References

[1]   P. Gamonal-Repiso, T. Abt, M. Sánchez-Soto, S. Santos-Pinto, and M. L. Maspoch, "Influence of topographical features on the surface appearance measurement of injection moulded components", *Polym. Test.*, vol. 93, 2021, doi: 10.1016/j.polymertesting.2020.106968.

[2]   F. Blateyron, "New 3D parameters and filtration techniques for surface metrology", Qual. Mag. (2006) 1–7.

[3]   P. Gamonal-Repiso, M. Sánchez-Soto, S. Santos-Pinto, and M. L. Maspoch, "Improvement of the replication quality of randomly micro-textured injection-moulding components using a multi-scale surface analysis", *J. Manuf. Process.*, vol. 42, no. April, pp. 67–81, 2019, doi: 10.1016/j.jmapro.2019.04.010.

[4]   R. J. Woodham, "Photometric Method For Determining Surface Orientation From Multiple Images", *Opt. Eng.*, vol. 19, no. 1, pp. 139–144, 1980, doi: 10.1117/12.7972479.

[5]   G. Tosello, H. Haitjema, R. K. Leach, D. Quagliotti, S. Gasparin, and H. N. Hansen, "An international comparison of surface texture parameters quantification on polymer artefacts using optical instruments", *CIRP Ann. - Manuf. Technol.*, vol. 65, no. 1, pp. 529–532, 2016, doi: 10.1016/j.cirp.2016.04.003.

[6]   JCGM 100:2008, "Evaluation of measurement data – Guide to the expression of uncertainty in measurement", Jt. Comm. Guid. Metrol. (2008). https://doi.org/10.1373/clinchem.2003.030528

[7]   D. G. Pelli and P. Bex, "Measuring contrast sensitivity", *Vision Res.*, vol. 90, pp. 10–14, 2013, doi: 10.1016/j.visres.2013.04.015.

[8]   A. Michelson. "Studies in optics". U. of Chicago Press, 1927.

[9]   F. Nicodemus, J. Richmond, and J. Hsia, "Geometrical considerations and nomenclature for reflectance", *Sci. Technol.*, vol. 60, no. October, pp. 1–52, 1977, doi: 10.1109/LPT.2009.2020494.

[10]   E. F. Taylor. "Illumination fundamentals". Rensselaer, 2000..

[11]   P. Gamonal-Repiso, M. Sánchez-Soto, S. Santos-Pinto, and M. L. Maspoch, "Influence of topography on the scratch and mar visibility resistance of randomly micro-textured surfaces", *Wear*, vol. 440–441, no. October, 2019, doi: 10.1016/j.wear.2019.203082.

[12]   F. Leloup, P. Hanselaer, J. Versluys, S. Forment, "BRDF and gloss measurements", CIE Expert Symp. (2007) 1–6.

[13]   A. C. Chadwick and R. W. Kentridge, "The perception of gloss : A review", *Vision Res.*, vol. 109, pp. 221–235, 2015, doi: 10.1016/j.visres.2014.10.026.

[14]   S. Ignell, U. Kleist, and M. Rigdahl, "Visual perception and measurements of texture and gloss of injection-molded plastics", *Polym. Eng. Sci.*, vol. 49, no. 2, pp. 344–353, 2009, doi: 10.1002/pen.21279.

[15]   S. Ignell, U. Kleist, and M. Rigdahl, "On the relations between color, gloss, and surface texture in injection-molded plastics," *Color Res. Appl.*, vol. 34, no. 4, pp. 291–298, 2009, doi: 10.1002/col.20510.

Chapter 6:   Influence of textures on the scratch visibility resistance

Original roughness

Ra= 5,0 µm

Shoulder roughness

Ra= 7,5 µm

$$\frac{Shoulder\ Ra}{Original\ Ra}$$

Scratch visibility
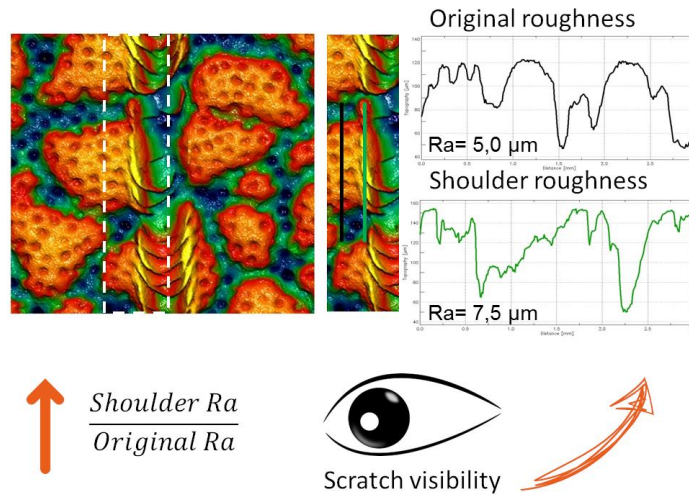
The influence of the texture on both the scratch hardness (Hs) and the scratch visibility resistance have been studied in this chapter. Although the addition of textures is not relevant for improving the scratch hardness it resulted a suitable way for hiding the scratch damage when high loads were applied on the surface.

Publication derived from this work [1]

Influence of topography on the scratch and mar visibility resistance of randomly micro-textured surfaces

P. Gamonal-Repiso [a,b], M. Sánchez-Soto [a,*], S. Santos-Pinto [b], M. Ll Maspoch [a]

[a] *Centre Català del Plàstic, Universidad Politécnica de Catalunya Barcelona Tech (UPC-EEBE), C/Colom 114, 08222, Terrassa, Spain*
[b] *Departamento de Tecnología de Materiales de SEAT S.A, Autovía A-2, Km 585, Apartado de Correos 91, 08760, Martorell, Spain*

6.1. Experimental section

6.1.1. Material

In all cases, the material used was a black polypropylene copolymer filled with 5% talc, HC TKC 2007N from Basell S.L (Tarragona, Spain).

6.1.2. Samples preparation

Squared samples with dimensions 100 x 100 x 3 mm^3 (length x width x thickness) were obtained by injection moulding.

Five different texture types were studied in this chapter:

1. The smooth texture: obtained from replicating a mirror-like polished mould cavity.

2. The fine texture: obtained from the described chemical engraving process.

3. The leather texture: obtained from the described chemical engraving process.

4. The leather texture + micro-features: obtained from a mould treatment which adds micro-features on the original leather texture. Encoded as Leather+T1.

5. The leather texture + mould coating: obtained from a mould treatment which adds a coat on the original leather texture. Encoded as Leather + T2.

Leather texture types were encoded as follows:

Table 6.1 Code of the leather texture types.

Leather texture type	Code
Original leather texture	Texture A
Leather texture + micro features	Texture B
Leather texture + coating	Texture C

6.1.3. Surface characterization

The surface topography was analysed using the chromatic confocal microscope, equipped with a chromatic white light sensor (CWL) having 30 nm and 6 µm of vertical and lateral resolution, respectively.

The evaluation area 3.65 x 3.65 mm^2 and the lateral resolution of 10 µm were selected. Filters such as S-filter or L-filter govern the limited scales of the surface, in this case the S-filter was fixed at 0.01 mm and the L-filter was varied between 0.01 mm to 3 mm, making possible the surface analysis at multiple scales from the micro to the macro-texture [2].

The macro-scale analysis was carried out at the limited-scale S-L 0.01-3, where S-L denotes the surface type, 0.01 mm is the S-filter setting and 3 mm is the L-filter value, whereas the micro-scale analysis was conducted at two limited-scales denoted S-L 0.01-0.05 and S-L 0.01-0.2.

6.1.4. Scratch resistance

6.1.4.1. *Characterization of the scratch groove*

An evaluation area of 3.65 x 3.65 mm^2 and a lateral resolution of 20 µm were selected in the CWL confocal microscope to analyse scratch groove characteristics such as width, depth and height as a function of the applied load. This selection was because the ability of the humans for identifying scratch damage is limited by the visual capabilities of their eyes [3]. An average human eye is capable to resolve a spatial pattern separated by a visual angle of 1/60º, which for a viewing distance of ≈ 200 mm represents an object with lateral dimensions of approximately 60 µm [4]. Therefore, a lateral resolution of 20 µm is high enough to guarantee that all detectable surface and groove features are accurately reconstructed.

6.1.4.2.   Determination of the scratch hardness

The scratch resistance (scratch hardness) was calculated according to Equation 6.1.

$$Hs = \frac{W}{A} = \frac{q4W}{\pi d^2} \qquad (6.1)$$

Where the *Hs* is the scratch hardness, *W* is the load applied, *A* is the projected area, *d* is the recovered width of the scratch path and the parameter q varies according to the indenter material response (q≈2 for rigid plastics and q > 1 for viscoelastic plastics). In the current work q = 1.5 was selected [14].

The groove left by the indenter was reconstructed by means of three dimensional (3D) techniques. In that particular case the CWL sensor was employed to measure the width (W), the height (H) and the depth (D) of the groove as it is depicted in Figure 6.1. Two-dimensional roughness data was extracted from the 3D surface taking a profile length of 3 mm. Measurements were conducted after 24 h which allows for viscoelastic recovery of the material. The results were the average of 5 different measurements for each texture and scratch condition.
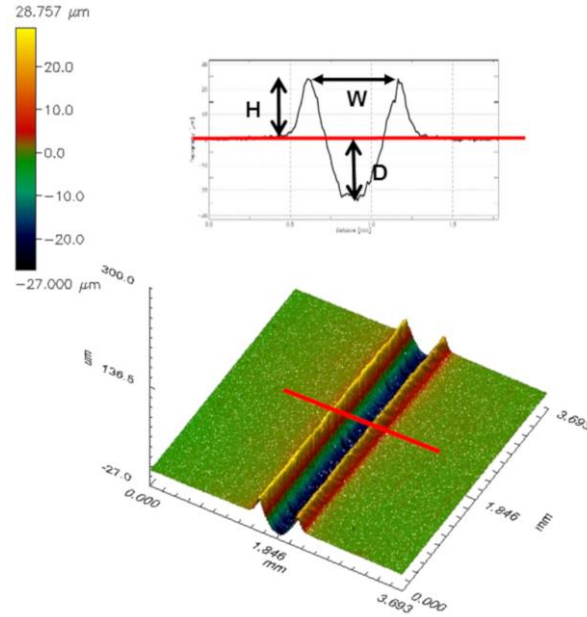
Figure 6.1 Groove depth (D), shoulder height (H) and width (W) measurements from the 3D surface reconstruction. The total groove height is the sum of D and H.

6.1.4.3. *Evaluation of the scratch visibility resistance*

The samples after scratch and mar tests were analysed in terms of visibility of the created damage and compared with the pristine surface.

The scratch visibility resistance was quantified considering the following variables.

1. The applied normal load.

2. The groove depth and shoulder height.

3. The roughness ratio between the groove or shoulders with its surroundings

4. The normalized lightness variation (ΔL^*) between the original surface (L_o^*) and the 40 x 40 mm^2 crosshatch pattern created by the scratch tip (L_i^*) (Figure 6.2)

$$\frac{\Delta L^*}{L_0} = \frac{L_i - L_0}{L_0} \; x \; 100 \qquad\qquad (6.2)$$
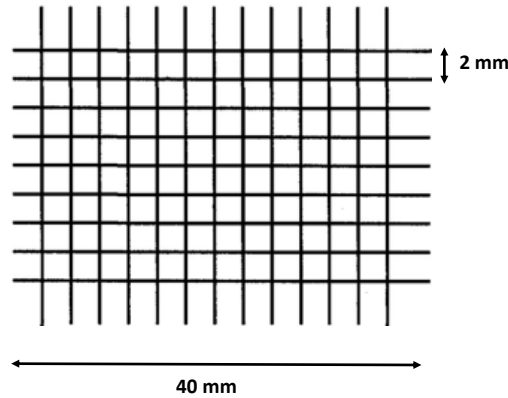
Figure 6.2 Crosshatch pattern created after performing the scratch test.

A Spectro-Guide 45/0 Gloss-spectrophotometer from BYK-Gardner GmbH (Geretsried, Germany), with 45/0º measuring geometry and D65/10º as illuminant was used to measure the ΔL^*. The ΔL^* was the result of averaging 5 measurements on the original texture and the resultant crosshatch pattern. It was measured for each texture and test condition.

The roughness difference between the original texture, the groove and its shoulders was normalized according to Equation 6.3.

$$\frac{\Delta R_a}{R_a} = \frac{R_a^* - R_a}{R_a} \; x \; 100 \tag{6.3}$$

Where R_a^* is the arithmetic roughness average of the groove or shoulder and R_a is the one of the original sample. All the results were the average of at least five measurements of each parameter.

6.1.5. Mar resistance

6.1.5.1.   Characterization of the mar damage

As the damage created on the surface by mar testing is very small, high precision measurements were utilized to study the surface evolution as a function of the applied load. A high-resolution confocal microscope, S lynx from Sensofar Metrology S.L (Terrassa, Spain),

205

equipped with a 20x magnification lens having 0.69 µm and 8 nm of lateral and vertical resolution, respectively, was employed to measure the topography at the micro-scale. The evaluation area was 877 x 660 µm^2.

In addition, a scanning electron microscope (SEM), Zeiss Sigma 300 VP (Jena, Germany), was also utilized for analysing the surfaces as well as the scratch and mar morphologies.

6.1.5.2.   Evaluation of the mar visibility resistance

The mar visibility was quantified taking into account the gloss and contrast variation. The gloss variation was normalized taking into account the gloss increment (ΔG) between the original surface and the tested area Equation 6.4. The contrast was obtaining after applying Equation 6.5.

$$\frac{\Delta G}{G_0} = \frac{G_i - G_0}{G_0} \; x \; 100 \tag{6.4}$$

$$C = \frac{G_i - G_0}{G_i + G_0} \; x \; 100 \tag{6.5}$$

Where ΔG is the gloss variation, C is the contrast, G_i, and G_0 are the tested area and the background gloss, respectively.

Gloss measurements were carried out using the ZGM 1120 glossmeter from Zehntner GmbH Testing Instruments (Sissach, Switzerland) with 60° geometry and a measuring area 4.7 x 2 mm^2 (length and width). A high resolution digital microscope, Dino-lite from AnMo Electronics Corporation (New Taipei City, Taiwan) was used to capture micrographs of the scratch damages. A normalized light box, Variolux from Heraeus GmbH (Hanau, Germany), equipped with a D65 light source was employed to illuminate the samples and take the images of the scratch visibility. The camera was fixed at an angle of 45º from the normal and the specimen angle was 45º from the light source (Figure 6.3).
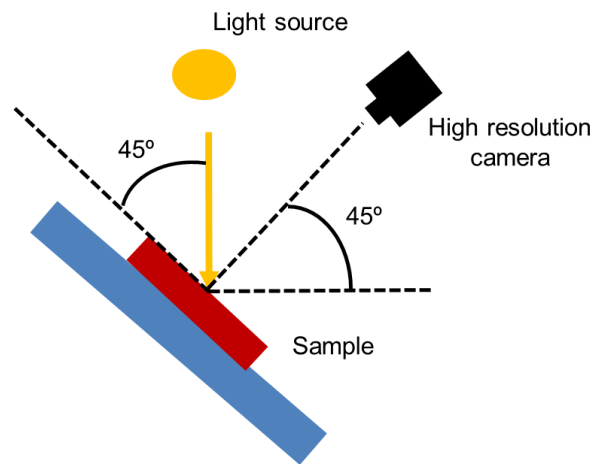
Figure 6.3 Camera setup for capturing images of scratched surfaces.

6.1.6. Surface parameters

Amplitude and functional surface parameters were employed to characterize the surface topographies. From the amplitude parameter family, the arithmetical mean height (Sa), the root mean square height (Sq), the skewness (Ssk) and the kurtosis (Sku) were selected. They are defined by (Equations6.6-6.9) respectively.

Sa and Sq represent the overall surface roughness, although they are insensitive in differentiating peaks and valleys. Both Ssk and Sku represent the symmetry deviation from the normal distribution (e.g. bell curve). Ssk defines the degree of symmetry of the surface height with respect to the mean plane. The sign of Ssk indicates the predominance of peaks (Ssk >0) or valleys (Ssk <0) whereas a normal distribution is reached with Ssk =0. On the other hand, Sku indicates the presence of extreme high peaks or deep valleys (Sku >3) or the lack of them (Sku <3). A normal distribution is reached with Sku = 3.

From the functional parameter family, the core height (Sk), the reduced peak height (Spk) and the reduced dale height (Svk) were used. They are obtained from the areal material

ratio curve also known as the Abbot Firestone curve, which is established by evaluating the

material ratio at various levels from the highest peak to the lowest valley [5]

$$Sa = \frac{1}{A} \iint_A |z(x,y)| dxdy \qquad (6.6)$$

$$Sq = \sqrt{\frac{1}{A} \iint_A |z^2(x,y)| dxdy} \qquad (6.7)$$

$$Ssk = \frac{1}{S_q^4} \left[\frac{1}{A} \iint_A z^4(x,y) dxdy \right] \qquad (6.8)$$

$$Sku = \frac{1}{S_q^3} \left[\frac{1}{A} \iint_A z^3(x,y) dxdy \right] \qquad (6.9)$$

The relationship between the texture and its scratch visibility resistance was established

by the introduction of three new parameters, namely, the absolute functional height (AFH),

the residual background height (RBH) and the shoulder roughness ratio ($\Delta R_i/R_0$).

The AFH is defined as the sum of the three above described functional parameters (Spk

+ Sk + Svk). This parameter allows determining the averaged texture depth within the

sampling area. The RBH is the texture height after performing scratching. It was decomposed

in terms of the different functional heights. Equation 6.10 defines the shoulder roughness ratio,

which is the roughness difference between the original texture and the shoulder created side

to side of the groove.

$$\frac{\Delta R_a}{R_a} = \frac{R_a^* - R_a}{R_a} \; x \; 100 \qquad (6.10)$$

Where R_a^* is the arithmetic roughness average of the shoulder and R_a is the one of the

original sample.

6.2. Results and discussion

6.2.1. Surface characterization

Figure 6.4a-e shows the obtained 3D surface reconstruction of the original textures using the CWL sensor. Usually, textures are added to polymeric materials with the intention of enhancing the aspect and obtaining matte and uniform appearance [2]. In addition, surface texturing can play the role of slip agent as in the case of the smooth surfaces which reduces the frictional force [6], [7]. Hence, analysing the surface topography is essential for the better understanding of the effect of texturing.
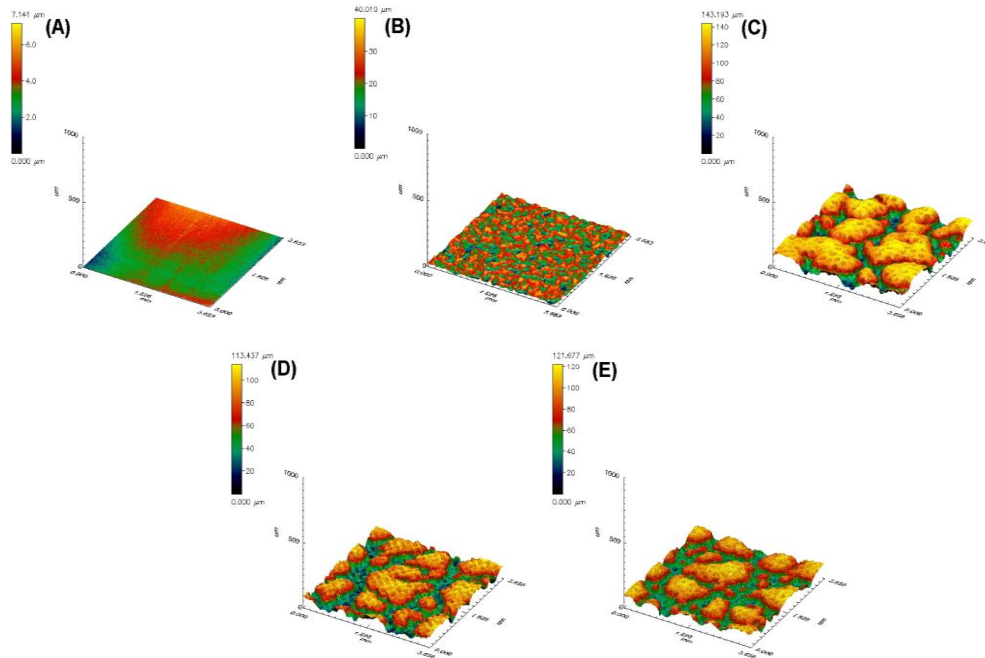
Figure 6.4 Topography reconstruction in 3D of the (A) smooth, (B) fine, (C) Texture A, (D) Texture B and (E) Texture C textures.

Figure 6.5 shows the topographical results obtained at the macro-scale analysis (S-L 0.01-3). The figure depicts the smooth surface that includes sub-micro roughness values with Sa and Sq of 0.70 and 0.87 µm, respectively. The fine texture type had Sa and Sq of 5.1 and 6.2 µm, respectively. On the other hand, the leather textures showed the coarser finishes, yielding the higher values of Sa and Sq. Texture A had 26.0 and 30.9 µm in Sa and Sq in

average, respectively. On the other hand, the Sa and the Sq of the treated surfaces slightly dropped to 22.1 µm in Sa and 25.3 µm in Sq in the Texture B case. The Sa and Sq of the Texture C surface were of 21.9 and 24.8 µm, respectively. Therefore, the roughness differences in the leather texture types were not much representative. This was because the amplitude parameters only measure absolute heights within the evaluated area, without making any distinction between peaks and valleys. Therefore, functional parameters were considered in order to differentiate between peaks and valleys.

The absolute functional height (AFH = Spk+Sk+Svk) as well as the relative distribution of each component are collected in Table 6.2.
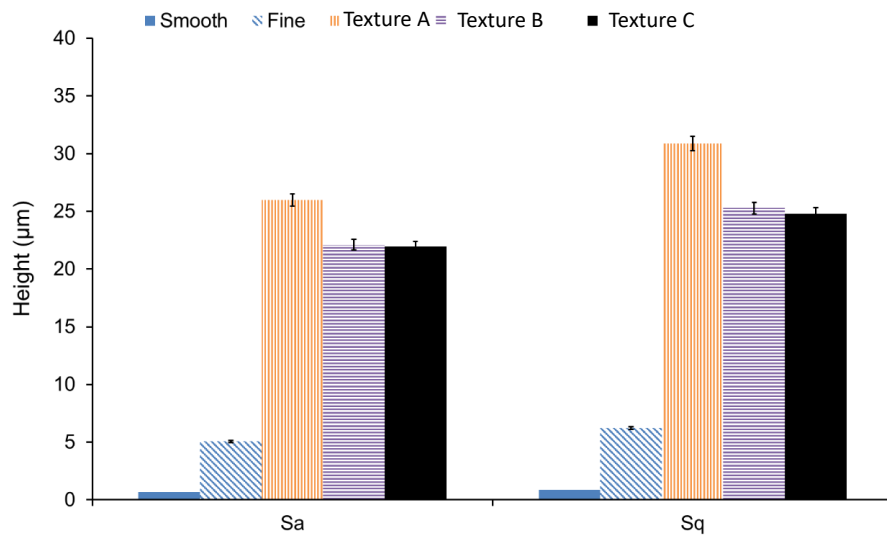
Figure 6.5 Topographic results of all textures under study at the macro scale S-L 0.01-3

Table 6.2 Absolute and relative values of each functional parameter in regards to its AFH

Surface parameter (µm)	Smooth	Fine	Texture A	Texture B	Texture C
Spk	0.9 (22.5%)	4.1 (15.5%)	4.1 (3.7%)	5.7 (6.3%)	4 (4.5%)
Sk	2.3 (57.5%)	17.0 (64.1%)	55.1 (49.4%)	63.2 (70.0%)	73 (82.5%)
Svk	0.8 (20%)	5.4 (20.4%)	52.3 (46.9%)	21.4 (23.7%)	11 (13.0%)
AFH	3.9	26.5	111.5	90.4	88.0

The AFH of the leather textures displayed the higher functional height compared to the smooth surface and fine texture. This was in accordance with their Sa and Sq values. The AFH of the three leather textures were very similar although the addition of treatments resulted in a reduction of the original texture height (Texture A) from 111 µm to 90 µm for Texture A and 111 µm to 88 µm for Texture C. The main difference between the leather texture types was found in the distribution of heights, especially in the valley (Svk) and peak-to-valley (Sk) heights. Figure 6.6 depicts the distribution of the functional parameters on a 2D-profile extracted from the 3D areal reconstruction of each leather texture. The skewness (Ssk) and kurtosis (Sku) parameters are shown to evaluate the symmetry of the surface as well as the presence of aberrant peaks or valleys. The mean plane (horizontal dashed line) corresponds to the height at which half of the material is above the line and the other half is below it. As it can be seen, the untreated Texture A (Figure 6.6a) had by far the smallest relative Sk value (49%), which implies an uneven distribution of peaks and valleys throughout the entire topography. The Ssk (-0.64) supports the uneven distribution. The Ssk was double the value obtained by the treated textures, indicating a topography strongly governed by valleys. Nevertheless, the valleys are not aberrant due to the Sku (2.31) being lower than 3. On the other hand both the Texture B (Figure 6.6b) and the Texture C (Figure 6.6c) had the largest relative Sk height, that accounted for 70% and 82% of their topography, respectively. Therefore, a greater balance between peaks and valleys was expected. This was supported by their Ssk and Sku values that although indicated a predominance of valleys (Ssk < 0) were

approaching a symmetric distribution of heights ($Ssk = 0$). In addition, the existence of aberrant peaks or valleys was also discarded because the Sku was lower than 3.
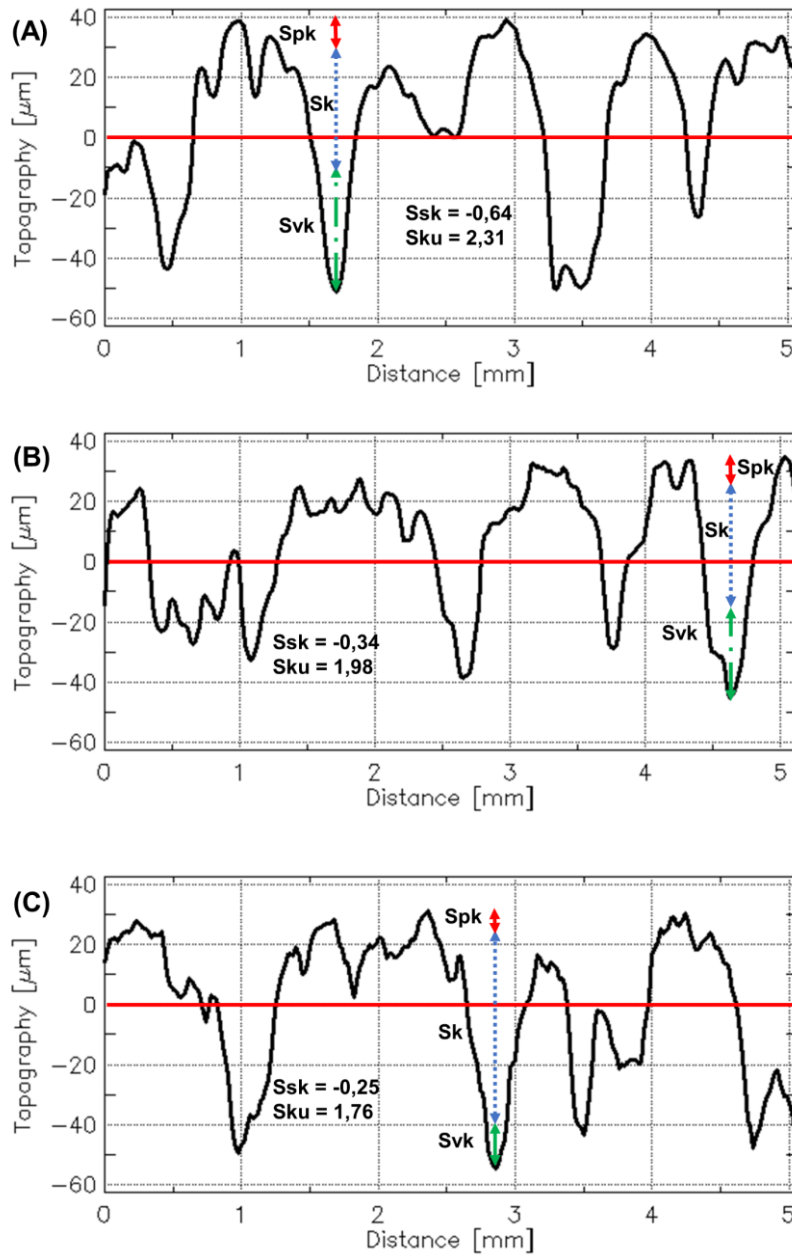

Figure 6.6 Functional distribution heights of Texture A (A), Texture B (B) and Texture C (C).

The above surface assessment can be used for predicting the behaviour of light when interacting with the surface. For instance, the peak portion is uniformly illuminated since the incident light comes in contact with all the material. On the contrary, the reflected light that leaves from valleys is hindered by the surrounding features leading to a reduction of the reflectance in this surface portion [13]. Therefore, it is expected that surfaces having a large number of deep valleys result in a light/dark contrast between the upper (lighter) and the bottom (darker) portion of the surface. Light/dark contrast influences the scratch visibility resistance and the detection of the damage [20]. The scratch tip creates a groove that modifies the in-light behaviour of the surface. The reflectance mode of the surface changes from specular to diffuse which is normally lighter.

6.2.2. Effect of the texture on the scratch hardness (Hs)

The width of the groove created after the indentation was measured from the 3D areal reconstruction of the scratched surface as described in the experimental section (Figure. 6.1). The results of the scratch hardness (Hs) as a function of the applied load and the surface texture are collected in Table 6.3. Figure 6.7 shows the scratch morphology of each texture as a function of the applied load. As it can be seen, at low applied forces (7 N) with the exception of the smooth surface, there was almost no indenter penetration, which resulted in the smoothing of top asperities. In the case of the fine, Texture B and Texture C textures, it was not possible to distinguish between the scratch path and the underlying texture. This was because of the original texture hid the scratch and did not allow differentiating the shoulders clearly, resulting in unreliable measurements of the groove width and consequently a large dispersion in the Hs.

213

Table 6.3 Results of the scratch hardness (Hs) as a function of the applied load and texture.

	Hs (MPa)				
	Smooth	Fine	Texture A	Texture B	Texture C
7 N	91±2	--	96±11	--	--
10 N	97±9	95±5	106±5	117±9	101±3
15 N	100±2	106±4	111±7	117±12	109±6

By increasing the applied load from 7 to 10 N, the deformation of the surface increased as well, overpassing the micro-asperities level and affecting to the macro-texture. This resulted in an increase of the total groove height from 5 to 19 µm (Figure 6.8). The increase of the load causes the stick-slip mechanism were the material piles up in front the scratch tip and creates parabolic features known as fish scales. The result is a well-shaped and spaced pattern of parabolic features as it can be seen for the smooth surface and fine texture in Figure 6.7. These two surfaces had the lower values of roughness and AFH and thus larger contact areas, yielding higher frictional tangential forces between the indenter and the surfaces. Therefore, it was expected finding similar scratch hardness between the smooth surface and fine texture after applying 10 N loading. As the textures become coarser, smaller fish-scale marks behind the tip are detected because both the tangential force and the contact area decreased. For this reason, the Hs of the three leather textures was higher than the ones found for the smooth surface and fine texture at 10 N loading. The AFH of the leather textures was higher than the ones of the smooth surface and fine texture. Hence, the material removed was relatively lower, leaving part of the original texture under the scratch damage.

Eventually, at the highest contact load (15 N), the scratch hardness was confined to a narrow interval regardless of the surface texture type because both the micro- and macro-texture were removed during the scratching as it is shown in Figure 6.7. The distance between fish-scale marks increases with the normal load, especially in the coarser textures. A higher normal load results in higher frictional tangential forces, allowing the indenter to displace the

piled material over a longer distance. A large amount of material is then moved to the groove sides, obtaining higher shoulders. Therefore, it can be said that the introduction of textures into a certain surface have a positive effect on the scratch resistance. The effective contact area between the indenter and the surface is limited to the higher asperities, leading to a decrease of the adhesive component of the friction force and to a reduction of the friction coefficient [8]–[10]. Therefore, to induce surface deformation higher loads are needed, enhancing the polymer scratch resistance.
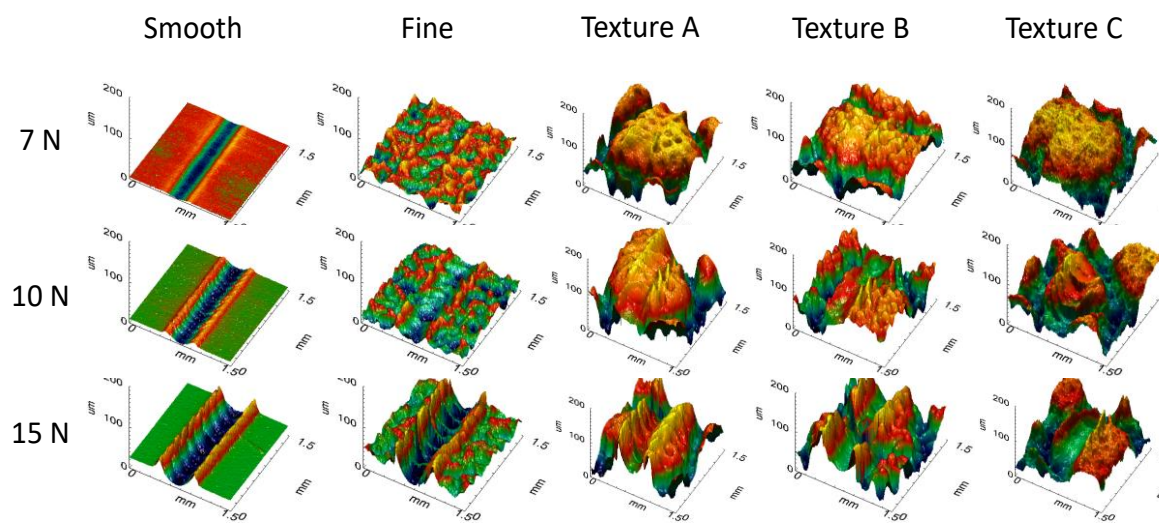
Figure 6.7 Scratch damage appearance as a function of the texture and the applied load, 7 N, 10 N or 15 N.
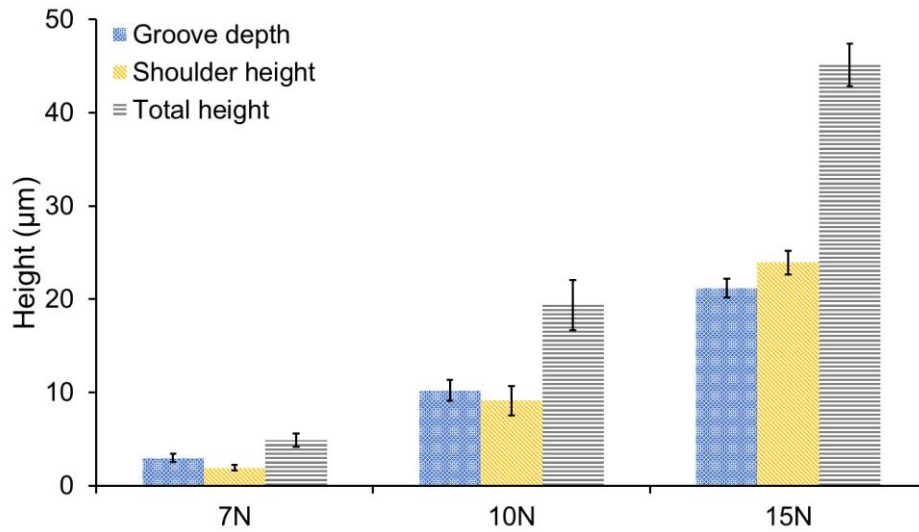
Figure 6.8 Evolution of the different heights after scratching as a function of the applied load. Groove depth, shoulder height and total groove height.

6.2.3. Evaluation of the scratch visibility

The scratch visibility resistance was studied by characterizing the remaining residual texture after scratching. Features such as the groove and shoulders roughness have been considered for understanding the effect of the topography on the scratch visibility resistance. The normalized lightness variation (ΔL^*) has been used to quantify the scratch visibility (Equation 6.2). Two additional parameters have been used, the AFH and the residual background height (RBH), defined as the amount of original height that remains after scratching.

Table 6.4 collects the AFH and RBH of the different textured surfaces as a function of the applied load. The RBH is defined as the remained texture after scratching and it was calculated by subtracting the groove depth from the AFH of each texture (RBH ≥ 0 μm). It can be appreciated that for the case of the smooth surface there was almost no RBH remaining under the groove. This leads to a poor scratch visibility resistance, because the differences between the induced pattern and the original texture yield a different in-light behaviour. The

reflectance mode of the scratched surface is diffuse whereas in the original surface it is in the specular mode, resulting in a high contrast that makes the scratch easily detectable.

Table 6.4 Functional heights and relative background height loss as a function of the applied load.

		RBH (µm)		
	AFH (µm)	7 N	10 N	15 N
Smooth	4	1.1 ± 0.4	0	0
Fine	26	23.1 ± 0.4	15.8 ± 1.1	4.8 ± 1.0
Texture A	111	108.1 ± 0.4	100.8 ± 1.1	89.8 ± 1.0
Texture B	90	87.1 ± 0.4	79.8 ± 1.1	68.8 ± 1.0
Texture C	88	85.1 ± 0.4	77.8 ± 1.1	66.8 ± 1.0

The fine texture lost only an 11% of the AFH at the lowest contact load. However, when the applied force was increased to 10 N, the RBH dropped to 15.8 µm and when it was increased to 15 N, it dropped to 4.8 µm. In the latter case, almost the entire original texture under the groove was removed. Consequently, a more detectable scratch damage is expected because the scratch damage, normally lighter, interacts with the remained RBH, which pertained only to the deep valleys (darker). On the other hand, regardless of the applied force, the three leather textures maintained more than 50% of their original texture under the groove. This was due to the coarser nature of these surfaces which have the higher AFHs. Therefore, a better performance of scratch visibility resistance is likely in a coarser texture rather than in a smooth or fine ones.

Differences in the distribution of heights under the groove for leather textures influence the scratch visibility resistance. For instance, although Texture A had the higher AFH, the distribution of heights under the scratch path was slightly different in comparison to the treated ones. Texture A held approximately 108, 100 and 90 µm of RBH after applying 7 N, 10 N and 15 N loading, respectively. This was because the scratch tip performed from top to bottom of the texture, removing the peak portion of the surface. The portion of valleys (Svk) remained intact regardless of the applied load. The portion of peaks (Spk) and the peak-to-valley height (Sk) were reduced after loading. Therefore, the relative amount of deep valleys increased proportionally to the load increment. Texture A had initially 47% of deep valleys. After applying 7 N, 10 N and 15 N loading, the amount of deep valleys increased to approximately 48%, 52% and 58%, respectively.

On the other hand, although the RBH that remained after scratching in the treated textures was lower, the relative contribution of deep valleys (Svk) dropped dramatically. For Texture B case, the percentage of deep valleys in the RBH dropped from 58% of Texture A to about 30% after 15 N loading. But the highest decrement was observed in Texture C, having a representation of deep valleys 16% after 15 N loading. Therefore, it is expected that surfaces with less amount of deep valleys either in their original topographies or in their RBH yield less light/dark contrast with the scratched surface, diminishing the visibility of the scratch damage.

Figure 6.9 shows the roughness ratio of both the groove (Figure 6.9a) and the shoulders (Figure 6.9b) with respect to the original texture. As it can be seen in Fig. 8a, the majority of the samples displayed a negative roughness ratio of the groove. This indicates an ironing mechanism where the induced pattern in the groove is smoother than its surroundings. When the load was increased for the smooth surface and the fine texture, a positive roughness ratio of the groove was seen. A positive ratio indicates a higher groove roughness than the original surface and can be seen a well-defined fish scale pattern. On the contrary, the three leather textures exhibited negative roughness ratio even at high applied loads (10 N and 15 N). The

pattern induced by the scratch tip was smoother than the original leather texture. In fact, the central path was smoothed by the indenter. This is due to higher tangential forces allowing for larger spaced out fish scales on the texture as more material can be piled up. In the smooth surface there is total contact with the indenter obtaining well-spaced and shaped fish scale patterns. However, in textured surfaces almost all material was removed side to side of the groove path. These effects can be observed by comparing Figure. 6.7.

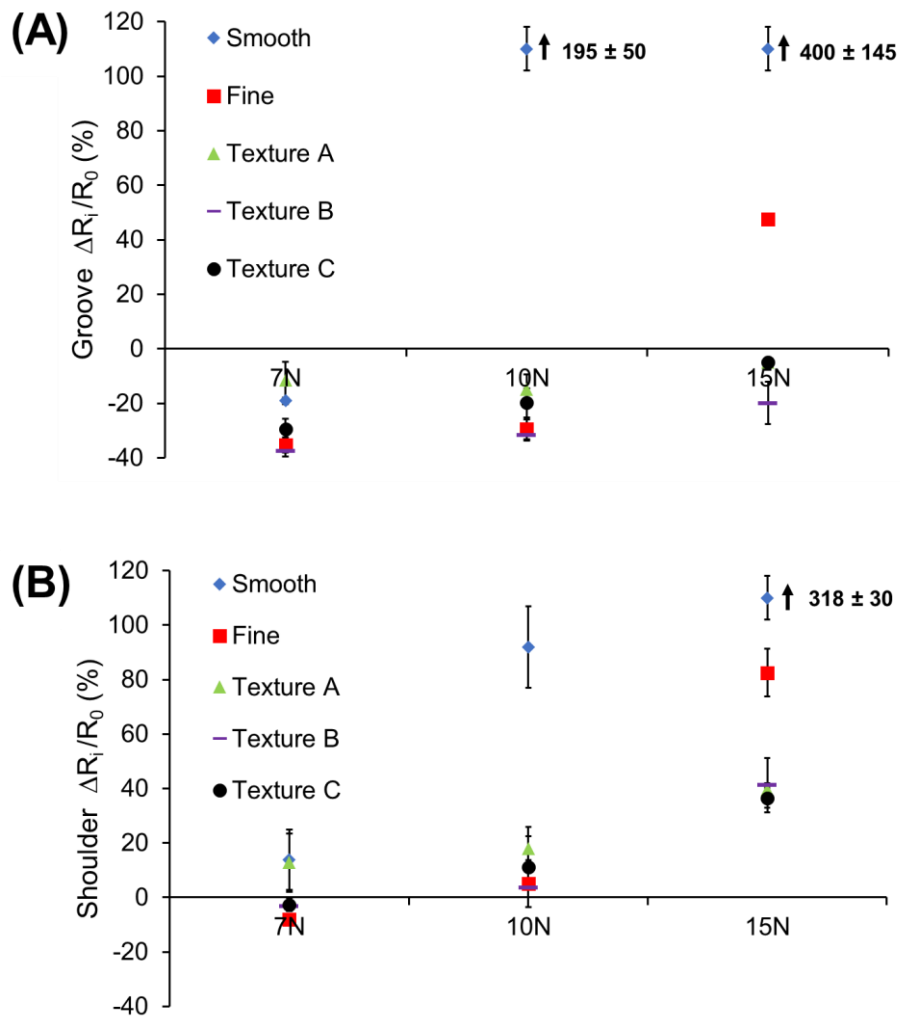**Figure 6.9** Roughness ratio between the groove path and the original texture (A) and roughness ratio between shoulders and the original texture (B).

The smooth surface had a higher groove roughness ratio than shoulders roughness ratio at high loading (10 N and 15 N). The effect of surface texturing is to maintain the groove roughness but to increase the shoulder roughness because the material is moved to the sides to

create the shoulders. The shoulders are mainly responsible for increasing the roughness ratio in regards to the original texture, switching the surface reflectance mode from specular to diffuse [11].

Table 6.5 Results of the normalized lightness variation as a function of the applied load per each studied texture.

	ΔL^* (%)		
	7 N	10 N	15 N
Smooth	24.2	52.7	69.3
Fine	-2.2	0.2	6.7
Texture A	-1.7	1.0	4.5
Texture B	-1.8	-0.3	2.8
Texture C	0.14	0.12	2.6

Table 6.5 collects the normalized ΔL^* between the crosshatch pattern and the original surface. When the ΔL^* is negative, the damage was darker than its background. Increasing the normal load, ΔL^* was positive, the damage was lighter than its background, leading to a higher contrast. The ΔL^* increased in parallel to the increase of the shoulders roughness ratio. The amount of material moved to the groove sides increases as a function of the applied load, resulting in a punctual roughness increment in this surface portion. Figure 6.10 shows the relation between the initial topographic features, AFH and Svk, that affect to the scratch visibility (ΔL^*) after applying 15 N load. It can be seen that surfaces with different topographic nature (smooth, fine and Texture A) the AFH was the most representative parameter for hiding the scratch damage, yielding lower ΔL^* textures with higher AFH. On the contrary, the Svk was the most important parameter among surfaces with similar topographic features such as

the leather texture types, resulting in lower ΔL^* the ones with less valley depth. It can be used for predicting the surface performances against scratching.
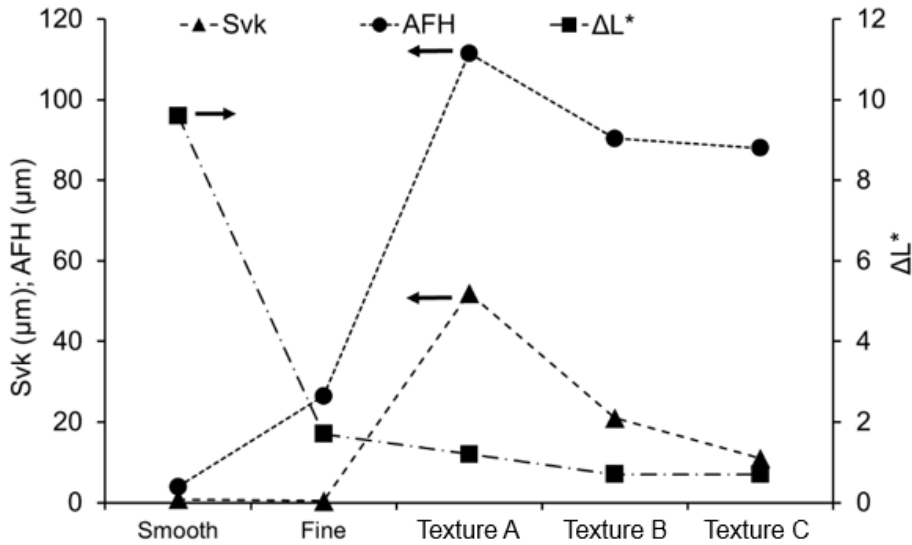

Figure 6.10 Relationship between the absolute functional height (AFH) and valleys depth (Svk) with the scratch visibility (ΔL^*). Lines are only guides for the eyes.

6.2.4. Evaluation of the mar visibility

Mar damage is the first mechanism of deformation that takes place in all type of materials when they are subjected to a compressive dynamic load. In the compression occurring during indentation, a certain amount of the material located on the top of the surface is plastically deformed. The mar damage is manifested through a variation in the surface gloss. In rough surfaces, the ironing of micro-asperities changes the in-light interaction by increasing the specular component of the reflected light. This effect can be studied through the evolution of the roughness parameters such as Sa and Sq.

In this section the smooth surface has been not considered because of the mar test can be only applied on textured surfaces.

Table 6.6 collects the roughness values of the four textured surfaces (fine, Texture A, Texture B and Texture C) and the gloss level of each surface finish. As it can be seen, the gloss

221

level decreased when the amount of micro-roughness increased. This matched well with the concept of diffuse reflectance light mode, where the micro-asperities control the amount of light reflected from the surface.

Table 6.6 Micro-roughness and gloss level results as a function of the texture type.

	Fine	Texture	Texture B	Texture C
Sa (µm)	1.4 ± 0.1	1.7 ± 0.1	2.4 ± 0.1	1.9 ± 0.1
Sq (µm)	1.8 ± 0.1	2.2 ± 0.1	2.8 ± 0.1	2.3 ± 0.1
Gloss (60º) (GU)	2.2 ± 0.1	1.7 ± 0.1	1.2 ± 0.1	1.3 ± 0.1

Figure 6.11 shows the Sa and gloss evolution as a function of the applied load. As can be seen, in all textures there was a decrement of roughness due to the micro-asperities ironing. Consequently, the surface gloss was increased. Despite having lower roughness variation than leather types, the fine texture exhibited the highest increase of gloss. In this case, the damaged area created on the surface was continuous and higher than in the other cases. For leather textures, the indenter was unable to reach the valleys of the surfaces, yielding a discontinuous track which resulted in lower gloss variations. The untreated leather texture showed the lowest variation in both Sa and Sq, and the lowest increase of gloss. Both Texture B and Texture C, which had the higher initial micro-roughness level, resulted in the higher variation of both roughness and surface gloss.
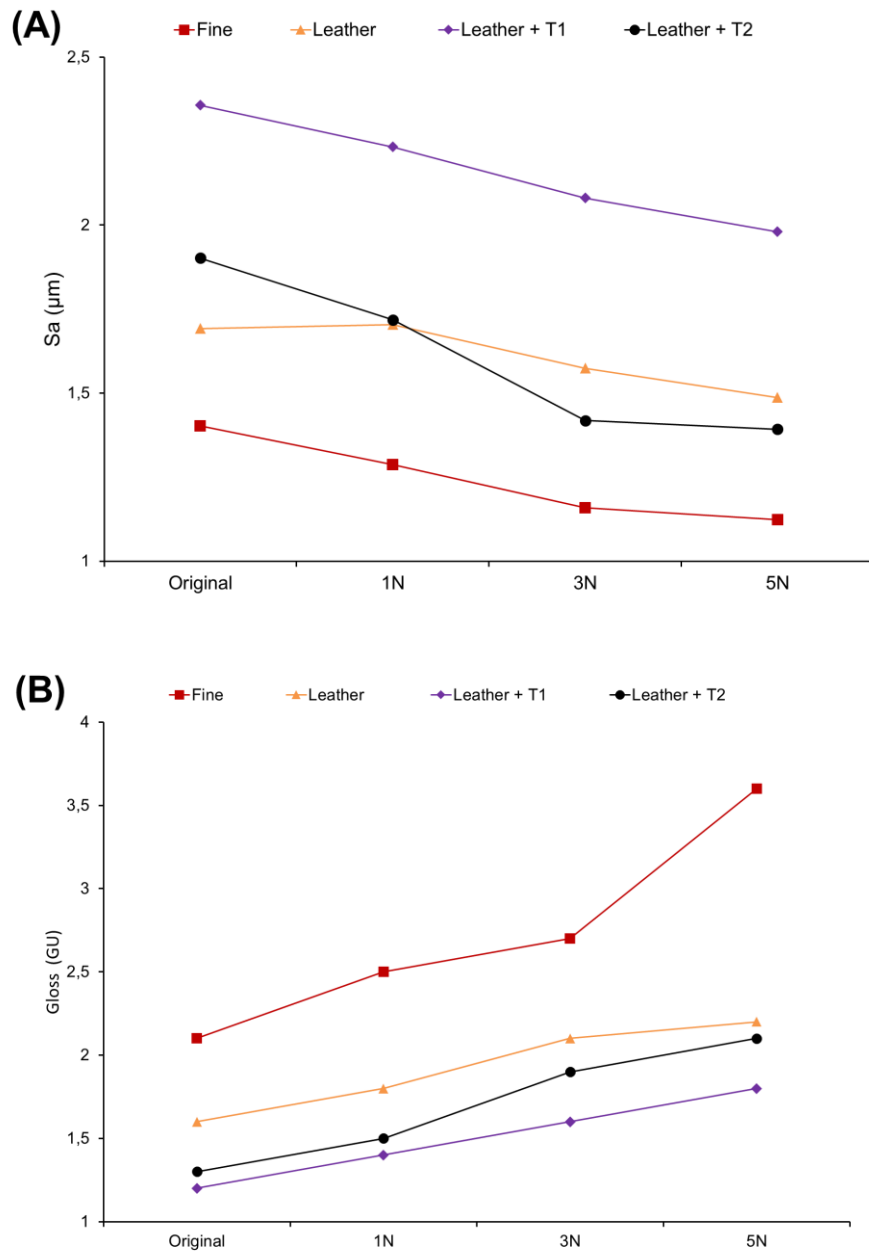
Figure 6.11 Evolution of the Sa (A) and surface gloss (B) as a function of the applied load.

The contrast measurements of all considered surfaces are represented in Figure 6.12. As it can be expected, the contrast changed in a similar way to gloss. In general, the fine texture showed the highest measured contrast, followed by Texture C and Texture B. At the applied forces, the mark left was the consequence of ironing the top micro-asperities, leading to an increase of the specular component. Therefore, it can be concluded that for a given load, the

223

larger the initial micro-roughness the larger the gloss variation reached during the mar testing, leading to easier damage detection.
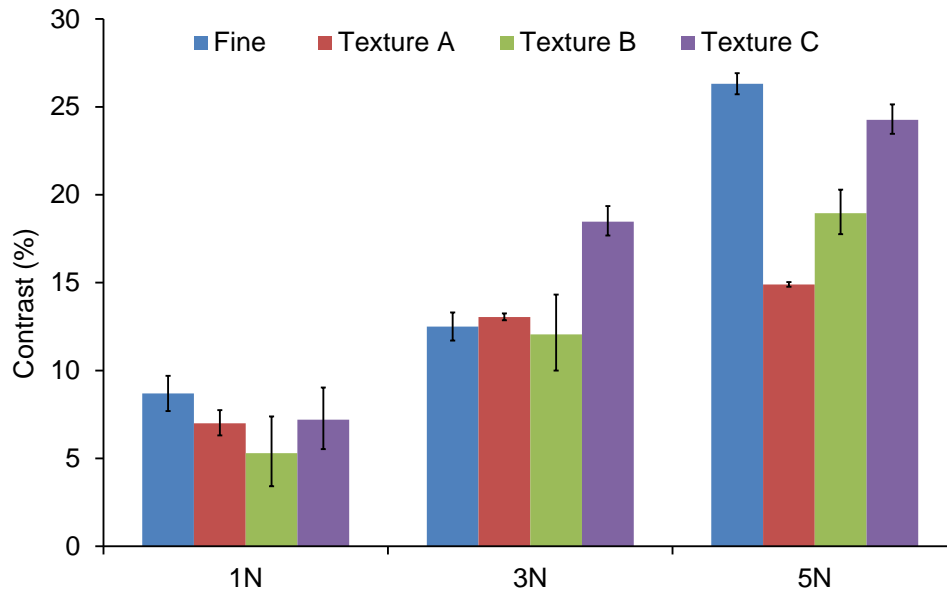

Figure 6.12 Evolution of the contrast measurements as a function of the applied load.

The mar damage created after applying a 5 N load is depicted in Figure 6.13 for the three leather textures. As it is shown, in the case of Texture A (Figure 6.13a), no significant differences can be seen between the damaged and the undamaged area. This was due to the low level of micro-roughness located on top of the surface, which yielded less plastic deformation of the micro-asperities in the direction of the indenter motion, resulting in less variation of both roughness and gloss. On the contrary, in the case of Texture B (Figure 6.13b) and Texture C (Figure 6.13c) textures, slight plastic deformation of the micro-asperities (indicated by black arrows) were found in the damaged area following the direction of the indenter motion. The resultant micro-roughness of the surfaces after the mar testing were slightly brushed, resulting in a smoother topography. The specular component increased and consequently high gloss and contrast variation were found. Therefore, in terms of mar visibility resistance, Texture A was the most suitable for obscuring the damage and thus minimizing its visibility.
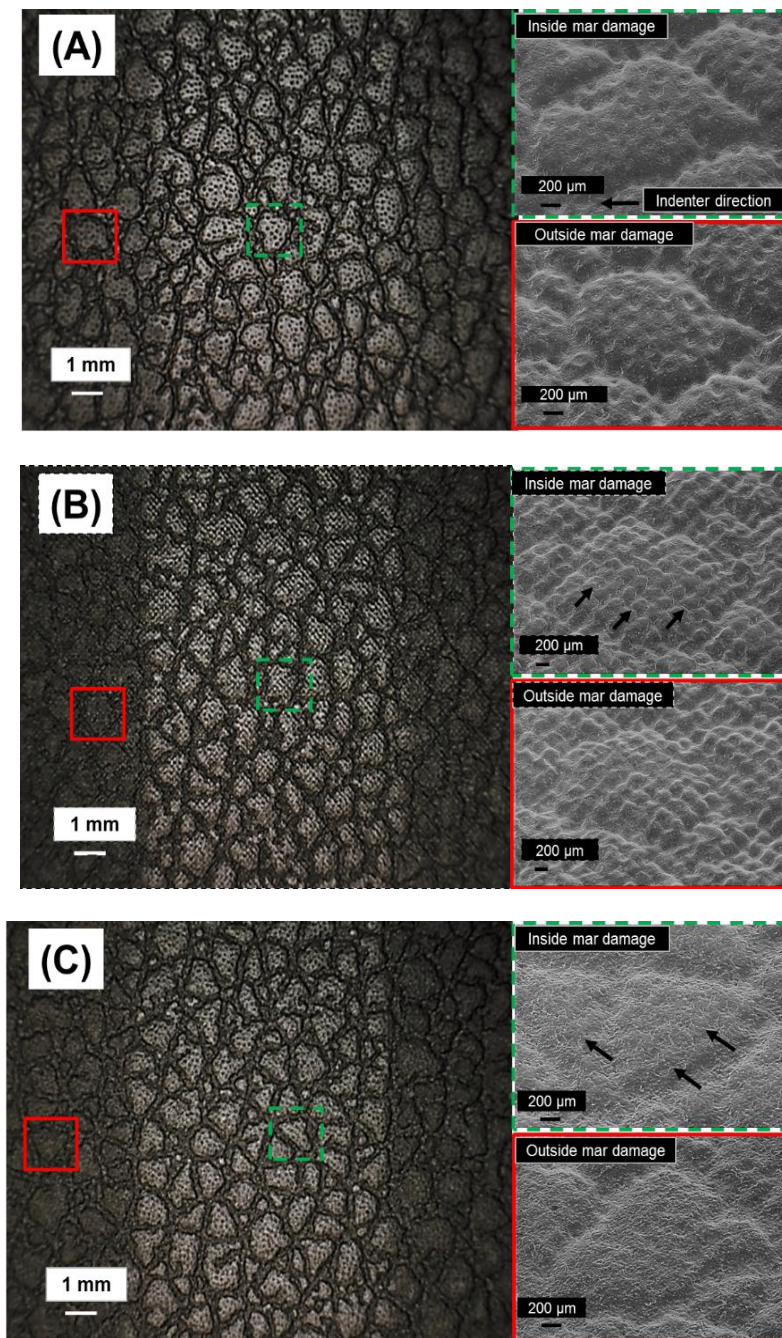
224

Figure 6.13 Mar damage visibility on (A) leather, (B) leather+T1 and (C) leather+T2 textures after applying 5N load. The black arrows in (B) and (C) show the damage induced by brushing the micro asperities in the indenter direction.

6.3. Conclusions

Surface texturing had a slight influence in enhancing the scratch hardness of polymer surfaces at low applied loads. The contact area between the indenter and the surface was limited to the finer micro-asperities, diminishing the mark left by the indenter. However, at high applied loads, surface texture had no effect. By increasing the normal load, both the micro- and the macro-texture were affected by the indenter, levelling off the scratch hardness regardless of the surface texture. Nevertheless, surface texture had an important influence on scratch visibility resistance, hiding the scratch damage.

The scratch visibility resistance of textured surfaces strongly depends on both parameters: the residual background height (RBH) and the roughness ratio between the shoulders of the groove and the original surface.

The mar visibility resistance was strongly connected with the amount of micro-asperities. The larger the micro-roughness was, the larger the gloss variation. Therefore, a higher contrast between the damaged area and its surroundings leads to an easy detection of the damaged area.

6.4. References

[1]   P. Gamonal-Repiso, M. Sánchez-Soto, S. Santos-Pinto, and M. L. Maspoch, "Influence of topography on the scratch and mar visibility resistance of randomly micro-textured surfaces," *Wear*, vol. 440–441, no. October, 2019, doi: 10.1016/j.wear.2019.203082.

[2]   C. A. Brown *et al.*, "Multiscale analyses and characterizations of surface topographies," *CIRP Ann.*, vol. 67, no. 2, pp. 839–862, 2018, doi: 10.1016/j.cirp.2018.06.001.

[3]   H. Jiang, R. L. Browning, M. M. Hossain, H. J. Sue, and M. Fujiwara, "Quantitative evaluation of scratch visibility resistance of polymers," *Appl. Surf. Sci.*, vol. 256, no. 21, pp. 6324–6329, 2010, doi: 10.1016/j.apsusc.2010.04.011.

[4]   F.W. Campbell, R.W. Gubisch, Optical quality of the human eye, The journal of physiology. 186 (1966) 558–578.

[5]   ISO 25178-2, Geometrical Product Specifications (GPS) - Surface texture: Areal - Part 2: Terms, definitions and surface texture parameters, First ed., 2012.

[6]   R. Browning, M. M. Hossain, J. Li, S. Jones, and H. J. Sue, "Contrast-based evaluation of mar resistance of thermoplastic olefins," *Tribol. Int.*, vol. 44, no. 9, pp. 1024–1031, 2011, doi: 10.1016/j.triboint.2011.04.009.

[7]   M. Hamdi and H. J. Sue, "Effect of color, gloss, and surface texture perception on scratch and mar visibility in polymers," *Mater. Des.*, vol. 83, pp. 528–535, 2015, doi: 10.1016/j.matdes.2015.06.073.

[8]   B. He, W. Chen, and Q. Jane Wang, "Surface texture effect on friction of a microtextured poly(dimethylsiloxane) (PDMS)," *Tribol. Lett.*, vol. 31, no. 3, pp. 187–197, 2008, doi: 10.1007/s11249-008-9351-0.

[9]   C. Yu, H. Yu, G. Liu, W. Chen, B. He, and Q. J. Wang, "Understanding topographic dependence of friction with micro- and nano-grooved surfaces," *Tribol. Lett.*, vol. 53, no. 1, pp. 145–156, 2014, doi: 10.1007/s11249-013-0252-5.

[10]   H. Jiang, R. Browning, J. Fincher, A. Gasbarro, S. Jones, and H. J. Sue, "Influence of surface roughness and contact load on friction coefficient and scratch behavior of thermoplastic olefins," *Appl. Surf. Sci.*, vol. 254, no. 15, pp. 4494–4499, 2008, doi: 10.1016/j.apsusc.2008.01.067.

[11]   C. J. Barr, L. Wang, J. K. Coffey, and F. Daver, "Influence of surface texturing on scratch/mar visibility for polymeric materials: a review," *J. Mater. Sci.*, vol. 52, no. 3, pp. 1221–1234, 2017, doi: 10.1007/s10853-016-0423-5.

Chapter 7: Conclusions

The research work carried out in this thesis deals with the improvement of the perceived quality of car interiors. An innovative measuring methodology based on three-dimensional techniques which allows assessing the appearance of textured injection moulded components has been developed.

1. Sampling conditions that mimic the human eye capabilities were determined. This resulted in a lateral resolution of 40 µm, for a visual distance of 200 mm, and a sampling area of 418 mm^2.

2. The effect of the injection conditions on the replication quality of the textured mould cavity was studied. The holding pressure was the most important parameter for reaching high ratios of replication. In addition, under sampling conditions that mimic the human eye, only features in the large space domain such as waviness and form can be detected.

3. The replication ratio was quantified at the micro-scale. Surface features with a size of 20-30 µm were the most representative for accurately achieving a good replica of the mould texture.

4. The new surface appearance measuring instrument named Total Appearance Measurement (TAM) was tested and set as a function of the topographical features. It was demonstrated that the TAM was a suitable device for measuring and quantifying the reflected light coming from both valleys and peaks portions, resulting in the reflectivity contrast.

5. New surface parameters such as absolute functional height (AFH), functional height distribution (FHD), texture slope (TS) and texture aperture angle (TAA) were introduced.

6. High reflectivity contrast was obtained in textures with large number of deep valleys (Svk) in their FDH and sharp TS and TAA. On the contrary, textures with a FDH governed by the core roughness height (Sk) and having less acute TS and TAA, similar reflectivity contrast to that obtained by the painted texture can be achieved.

7. The addition of treatments to the mould cavity was a suitable alternative to secondary operations such as painting with the aim of achieving greater visual appearance surfaces.

8. Texture had a positive effect on scratch harness at low applied loading. On the contrary, when high loading was applied the texture had no effect on scratch hardness.

9. Two new parameters namely, residual background height (RBH) and the roughness ratio between the shoulders of the groove and the original texture were introduced for the better understanding of the texture effect on the scratch damage visibility.

10. Textures with a RBH governed by the core roughness (Sk) and similar roughness values than those imposed by the groove shoulders were better suitable for hiding scratch damage.

11. Mar visibility resistance was strongly connected with the amount of micro-roughness of the texture. The larger number of micro-asperities the greater the contrast in gloss, leading to an easy detection.

7.1. Future research works

In order to achieve textured surfaces with a high aspect ratio and high scratch visibility resistance further research is needed. The following topics are suggested for obtaining a deeper knowledge on the appearance measurement of micro-textured components:

- Extension of the investigation of the appearance measurement and scratch visibility resistance on other textures types.

- Extension of the investigation of the appearance measurement and scratch visibility resistance on other material types such as amorphous polymers.

- Development of new textures with topographic features that enhance the appearance and the scratch visibility resistance properties.

- Study on the appearance perception by comparing textures obtained by chemical and laser engraving methodologies.

- Study on the scratch visibility resistance by comparing textures obtained by chemical and laser engraving methodologies.

Appendix:

List of publications

Publications in journals

Improvement of the replication quality of randomly micro-textured injection-moulding components using a multi-scale Surface analysis

Influence of topography on the scratch and mar visibility resistance of randomly micro-textured surfaces
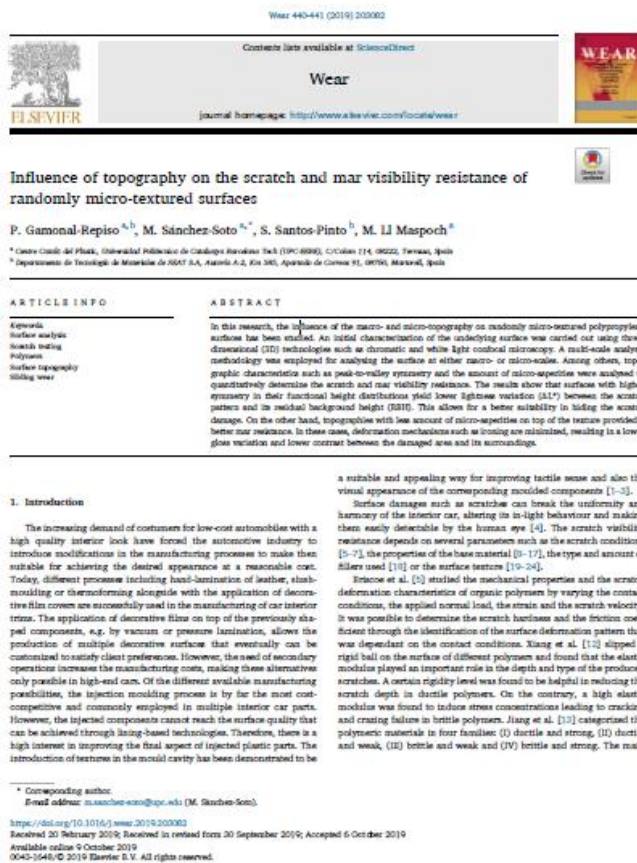
Journal: Journal of Wear.

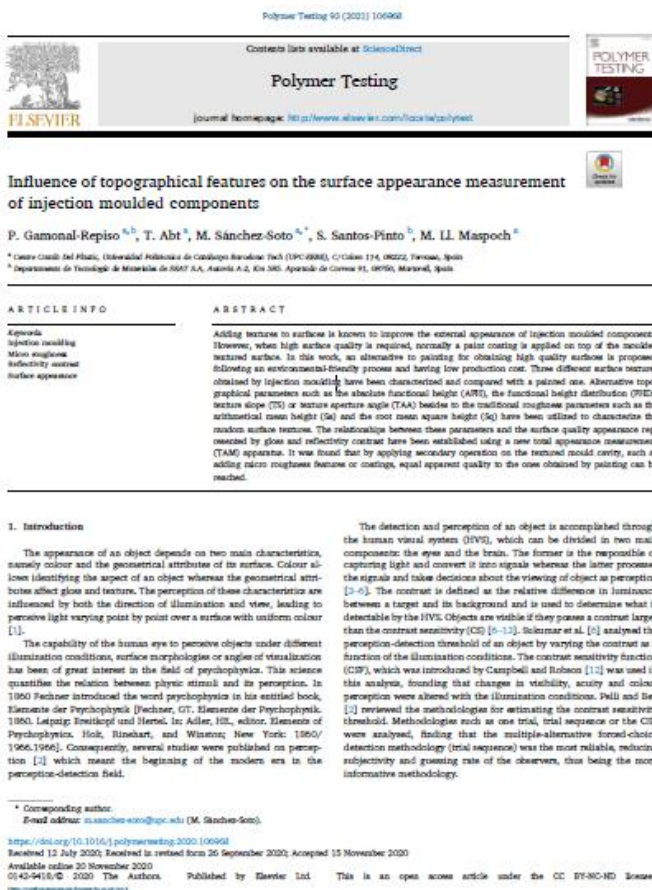**Authors:** P.Gamonal-Repiso, M.Sánchez-Soto, S. Santos-Pinto, M. Ll. Maspoch.

Year: 2019.

Volume: 440-441.

Article: 203082.

ISSN: 0043-1648.

DOI: 10.1016/j.wear.2019.203082

Influence of topographical features on the surface appearance measurement of injection moulded components

Publications derived from conferences

Surface quality: Improving quality perception of moulded parts

Surface quality: Improving quality perception of moulded parts

PhD candidate **P.Gamonal-Repiso**,SEAT S.A, Martorell (Spain);
Dr. **J.M.del-Mazo**, SEAT S.A, Martorell (Spain);
Prof.Dr. **M.Sánchez-Soto**, Centre Català del Plàstic/Universitat Politècnica de Catalunya-BarcelonaTech, Terrassa/Barcelona (Spain);

Abstract

A novel assessment method based on three dimensions technology has been proposed to analyse the surface quality of injection moulded parts. Starting from a mould having a leather texture engraved on it, the quality of the replication on the surface of a polypropylene moulded part has been studied as a function of the injection parameters. In order to establish a relationship between quality appearance and surface topography, amplitude parameters and functional parameters have been compared. White light interferometer (WLI) was used to assess the surface and scanning electron microscope (SEM) was employed to detect small features on the surface. The results indicated that, in terms of quality sensation, functional parameters are more accurate than amplitude parameters for quantify the mould replication on the polypropylene surface.

1. Introduction

Quality appearance is of great importance in the production of automotive interior parts, it is strongly connected with quality perception. The uniformity and interior harmony are the main goals to be achieved because surface differences between adjacent components gives to the customer a low quality sensation.

Nowadays, the method for assess the surface appearance is based on subjectivity and 2-dimension measurements [1]. However, this method does not provide enough surface information and several loops of optimization have to be made in order to achieve the optimal matching between components. Therefore, a novel surface assessment method based on three dimensions (3D) is necessary to adequately guarantee that the surface appearance of each component is according to the requirements.

Reaching the aims of the new method needs the standardization of the surface assessment. Suitable setting of several parameters such as, sampling area (A), sampling length (Δx, Δy) and number of data points (N, M) is required for each kind of texture. Several research have been made in order to related the surface topographic and surface appearance, for example,

Journal: Plastics in Automotive Engineering

Authors: P.Gamonal-Repiso, J. M. del-Mazo, M.Sánchez-Soto,

Year: 2017.

Conferences

Surface quality: Improving quality perception of moulded parts

Conference: XV Jornada Internacional de Plásticos en Automoción

Authors: P.Gamonal-Repiso, J. M. del-Mazo, M.Sánchez-Soto,

Date: 16th-17th May 2017.

Place: Barcelona, Spain.

Multi-scale surface analysis on polypropylene micro-textured injected samples using 3D non-contact techniques

XV Reunión del grupo especializado de polímeros (GEP)

Punta Umbría, Huelva, Spain. 24-27 September 2018.

Conference: XV Reunión del grupo especializado de polímeros (GEP)

Authors: P.Gamonal-Repiso, M.Sánchez-Soto, S. Santos-Pinto, M. Ll. Maspoch.

Date: 24th-27th September 2018.

Place: Huelva, Spain.